Numerical ice sheet modeling of Heinrich Events

by

A thesis submitted to the

School of Graduate Studies

in partial fulfilment of the

requirements for the degree of

Doctor of Philosophy

Department of Physics and Physical Oceanography

Memorial University of Newfoundland

January, 2024

St. John's Newfoundland

Abstract

Layers of Ice-Rafted Debris (IRD) found in sediment cores from the North Atlantic are attributed to quasi-periodic episodes of iceberg discharge from the Hudson Bay/Hudson Strait region. At least six such so-called Heinrich Events (HEs) have been identified during the Last Glacial Cycle (LGC). Due to the associated release of freshwater, HEs are inferred to cause climatic changes on a global scale. Several hypotheses for generating HEs, including an internally driven binge-purge model, an ice shelf buildup-collapse mechanism, and a hypothesis encompassing underwater melt modulated by Glacial Isostatic Adjustment (GIA), have been proposed in the literature. However, a comprehensive study identifying the role of individual system processes such as GIA is still missing. Here, I use 3D thermo-mechanically coupled ice sheet models, primarily the Glacial Systems Model (GSM), to identify the numerically most robust model configuration within a HE framework. Based on these results, I determine the importance of different system processes in a HE context. Model setups with varying complexity are used, including the first transient HE study covering the full LGC. Another major step forward is the first use of a fully coupled sediment model to determine the sediment discharge during HEs. To partly address potential non-linear dependencies of model results on ensemble parameters, all experiments are run with high-variance ensembles instead of a single parameter vector. Model results are then evaluated with respect to numerical uncertainties, a subset of structural uncertainties, and (revised) proxy data estimates (e.g., sediment discharge during a HE). The key takeaways of this study are the relevant physical and

numerical sensitivities in a HE context. For example, including sub-temperate basal sliding can reduce the resolution dependence of surge characteristics. However, the surge pattern is highly sensitive to the poorly constrained geothermal heat flux in the Hudson Bay and Hudson Strait. Model results further indicate that sub-surface ocean warming and ice shelves in the Labrador Sea are unlikely to be the main driver of HEs. HE characteristics based on the sediment flux modeled with the most comprehensive GSM setup generally agree with proxy constraints. However, the mid-Hudson Strait ice flux shows only a weak correlation with the sediment flux and should not be used as a metric to identify HEs. This weak correlation indicates that Heinrich Layers do not necessarily record large-scale Hudson Strait surges and questions the previously inferred climatic implications of Heinrich Events.

Dedication

For Erika and Günther.

"The greatest teacher, failure is."

— Jason Fry

Acknowledgements

I am deeply grateful to all those who have supported and encouraged me throughout this journey. I wish to express my special thanks to:

My advisor, Lev Tarasov, for his guidance and scientific support in completing my PhD and this thesis.

My co-author, Elisa Mantelli, for her mathematical insight and general support throughout the submission of my first paper.

The ArcTrain programm and all its members for providing an incredible networking and research exhange opportunity. I want to explicitly thank Anne de Vernal for her advice regarding the interpretation of proxy records.

All the fellow students of the Glacial Systems Dynamics research group at the Department of Physics and Physical Oceanography at Memorial University of Newfoundland: Benoit Lecavalier, Ryan Love, Heather Andres, and my two favorite climate modelers, Marilena Geng and Audrey Parnell. I am particularly grateful to my office mates Matthew Drew and Alexis Goffin for lighthearted yet invaluable discussions!

My good friends André, Daniel, Jonas, and Paul who started their academic journey with me.

My close friend and roommate Abdelrahman for his unwavering support and consistently being there whenever I needed assistance.

My childhood friends (in alphabetical order) Alexander, Alica, Joachim, Juliane, Lena, Madlen, Maximilian, Nikolas, Patrick, Raphael, and Tobias who continue to support me even though I moved to a different country.

Last, my family, especially my parents Erika and Günther, for their encouragement and support from the very beginning to this day.

Co-Authorship Statement

Overall thesis project and thesis introduction

The overall research project was initially described by the thesis supervisor, Dr. Lev Tarasov, and later refined by Kevin Hank. The thesis abstract, introduction, and conclusions were written by Kevin Hank with editorial input by Lev Tarasov, James LeBlanc, and Audrey Parnell.

Modeling sensitivities of thermally and hydraulically driven ice stream surge cycling

The content of this chapter is a one-to-one copy of Hank et al. (2023). Kevin Hank and Lev Tarasov conceptualized the ideas behind this study. All the authors (Kevin Hank, Lev Tarasov, and Elisa Mantelli) were involved in designing the experimental setup of the GSM. Kevin Hank designed the experimental setup for PISM and performed the modeling analysis for both models under the supervision of Lev Tarasov. All the authors contributed to the results, interpretation, and writing of the paper. The initial manuscript was greatly improved through two anonymous reviewers and the Geoscientific Model Development editor Ludovic Räss.

The comparative role of system processes in Hudson Strait ice stream cycling: a comprehensive model-based test of Heinrich event hypotheses

Kevin Hank prepared the experimental design, analysed the results, and wrote the manuscript with contributions from the co-author Lev Tarasov. Lev Tarasov provided the initial parameter vector ensemble based on a history-matching approach. Alexis Goffin provided further editorial comments.

Laurentide ice sheet sediment discharge during simulated Heinrich events with a comprehensive glaciological and sediment processes model

Kevin Hank prepared the experimental design, analysed the results, and wrote the manuscript with contributions from the co-authors Lev Tarasov and Matthew Drew. Matthew Drew provided the linked-cavity basal hydrology and sediment parameter vectors and assisted with advice regarding the sediment model.

Editorial contributions to the thesis by co-authors and colleagues did not extend to providing substantive writing for any component. Editorial contributions amounted to assisting in clarifying language to enhance readability and suggestions for contextual content.

Contents

List of Tables

List of Figures

List of Abbreviations

- AHE: Atypical Heinrich Event
- AICC: Antarctic Ice Core Chronology
- AIS: Antarctic Ice Sheet
- AMJJAS: April/May/June/July/August/September
- AMOC: Atlantic Meridional Overturning Circulation
- BP: Before Present
- CCSM3: Community Climate System Model Version 3
- CFL: Courant–Friedrichs–Lewy
- DO: Dansgaard–Oeschger
- DSDP: Deep Sea Drilling Project
- EDML: EPICA Dronning Maud Land
- EPICA: European Project for Ice Coring in Antarctica
- FB: Foxe Basin

- GHF: Geothermal Heat Flux
- GIA: Glacial Isostatic Adjustment
- GISP2: Greenland Ice Sheet Project 2
- GRIS: Greenland Ice Sheet
- GSM: Glacial Systems Model
- HB: Hudson Bay
- HE: Heinrich Event
- HEINO: Heinrich Event INtercOmparison
- HS: Hudson Strait
- HSE: Hudson Strait East
- HSHE: Hudson Strait Heinrich Event
- HSN: Hudson Strait North
- HSS: Hudson Strait South
- HSW: Hudson Strait West
- IRD: Ice-Rafted Debris
- ISM: Ice Sheet Model
- ISMIP-HEINO: Ice-Sheet Model Intercomparison Project-Heinrich Event INtercOmparison

- JJA: June/July/August
- LGC: Last Glacial Cycle
- LIS: Laurentide Ice Sheet
- MICI: Marine Ice Cliff Instability
- MIS3: Marine Isotope Stage 3
- MNEE: Minimum Numerical Error Estimate
- NGRIP: North Greenland Ice Core Project
- OF: Ocean Forcing
- OTA: Ocean Temperature Anomaly
- PDB: PeeDee Belemnite
- PDD: Positive Degree Day
- PGI: Penultimate Glacial Interval
- PISM: Parallel Ice Sheet Model
- PM: Pressure Melting
- RMSE: Root Mean Square Error
- SD: Standard Deviation
- SIA: Shallow-Ice Approximation

- SSM: Sub-Shelf Melt
- SSOW: Sub-Surface Ocean Warming
- SSS: Shallow-Shelf Approximation
- SST: Sea Surface Temperature
- Sed: Sediment
- THC: ThermoHaline Circulation
- TraCE: Transient Climate Evolution
- UB: Ungava Bay
- WAIS: Western Antarctic Ice Sheet
- dpm: disintegrations per minute
- wrt: with respect to

Chapter 1

Introduction

As the consequences of climate change begin to unfold (e.g., IPCC, 2023), it is increasingly important to provide confident predictions of future climate change to society for implementation in climate adaptation. Of the climate changes we face, instabilities within the climate system are potentially the most impactful. Instabilities are usually attributed to rapid changes followed by a cascade of events shifting the climate system from one state to another. However, instabilities are generally highly non-linear and, thereby, potentially highly sensitive to small-scale noise forcing. They are thus particularly difficult to constrain and pose substantial challenges when deciphering past dynamics (e.g., lead/lag relationships) as well as in modeling studies (e.g., deciphering between system instabilities and those triggered by numerical sensitivities).

One example of a coupled ice-climate instability are the so-called Heinrich Events (HEs). HEs are usually attributed to large armadas of icebergs drifting across the North Atlantic (40° - 55°N, Fig. 1.3) while depositing layers of Ice-Rafted Debris (IRD). At least six Heinrich Layers have been identified in sediment cores from the

North Atlantic. Heinrich Layers mainly occur between 60 kyr BP (before present) and 15 kyr BP, but there is evidence for earlier events (Table 1.2). The melting of the icebergs releases large amounts of freshwater over centuries to millennia, which has been inferred to affect the climate on a global scale (Hemming, 2004; Srokosz et al., 2012; Lauterbach et al., 2020).

While there are several hypotheses for generating Heinrich Layers, the exact mechanism remains elusive. The proposed mechanisms include an internally driven binge-purge model (MacAyeal, 1993), an ice shelf buildup-collapse mechanism (Hulbe, 1997; Hulbe et al., 2004), and underwater melt modulated by glacial isostatic adjustment (GIA, Bassis et al., 2017). However, no study, to date, has simultaneously investigated the relative role of all the relevant system processes in a model with the required minimal complexity to do so.

Abrupt system changes such as HEs are challenging to robustly model given their potential sensitivity to numerical choices and details of how the relevant dynamical equations are discretized. It is problematic that none of the modeling studies examining HEs to date have examined the numerical and discretization sensitivities in their models for these contexts (e.g., MacAyeal, 1993; Hulbe, 1997; Hulbe et al., 2004; Bassis et al., 2017; Schannwell et al., 2023). For example, a study based on a modified version of the frequently used Parallel Ice Sheet Model (PISM) reports opposite (HEs versus continuous ice streaming) model responses for different horizontal grid resolutions. However, it fails to further examine this resolution-dependency (Ziemen et al., 2019).

The purpose of this research is to improve the understanding of the underlying HE mechanism by exploring the role of system processes such as basal hydrology and

GIA while taking into account the numerical uncertainties. Due to the inclusion of the LIS in all hypotheses, the focus is specifically on the ice sheet/ice shelf part of HEs, including the role of sediment availability (later deposited as IRD in the North Atlantic) in the provenance region. The overall structure of this project follows the questions outlined below:

1. How can we differentiate the physical effect of HE-relevant processes (e.g., basal hydrology) from numerical sensitivities (e.g., specifics of the numerical solver)?

2. What are the controls on HEs?

3. Which system processes have the highest impact on HEs?

4. How much sediment is transported out of the Hudson Strait during HEs? How does this compare to the IRD records?

5. Does ice streaming continue as sediment transport across the North Atlantic ceases (longer duration of freshwater release than suggested by IRD layers)?

The following sections provide the background information and methodology necessary to conduct the research outlined above. All relevant processes are addressed in detail, starting with a broad overview of the climatic setting.

1.1 Climatic setting

In order to study HEs, it is important to understand the climatic setting in which they occurred. Most relevant processes last longer (10^2 to 10^5 yr) than our direct observations. Therefore, information about past climate changes must be obtained

from proxy records. Proxy records are found in archives of various kinds, including tree rings, ice core records, corals, speleothems, and marine and lake sediments (Bradley, 2014). They reflect climate parameters such as temperature, atmospheric composition, and sea level. Arguably, one of the most important proxy records is the δ^{18}O ratio. Briefly summarised, it provides an estimate of temperature and ice volume variations by comparing the relative proportions of ^{16}O and ^{18}O stable isotope content of water molecules with a Standard Mean Ocean Water (SMOW) (Bradley, 2014).

$$\delta^{18}\mathrm{O} = \frac{(^{18}\mathrm{O}/^{16}\mathrm{O})_{\mathrm{sample}} - (^{18}\mathrm{O}/^{16}\mathrm{O})_{\mathrm{SMOW}}}{(^{18}\mathrm{O}/^{16}\mathrm{O})_{\mathrm{SMOW}}} \cdot 10^3‰.$$

Water molecules containing the ^{16}O isotope ($H_2^{16}O$) are lighter and have a higher vapor pressure than $H_2^{18}O$. Therefore, $H_2^{16}O$ evaporates (condensates) more (less) readily, resulting in ^{18}O-depleted vapor and ^{18}O-enriched seawater. Some of the vapor is then transported to the ice sheet regions, where it initially accumulates as snow and later compacts into ^{18}O-depleted ice. This imbalance is more pronounced during cold periods, resulting in lower δ^{18}O values in ice core records. Accordingly, marine δ^{18}O records reflect the relative depletion of $H_2^{16}O$ (as it accumulates in growing glacial ice sheets) as well as temperature effects. A similar analysis can be performed for deuterium.

In this way, temperature changes of the past 800 kyr can be reconstructed from ice core records revealing eight alternating cold (glacials) and warm periods (interglacials). For the past 800 kyr, a glacial/interglacial interval lasts roughly 100 kyr (Fairbridge, 1972) and is associated with non-monotonic ice sheet growth/retreat. The Termination, a rapid warming after the maximum extent of glaciers/ice sheets

(glacial maximum), marks the end of each glacial interval. Insolation changes driven by orbital oscillations (following Milankovitch's theory (Milanković, 1941), Sec. 1.1.1) are generally accepted as the ultimate driver of glacial/interglacial intervals.

1.1.1 Milankovitch's theory

Milankovitch's theory links glacial cycle changes in Earth's climate to orbital variations in eccentricity, obliquity, and precession. Due to the gravitational effects of other planets, the Moon, and the Sun, all of the above parameters vary over time. The Earth moves on an elliptical orbit around the Sun (eccentricity). The eccentricity varies from almost circular to a maximum solar radiation difference (outside the atmosphere) of 30 % between the perihelion (position when Earth is closest to the Sun) and aphelion (Earth is farthest from the Sun, Bradley, 2014). Changes of eccentricity occur with periodicities of $\sim$ 95 kyr and $\sim$ 123 kyr as well as a long-term periodicity of $\sim$ 412 kyr. The tilt of Earth's rotational axis (obliquity) alters between 21.8° and 24.4° with a mean period of 41 kyr. Precision describes the timing of the perihelion with respect to Earth's seasons and shows periods of 23.7 kyr, 22.4 kyr, and 19 kyr. Together, the superimposition of eccentricity, obliquity, and precession alter the solar radiation received outside of the atmosphere in a complex manner (Bradley, 2014).

Milankovitch's theory is the generally accepted explanation for glacial/interglacial cycles. It is often used to tune chronologies of paleoclimate proxies to its orbital frequencies (Bradley, 2014). However, determining the exact phasing of an individual record to orbitally induced insolation changes is difficult, especially when the sedimentation rate for the record changes over time. Therefore, caution should be used

when using interpretations based upon orbitally tuned records.

Superimposed on the glacial cycles are rapid climate changes (on the order of centuries to millennia, Fig. 1.1). The most reliable temperature reconstructions of these changes are obtained for the Last Glacial Cycle (LGC). The LGC spans the interval from about 120 kyr BP (before present) to near present. Millennial-scale climate changes during the LGC, in particular between 60 and 20 kyr BP, are bundled into so-called Bond cycles. A Bond cycle is generally characterized by a sharp temperature increase followed by successively cooler Dansgaard-Oeschger Events (DO events) culminating in a HE (Bond et al., 1993; Lehman, 1993; Hicock et al., 1999; Clement and Peterson, 2008; Hodell et al., 2010). While HEs tend to occur within the coldest phases of Bond cycles, the exact sequence of events differs between individual Bond cycles in the LGC (see Fig. 1.1 for timing of events).

1.1.2 Dansgaard-Oeschger events

Abrupt climate changes within the LGC, especially between 60 kyr BP and 20 kyr BP, occur roughly every 1500 yr (Fig. 1.1) and are particularly well-dated in Greenland ice core records (Clement and Peterson, 2008). With their rapid warming (order of decades) of up to 10°C followed by a more gradual decrease (centuries), the so-called Dansgaard-Oeschger (DO) cycles have evoked interest throughout the paleoclimatological-research community (e.g., Clement and Peterson, 2008; Wunsch, 2006; Kaspi et al., 2004; Seager and Battisti, 2007). Similar cycles have been observed in paleoclimatic records around the globe, but it is challenging to determine if they are related to the DO events (abrupt warming) inferred from Greenland records

(Clement and Peterson, 2008). However, recent work indicates that the duration of DO interstadials (warm phases of DO cycles) is strongly correlated with Antarctic temperatures (Buizert and Schmittner, 2015). Long DO interstadials coincide with a warm southern hemisphere, and short DO interstadials with a cold southern hemisphere. Furthermore, there is evidence that the Antarctic temperature response to the DO cycle is a superposition of a *"spatially homogeneous oceanic bipolar seesaw mode that lags behind Northern Hemisphere climate by about 200 years, and a spatially heterogeneous atmospheric mode that is synchronous with abrupt events in the Northern Hemisphere"* (Buizert et al., 2018).

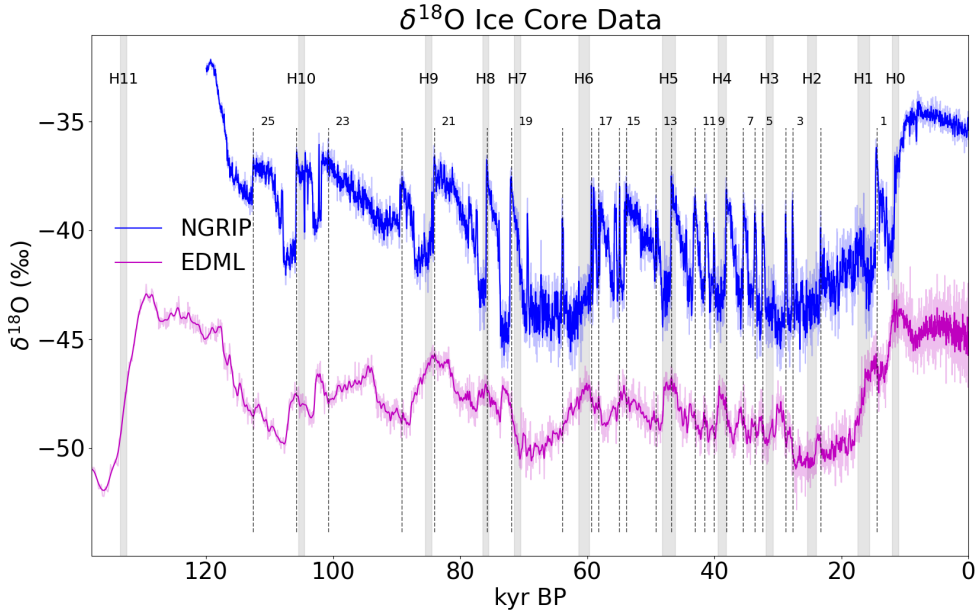

Figure 1.1: $\delta^{18}0$ records from the NGRIP (located on the Greenland Ice Sheet (GRIS)) and EDML Ice Cores (located on the Antarctic Ice Sheet (AIS)) on the synchronized time scale AICC2012 (Bazin et al., 2013; Veres et al., 2013). Refer to Tab. 1.1 and Fig. 1.3 for further information. Dansgaard-Oeschger Events (DO Events) and Heinrich Events (HEs) are marked with dashed vertical lines and grey boxes, respectively. HE time estimates are the average values in Table 1.2. Temporal uncertainties range from annual in the uppermost layers to roughly ±5 kyr at the bottom of the ice cores.

What causes DO events is still a matter of debate. The theories discussed in the literature include:

1. Freshwater input to the high-latitude North Atlantic, weakening the Thermohaline Circulation (THC) and thus altering the Atlantic Meridional Overturning Circulation (AMOC, e.g., Bond et al., 1993)

2. Ice and meltwater discharge slightly (order of 5 Sv) weakening the THC, leading to a rapidly changing sea ice distribution and thus affecting the climate through albedo and air-sea heat exchange (e.g., Kaspi et al., 2004; Wunsch, 2006)

3. Tropical processes, although no individual process in the tropics has yet been found that could account for a millennial time scale behavior (Seager and Battisti, 2007; Clement and Peterson, 2008)

4. Athmosphere, sea-ice, ocean feedback loops leading to an oscillatory climate mode that does not require a systematic trigger (Li and Born, 2019; Pedro et al., 2022)

The THC is defined as ocean currents driven by density gradients, which in turn are caused by differences in temperature (thermo) and salinity (haline). The AMOC is the zonally integrated mass circulation in the North Atlantic accounting for northward flow in the upper ocean layers and southward flow at depth. (Wunsch, 2002). Thus, the AMOC can be determined in practice, whereas the THC cannot be measured directly (Srokosz et al., 2012). THC only partially contributes to the AMOC, additional processes include wind-driven currents and tidal mixing (e.g., Bond et al., 1993).

1.2 Heinrich Events

1.2.1 Characteristics

HEs are associated with large amounts of Ice-Rafted Debris (IRD) in ocean sediment cores from the North Atlantic, particularly the Ruddiman Belt (40° - 55°N, Fig. 1.3, Ruddiman, 1977). During a HE, relatively coarse englacial sediments in icebergs and/or sea ice drift across the ocean. When the enclosing ice melts, the IRD settles on the seafloor. Proxy records indicate that these Heinrich Layers are accompanied by low salinity, temperature, and δ^{18}O values (ice cores) in the northern North Atlantic/Greenland. Temperature changes in at least the Northern Hemisphere, changes in the AMOC, and variations of the Asian-Monsoon pattern have been attributed to the release of freshwater caused by iceberg melting (Hemming, 2004; Srokosz et al., 2012; Lauterbach et al., 2020).

During the LGC, at least six IRD layers with varying characteristics (different types) have been identified in sediment records (Fig. 1.2). The average thickness of the sediment layer is about $10 - 15$ cm, leading to a total volume of 100 to 400 km^3 (Hemming, 2004). However, the IRD records are noisy (e.g., Fig. 1.2), and the associated uncertainties are large. Inferences about the duration of sediment deposition vary between 200 and 2280 yr (Hemming, 2004) with a recurrence period of 4 to 15 kyr (Table 1.2).

1.2.2 Proxy data - Ice Rafted Debris

Bramlette and Bradley (1940) were among the first to document IRD in sediments

Abbreviation	Core Name	Lat	Lon	Water depth	Uncertainty	Reference
M	MD04-2845	45.35°N	05.22°W	4100 m	500 years	Sanchez Goñi et al. (2013)
N	NEAP18K	52.77°N	30.35°W	3275 m	1 - 2 cm	Chapman and Shackleton (1999)
K	KN166-14-JPC-13	53.06°N	33.53°W	3082 m	124 years (2.5 cm)	Hodell et al. (2010)
D	DY081-GVY01	50.16°N	45.51°W	3721 m	5 cm	Zhou et al. (2020)
E	EW9303-37JPC	43.68°N	46.28°W	3981 m	2 cm	Zhou et al. (2020)
DS	DSDP94-609	49.88°N	24.24°W	3884.0 m	120 - 730 years	Bond et al. (1992)

Abbreviation	Core Name	Lat	Lon	Ice depth	Maximum age	Reference
G	GISP2	72.60°N	38.5°W	3200 m	90 ± 300 kyr	Blunier and Brook (2001)
NG	NGRIP	75.10°N	43.32°W	3084.73 m	120 ± 5 kyr	Bazin et al. (2013); Veres et al. (2013)
ED	EDML	75.00°S	0.07°E	2415.75 m	144 ± 5 kyr	Bazin et al. (2013); Veres et al. (2013)

Table 1.1: Core site Information

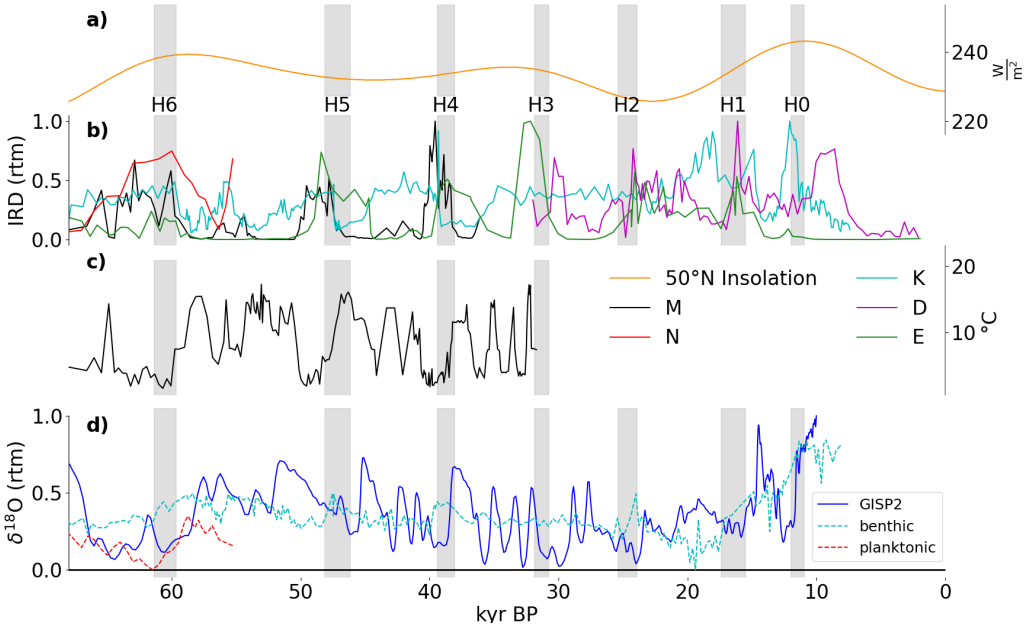

Figure 1.2: Proxy records from various core sites (references and further information are provided in Tab. 1.1). From top to bottom: **a)** 50°N summer half-year (AMJJAS) surface insolation (Tarasov, 2019), **b)** IRD (rtm = relative to maximum value), **c)** Sea Surface Temperature (SST) reconstructions, and **d)** δ^{18}O records. The color coding matches Fig. 1.3. Surface insolation is computed from the incident solar radiation at the top of the atmosphere, taking into account the zenith angle (optical mass/transmissivity) and a cloud radiative transmission factor. δ^{18}O records are benthic or planktonic (dashed lines), except for the blue line representing the GISP2 ice core record (Blunier and Brook, 2001). Benthic and planktonic δ^{18}O data have been reversed to match the pattern observed in ice cores. Heinrich Events (HE) are marked with grey boxes (time estimates are the average values in Table 1.2). Temporal uncertainties are generally not well documented for IRD records and are often stated in cm (depth within the core) without conversion to years. The uncertainties reported for the records presented here range from 120 to 730 yr. The temporal uncertainties for the ice core record GISP2 are 100 to 300 yr.

from the North Atlantic. Before the classic paper of Heinrich (1988), Ruddiman (1977) aroused interest in IRD layers in the North Atlantic within the paleoclimatic community. The term "Heinrich Events" then first appeared in Broecker et al. (1992). Up to this point, numerous definitions of HEs exist within the literature. Generally, sediment composition, particularly IRD content compared to foraminifera, and

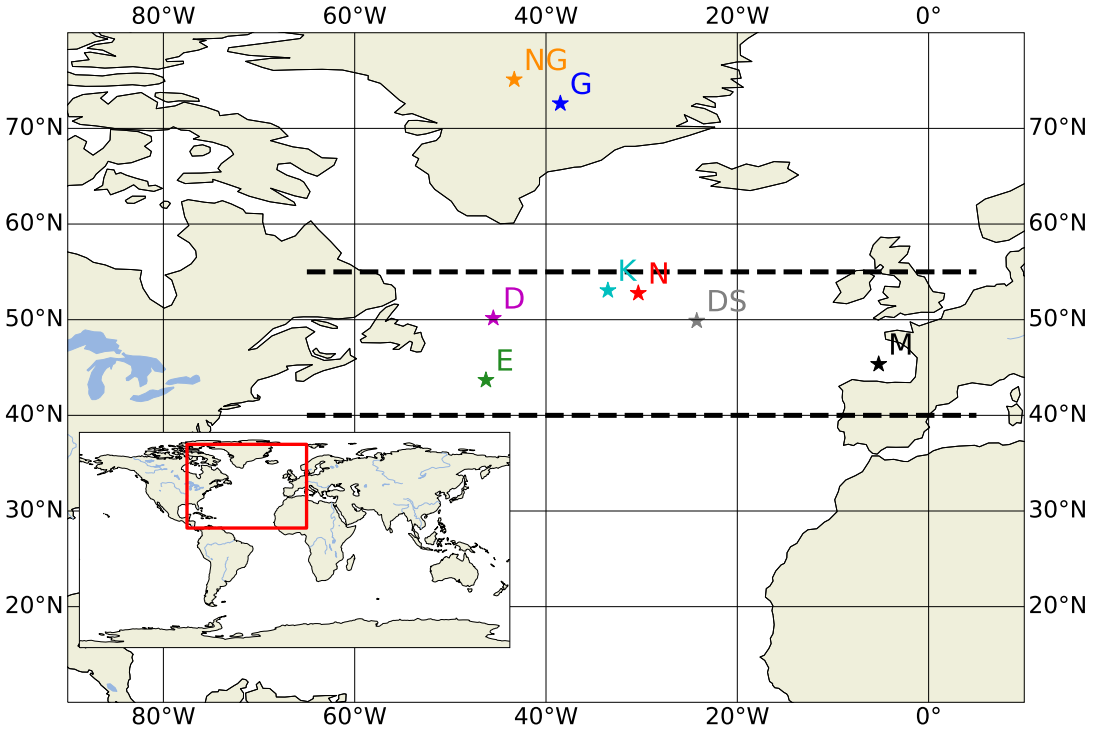

Figure 1.3: Core site locations (references and further information provided in Tab. 1.1). Dashed lines frame the Ruddiman Belt (Ruddiman, 1977). Colors and abbreviations match Fig. 1.2.

magnetic susceptibility are used to identify HEs. Foraminifera are single-celled organisms characterized by an agglutinated or secreted shell sometimes referred to as a *"test"*. With at least 38000 fossil and living species and a variable natural habitat, foraminifera are indicative of different environmental conditions. They are most abundant within seafloor sediments, near the bottom of the ocean (benthic) and the upper ocean water column (planktonic, Jones, 2014).

Following the recommendations of Andrews and Voelker (2018), *"IRD-rich events that can be attributed to a Hudson Strait mineral/geochemical source, or are located along the iceberg drift trajectory, be called Hudson Strait Heinrich events"* (HSHEs). H1, H2, H4, and H5 fall within this category (Fig. 1.2). Characteristics of HSHE

include high detrital carbonate concentration, low abundance of organic carbon and terrigenous lipids, and high magnetic susceptibility (Hemming, 2004). The remaining two events, H3 and H6 (Fig. 1.2), show additional evidence for a European source region (e.g., Iceland, Gwiazda et al., 1996b; Hemming, 2004) and are therefore referred to as Atypical Heinrich Events (AHEs, Zhou et al., 2021). Some authors even argue that AHEs do not correspond to high IRD events but low foraminifera events (Gwiazda et al., 1996b).

Uncertainties associated with Heinrich Layers

There are some difficulties when it comes to the identification of Heinrich Layers and their characteristics. First of all, Heinrich Layers are difficult to observe outside of the Ruddiman Belt (Hemming, 2004) and the layer thickness decreases towards the east of the North Atlantic (Grousset et al., 1993; Roberts et al., 2014).

Furthermore, IRD records are often noisy and the timing of HEs does not always correlate well between different core sites, even when age uncertainties are taken into account (Fig. 1.2 and Tab. 1.1). In other words, IRD records are not simple on/off records ("on" whenever a HE occurs) but also show peaks in between identified Heinrich events. For example, record K indicates high IRD content between H2 and H3 as well as H3 and H4 (Fig. 1.2). The close-by-record N (Fig. 1.3) does not cover these early events but is in good agreement for the time around H6. The two records on the west side of the Ruddiman Belt are relatively close to each other, with E located further to the South than D. They are in good agreement for H1 and H2 but place H3 at a slightly different time (Fig. 1.2). Varying age estimates derived from different proxy records can also be found in Tab. 1.2.

Heinrich Event	Marine sediments	Sanchez Goñi and Harrison (2010)	Speleothems	Average
H0	11		11.5-12.5	11-12
H1[a]	16-17.25	15.6-18.0	15.0-17.0	15.5-17.4
H2[a]	24-25.2	24.3-26.5	23.5-24.5	23.9-25.4
H3[b]	31	31.3-32.7	30.5-31.5	30.8-31.9
H4[b]	38	38.3-40.2	38.5-39.5	38.1-39.4
H5[b]	∼45	47.0-50.0	47.0-49.0	46.2-48.2
H6[b]	∼60	60.1-63.2	59.5-60.5	59.7-61.4
H7	∼71			70.5-71.5
H8	∼76			75.5-76.5
H9	∼85			84.5-85.5
H10	∼105			104.5-105.5
H11	∼133			132.5-133.5

Table 1.2: Heinrich Event age estimates [kyr BP] from Table 6.3 in Bradley (2014). The Sanchez Goñi and Harrison (2010) estimates are based on changes in vegetation indicated by pollen records. The speleothem estimates are based on the assumption that HEs were accompanied by changes in the THC. The average values are used as HE estimates throughout this thesis. For HE estimates without a range, we use ±0.5 kyr. [a] radiocarbon dates adjusted to calendar years (Hemming, 2004). [b] correlation to Greenland ice core δ^{18}O (Hemming, 2004). H7 to H11 estimates based on McManus et al. (1994) with uncertainties of probably ±5%.

Additionally, there is no clear consensus on what is considered IRD (Andrews and Voelker, 2018). In his classic paper, Heinrich (1988) used grain sizes between 180 μm and 3 mm. In contrast, Ruddiman (1977) defined grain sizes larger than 150 μm as IRD. This is rather problematic because the grain size distribution is not uniform but multi-modal (Andrews, 2000).

Further issues arise concerning the origin of Heinrich Layers. Geochemical proxies, such as Pb, Sm-Nd, Rb-Sr, and K/Ar isotopes, can determine the sediment's age and provenance. However, some of these isotope systems, for example, K/Ar, are easily disturbed by geological processes (e.g., metamorphic resetting by a break down and

reformation of the mineral host) and thus might reflect only the age of the last disturbance (Hemming, 2004).

Sediment flux estimates can be derived from $^{230}\mathrm{Th}_{\mathrm{excess}}$ data (McManus et al., 1998). The ocean water is well mixed with respect to ^{234}U and ^{238}U (residence time of $\sim 4 \cdot 10^5$ yr). Their daughter isotope ^{230}Th is extremely particle reactive and rapidly removed from the water column. The quantity of ^{230}Th available for burial thus depends mostly on the water depth (larger quantities for increasing water depth). Once buried, ^{230}Th is unsupported by (separated from) further decay of ^{234}U and ^{238}U (parent isotopes), a process known as daughter excess (Bradley, 2014). Under the assumption of a constant burial rate and independently derived ages, sedimentation rates can then be derived from sediment cores (McManus et al., 1998; Hemming, 2004). HEs are represented as minima (high sediment flux) in the $^{230}\mathrm{Th}_{\mathrm{excess}}$ records (Fig. 1.4). The $^{230}\mathrm{Th}_{\mathrm{excess}}$ record can be converted into mass flux F $\left[\frac{\mathrm{g}}{\mathrm{cm}^2\mathrm{ka}}\right]$ by using

$$F = \frac{Bz}{^{230}\mathrm{Th}_{\mathrm{xs}}} \tag{1.1}$$

where B is the rate of production of ^{230}Th from ^{234}U in seawater (B $= 2.63 \cdot 10^{-5} \frac{\mathrm{dpm}}{\mathrm{cm}^3\mathrm{ka}}$, dpm = disintegrations per minute) and z is water depth in cm (McManus et al., 1998).

The sediment flux records, as well as the IRD records, show evidence of ice-rafting cycles in intervals between HEs (Fig. 1.2 and 1.4). Bond and Lotti (1995) find a $2-3$ kyr periodicity coinciding with DO events and suggest a climate or climate-related forcing mechanism.

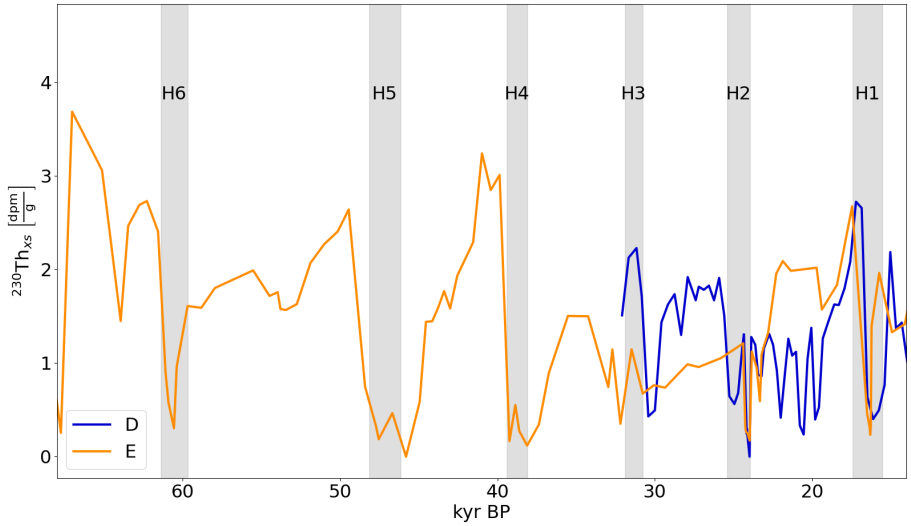

Figure 1.4: Two $^{230}Th_{excess}$ records from North Atlantic core sites (dpm = disintegrations per minute). Heinrich Events (HEs) are marked with grey boxes (time estimates are the average values in Table 1.2). Refer to Tab. 1.1 and Fig. 1.3 for references and further information regarding the cores.

Evidence of earlier HEs

In addition to the classic six HEs (H1 - H6), further IRD peaks can be identified in sediment records (Fig. 1.5 and Tab. 1.2, Rasmussen et al., 2003; Bradley, 2014). Record M, located at the eastern end of the Ruddiman Belt (Fig. 1.3), shows only small peaks or no signs for some of these older events (H7 - H10), possibly indicating that they did not reach this far east. Furthermore, there is little evidence of events H7 - H9 in record E (Fig. 1.5), indicating that these events did not reach as far south.

Going back even further in time, e.g., to the Penultimate Glacial Interval (PGI), less information about HEs is available (Hemming, 2004). However, the first occurrence of HEs (detrital carbonate layers) is dated to about 650 kry BP (Hodell and Curtis, 2008; Hodell and Channell, 2016). Whether these early events were driven by

the same processes and had the same provenance as during the LGC is unclear.

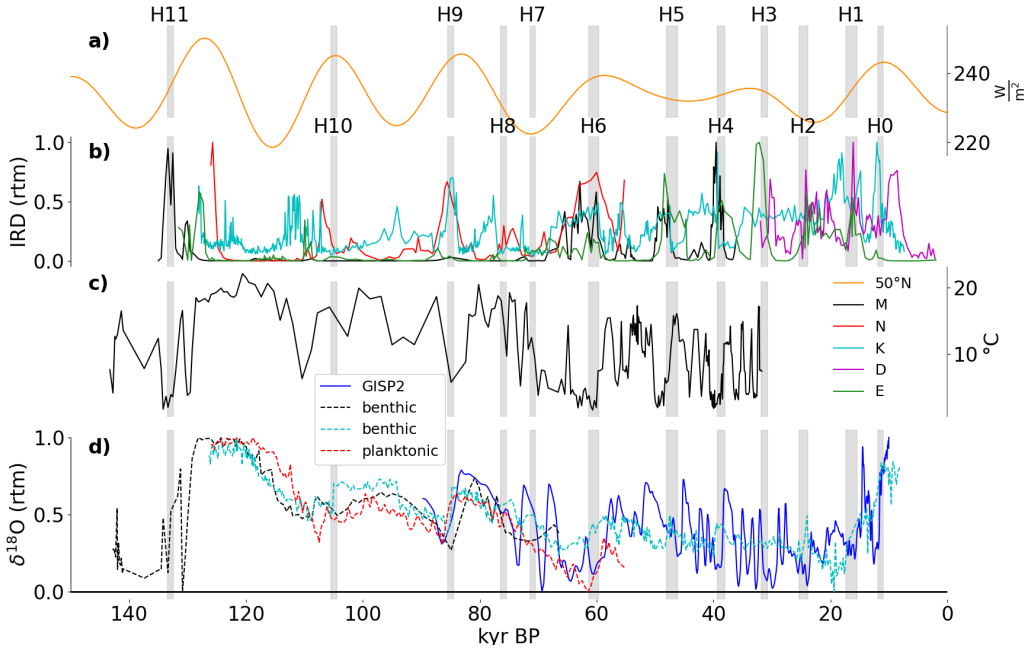

Figure 1.5: Proxy records from various core sites (references and further information are provided in Tab. 1.1) from 150 kyr BP to present-day. From top to bottom: **a)** 50°N summer half-year (AMJJAS) surface insolation (Tarasov, 2019), **b)** IRD (rtm = relative to maximum value), **c)** Sea Surface Temperature (SST) reconstructions, and **d)** δ^{18}O records. The color coding matches Fig. 1.3. Otherwise as Fig. 1.2.

1.2.3 Hypotheses and driving mechanisms

Several different HE hypotheses have been suggested over the years, three of which are discussed here. The hypotheses are an internally driven binge-purge model (Sec. 1.2.3.1), an ice shelf buildup-collapse mechanism (Sec. 1.2.3.2), and underwater melt modulated by glacial isostatic adjustment (Sec. 1.2.3.3). A brief description followed by a critical evaluation is provided for each mechanism. First, the criteria according to which the hypotheses will be evaluated are defined. A successful HE

mechanism must fulfill various requirements:

- Production of sufficient IRD
- Distribution across the North Atlantic
- Limited North American provenance and synchronization with Icelandic and European sediment discharge
- Association with the Bond cycles (occurrence within coldest phases, followed by a sharp temperature increase)
- Ocean circulation changes in, at least, the North Atlantic indicated by proxy records (e.g., ^{13}C, ^{14}C, Cd/Ca (cadmium-to-calcium ratio) in planktonic and benthic foraminifera Srokosz et al., 2012)

1.2.3.1 Internally driven binge-purge model

The first proposed HE mechanism is an internally driven binge-purge model. In his original modeling experiments, MacAyeal (1993) assumes a fixed external climate system (e.g., snow accumulation rate) with a uniform sea-level temperature below the melting point of ice. He further assumes a constant atmospheric lapse rate and Geothermal Heat Flux (GHF). The effects of slow, creeping ice flow are disregarded, and a cold-based ice column is therefore assumed to be stagnant. Changes in ice thickness (equal to the surface elevation because the ice sheet rests on a sea-level bedrock platform) are then defined by the atmospheric lapse rate and Clausius-Clapyron relationship. The GHF is set to a sufficiently large value to eventually overcome the effect of heat conduction to the surface and thus warms the base of the ice column to the pressure melting point. Once the melting point is reached, the ice column starts to flow and thin (surge onset). MacAyeal (1993) uses a simple e-fold decay time

constant to determine the thinning rate. The ice bed is kept at the pressure melting point by a combination of frictional energy dissipation and GHF. Once the temperature gradient in the ice column becomes too large, the bed starts to refreeze and ends the surge. This marks the start of the next binge phase. Despite the simplicity of this approach, the mechanism is capable of predicting HE periodicities within the range of recurrence times of Heinrich Layers (e.g., Hemming, 2004). However, the exact periodicity depends on several variables, including the atmospheric lapse rate and sea level temperature of the atmosphere (MacAyeal, 1993).

When additionally considering the heat source contributions from deformation work and basal sliding, a surge can be caused by the upstream migration of fast ice flow (Payne, 1995; Calov et al., 2002, e.g.,). Localized warm-based ice streaming near the ice sheet margin increases the ice sheet surface gradient (steeper slope) at the warm/cold-based transition point, leading to an increase in driving stress. The generation of additional heat warms the surrounding ice to the pressure melting point. The presence of water at the ice sheet/bed interface as well as in a deformable sediment layer can further increase ice velocities. Fowler and Schiavi (1998) call this sequence of events the propagation of an *"activation wave"*. Instead of the slow deformation flow (ice creep), the ice sheet now destabilizes rapidly (purge phase). As a consequence of the high ice velocities, the ice sheet thins and cold ice is advected from either upstream or the boundaries of the ice stream. Cold ice advection in combination with changing heat source contributions (from both deformation work and basal sliding) and lowering of the pressure melting point as ice thins eventually leads to refreezing of the ice/bed interface. The first localized frozen patch of ice acts as a *pinning point*, supporting some of the driving stress and decreasing the

velocities and heat generation in the surrounding. This *"deactivation wave"* (Fowler and Schiavi, 1998) ends the surge and the ice sheet enters the next binge phase.

Refer to Chapters 2 and 3 for a description of ice stream surge cycling (binge-purge mechanism) in the GSM.

The binge-purge mechanism is consistent with the sharp onset of HEs, and the freshwater flux related to the surge phase is capable of explaining ocean circulation changes as well as possible effects on the global climate. However, none of the external (non-LIS) relations are explicitly considered in the mechanism. Thus, it fails to explain the synchronization with Icelandic and European sediment discharge and the timing with the coldest phases of the Bond cycles. Calov et al. (2002) argue that the timing of the surges might be phase-locked to the DO events by small ice shelf perturbations in the Hudson Strait mouth recurring every 1500 yr. Sea level rise caused by other ice sheets is cited as a potential driver of the ice shelf perturbation (Calov et al., 2002), but this has yet to be confidently tested. The focus on Hudson Bay/Hudson Strait limits the source region of IRD, but sediment availability, entrainment, and transport across the North Atlantic are generally not considered in the original study (MacAyeal, 1993). Outstanding questions associated with this mechanism are:

1. What ultimately initiates a surge and controls the period and duration?

2. What mechanism can link surges to the observed LIS-external relations, e.g., the approximate synchronization with the coldest phases of the Bond cycles and inferred ocean circulation changes (Sec. 1.2.1)?

3. Given the topographic lateral bounds of the Hudson Strait, what is the role of topography on surges?

4. In what ways are sedimentary processes involved?

1.2.3.2 Ice shelf buildup-collapse mechanism

Similar to the disintegration of the Larsen A and B ice shelf (Hulbe et al., 2004), Hulbe (1997) postulates ice shelf buildup/collapse as the driving mechanism of HEs. Ice shelves in the Labrador Sea (or fringing ice shelves along the Canadian coast) grow during the cold phases of the Bond cycles. Sediment-laden icebergs calved from the ice shelf front drift across the North Atlantic and deposit IRD in the Ruddiman Belt. The warming attributed to DO events causes ice-shelf retreat and the end of IRD transport across the ocean.

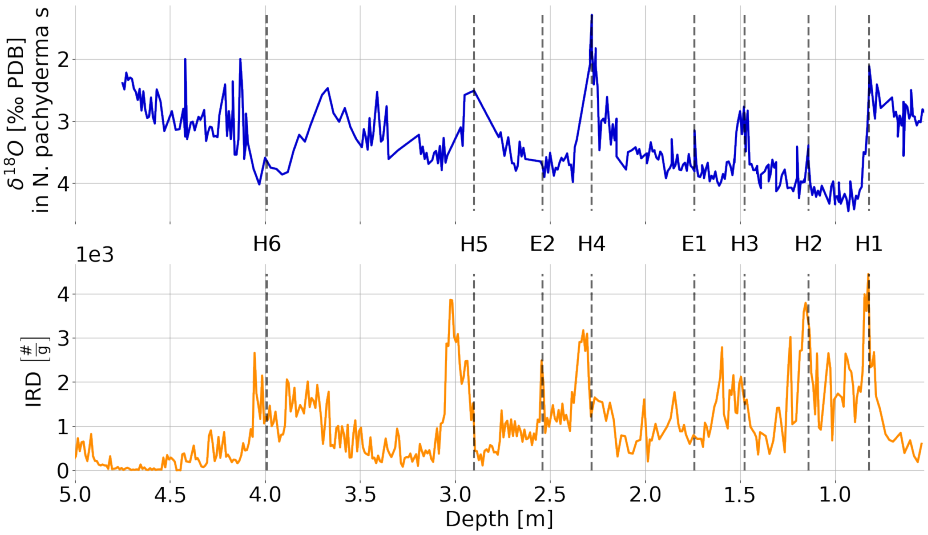

Figure 1.6: δ^{18}O data (top) and IRD (bottom) from the DSDP (Deep Sea Drilling Project) core 94-609 (Bond et al., 1992). δ^{18}O values were determined in Neogloboquadrina pachyderma sinistral with respect to PDB (PeeDee Belemnite) standard and IRD was counted for the > 150 μm fraction. Vertical dashed lines mark the warmest point of the sharp temperature increase after each HE (H1 - H6). E1 and E2 represent exceptions from the regular pattern. Refer to the text, Tab. 1.1 and Fig. 1.3 for further information.

In contrast to the binge-purge model, this mechanism is driven by external climate forcing (Hulbe, 1997). Surges of the LIS are not required. However, the ultimate driver of DO events and the associated ice shelf growth/disintegration cycle remains debated (Sec. 1.1.2 and Hulbe et al., 2004). Additionally, not every DO event leads to an IRD layer (Fig. 1.1), suggesting a threshold within the system. This threshold could be related to the magnitude or duration of each cold period (Hulbe, 1997). Therefore, only the most extreme atmospheric and sea surface cold conditions would allow ice shelf buildup. In general, these extreme cold conditions are consistent with IRD layers recorded in the DSDP609 (Fig. 1.6) and V23-81 cores (Bond et al., 1992; Broecker et al., 1992; Hemming, 2004). However, IRD datasets are noisy and contain exceptions to this general pattern. For example, some warm peaks do not immediately follow an increase in IRD counts (e.g., Fig. 1.6 E1), and some IRD peaks do not show a corresponding temperature increase (e.g., Fig. 1.6 E2). Furthermore, proxy data showing warm surface waters preceding some HEs and continuously active primary productivity (e.g., foraminifera, both indicating a mostly ice-free ocean) in the Labrador Sea have raised concerns about an ice shelf mechanism (Hesse et al., 1999; Vernal et al., 2000; Gibb et al., 2014).

Leaving the above issues aside for now, the ice shelf buildup/collapse hypothesis directly incorporates sedimentary processes. Ice streams (not necessarily surging) transport terrigenous sediments to the ice shelf. The deepest parts of the ice shelf melt, depositing IRD in the Labrador Sea and creating buoyant meltwater plumes. These plumes refreeze and underplate the flanks of the ice shelf, increasing the residence time in ice drifting across the North Atlantic (Hulbe, 1997). In the revised ice shelf mechanism, capsized icebergs allow IRD to be transported over even longer

distances and provide an explanation for gradual debris melt-out (Hulbe et al., 2004). As for the binge-purge hypothesis, changes in ocean circulation and possible global climate impacts are explained by freshwater fluxes. Since this hypothesis does not necessarily involve a surge and, therefore, only a smaller increase in freshwater flux due to the ice shelf collapse, this explanation is weaker than for the binge-purge hypothesis. Questions arising when dealing with this mechanism are:

1. How are the (fringing) ice shelves distributed and is that distribution in line with a limited provenance?

2. Is there a temperature/duration threshold for ice shelf buildup that can explain the inferred phasing with Bond cycles?

3. Are the proposed sedimentary processes sufficient to explain the observed IRD layers?

4. Can the disintegration of an ice shelf (including the potential decrease in buttressing) and the consequential increase in freshwater flux explain the inferred ocean circulation changes?

1.2.3.3 Underwater melt modulated by glacial isostatic adjustment

A more recent study suggests increased underwater melt caused by variations in the overturning circulation as the driving force of HEs (Bassis et al., 2017). In this model, a marine-based ice stream rests on a reverse-sloping bed. A marine-based ice stream (or ice sheet) is grounded below sea level and its margin terminates in the ocean. A present-day example of a marine-based ice sheet is the Western Antarctic

Ice Sheet (WAIS). In contrast, terrestrial ice sheets (e.g., the Greenland Ice Sheet (GRIS)) rest predominantly on land. Ice shelves are not considered in this model. At its most advanced position, the marine-based ice sheet terminus extends beyond a glacial isostatically depressed sill and is vulnerable to sub-surface ocean warming. Bassis et al. (2017) choose to apply a simplified sub-marine melt rate. In particular, an effective ablation rate that is largest at the ice sheet terminus and 0 at a horizontal distance of one ice thickness is used. This imposed gradient in applied sub-marine melt steepens the ice sheet surface slope and thus increases the driving stress near the ice sheet front. Following the Marine Ice Cliff Instability (MICI), calving increases and the ice sheet retreats. The MICI postulates that the yield strength of ice (about 1 MPa) limits the sub-aerial ice cliff height (above water) at the grounding line. Once longitudinal stresses exceed the yield strength, catastrophic cliff failures occur.

The retreat ceases when GIA uplifts the bed and an elevated sill isolates the ice sheet from ocean forcing. The subsequent decreases in ablation, surface slope, driving stress, and calving stabilize the ice sheet and enable the advance to its previous extent. During the regrowth phase, the uplifted bed and sill protect the ice sheet from the next sub-surface ocean warming. Pulses of sub-surface (below 250 m in Bassis et al., 2017) ocean warming are prescribed for every DO-event and, therefore, also occur between HEs.

This model is consistent with cold air temperatures during HEs and requires no ice shelf. In contrast to the two previously presented hypotheses, changes in ocean circulation are not merely a cause of freshwater fluxes but an actual trigger.

As for the ultimate driver of the ice shelf buildup-collapse mechanism, different hypotheses regarding the cause of the sub-surface ocean warming pulses during DO-

events are under ongoing debate (Sec. 1.1.2).

Applying a constant atmospheric forcing and identical ocean forcing for all DO-stadials (cold periods), the model of Bassis et al. (2017) is in general agreement with the timing and magnitude of all HEs except HE 5a, which has not been considered in this evaluation so far. Here, magnitude refers to a rise in the eustatic sea level caused by the retreat of the LIS. Estimated values in the literature range from 2 ± 1 m (Roberts et al., 2014) to $3 - 15$ m (Hemming, 2004). Bassis et al. (2017) predict an average rise of 2 m.

It is, however, not surprising that the timing of Heinrich Events in the model agrees with proxy records since the sub-surface ocean warming pulses are aligned with the DO-events observed in the NGRIP ice core record. Furthermore, model results in agreement with proxy records do not necessarily validate the physical model itself, especially given the uncertainties associated with proxy records and simplifying assumptions used in the model setup. The most relevant of these assumptions is the exclusion of thermodynamics, which automatically rules out the possibility of HEs triggered by a binge-purge type mechanism. While using a 2D flowline/3D regional model restricted to the Hudson Strait ice stream catchment basin ensures a limited source region, it also neglects possible interactions with ice sheet processes outside of this domain (Bassis et al., 2017). Sediment processes are not directly considered. Furthermore, the implementation of sub-marine melt as surface ablation (increasing the driving stress near the ice sheet front) does not represent the actual physical process, and the assumption of identical ocean forcing for all DO-stadials does not account for the variability of DO-events observed in ice core records (Fig. 1.1).

The model also displays small calving events in between HEs. Observations off-

shore of the Hudson Strait provide evidence for these smaller peaks, but due to the inherent uncertainties (in, e.g., time scales and interpolations between radiocarbon dates), they should be treated with caution (Andrews and Barber, 2002). Furthermore, HE characteristics in the model show high sensitivity to GIA parameters, e.g., mantle viscosity (Bassis et al., 2017), which are known to be poorly constrained (Rovere et al., 2014; Dutton et al., 2015).

Unresolved questions related to this HE hypothesis are:

1. What is the exact form of the ocean forcing, and what ultimately causes it?
2. What is the role of small calving events in between HEs?
3. What are the effects of the LIS outside of the modeled domain on this HE mechanism?
4. How sensitive is this mechanism to GIA and its parameters?
5. In what ways are sedimentary processes involved with respect to generating the observed IRD record?

1.2.3.4 Role of system processes

Only one of the above HE hypotheses discussed directly addresses sedimentary processes. As outlined in Sec. 1.2.2, the estimates of, e.g., the duration and period of HEs were mainly retrieved from IRD data. However, the link between sediment deposition in the Ruddiman Belt and the HE mechanism at the source region is not straightforward and requires careful consideration of sediment availability, entrainment, and transport. Otherwise, all the information is based on the assumption that sediment

transport correlates reasonably well with ice flux (in the form of icebergs and/or sea ice) across the North Atlantic. However, to date, this critical assumption of correlation has not been tested by data or modeling. Even for a continuously active Hudson Strait ice stream during the LGC, the sediment discharge might vary depending on the englacial sediment concentration. The englacial sediment volume and distribution are determined by the sediment availability in the source region, the respective entrainment mechanism, and englacial sediment transport. Another aspect affecting the North Atlantic sediment deposition is the preservation of englacial sediment in the icebergs until the Ruddiman Belt is reached (e.g., Fendrock et al., 2023). Therefore, the duration of high ice flux might be longer than suggested by the IRD records.

In conclusion, all of the proposed mechanisms have their advantages and drawbacks. Furthermore, it may well be that a combination of processes is involved (Hemming, 2004). For example, ocean warming leads to the removal of the buttressing effect of ice shelves on a marine-based ice sheet. The ice sheet terminus retreats over a reverse-sloping bed, fostering increased ice flux. Glacial isostatic uplift isolates the ice sheet front from the warm ocean water and allows the ice sheet to regrow.

A mechanism combining the original hypotheses also inherits some of their issues. Topography now determines the path of ice streams, directly affects HEs via different reverse-sloping beds, and is sensitive to the GIA model (including the GIA parameters). In addition to their role as a source of icebergs, the buttressing effect of (fringing) ice shelves now plays a critical role in the timing of surges. Therefore, determining the ice shelf distribution becomes an even more important component. Since the ocean forcing interferes with ice shelf buildup and causes ice sheet retreat, constraining its form and possible causes is essential. Finally, sedimentary processes

have to be considered for ice streams and ice shelves simultaneously. These key aspects have led to the research questions outlined in Sec. 1.4.

1.3 Thesis outline

The overall structure of the thesis is as follows:

- Chapter 2: Publication 1 (**P1**) - Modeling sensitivities of thermally and hydraulically driven ice stream surge cycling
- Chapter 3: Publication 2 (**P2**) - The comparative role of system processes in Hudson Strait ice stream cycling: a comprehensive model-based test of Heinrich event hypotheses
- Chapter 4: Publication 3 (**P3**) - Laurentide ice sheet sediment discharge during simulated Heinrich events with a comprehensive glaciological and sediment processes model
- Chapter 5: Conclusions

1.4 Research questions

The issues identified above relating to HEs and their potential causes lead to the research questions addressed in this study:

RQ_1 How accurately can a numerical ice sheet model (North American model domain, transient LGC climate forcing, no additional HE triggers) capture the

HE characteristics observed in proxy records (**P1**,**P2**,**P3**)? Aspects considered include:

- timing of HEs within the LGC, especially in relation to Bond cycles and DO events
- HE duration and periodicity
- uncertainties associated with the numerical model and the proxy records

RQ_2 What are the relative roles of different aspects of the interconnected glacial system in HEs (**P1**,**P2**)? System components considered include:

- topography
- GIA
- basal hydrology
- thermal processes at the ice sheet bed
- sub-surface ocean warming
- ice shelf dynamics

RQ_3 How much sediment is discharged during an average HE, and what are the key North American provenances (**P3**)?

RQ_4 How well correlated is sediment discharge with the occurrence of ice stream surge cycling (**P3**)?

Preface to Chapter 2: "P1: Modeling sensitivities of thermally and hydraulically driven ice stream surge cycling"

The content of this chapter is a one-to-one copy of Hank et al. (2023). The GSM is run with an idealized down-scaled North American geometry and simplified climate representation. The numerical and discretization sensitivities examined here are used to identify the numerically most robust model configuration later adapted in Chap. 3 and 4. The results and conclusions lay the groundwork to determine the physical significance of all results presented within this thesis.

Chapter 2

P1: Modeling sensitivities of thermally and hydraulically driven ice stream surge cycling

Abstract

Modeling ice sheet instabilities is a numerical challenge of potentially high real-world relevance. Yet, differentiating between the impacts of model physics, numerical implementation choices, and numerical errors is not straightforward. Here, we use an idealized North American geometry and climate representation (similarly to the HEINO (Heinrich Event INtercOmparison) experiments – Calov et al., 2010) to examine the process and numerical sensitivity of ice stream surge cycling in ice flow models. Through sensitivity tests, we identify some numerical requirements for a more robust model configuration for such contexts. To partly address model-specific de-

pendencies, we use both the Glacial Systems Model (GSM) and the Parallel Ice Sheet Model (PISM). We show that modeled surge characteristics are resolution dependent, though they converge (decreased differences between resolutions) at finer horizontal grid resolutions. Discrepancies between fine and coarse horizontal grid resolutions can be reduced by incorporating sliding at sub-freezing temperatures. The inclusion of basal hydrology increases the ice volume lost during surges, whereas the dampening of basal-temperature changes due to a bed thermal model leads to a decrease.

2.1 Motivation and background

The use of ice sheet models has grown by at least 1 order of magnitude over the last 2 decades. The relevance of such modeling studies to the actual physical system can be unclear without careful consideration and testing of numerical aspects and implementations. This is especially true when modeling the highly non-linear ice sheet surge instability, which has significant implications not only for the ice sheet itself but also for the climate. In fact, it is often difficult to assess whether model results are physically significant (effects of physical system processes), a consequence of model-specific numerical choices, or a combination of both. Whether ice sheet instabilities observed in numerical simulations are the result of physical instabilities of the underlying continuum models or of spurious effects of the discretization and numerical implementation of said models has long been debated (e.g., Payne et al., 2000; Hindmarsh, 2009) and is a consequential matter. The present study is concerned with characterizing the impact of model physics, numerical choices, and numerical errors on ice stream surge cycling.

Binge–purge ice stream cycling was first introduced in the glaciological literature by MacAyeal (1993) as an explanation for Heinrich events arising from the former Laurentide Ice Sheet (LIS) in the Hudson Bay–Hudson Strait region. The key idea is that the ice stream gradually grows to a threshold thickness (binge phase) driven by surface accumulation. Once the ice stream is thick enough to sufficiently isolate the ice stream base from the cold surface, heat from geothermal and deformation work sources can slowly bring the basal temperature to the pressure-melting point. The bottom layer of the ice stream is no longer frozen to the bed and thus enables basal sliding. Localized warm-based ice streaming increases the ice stream surface gradient (steeper slope) at the warm–cold-based transition point, leading to an increase in driving stress. The resultant increase of heat from deformation work can warm the surrounding ice (close) to the pressure-melting point, thus enabling (sub-temperate) basal sliding (Fowler, 1986). When the melting point is reached, the presence of water at the ice sheet–bed interface (Fowler and Schiavi, 1998) and in a deformable sediment layer (Bueler and Brown, 2009) can further increase sliding velocities. Instead of the slow deformation flow (ice creep), the ice stream now flows rapidly (purge phase). As a consequence of the high ice velocities, the ice stream thins, and cold ice is advected from either upstream or the lateral boundaries of the ice stream. Cold ice advection in combination with changing heat source contributions (from both deformation work and basal sliding) and lowering of the pressure-melting point as ice thins eventually leads to refreezing of the ice–bed interface. The first localized frozen patch of ice acts as a sticky spot, supporting some of the driving stress and decreasing the velocities and heat production in the adjacent ice. This marks the end of the surge, thus enabling the ice stream to enter the next binge phase. Whether hydraulically or thermally

driven, these activation (purge) and stagnation (binge) phases can alternate in a quasi-periodic fashion (e.g., Souček and Martinec, 2011) – this is what we refer to as ice stream surge cycling in the remainder of this paper.

As a result of the physics involved and the behaviors expected, modeling of ice stream surge cycling is challenging. The challenges entail, among others, rapid surge onset, high ice velocities, and non-linear (thermo-viscous, hydraulic, and thermo-frictional) feedbacks. In addition to the physical complexity, further challenges arise in the numerical modeling of ice stream surge cycling, whether in terms of model choices (e.g., choice of mechanical model, thermal modeling of the substrate, accounting for sub-glacial hydrology) and/or in terms of their numerical implementation (e.g., grid size, convergence under grid refinement).

Our focus here is on the challenges arising from numerical modeling, both those related to the physical system being modeled and those related to the numerical implementation. The effects of different approximations of the Stokes equations have been previously addressed (e.g., Brinkerhoff and Johnson, 2015) and are therefore not discussed here.

The discretization and related numerical implementation choices (e.g., grid resolution and grid orientation) have been shown to affect numerical results (e.g., Calov et al., 2010; Roberts et al., 2016; Ziemen et al., 2019). As far as the choice of grid is concerned, Ziemen et al. (2019), for example, find a constantly active ice stream at 40 km grid resolution and oscillatory behavior at 20 km grid resolution. They argue that this finer grid resolution is necessary to resolve the Hudson Strait properly. A few other studies examine the effect of different grid resolutions on surge behavior (e.g., Payne and Dongelmans, 1997; Greve et al., 2006; Van Pelt and Oerlemans,

2012; Brinkerhoff and Johnson, 2015; Roberts et al., 2016), but an in-depth numerical analysis of Hudson Strait ice stream surge cycling (to whatever idealized form) is entirely absent from the literature. In terms of grid rotation, Greve et al. (2006) and Takahama (2006) show only a minor effect of grid rotation on the general features of the oscillations.

An additional level of complexity in the modeling of ice sheet surge cycling arises from the fact that small perturbations of the initial or boundary conditions can significantly vary the surge characteristics (Souček and Martinec, 2011; Mantelli et al., 2016). For example, Souček and Martinec (2011) show that low levels of surface temperature noise can lead to chaotic behavior in the periodicity of ice stream oscillations, with mean periods varying by $\pm 2\,\mathrm{kyr}$ ($\sim 20\,\%$ of the characteristic period of the oscillations – Fig. 8 in Souček and Martinec, 2011). Moreover, Souček and Martinec (2011) find differences in the form, period, and amplitude of oscillations when using two different numerical implementations for calculating the basal temperature for thermal activation of basal sliding. However, whether this observed sensitivity arises from physical grounds (e.g., as in Mantelli et al., 2016) or is a spurious numerical effect, the numerical error remains unclear. Souček and Martinec (2011) thus rightfully conclude that "... the implementation of surge-type physics in large-scale ice-sheet models is rather problematic since the information about the physical instability may be lost in the numerics".

2.1.1 Study overview

Herein, we disentangle the effects of numerical choices (e.g., grid size) and physical system processes (e.g., sub-temperate basal sliding) on ice sheet surges via numerical experiments.

In terms of ice flow models, we primarily use the 3D Glacial Systems Model with hybrid shallow-shelf–ice physics (GSM, Tarasov et al., 2023). However, to mitigate the possibility that our conclusions are biased by specific numerical and/or modeling choices within the GSM, we repeat experiments that do not require the implementation of novel physics with the widely used Parallel Ice Sheet Model (PISM, Bueler and Brown, 2009; Winkelmann et al., 2011). As the two model setups and physics are somewhat different (see Table 2.2 for details), this permits more confident conclusions that are not model specific. To partly address potential non-linear dependencies of surge cycling on model parameters, we run each numerical experiment with a high variance ensemble of five GSM and nine PISM parameter vectors instead of just a single run.

In terms of different numerical choices, the impact on model results is usually determined by calculating the model error in relation to the exact analytical solution. However, the theory behind the surge instability is not fully developed (no analytical solution exists) in the context of a spatially extended 3D system, thus precluding systematic benchmarking of numerical models.

To overcome this issue and to provide at least a minimum estimate of the numerical model error, we first determine minimum numerical error estimates (MNEEs). This is a minimal threshold to resolve whether a change in surge characteristics due to

changes in the model configuration is significant (see Sec. 2.2.3 for details).

Equipped with these tools, we set out to tackle the research questions detailed in Sec. 2.1.2, which we denote with the labels Q_1–Q_{11}. The remainder of the paper is then structured as follows: we start by describing our models and experimental setups in Sec. 2.2. We then present detailed results that allow us to answer our research questions in Sec. 2.3, with a concise summary and discussion provided in Sec. 2.4. The results are organized into the following main themes: key surge characteristics of the reference setup (Sec. 2.3.1), MNEEs (Sec. 2.3.2), sensitivity experiments with and without a significant (with respect to the MNEEs) effect on the results (Sec. 2.3.3), and convergence study (Sec. 2.3.4).

2.1.2 Research questions

In this subsection, we detail the key research questions that we address through numerical experiments. Following the above-described structure in the description of the results, the research questions are divided into three sub-categories: minimum numerical error estimates (MNEEs), sensitivity experiments, and convergence study.

2.1.2.1 Minimum numerical error estimates

Q_1 What is the threshold of MNEEs in the two models (Sec. 2.3.2)?

2.1.2.2 Sensitivity experiments

We examine the significance of different model configurations to the surge characteristics. We are particularly interested in model configurations affecting the basal temperature and thus the surge behavior. Therefore, we first discuss the change in

surge characteristics due to a bed thermal model (Q_2) and modeling choices affecting the basal temperature at the grid cell interface where the ice velocities are calculated (Q_3 and Q_4), including the basal-sliding thermal-activation criterion (Q_5). Previous studies examining the effects of ice stream behavior are often based on an idealized basal topography and sediment distribution and do not consider sub-glacial hydrology (e.g., Calov et al., 2010; Brinkerhoff and Johnson, 2015). Therefore, we determine the change in surge characteristics due to these aspects in Q_6, Q_7, Q_8, and Q_9. Since thermally and hydraulically driven ice stream surges are not exclusive, we also investigate the differences between the two mechanisms when used as the primary smoothing mechanism at the warm–cold-based transition zone (Q_{10}).

Q_2 Is the inclusion of a bed thermal model a controlling factor for surge activity (Sec. 2.3.3.1)?

Except for PISM, all models in the HEINO (Heinrich Event INtercOmparison) experiments did not include a bed thermal model (Calov et al., 2010). PISM is one of the few models that did not show oscillatory behavior in the HEINO experiments (except for experiment T1 (10 K colder minimum surface temperature; Calov et al., 2010)). We explore the role of the additional heat storage in surge activity by deactivating a 1 km deep bed thermal model in the GSM and PISM.

Q_3 Do different approaches to determining the grid cell interface basal temperature significantly affect surge behavior, and if yes, which one should be implemented (Sec. 2.3.3.2)?

On a staggered grid (commonly Arakawa C grid; Arakawa and Lamb, 1977), the

velocities are calculated at the grid cell interfaces, whereas basal temperatures are situated in the grid cell center. Therefore, the basal temperature at the grid cell interface needed for the thermal activation of basal sliding needs to be determined as a function of the basal temperatures at the adjacent grid cell centers. Here we examine surge sensitivity to different interpolation schemes (see Sec. 2.3.3.2).

Q_4 How much of the ice flow should be blocked by upstream or downstream cold-based ice, or equivalently, what weight should be given to the adjacent minimum basal temperature (Sec. A.8.1)?

At relatively coarse horizontal grid resolutions (e.g., 25 km), the basal temperatures at the adjacent grid cell centers are of physical relevance. For example, a cold-based grid cell in the downstream direction should block at least part of the ice flow across a 25 km long warm-based interface (Eq. A.1). Here we examine surge sensitivity to a change in the weight of the adjacent (grid cell center) minimum basal temperature when calculating the grid cell interface temperature.

Q_5 How different are the model results for different basal- temperature ramps? And what ramp should be used (Sec. 2.3.3.3)?

Another issue that is often ignored is the basal-sliding thermal-activation criterion. Based on the results of Souček and Martinec (2011), the basal temperature is a critical factor in the onset and termination of (surging) ice streams. Mantelli et al. (2019) show that an abrupt onset of sliding at the transition from a cold-based ice sheet to an ice sheet bed at the pressure-melting point

causes refreezing on the warm-based side and, therefore, cannot exist. Observational and experimental evidence for sub-temperate sliding further supports a smooth transition from cold-based no-sliding conditions to fully warm-based sliding, with sliding velocities increasing as the basal temperature approaches the pressure-melting point (Barnes et al., 1971; Shreve, 1984; Echelmeyer and Zhongxiang, 1987; Cuffey et al., 1999; McCarthy et al., 2017).

An additional argument for sub-temperate sliding can be made on numerical grounds for coarse horizontal grid resolutions. It is unlikely that an entire grid cell reaches the pressure-melting point within one time step (e.g., $25 \times 25\,\mathrm{km}$ in $1\,\mathrm{year}$). Furthermore, a sub-grid path at the pressure-melting point would likely occur before the whole grid cell reaches the pressure-melting point. As such, the activation of basal sliding should start at grid cell basal temperatures below the pressure-melting point and ramp up as the pressure-melting point is approached. As the horizontal grid resolution becomes finer, the range of sub-grid temperatures in a grid cell decreases (e.g., Fig. 2.10, A.27, and A.28). Consequently, the thermal-activation ramp should be sharper (smaller transition zone) for finer horizontal grid resolutions.

Experimental work (e.g., Barnes et al., 1971; McCarthy et al., 2017) supports the notion of sub-temperate sliding within a narrow range of temperatures below the pressure-melting point ($< 5\,^{\circ}\mathrm{C}$). A wide temperature ramp (e.g., $T_{\mathrm{ramp}} = 1\,^{\circ}\mathrm{C}$, see Eq. 2.9) enables an earlier sliding onset (for increasing basal temperature), spatially extended sliding, and a prolonged sliding duration (for decreasing basal temperature).

We use basal-temperature gradients in fine-resolution runs and approximations of the sub-grid warm-based connectivity between the faces of, e.g., a 25 km grid cell (there should be no ice streaming across the grid cell if a frozen sub-grid area disconnects warm-based patches) to constrain an a priori functional form of the basal-temperature ramp. We then use upscaling and resolution-scaling experiments to constrain the dependency of the ramp on horizontal grid resolution.

Q_6 Does the abrupt transition between a soft and hard bed significantly affect surge characteristics (Sec. 2.3.3.4)?

An abrupt transition from hard bedrock to soft sediment (as, e.g., used in the HEINO experiments; Calov et al., 2010) can lead to additional localized shear heating caused by the difference in basal resistance and therefore sliding velocities at that transition. We explore the impact of the bed-type transition on surge characteristics by incorporating a smooth transition from 0 % sediment cover (hard bedrock) to 100 % (soft) sediment cover, effectively changing the basal-sliding coefficient C in Eq. (2.6b).

Q_7 How does a non-flat topography affect the surge behavior (Sec. 2.3.3.4)?

Given the topographic lateral bounds of the Hudson Strait, we examine the effects of a non-flat topography on the surge characteristics.

Q_8 What is the effect of a simplified basal hydrology on surge characteristics in the GSM (Sec. 2.3.3.5)?

The implementation of a fully coupled basal-hydrology model changes the basal

drag and, therefore, has the potential to affect the surge characteristics. A basal-hydrology model coupled to an effective-pressure-dependent sliding law or a Coulomb-plastic bed (as in PISM) introduces a positive feedback such that larger sliding speeds increase frictional heating and thus meltwater availability, which further weakens the bed and leads to even faster sliding. Different basal-hydrology process representations have been proposed in the literature (e.g., a 0D (Gandy et al., 2019), poroelastic (Flowers et al., 2003), or linked cavity hydrology model (Werder et al., 2013)), and in-depth comparison is currently under review (Drew and Tarasov, 2022). Here, we compare GSM surge statistics with and without a fully coupled 0D hydrology model.

Q_9 How significant are the details of the basal-hydrology model to surge characteristics in PISM (Sec. A.8.2)?

PISM surge characteristics are compared for local and mass-conserving horizontal-transport hydrology models.

Q_{10} What are the differences (if any) in surge characteristics between local basal hydrology and a basal-temperature ramp as the primary smoothing mechanism at the warm–cold-based transition zone (Sec. A.8.3)?

While both sub-glacial hydrology and a basal-temperature ramp provide a means for a smooth increase in sliding velocities, these processes operate in slightly different temperature regimes. The basal-temperature ramp enables sub-temperate sliding, and the maximum velocities occur once the pressure-melting point is reached. In contrast, a local basal-hydrology model increases sliding velocities once the basal temperature reaches the pressure-melting point

(basal melting), and basal-ice velocities further ramp up with decreasing effective pressure (ice overburden pressure minus basal water pressure). Note that sub-glacial hydrology is not an alternative for a basal-temperature ramp. The ramp is still needed to prevent refreezing even when a description of sub-glacial hydrology is included (Mantelli et al., 2019).

2.1.2.3 Convergence study

Q_{11} Do model results converge (decreasing differences when increasing horizontal grid resolution – Sec. 2.3.4)?

Incorporating the findings of the above experiments, we study numerical convergence with respect to horizontal grid resolution for surge cycling. By convergence, we mean decreasing differences between simulations when increasing the resolution.

2.2 Methods

2.2.1 GSM

2.2.1.1 GSM model description

The 3D thermo-mechanically coupled Glacial Systems Model (GSM) has developed over many years (e.g., Tarasov and Peltier, 1997; Tarasov et al., 2012; Bahadory and Tarasov, 2018). It includes an energy-conserving finite-volume ice and bed thermodynamics solver. The current hybrid shallow-shelf–ice physics is based on a slight variant of the ice dynamical core of Pollard and DeConto (2012). As is standard

for thermo-mechanically coupled glaciological ice sheet models, the GSM has a default explicit time step coupling between the thermodynamics and ice dynamics but also includes an optional implicit coupling scheme (Sec. 2.3.2.2). Ice dynamical time stepping is subject to CFL (Courant–Friedrichs–Lewy) constraint (Courant et al., 1928), with further automated reductions upon ice-dynamical solver convergence failure. The source code of the model version used in this paper can be found in the supplementary material (Tarasov et al., 2023).

The GSM is run with an idealized down-scaled North American geometry (Fig. 2.1, modified following the ISMIP–HEINO (Ice-Sheet Model Intercomparison Project–Heinrich Event Intercomparison) setup – Calov and Greve, 2006) and simplified climate representation. The surface temperature forcing in the GSM is given by

$$T_{\text{surf}} = \text{rTsurf} + \text{lapsr} \cdot H + T_{\text{asym}}, \tag{2.1}$$

where rTsurf and lapsr are input parameters for the domain-wide surface temperature constant and atmospheric lapse rate, respectively (Table 2.1); H is the ice sheet thickness; and T_{asym} is the asymmetric (in time) temperature forcing (maximum difference of 10 °C – orange line in Fig. A.1 in the Supplement) calculated according to

$$T_{\text{asym}} = \left(\left| \frac{t}{200 \text{ kyr}} \cdot 3 + 2 \right| - 1 \right) \cdot 5 \,^{\circ}\text{C}, \tag{2.2}$$

where t is the model time ranging from −200 to 0 kyr (instead of 0 to 200 kyr). The asymmetric temperature forcing enables the analysis of the timing of cycling onset and termination under different physical and numerical conditions (a comparison of

ice stream ice volume evolution under constant and asymmetric temperature forcing is shown in Fig. A.2 for one parameter vector).

The surface mass balance forcing is then determined by

$$M_{\text{tot}} = M_{\text{acc}} - M_{\text{melt}}, \tag{2.3}$$

where M_{acc} and M_{melt} are the surface accumulation and melt, respectively. The surface accumulation is defined by

$$M_{\text{acc}} = \text{precRef} \cdot \exp\left(\text{hpre} \cdot T_{\text{surf}}\right), \tag{2.4}$$

where precRef and hpre are the precipitation coefficient input parameters. Surface melt is calculated according to a positive degree day (PDD) approach:

$$\begin{aligned} M_{\text{melt}} &= \text{rPDDmelt} \\ &\quad \cdot \max\left(0.0, \text{POSdays} \cdot (T_{\text{surf}} + 10.0\,^{\circ}\text{C})\right), \end{aligned} \tag{2.5}$$

where rPDDmelt is the input parameter for melt per PDD, and the PDD constant POSdays is set to $100\,\text{d}\,\text{yr}^{-1}$. Note that we set $T_{\text{surf}} = 0.1\,^{\circ}\text{C}$ and $M_{\text{tot}} = -100\,\text{m}\,\text{yr}^{-1}$ for ocean grid cells, and $T_{\text{surf}} = 0.1\,^{\circ}\text{C}$ and $M_{\text{tot}} = -200\,\text{m}\,\text{yr}^{-1}$ at the boundaries of the model domain.

The GSM is initialized from ice-free conditions. The coarsest horizontal grid resolution is $25 \times 25\,\text{km}$ and is progressively refined (halved) to $3.125 \times 3.125\,\text{km}$. This gives a total of four different horizontal grid resolutions. The maximum time step size is 1 year (automatically decreased as needed to meet the CFL constraint or

when convergence fails).

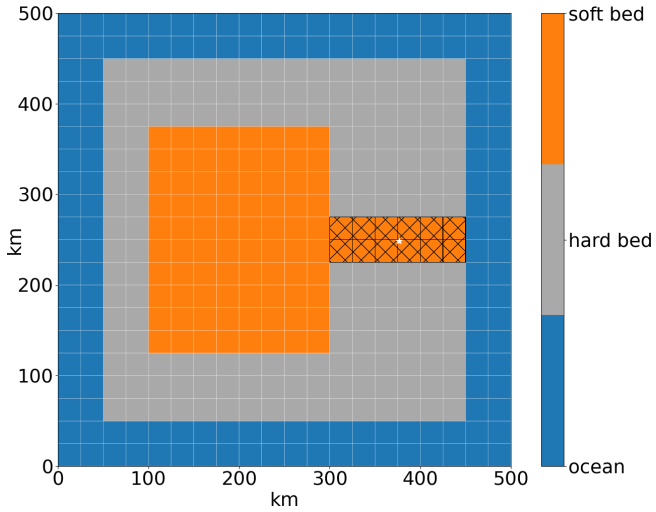

Figure 2.1: Modified ISMIP–HEINO geometry (Calov and Greve, 2006). The model domain is reduced to 500×500 km to enable horizontal grid resolutions up to 3.125 km. The shown grid resolution is 25×25 km. The basal topography is flat, and the hatched area marks the soft-bedded pseudo-Hudson Strait. The white star indicates the location of the grid cell shown in Fig. 2.8 and S21.

While Mantelli et al. (2019) conclude that Stokes mechanics are needed to arrive at a mathematically well-posed model, running numerical experiments with a thermo-mechanically coupled Stokes model is currently unfeasible over glacial-cycle timescales. Previous ice stream surge modeling studies are often based on zeroth-order, thin-film approximations of the Stokes problem, like the shallow-ice approximation (SIA, e.g., eight out of nine models in the ISMIP–HEINO experiments – Calov et al., 2010). While resolving vertical shear, which is the dominant mode of motion in slow-flowing regions, SIA-based models neglect longitudinal stress gradients and horizontal shear, which are known to be important for fast ice streams (Hindmarsh, 2009) and are instead captured by the zeroth-order shallow-shelf approximation (SSA).

To partially offset the limitations of the zeroth-order approximations, the GSM

uses hybrid SIA–SSA ice dynamics (Pollard and DeConto, 2007, 2012). The hybrid SIA–SSA ice dynamics are activated for grid cells with an SIA velocity exceeding $30\,\mathrm{m\,yr^{-1}}$. Changing these activation velocities (20 and $40\,\mathrm{m\,yr^{-1}}$) has no significant effect on the surge characteristics (Table S1 in the Supplement). Activating the SSA everywhere leads to more surges that are also shorter and weaker because no threshold velocity needs to be overcome to initiate basal sliding (Sec. A.1.2). Note that we set an upper limit of $40\,\mathrm{km\,yr^{-1}}$ for the SSA velocity to ensure that sliding velocities stay within a physically reasonable range.

We configure the GSM with a 1 km deep (17 non-linearly-spaced levels) bed thermal model. A basal-temperature ramp is used to ensure a smooth transition between cold-based regions of no sliding and temperate sliding, to account for observational evidence of sub-temperate sliding, and to more accurately represent the sub-grid warm-based ice fraction in a grid cell and therefore more accurately represent sliding onset for coarse grid resolutions (Q_5 in Sec. 2.1.2). However, the shape of such a basal-temperature ramp is not well constrained. In the GSM, the basal-temperature ramp is incorporated into a Weertman-type power law,

$$\vec{u}_\mathrm{b} = C_\mathrm{b}\,|\boldsymbol{\tau}_\mathrm{b}|^{n_\mathrm{b}-1}\,\boldsymbol{\tau}_\mathrm{b}, \tag{2.6a}$$

as a dependence of the basal-sliding coefficient C_b on the estimated warm-based fraction of a grid cell (indirectly accounting for sub-temperate sliding) F_warm (Eq. 2.8):

$$C_\mathrm{b} = (1 - F_\mathrm{warm})\,C_\mathrm{froz} + F_\mathrm{warm} C, \tag{2.6b}$$

where $\vec{u}_\mathrm{b}$ is the basal-sliding velocity, $\boldsymbol{\tau}_\mathrm{b}$ is the basal stress, n_b is the bed power strength (Table 2.1), and C is the fully warm-based sliding coefficient (depending on the bed properties; see also Fig. A.4). C_froz is the fully cold-based sliding coefficient for numerical regularization:

$$C_\mathrm{froz} = 2 \times 10^{-3}\,\mathrm{m\,yr^{-1}} \left(5 \times 10^{-6}\,\mathrm{Pa^{-1}}\right)^{n_\mathrm{b}}. \tag{2.7}$$

F_warm is calculated according to

$$F_\mathrm{warm} = \max\left[0, \min\left(1, \frac{T_\mathrm{bp,I} + T_\mathrm{ramp}}{T_\mathrm{ramp}}\right)\right]^{T_\mathrm{exp}}, \tag{2.8}$$

where $T_\mathrm{bp,I}$ is the grid cell interface basal temperature relative to the pressure-melting point, negative T_ramp is the temperature below which the entire grid cell is cold-based, and T_exp is the exponent used for the ramp. The values used in previous GSM modeling studies ($T_\mathrm{ramp} = 1.0\,^\circ\mathrm{C}$ and $T_\mathrm{exp} = 28$ – e.g., Bahadory and Tarasov, 2018) were based on horizontal basal-temperature gradients around the basal-sliding activation zone, with consideration of the sub-grid warm-based connectivity between grid cell interfaces (as basal sliding requires a connected sub-grid warm-based path). Different values for T_ramp and T_exp are explored within this paper. T_ramp can be chosen as either a constant or depending on the horizontal grid resolution (res – equal extent in x and y directions):

$$T_\mathrm{ramp} = P_{T_\mathrm{ramp}} \cdot \frac{\mathrm{res}}{50\,\mathrm{km}}\,^\circ\mathrm{C}. \tag{2.9}$$

This choice of resolution dependence leads to a sharper temperature ramp for finer horizontal grid resolutions. The parameter P_{T_ramp} is used to conduct experiments with

different temperature ramps at the same horizontal grid resolution (Sec. 2.3.3.3). The temperature ramps for all four horizontal grid resolutions and $P_{T_{\text{ramp}}} = 1$ (default value) are shown in Fig. 2.2. For comparison, a temperature ramp similar to the one suggested by Fowler (1986) and later by Mantelli et al. (2019),

$$F_{\text{warm}} = \exp\left(\frac{T_{\text{bp,I}}}{\delta}\right) \quad \text{for} \quad T_{\text{bp,I}} \leq 0, \tag{2.10}$$

is shown for $\delta = 0.01$, where δ is a parameter controlling the width of the transition zone. Based on experiments conducted by Barnes et al. (1971), Mantelli et al. (2019) expect δ to be small.

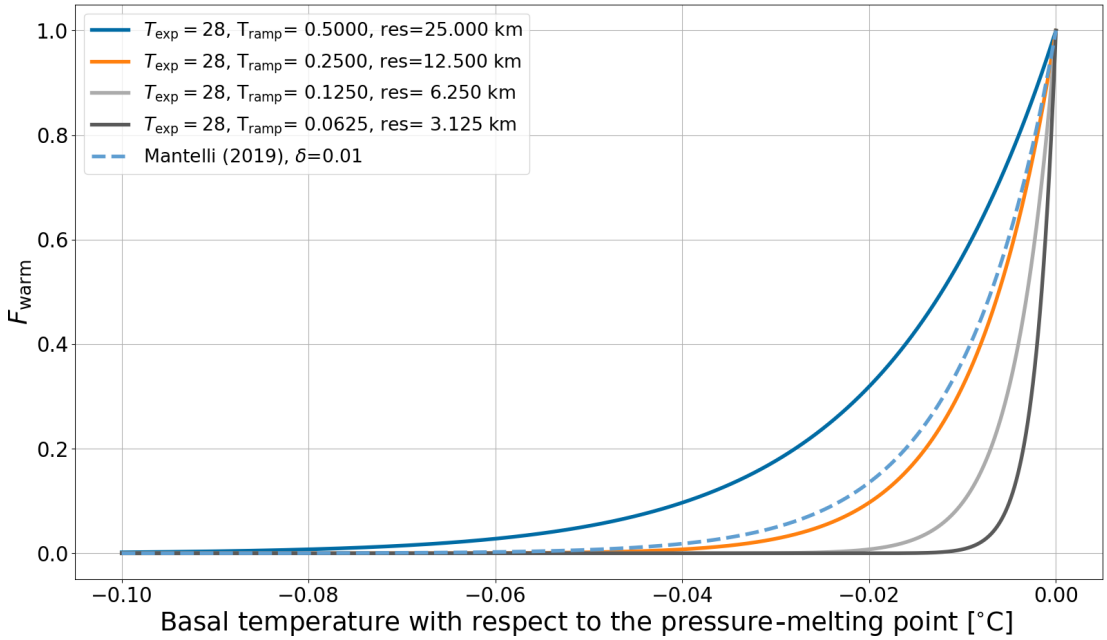

Figure 2.2: Temperature ramps for different values of T_{ramp} which depend on the horizontal grid resolution. A temperature ramp similar to the one suggested by Mantelli et al. (2019) (Eq. 2.10) is shown for $\delta = 0.01$.

2.2.1.2 GSM ensemble input parameter vectors

Each GSM experiment is run with an ensemble based on five input parameter vectors. The current idealized setup encompasses a maximum of eight input parameters (Table 2.1) per parameter vector. The five parameter vectors used in this study are hand-picked from an exploratory ensemble (Fig. A.3). The criteria for these five parameter vectors were the highest subset variance in surge characteristics and the soft-bed sliding-law exponent. Note that the soft- and hard-bed sliding-law exponents in this study are equal (n_b in Table 2.1). Due to the significantly increased model run time, sliding-law exponents larger than 3 are not considered here. To isolate interactions, the GSM reference setup used in this paper does not incorporate basal hydrology and glacial isostatic adjustment (GIA). Processes associated with basal hydrology, such as lubrication of the bed and decoupling of the ice sheet from the bed, are likely to have a major effect on surge patterns. To determine the impact of these effects, we run the GSM with local basal hydrology enabled (Eq. 2.19 to 2.21, Sec. 2.3.3.5) and examine resolution scaling (Sec. A.9.2). However, experiments done with and without basal hydrology lead to qualitatively similar results (e.g., same conclusions from upscaling experiments in Sec. 2.3.3.3). We therefore omit sub-glacial hydrology coupling for the main analysis.

2.2.1.3 GSM model setups

The reference setup (Table 2.2) has a 3.125 km horizontal grid resolution and a 1-year maximum time step size. The bed topography is flat (at sea level), and an asymmetric temperature forcing is used (Fig. A.1). For the sake of generality, we chose a flat

Category	Parameter	Description	Range	Unit
Ensemble parameter – ISM	C_{rmu}	soft-bed sliding coefficient (Eq. 2.6b)	0.3–1	
	C_{fslid}	hard-bed sliding coefficient (Eq. 2.6b)	0–3	
	lapsr	atmospheric lapse rate (Eq. 2.1)	-5 to -10	$^{\circ}\mathrm{C\,km^{-1}}$
	PDDmelt	melt per positive degree day (PDD, Eq. 2.5)	0.005–0.012	$\mathrm{m\,PDD^{-1}\ (^{\circ}C)^{-1}}$
	hpre	precipitation coefficient (Eq. 2.4)	0.02–0.2	$(^{\circ}\mathrm{C})^{-1}$
	PrecRef	precipitation coefficient (Eq. 2.4)	1–3	$\mathrm{m\,yr^{-1}}$
	rTsurf	domain-wide surface temperature constant (Eq. 2.1)	-9 to -15	$^{\circ}\mathrm{C}$
	n_{b}	soft- and hard-bed sliding-law exponent, bed power strength (Eq. 2.6a)	1–3	
Hydrology parameters	$h_{\mathrm{wb,Crit}}$	effective bed roughness scale (Eq. 2.19)	0.01–1	m
	rBedDrainRate	constant bed drainage rate	0.001–0.01	$\mathrm{m\,yr^{-1}}$
	$N_{\mathrm{eff,Fact}}$	effective-pressure factor (Eq. 2.21)	2×10^{4}–2×10^{5}	Pa
Additional parameters	$P_{T_{\mathrm{ramp}}}$	basal-temperature-ramp scaling factor (Eq. 2.9)	0.125–16 (**1**)	
	T_{ramp}	basal temperature (with respect to the pressure-melting point) at which sub-temperate sliding becomes important (Eq. 2.8, 2.9)	0.03125–1 (**0.0625**)	$^{\circ}\mathrm{C}$
	T_{exp}	basal-temperature-ramp exponent (Eq. (2.8))	5–56 (**28**)	
	$W_{\mathrm{Tb,min}}$	weight of adjacent minimum basal temperature for basal-sliding temperature ramp (Eq. (S1))	0.0–1.0 (**0.5**)	

Table 2.1: Model parameters are listed with respect to their purpose or category. Ice sheet model – ISM. Hydrology parameters used when running the GSM with local basal hydrology. Additional (non-regular) input parameters that are usually set to a fixed value. The default values of the 3.125 km horizontal grid resolution reference setup are shown as bold values (in brackets) for the additional parameters.

topography for the reference setup, while the effect of a basal trough is investigated at a later stage (Sec. 2.3.3.4). Branching off this reference setup, we carry out one-factor-at-a-time sensitivity experiments to isolate numerical and process impacts. These experiments, in turn, examine the response to three numerical aspects related to the MNEEs, four model aspects affecting the thermal onset of basal sliding, a change in sediment cover, a non-flat topography, the addition of local basal hydrology, and different horizontal grid resolutions (25, 12.5, 6.25 km). The three numerical aspects

are stricter numerical convergence criteria, the addition of surface temperature noise (± 0.1 and $\pm 0.5\,^{\circ}\mathrm{C}$), and an approximate implicit time step coupling between the thermodynamics and ice dynamics. The four thermal model aspects are switching to a thin (20 m)-bed thermal model, different approaches to determining the basal temperature at the grid cell interface, different weights of the adjacent minimum basal temperature for the basal-sliding temperature ramp ($W_{\mathrm{Tb,min}}$), and different basal-temperature ramps (T_{ramp} and T_{exp}) for thermal activation of basal sliding. See Table 2.1 for details on parameter ranges.

2.2.2 PISM

2.2.2.1 PISM model description

In contrast to the GSM, the Parallel Ice Sheet Model (PISM) is not specifically developed for glacial-cycle ensemble modeling. Therefore, the two models use distinct sets of numerical optimizations for computational speed. To minimize the model dependency of our analysis, experiments are also carried out with v2.0.2 of PISM.

Similarly to the GSM, PISM is a 3D thermodynamically coupled ice sheet model, and the SSA is used as a sliding law once the sliding velocity exceeds $100\,\mathrm{m\,yr^{-1}}$. For further details on the model itself, refer to Bueler and Brown (2009) and Winkelmann et al. (2011). The details on the default PISM setup, together with the default GSM values, are listed in Table 2.2. Given the higher computational cost of PISM experiments, the relatively high sensitivity of PISM to the number of parallelized cores for these experiments (Table 2.6), and the run time limitations of the computational cluster, the reference setup is run at 25 km horizontal grid resolution.

For stability reasons, the PISM adaptive time-stepping ratio (used in the explicit scheme for the mass balance equation) was reduced to 0.01 when using small till friction angles (Constantine Khrulev, personal communication, 26 May 2021).

The default sliding law in PISM is a purely plastic (Coulomb) model, where

$$|\boldsymbol{\tau}_\mathrm{b}| \leq \tau_\mathrm{c} \quad \text{and} \quad \boldsymbol{\tau}_\mathrm{b} = -\tau_\mathrm{c}\frac{\boldsymbol{u}}{|\boldsymbol{u}|} \quad \text{if} \quad |\boldsymbol{u}| > 0. \tag{2.11}$$

Therefore, the basal-shear stress $\boldsymbol{\tau}_\mathrm{b}$ can never exceed the yield stress τ_c, and basal sliding only occurs when $\boldsymbol{\tau}_\mathrm{b}$ reaches τ_c.

Setup component	GSM	PISM
Horizontal grid resolution	$3.125\,\mathrm{km} \times 3.125\,\mathrm{km}$	$25\,\mathrm{km} \times 25\,\mathrm{km}$
Number of grid cells	160×160	120×120
Model domain	$500\,\mathrm{km} \times 500\,\mathrm{km}$	$3000\,\mathrm{km} \times 3000\,\mathrm{km}$
Vertical layers	65	60
Run time	200 kyr	200 kyr
Maximum time step size	1 year	1 year
Number of processor cores	1	8
Ice dynamics	hybrid SIA–SSA	hybrid SIA–SSA (maximum SIA diffusivity of $1000\,\mathrm{m^2\,s^{-1}}$)
Sliding law	Weertman-type power law (Eq. 2.6a)	Coulomb friction law (Eq. 2.11)
Bed topography	flat (at sea level)	flat (at sea level)
Bed thermal model	1 km deep (17 non-linearly spaced levels)	1 km deep (20 equally spaced levels)
Basal hydrology	not included	local basal hydrology model based on an undrained plastic bed model (Tulaczyk et al., 2000a)

Table 2.2: Comparison between the GSM and PISM reference setup.

2.2.2.2 PISM ensemble input parameter vectors

The PISM configuration encompasses six model input parameters (Table 2.3). These parameters define the input fields for surface temperature, surface accumulation, and till friction angle. As for the GSM, PISM is initialized from ice-free conditions. Similarly to Calov and Greve (2006), the surface temperature at every grid cell is

calculated as follows:

$$T_{\text{surf}} = T_{\text{min}} + S_{\text{t}} \cdot d^3, \tag{2.12}$$

where S_{t} represents the horizontal surface temperature gradient; d represents the distance from the domain center (x_{center}, y_{center}) in kilometers, defined as

$$d = \sqrt{(x - x_{\text{center}})^2 + (y - y_{\text{center}})^2} < R; \tag{2.13}$$

and R denotes the radius and sets an upper limit for d. A comparable equation is used to calculate the surface mass balance (accumulation–ablation) rate input field:

$$B_{\text{surf}} = B_{\text{max}} - S_{\text{b}} \cdot d^5, \tag{2.14}$$

where S_{b} is the horizontal surface mass balance gradient. The input field for the till friction angle is defined by simple grid assignment and a somewhat smoothed transition between the soft- and hard-bed region. Input fields for one parameter vector are shown for surface temperature, surface accumulation, and till friction angle in Fig. A.6, A.7, and A.8, respectively.

The 6 model ensemble parameters (Table 2.3) were selected via Latin hypercube sampling. After sieving an ensemble of 100 runs for those that show oscillatory behavior, a nine-member high-variance (with respect to the surge characteristics) subset was extracted by means of visual identification (Fig. A.10)). Each PISM experiment is run with an ensemble based on these nine input parameter vectors.

Category	Parameter	Description	Range	Unit
Ensemble parameters	soft	soft bed till friction angle	0.5–12.0	°
	hard	hard bed till friction angle	15.0–30.0	°
	$B_{\max}$	maximum surface mass balance (accumulation–ablation) rate	50–450	$\mathrm{kg\,m^{-2}\,yr^{-1}}$
	S_{b}	horizontal surface mass balance gradient	$(0.15\text{–}1.00) \times 10^{-11}$	$\mathrm{kg\,m^{-2}\,yr^{-1}\,km^{-5}}$
	$T_{\min}$	minimum surface temperature	220–245	K
	S_{t}	horizontal surface temperature gradient	$(0.10\text{–}1.0) \times 10^{-8}$	$\mathrm{K\,km^{-3}}$
Constant parameters	x_{center}	location of the domain center in x-direction	1500	km
	y_{center}	location of the domain center in y-direction	1500	km
	R	maximum radius of the domain	1500	km

Table 2.3: Parameters used to generate the PISM input fields.

2.2.2.3 PISM bed properties

A PISM ensemble parameter restriction arose as experiments carried out with PISM only show oscillatory behavior for small yield stresses τ_{c}. This can be achieved by means of either a small till friction angle Φ or a low effective pressure on the till (N_{till}, Eq. A.2) (Bueler and Van Pelt, 2015):

$$\tau_{\mathrm{c}} = c_0 + \tan(\Phi)\, N_{\mathrm{till}}, \tag{2.15}$$

where $c_0 = 0\,\mathrm{Pa}$ is the till cohesion (Tulaczyk et al., 2000b). For convenience, we decide to vary only the till friction angle between 0.5 and 1°, for which PISM shows oscillatory behavior; otherwise, we use PISM default values (see Sec. A.2.3 for details).

The resulting very slippery beds enabled occasional maximum sliding velocities of up to $\sim 600\,\mathrm{km\,yr^{-1}}$ in the simulations (Fig. A.11, Sec. A.2.4). For comparison, observed outlet glacier velocities at Jakobshavn Isbræ(Greenland) approach $20\,\mathrm{km\,yr^{-1}}$ (Joughin et al., 2012, 2014). As for the GSM, we, therefore, set an upper limit of

$40\,\mathrm{km\,yr^{-1}}$ for the SSA velocity.

2.2.2.4 PISM model setups

As for the GSM, we carry out one-factor-at-a-time sensitivity experiments branching off the PISM reference setup (Table 2.2) for all nine parameter vectors. These experiments, in turn, examine the response to two numerical aspects related to the MNEEs, removing the bed thermal model, an abrupt sediment transition zone, a non-flat topography (Fig. A.9), a mass-conserving horizontal transport model for basal hydrology (Bueler and Van Pelt, 2015), and different horizontal grid resolutions (50, 12.5 km). The two numerical aspects are different number of processor cores ($n = 2, 4, 16, 32$) and the addition of surface temperature noise (± 0.1 and $\pm 0.5\,^{\circ}\mathrm{C}$).

2.2.3 Run analysis approach

2.2.3.1 Surge characteristics

The quantities being analyzed are the number of surges, the surge duration, the ice volume change during a surge, and the period between surges (Fig. 2.3). The surge time is defined as the time of minimum (pseudo-Hudson Strait) ice volume, and the duration of a surge includes the surge itself, as well as the time it takes the ice sheet to recover approximately half the ice volume lost during the surge (Sec. A.3). The calculated ice volume change is the difference between the pre-surge and minimum (pseudo-Hudson Strait) ice volume in that particular surge (Sec. A.3). The period between surges is the time span between two subsequent occurrences of minimum (pseudo-Hudson Strait) ice volume (not defined for the very last surge). The spin-up

interval (first 20 kyr of every run) is not incorporated in the analysis, and only surges with a (pseudo-Hudson Strait) ice volume change of more than 500 and 4×10^4 km^3 are considered in the GSM and PISM analyses, respectively ($\sim 5\,\%$ of mean ice volume across all runs). Note that this is a very conservative spin-up interval. For example, most GSM runs reach their mean pseudo-Hudson Strait ice volume after ~ 5 kyr (e.g., Fig. 2.11).

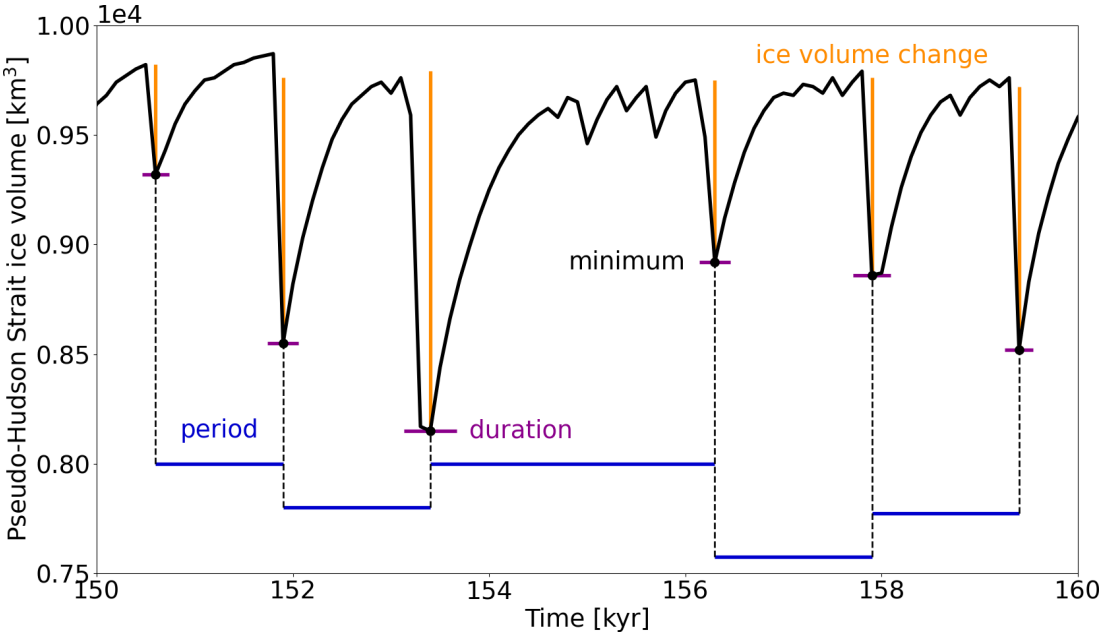

Figure 2.3: Pseudo-Hudson Strait ice volume of a GSM model run with visual illustration of the surge characteristics used to compare different model setups. The horizontal grid resolution is 3.125 km.

In addition to the surge characteristics, the root mean square error (RMSE) and mean bias are calculated as a percentage deviation from the reference (pseudo-Hudson Strait) ice volume time series for all setups (each parameter individually) and are then averaged over the five parameter vectors (Eq. A.3 and A.4). The full run time is considered (no spin-up interval).

2.2.3.2 Percentage differences

We compare different model setups by calculating the percentage difference between the reference setup and all other setups for every parameter vector individually and then average this difference over all parameter vectors. Crashed runs are not considered, and runs with less than two surges require special treatment (see Sec. A.5 for further details on the analysis).

2.2.3.3 Surge area

In the GSM, the whole pseudo-Hudson Strait (Fig. 2.1) is ice covered and at maximum ice volume at the beginning of a surge. Surges in the GSM, therefore, consistently appear as ice volume minima, which allows us to directly use the pseudo-Hudson Strait ice volume for the GSM results.

For PISM, a large fraction of the pseudo-Hudson Strait area is only ice covered when a surge occurs (e.g., Fig. 2.5), leading to an inconsistency in the surge detection. This issue is addressed by including the ice volume over the eastern half of the pseudo-Hudson Bay, the area most affected by the surge drained through the pseudo-Hudson Strait. See Sec. A.2.5 for further details and a comparison between the two approaches.

2.2.3.4 Minimum numerical error estimates

We compute the new minimum numerical error estimates (MNEEs) threshold by examining the model response to changes in the model configuration that are not part of the physical system. The MNEEs are defined as the percentage differences in

surge characteristics when applying a stricter (than default) numerical convergence in the GSM and changing the number of processor cores used in PISM. The differences between PISM runs with different numbers of processor cores can be caused by, for example, a different order of floating-point arithmetic operations and the processor-number-dependent preconditioner used in PISM (PISM 2.0.6 documentation, 2023). The MNEEs are then used as a threshold to determine if model sensitivities to changes in the model configuration that affect the physical system (e.g., the inclusion of a bed thermal model or sliding dependence on effective pressure from basal hydrology) are above the numerical errors induced by iterative numerical solvers in the model. We refrain from drawing conclusions about the effects of a change in model configuration with physical relevance when the model sensitivities in question are smaller than the MNEEs. In these cases, the actual physical response of the model might be hidden within the numerics.

While the MNEEs are useful for our purpose, we wish to emphasize that they can not replace proper model verification and validation and are missing uncertainties due to, e.g., different approximations of the Stokes equations and other physical processes not included in the models. Nonetheless, they provide a minimum estimate of the numerical model error, which is still a significant improvement over ignoring this issue entirely.

2.3 Results

2.3.1 Key surge characteristics of the reference setup

Before analyzing ensemble characteristics, it is crucial to understand how surges initiate, propagate, and terminate. Surges in the GSM originate at the pseudo-Hudson Strait mouth ($x = 450\,\mathrm{km}$, $y = 225$ to $275\,\mathrm{km}$) and propagate towards the center of the pseudo-Hudson Bay ($x = 200\,\mathrm{km}$, $y = 250\,\mathrm{km}$ – Fig. 2.1 and 2.4). The surging onset is a complex interplay between heating at the ice sheet bed, basal temperature, and ice sheet velocity. The beginning of a surge is shown in video 01 (Hank, 2023b) and Fig. 2.4. Just before the start of the surge, the entire south–north extent of pseudo-Hudson Strait grid cells close to the ocean is warm based. At $t = 6.69\,\mathrm{kyr}$, the SIA velocities exceed $30\,\mathrm{m\,yr^{-1}}$, and the SSA is activated (Sec. 2.2.1.1). The longitudinal stress gradient and horizontal shear terms provide additional heating. This leads to several small ice streams with relatively strong heating due to basal sliding ($\sim 10^7\,\mathrm{J\,m^{-2}\,yr^{-1}}$) at $t = 6.70\,\mathrm{kyr}$ in the video. This is 1 order of magnitude larger than heat production from deformation work. The additional heat fosters higher ice velocities, leading to even more heating, the extension of the warm-based area to the west, and therefore the upstream propagation of the small ice streams ($t = 6.71\,\mathrm{kyr}$). The narrow ice streams draw in warm-based ice from the surrounding grid cells, increasing the velocities and heat production in the area between the ice streams. This leads to a merger of the ice streams with now high velocities occurring over the full south–north extent of the pseudo-Hudson Strait ($t = 6.72\,\mathrm{kyr}$). The warm-based area rapidly extends towards the west due to the strong heating and high ice velocities, causing a pseudo-Hudson Strait surge.

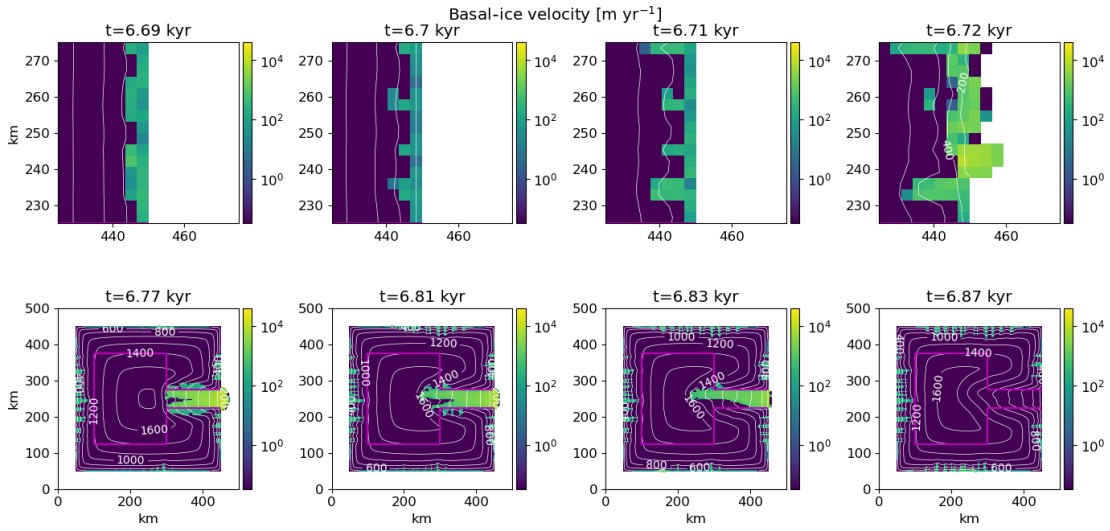

Figure 2.4: Basal-ice velocity for parameter vector 1 at different time steps using the GSM. The horizontal grid resolution is 3.125 km, and the maximum model time step is 1 year. The contour lines show the ice sheet surface elevation in meters. The magenta line outlines the soft-bedded pseudo-Hudson Bay and Hudson Strait. Note that the top and bottom rows show different areas of the domain, with the top zooming in on the surge onset area.

The surge propagates nearly symmetrically until the pseudo-Hudson Bay area is reached ($t = 6.77$ kyr in Fig. 2.4 and video 02 of Hank, 2023b). After this point, the northern branch of the ice stream propagates more rapidly and extends further to the west than the southern branch. While the smaller southern branch starts to shrink at $t = 6.81$ kyr, the northern part propagates until $t = 6.83$ kyr. At this time, the southern branch vanishes almost completely due to a thinner ice sheet (than at the start of the surge) and the advection of cold ice into the surge area. After $t = 6.83$ kyr, the available heating is no longer sufficient to keep the ice sheet bed at the pressure-melting point, and the northern part collapses as well. The surge ends after 150 years (at $t = 6.87$ kyr).

Since the GSM setup and climate forcing are symmetric about the horizontal axis in the middle of the pseudo-Hudson Strait ($y = 250$ km in Fig. 2.1), we interpret the

induced asymmetry to be "spontaneous symmetry breaking", similarly to the results described in Sayag and Tziperman (2011). We define the asymmetry as positive when the surge is stronger northward (Fig. 2.4 and video 02 of Hank, 2023b) or shifted northward. The asymmetry sign varies across the first surges (i.e., the surge least biased by previous asymmetries) of the five reference runs, ruling out any persistent numerical bias.

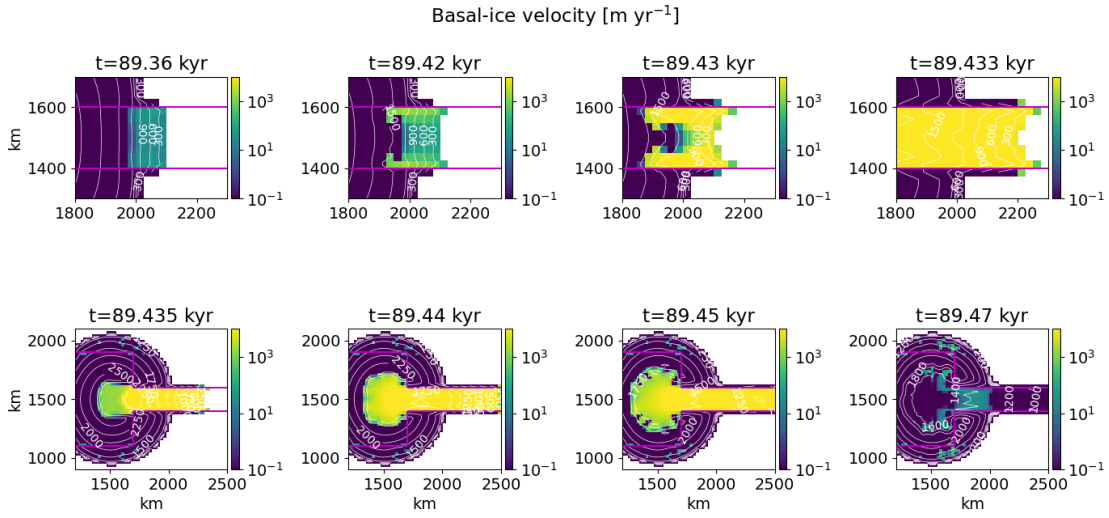

Figure 2.5: Basal-ice velocity for parameter vector 8 at different time steps using PISM. The horizontal grid resolution is 25 km, and the maximum model time step size is 1 year. Otherwise as in Fig. 2.4.

Surges in PISM originate at the ice sheet margin in the soft-bedded pseudo-Hudson Strait (exact position varies between runs) and propagate towards the center of the pseudo-Hudson Bay ($x = 1300\,\mathrm{km}$, $y = 1500\,\mathrm{km}$ – Fig. A.8 and 2.5). The ice near the margin is already flowing downstream before the start of the surge ($t = 89.36\,\mathrm{kyr}$). However, the basal temperature is below the pressure-melting point, and the ice velocities are low ($< 100\,\mathrm{m\,yr^{-1}}$). As the ice sheet upstream of the margin thickens, the warm-based area extends further downstream, particularly along the 100 % soft-

bedded contour line (magenta line in Fig. 2.5).

Once the warm-based area connects with the margin ($t = 89.42\,\mathrm{kyr}$), the ice velocities increase beyond $100\,\mathrm{m\,yr^{-1}}$, activating the SSA (Sec. 2.2.2.1). Similarly to the surges in the GSM, the sliding velocities then increase rapidly, quickly extending the warm-based area ($t = 89.43$ and $t = 89.433\,\mathrm{kyr}$). The surge propagates upstream into the pseudo-Hudson Bay, and the ice is transported along the pseudo-Hudson Strait into regions with increasingly negative surface mass balance rates ($t = 89.435$ to $t = 89.45\,\mathrm{kyr}$, Fig. A.7). The ice sheet thins; the basal temperature at the margin falls below the pressure-melting point, blocking parts of the upstream ice stream; and the surge ceases at $t = 89.47\,\mathrm{kyr}$ ($\sim 100\,\mathrm{year}$ surge duration). The ice volume in the surge-affected area continues to decrease for, on average, another 2.5 kyr due to the large amounts of ice in the negative surface mass balance regions. In contrast to the GSM, PISM results remain symmetrical at about $y = 1500\,\mathrm{km}$ throughout the surge.

Due to the differences in model setups, physics, and numerics (Table 2.2), the GSM and PISM reference setups yield different surge characteristics (Table 2.4). While resembling the inferred ice-rafted debris (IRD) interval duration as closely as possible is not a goal of this study, the modeled values are in agreement with the literature (200 to 2280 years, Hemming, 2004). The mean modeled GSM period is shorter than the observed period of, on average, 7 kyr (K.M. Cuffey and W.S.B. Paterson., 2010). However, exploratory GSM runs with a dimensionally accurate (not downscaled) model domain (but otherwise identical experimental setup) yielded periods within the range of geological inferences. The mean modeled PISM period is within limits set by the literature. The mean (pseudo-Hudson Strait) ice volume change in the GSM corresponds to 15 % of a 1.5 km thick ice sheet covering the

downscaled pseudo-Hudson Strait area ($150 \times 50\,\mathrm{km}$). In PISM, the mean ice volume change is 7.1 % of the mean (across reference setup runs) maximum ice volume in the eastern half of the pseudo-Hudson Bay and pseudo-Hudson Strait.

Metric	GSM reference setup	PISM reference setup
Number of surges	180 ± 100	35 ± 25
Mean period	$1.1 \pm 0.5\,\mathrm{kyr}$	$10 \pm 10\,\mathrm{kyr}$
Mean duration	$0.3 \pm 0.1\,\mathrm{kyr}$	$3 \pm 2\,\mathrm{kyr}$
Mean pseudo-Hudson Strait ice volume change	$1.7 \pm 0.2 \times 10^3\,\mathrm{km}^3$	$1.1 \pm 0.3 \times 10^5\,\mathrm{km}^3$

Table 2.4: Surge characteristics of the GSM ($T_{\mathrm{ramp}} = 0.0625\,^{\circ}\mathrm{C}$, $T_{\mathrm{exp}} = 28$ (black line in Fig. 2.2), $W_{\mathrm{Tb,min}} = 0.5$, TpmTrans for the interface calculation, sharp transition between hard and soft bed) and PISM reference setup (Table 2.2). No runs crashed, and all runs had more than one surge. The first 20 kyr of each run are treated as a spin-up interval and are not considered in the above.

2.3.2 Minimum numerical error estimates

Differences in surge characteristics (compared to the reference setup) are considered to be significant when they exceed the MNEEs given in Tables 2.5 and 2.6 for the GSM and PISM, respectively. However, this does not necessarily mean that smaller changes have no physical relevance but rather that their interpretation is difficult (if not impossible) because the physical response is hidden within the numerical sensitivities. Likely sources of the MNEEs are the iterative SSA solutions and floating-point accuracy.

To determine a minimum significant threshold in the GSM, we re-run a set of GSM runs with 3.125 km horizontal grid resolution, imposing a stricter numerical convergence (decreasing final iteration thresholds). In a second experiment, we additionally

increase the maximum iterations from two to three for the outer Picard loop solving for the ice thickness and from two to four when solving the non-linear elliptic SSA equation for horizontal ice velocities.

The largest differences between simulations occur for the mean period (7 %, Table 2.5) when using stricter convergence thresholds (no change in the maximum number of iterations). The standard deviations are of the same order of magnitude as the values themselves, indicating different responses across the five parameter vectors. Determining the MNEEs at 12.5 km instead of 3.125 km horizontal grid resolution yields similar results, except for the mean pseudo-Hudson Strait ice volume change (21 %, Table A.2).

Metric	Reference setup	Stricter numerical convergence [% difference]	Stricter numerical convergence with increased maximum iterations [% difference]
Number of surges	180 ± 100	$\mathbf{-4.1 \pm 4.9}$	-0.9 ± 3.6
Mean period	1.1 ± 0.5 kyr	$\mathbf{7.0 \pm 10.6}$	4.7 ± 10.6
Mean duration	0.3 ± 0.1 kyr	2.5 ± 3.2	$\mathbf{3.9 \pm 4.8}$
Mean pseudo-Hudson Strait ice volume change	$1.7 \pm 0.2 \times 10^3$ km^3	-1.1 ± 3.1	$\mathbf{4.6 \pm 4.6}$

Table 2.5: Percentage differences (except first column) of surge characteristics between GSM runs with regular and stricter numerical convergence and increased maximum iterations for the ice dynamics loops at 3.125 km horizontal grid resolution. The values represent the averages of five parameter vectors. No runs crashed, and all runs had more than one surge. The first 20 kyr of each run are treated as a spin-up interval and are not considered in the above. The bold numbers mark the largest MNEE for each surge characteristic.

MNEEs in PISM are determined by comparing runs with different numbers of cores. Although most parameter vectors show similar results at the beginning of the runs, minor differences can slowly accumulate and lead to significant discrepancies in surge activity by the end of the run (Fig. A.18). The largest differences occur for the

number of surges (16 %) and mean ice volume change (16 %) for nCores = 32, but the standard deviations are large due to a more than $\sim 200\,\%$ increase in both surge characteristics for parameter vector 6.

Setup	Number of surges	Mean period	Mean duration	Mean ice volume change	nS1
25 km reference setup	35 ± 25	10 ± 10 kyr	3 ± 2 kyr	$1.1 \pm 0.3 \times 10^5$ km^3	0
nCores = 2	-7.1 ± 19.5	6.8 ± 36.2	-0.4 ± 9.5	1.5 ± 10.3	0
nCores = 4	-8.2 ± 22.9	-3.8 ± 6.6	2.8 ± 18.3	0.6 ± 4.8	1
nCores = 16	-10.9 ± 26.0	$\mathbf{-8.2 \pm 14.7}$	7.6 ± 21.2	-0.7 ± 13.3	1
nCores = 32	$\mathbf{16.0 \pm 56.2}$	6.9 ± 48.5	$\mathbf{-8.0 \pm 17.4}$	$\mathbf{16.3 \pm 35.1}$	0

Table 2.6: Percentage differences of surge characteristics (except first row) between the PISM reference setup and setups with different numbers of cores at 25 km horizontal grid resolution. The values represent the averages of nine parameter vectors. No runs crashed, and all runs showed at least one surge. Runs with just one surge (nS1) are ignored when calculating the change in mean period. The first 20 kyr of each run are treated as a spin-up interval and are not considered in the above. The bold numbers mark the largest MNEE for each surge characteristic.

The differences in surge characteristics between different numbers of cores can be minimized (but not removed entirely) by decreasing the relative Picard tolerance in the calculation of the vertically averaged effective viscosity (10^{-4} to 10^{-7}) and the relative tolerance for the Krylov linear solver used at each Picard iteration (10^{-7} to 10^{-12} – Table A.5 and Fig. A.19). However, this leads to an unreasonable increase in model run time ($\sim 300\,\%$) that is not feasible for an ensemble-based approach (more than 50 % of all runs did not finish within the time limit of the computational cluster). Intermediate decreases in the relative tolerances still lead to significant differences in surge characteristics while increasing the model run time and are, therefore, not used in the PISM reference setup. Considering that small differences prevail for all tested relative tolerances, comparing model configurations with different numbers of cores for, e.g., finer-horizontal-grid-resolution experiments is not straightforward.

2.3.2.1 Adding surface temperature noise

Low levels of surface temperature noise have previously been shown to cause chaotic behavior in the mean periods of oscillations (Souček and Martinec, 2011). Adding low levels of uniformly distributed surface temperature noise (maximum amplitude of ± 0.1 and $\pm 0.5\,^{\circ}\mathrm{C}$) to the climate forcing (updated every 100 years) does not significantly affect the surge characteristics for the GSM (Table A.3). For example, the effect of adding $\pm 0.5\,^{\circ}\mathrm{C}$ surface temperature noise on the mean period is only 4 % (compared to the $\sim 20\,\%$ for $\pm 0.01\,^{\circ}\mathrm{C}$ reported by Souček and Martinec, 2011). Adding the same levels of uniformly distributed surface temperature noise to PISM increases the mean duration by 12 % (for $\pm 0.1\,^{\circ}\mathrm{C}$) but has no significant effect on the other surge characteristics (Table A.6).

2.3.2.2 Implicit thermodynamics–ice-dynamics coupling

In contrast to the commonly used explicit time step coupling between the thermodynamics and ice dynamics in glaciological ice sheet models, we test the impact of approximate implicit time step coupling via an iteration between the two calculations for each time step. The implicit coupling decreases the mean duration and pseudo-Hudson Strait ice volume change ($-13\,\%$ and $-25\,\%$, respectively). The number of surges and mean period show no significant change (Table A.4). While the changes in mean duration and pseudo-Hudson Strait ice volume change are larger than the MNEEs, they do not justify an increase in run time of $\sim 265\,\%$, and the implicit coupling is therefore omitted for the GSM reference setup.

2.3.3 Sensitivity experiments

Here, we discuss differences in surge characteristics due to changes in the model setup. An overview of the results can be found in Fig. 2.6 and 2.7 for the GSM and PISM, respectively. The exact values of the percentage differences are provided in the Supplement. We first examine the model aspects affecting the thermal activation of basal sliding (Sec. 2.3.3.1 to 2.3.3.3), followed by the analysis of a smooth sediment transition zone, non-flat topography, and local basal hydrology (Sec. 2.3.3.4 and 2.3.3.5). Experiments without significant differences in the surge characteristics are only briefly mentioned here (Sec. 2.3.3.6). A more in-depth discussion of these latter experiments is available in the Supplement.

2.3.3.1 Bed thermal model

First, we examine the effects of a 1 km deep bed thermal model on the basal temperature and the surge characteristics in the GSM and PISM. Both models show significant differences when limiting the bed thermal model to one layer (GSM) or when removing it entirely (PISM).

Advection of cold ice near the end of a surge rapidly decreases the basal-ice temperature and, therefore, increases the temperature gradient between the basal ice and the bed. In GSM runs with the 1 km deep (17 non-linearly spaced levels) bed thermal model (reference setup), this stronger gradient increases the heat flux from the bed into the ice and dampens the actual change in basal-ice temperature. Similarly, a rapid increase in basal-ice temperature due to higher basal-ice velocities at the beginning of a surge reverses the existing temperature gradient at the base of the ice sheet,

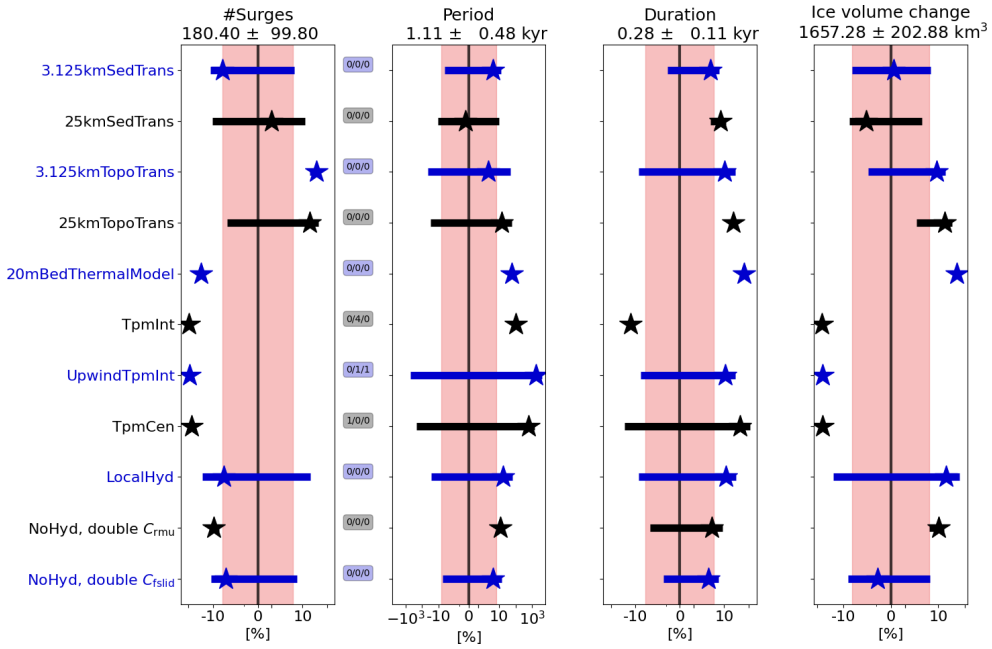

Figure 2.6: Percentage differences in surge characteristics compared to the GSM reference setup for model setups discussed in Sec. 2.3.3 (average of the five parameter vectors). The horizontal grid resolution is 3.125 km. The different colors were added for visual alignment of the individual model setups, the stars are the ensemble mean percentage differences, and the horizontal bars represent the ensemble standard deviations. The shaded pink regions mark the MNEEs (Table 2.5), and the black numbers in the title of each subplot represent the mean values of the reference setup. The three small numbers between the first two columns represent the number of crashed runs (nC), the number of runs without a surge (nS0), and the number of runs with only one surge (nS1). The first 20 kyr of each run are treated as a spin-up interval and are not considered in the above. The x axis is logarithmic. Further details of each individual experiment are provided in the subsequent sections and the Supplement. The model setups, from top to bottom, are as follows: 3.125 km wide sediment transition zone (instead of an abrupt transition in the reference setup), 25 km wide sediment transition zone, 3.125 km wide sediment transition zone with pseudo-Hudson Bay and Hudson Strait topography (instead of a flat topography in the reference setup), 25 km sediment transition zone with pseudo-Hudson Bay and Hudson Strait topography, 20 m deep (one layer) bed thermal model (instead of a 1 km deep bed thermal model (17 non-linearly spaced layers) in the reference setup), three different approaches to calculate basal grid cell interface temperature (TpmInt, upwind TpmInt, TpmCen), local hydrology (instead of no hydrology), and doubling the values of the soft- and hard-bed sliding coefficients (as an attempt to represent basal hydrology without actually adding it).

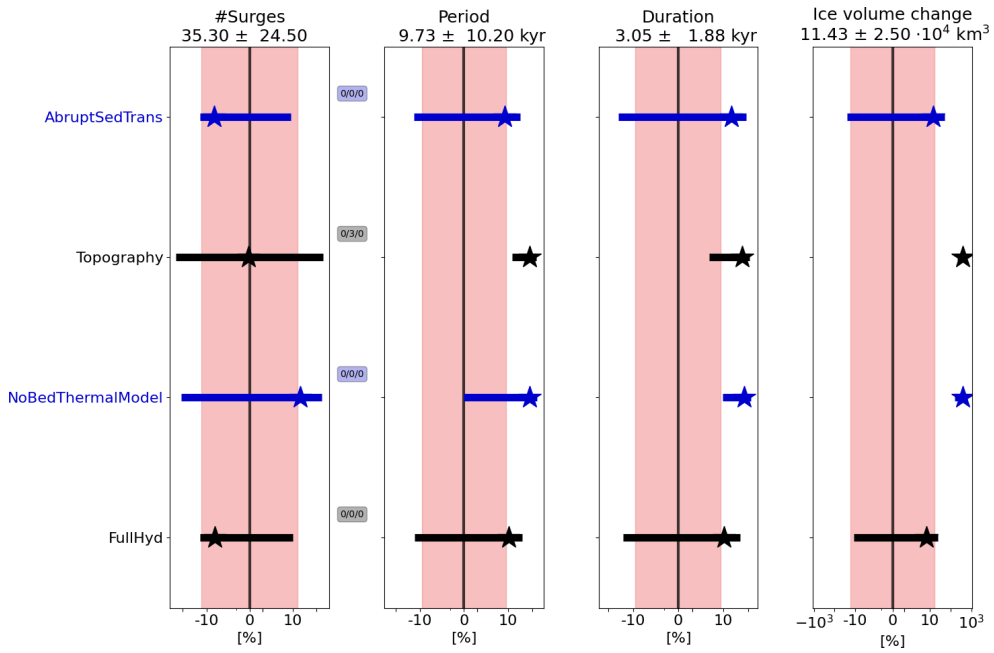

Figure 2.7: Percentage differences in surge characteristics compared to the PISM reference setup for model setups discussed in Sec. 2.3.3 (average of the nine parameter vectors). The horizontal grid resolution is 25 km. Otherwise same as Fig. 2.6. The model setups, from top to bottom, are as follows: abrupt sediment transition (instead of the transition shown in, e.g., Fig. A.8), pseudo-Hudson Bay and Hudson Strait topography (instead of a flat topography in the reference setup, Fig. A.9), no bed thermal model (instead of a 1 km deep bed thermal model (20 equally spaced layers) in the reference setup), and a mass-conserving horizontal transport model for basal hydrology (instead of a local hydrology).

leading to a heat flux from the ice into the bed. Consequently, less heat is available to warm the surrounding cold-based ice, counteracting the surge propagation (Fig. 2.8).

With only one bed thermal layer (20 m deep, removing most of the heat storage), the variance of the average basal temperature with respect to the pressure-melting point in the pseudo-Hudson Strait increases (Fig. A.20), and more heat is available to warm the surrounding ice (no or smaller heat flux into the bed, Fig. A.21). The additional heat increases the mean pseudo-Hudson Strait ice volume change and duration (50 % and 65 %, respectively – Fig. 2.6). Due to the larger changes in pseudo-Hudson

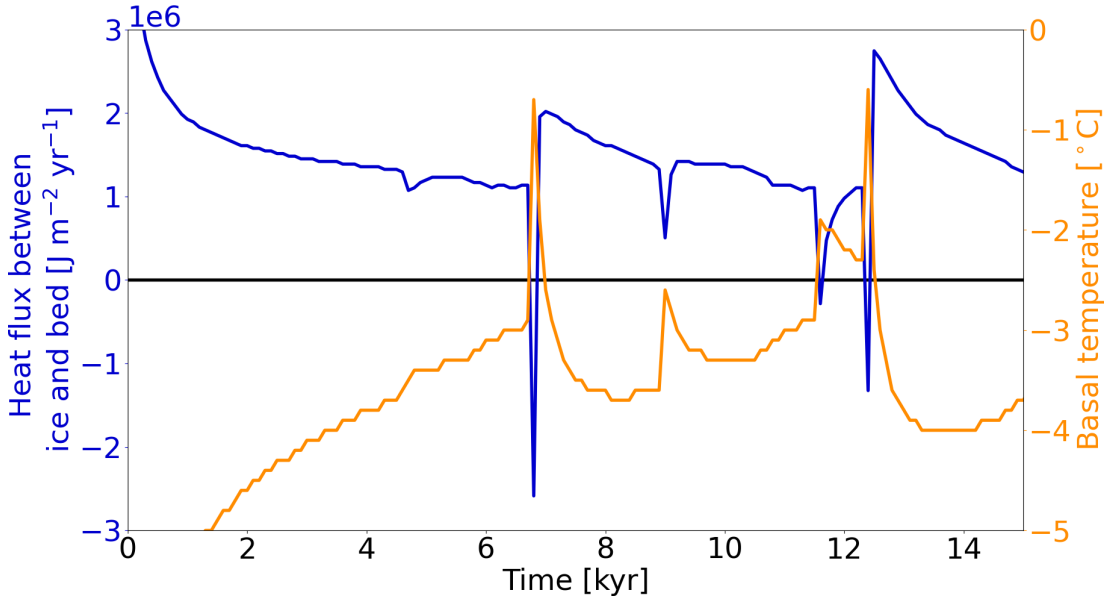

Figure 2.8: Heat flux at the base of the ice sheet (positive from bed into ice) and basal-ice temperature for a grid cell in the center of the pseudo-Hudson Strait (grid cell center at $x = 376.5625$ and $y = 248.4375$ km, white star in Fig. 2.1) and parameter vector 1 with the 1 km deep bed thermal model (17 non-linearly spaced levels) using the GSM. The horizontal grid resolution is 3.125 km.

Strait ice volume and average basal temperature with respect to the pressure-melting point, the ice sheet requires more time to reach the pre-surge state when only one bed thermal layer is used. Therefore, the period increases (60 %), while the number of surges drops. These differences in surge characteristics exceed the MNEEs (Table 2.5). The stronger surges (larger pseudo-Hudson Strait ice volume change) lead to overall less ice volume in the pseudo-Hudson Strait (Table A.7). Running PISM without the 1 km deep (20 equally spaced levels) bed thermal model yields similar behavior to the GSM, further underlining the impact of a bed thermal model. The mean period, mean duration, and mean ice volume change all increase (80 %, 70 %, and 396 %, respectively – Fig. 2.7). In contrast to the GSM characteristics, the number of surges increases for runs without a bed thermal model. However, the standard

deviation is large, and the change in the number of surges is somewhat misleading. The number of surges decreases for six out of nine runs. Parameter vectors showing an increase in the number of surges without a bed thermal model show very few surges (e.g., Fig. A.22) or transition to a constantly active ice stream when the bed thermal model is included. As for the GSM, the stronger surges lead to an overall smaller ice sheet in the surge-affected area (Table A.8).

2.3.3.2 Basal temperature at the grid cell interface

Another modeling choice that affects the thermal activation of basal sliding is the approach to determining the basal temperature at the grid cell interface. The most straightforward approach to determining the basal temperature with respect to the pressure-melting point at the grid cell interface ($T_{\mathrm{bp,I}}$) is to use the mean of the two adjacent basal temperatures with respect to the pressure-melting point at the grid cell centers (TpmCen):

$$T_{\mathrm{bp,I}} = 0.5 \cdot (T_{\mathrm{bp,L}} + T_{\mathrm{bp,R}}) \,, \tag{2.16}$$

where $T_{\mathrm{bp,L}}$ and $T_{\mathrm{bp,R}}$ are the grid cell center basal temperatures with respect to the pressure-melting point to the left and right of the interface, respectively. This is similarly the case for upper and lower grid cells adjacent to a horizontally aligned interface. However, this approach does not explicitly account for ice thickness changes at the grid cell interface.

TpmInt, on the other hand, calculates the basal temperature at the interface (T_{I}) by averaging the adjacent grid cell center basal temperatures (T_{L} and T_{R}, Eq. 2.17a). $T_{\mathrm{bp,I}}$ is then determined by using the interface ice sheet thickness (average of adjacent

grid cell center ice thicknesses H_{L} and H_{R}, Eq. 2.17b):

$$T_{\mathrm{I}} = 0.5 \cdot (T_{\mathrm{L}} + T_{\mathrm{R}}), \tag{2.17a}$$

$$T_{\mathrm{bp,I}} = T_{\mathrm{I}} + \beta_{\mathrm{P}} \frac{H_{\mathrm{L}} + H_{\mathrm{R}}}{2}, \tag{2.17b}$$

where $\beta_{\mathrm{P}} = 8.7 \times 10^{-4}\,^{\circ}\mathrm{C\,m^{-1}}$ is the standard basal-melting-point depression coefficient. When TpmInt is used with the upwind scheme and the basal-ice velocity exceeds $20\,\mathrm{m\,yr^{-1}}$, Eq. (2.17a) is replaced by $T_{\mathrm{I}} = T_{\mathrm{up}}$, where T_{up} is the upstream adjacent grid cell center basal temperature.

The last approach (TpmTrans) attempts to represent heat transfer from subglacial hydrology and ice advection by accounting for extra warming above the pressure-melting point, given by

$$T_{\mathrm{add}} = M_{\mathrm{b}} \cdot \frac{L_{\mathrm{H}}}{c_{\mathrm{H}}} \cdot \frac{1}{H_{\mathrm{b}}} \cdot \Delta t, \tag{2.18a}$$

where M_{b} is the basal mass balance in meters per year (positive for melt), $L_{\mathrm{H}} = 3.35 \times 10^{5}\,\mathrm{J\,kg^{-1}}$ is the specific latent heat of fusion of water–ice, $c_{\mathrm{H}} = 2097\,\mathrm{J\,kg^{-1}\,K^{-1}}$ is the heat capacity of ice at 273.03 K, H_{b} is the basal-ice layer thickness in meters, and Δt is the current model time step in years. In an intermediate calculation step, the temporary basal temperature at the grid cell center $T_{\mathrm{Im,C}}$ is calculated by accounting for the additional heating T_{add}:

$$T_{\mathrm{Im,C}} = T_{\mathrm{C}} + T_{\mathrm{add}}, \tag{2.18b}$$

where T_{C} is the basal temperature at the grid cell center. The basal temperature with respect to the pressure-melting point at each adjacent grid cell center $T_{\mathrm{bp,Im,C}}$ is then

calculated using the interface ice thickness.

$$T_{\mathrm{bp,Im,C}} = T_{\mathrm{Im,C}} + \beta_{\mathrm{P}} \frac{H_{\mathrm{L}} + H_{\mathrm{R}}}{2} \tag{2.18c}$$

In the intermediate steps to calculate the interface temperature (Eq. 2.18b and 2.18c), $T_{\mathrm{Im,C}}$ and $T_{\mathrm{bp,Im,C}}$ are allowed to exceed the pressure-melting point. This temporary higher basal temperature is an attempt to account for heat transported to the interface by ice advection and basal water.

$$\begin{aligned} &\text{if } T_{\mathrm{bp,Im,C}} > 0\,^{\circ}\mathrm{C}: \\ &\quad T_{\mathrm{bp,Im,C}} = \min\left(0.5^{\circ}\mathrm{C}, 0.5 \times T_{\mathrm{bp,Im,C}}\right) \end{aligned} \tag{2.18d}$$

Averaging the adjacent basal temperatures with respect to the pressure-melting point at the grid cell center ($T_{\mathrm{bp,Im,L}}$ and $T_{\mathrm{bp,Im,R}}$) yields the final basal temperature with respect to the pressure-melting point at the interface ($T_{\mathrm{bp,I}}$).

$$T_{\mathrm{bp,I}} = 0.5 \cdot \left(T_{\mathrm{bp,Im,L}} + T_{\mathrm{bp,Im,R}}\right) \tag{2.18e}$$

Note that neither the grid cell center nor the interface basal temperature may exceed the pressure-melting point (only the basal temperature in the intermediate calculation steps).

The GSM reference setup (no hydrology) uses TpmTrans. The additional heat embodied in T_{add} warms up the grid cell interface. Without the extra warming (TpmInt), four out of five parameter vectors do not show any surges. For the only run that still has cyclic behavior (parameter vector 1), the number of surges decreases

by 84 % (note that runs without surges are considered for the number of surges in Fig. 2.6). Using TpmInt with an upwind scheme leads to slightly more surges (difference of 7 % and, therefore, on the same order of magnitude as the MNEE (4 %, Table 2.5)). Sporadic surges now occur in all but one run, leading to a large increase in the mean period (1645 %, Fig. 2.6).

The most straightforward approach, TpmCen, leads to 75 % fewer surges and an increase in mean period and mean duration (609 % and 43 %, respectively). The mean pseudo-Hudson Strait ice volume change decreases (−61 %). Note that the TpmInt, TpmInt uwpind, and TpmCen surge characteristics are difficult to compare due to the different number of runs considered (except for the number of surges – decrease of 97 % vs. 90 % vs. 75 %, respectively). Due to significantly fewer surges, the mean pseudo-Hudson Strait ice volume increases for runs with TpmInt, TpmInt uwpind, and TpmCen (Table A.9).

2.3.3.3 Basal-temperature ramps at different resolutions

Here we examine the effect of different basal-temperature ramps (thermal-activation criteria for basal sliding) at 3.125 km horizontal grid resolution and determine ramps for the coarse-resolution runs that best match the 3.125 km model results (later used in Sec. 2.3.4.1). For coarse resolutions, changing the basal-temperature ramp can lead to a shift from oscillatory to non-oscillatory behavior (compare 25 km runs in Fig. A.23 and A.24).

When running the GSM at 3.125 km horizontal grid resolution, surges are apparent for all tested basal-temperature ramps. Due to an earlier sliding onset and easier surge propagation, increasing the width of the temperature ramp generally increases

the mean pseudo-Hudson Strait ice volume change and duration (Fig. 2.9). The ice sheet takes longer to recover from the surge (longer regrowth phase), increasing the mean period and decreasing the average number of surges. Running the GSM without a basal-temperature ramp leads to small but significant (according to the MNEEs) differences in the mean duration ($-7\,\%$).

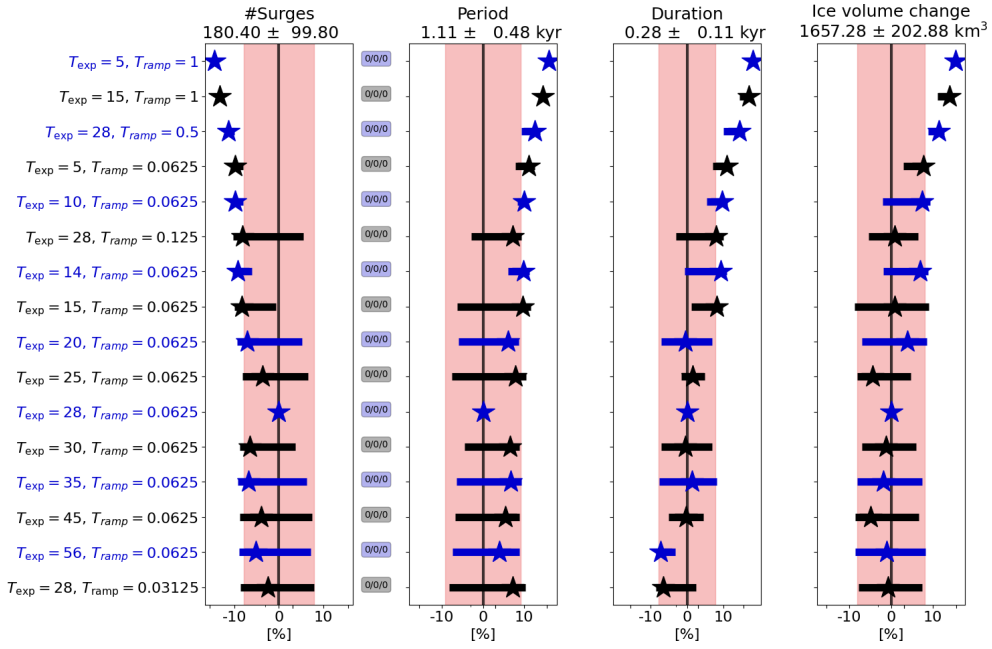

Figure 2.9: Percentage differences in surge characteristics compared to the GSM reference setup ($T_{\text{ramp}} = 0.0625$, $T_{\text{exp}} = 28$) for different basal-temperature ramps at 3.125 km horizontal grid resolution (average of the five parameter vectors). The ramps are sorted from widest (first row) to sharpest (last row; see Fig. A.25 for a visualization of all ramps). Otherwise the same as Fig. 2.6. No runs crashed, and all runs had more than one surge. The exact values are given in Table A.10.

Except for the three widest ramps, the mean ice volume bias is less than $1\,\%$. The RMSE, on the other hand, is roughly $8\,\%$, indicating that the average pseudo-Hudson Strait ice volume is similar, but the timing of surges varies even for small differences in the width of the ramp (Table A.10).

We compare the different temperature ramps at 25, 12.5, and 6.25 km horizontal grid resolution by calculating a single score for the mean and standard deviation of all surge characteristics (Sec. A.7.3). The ramps yielding the smallest differences compared to the 3.125 km reference setup are listed in Table A.11 and shown in Fig. A.26. These results may be different for a different reference setup (see Table A.22 for a comparison of different reference setups with local basal hydrology).

At 25 km horizontal grid resolution, only 3 out of 12 basal-temperature ramps remain after removing the ramps for which the sum of scores (score mean + score SD, last column in Table A.11) differs by more than 50 % from the minimum sum of scores (bold number in last column in Table A.11). The minimum scores for the mean and standard deviation occur for the same ramp ($T_{\text{exp}} = 5$, $T_{\text{ramp}} = 0.5$), clearly identifying it as the ramp that best resembles the 3.125 km horizontal grid resolution reference runs. For the two finer horizontal grid resolutions, the minimum mean and standard deviation scores arise for different temperature ramps, preventing the determination of a single best ramp.

A more physically-based approach to determining an appropriate scale-compensating temperature ramp stems from our motivation for research question Q_5 above. We bundle all 3.125×3.125 km grid cells of our reference runs into patches of, e.g., 64 grid cells. Each patch represents a coarser (e.g., 25×25 km) grid cell. We then determine the warm-based fraction (basal temperature at the pressure-melting point) and the mean basal temperature with respect to the pressure-melting point of each patch. We can then estimate the parameters T_{ramp} and T_{exp} of the basal-temperature ramp (Eq. 2.8) by plotting the warm-based fraction against the mean basal temperature for all patches (e.g., Fig. 2.10) and fitting a basal-temperature ramp with the prelim-

inary assumption that a corresponding coarse grid cell should have an ice-streaming fraction proportional to the sub-grid warm-based area.

However, this upscaling analysis does not account for the connectivity between the faces of, e.g., a 25 km grid cell. Without a continuous warm-based channel from one grid cell interface to another, there should be effectively no basal sliding across the grid cell, even when the average basal temperature is close to the pressure-melting point. Consequently, the best estimate for the two parameters of the basal-temperature ramp should be a lower bound to the points in the scatter plot.

Furthermore, the upscaling results depend on the bed properties (soft sediment vs. hard bedrock) and the specific scenario (surge vs. quiescent phase). Therefore, we only consider patches within the pseudo-Hudson Strait area during surges. Due to the limited storage capacity for the 10-year output fields, only the first 10 kyr after the first surge are used for the upscaling experiments.

The upscaling results agree well with the score analysis at 25 km horizontal grid resolution. Both indicate that, at this resolution, the ramp $T_{\text{exp}} = 5$, $T_{\text{ramp}} = 0.5$ (first row in Table A.11, Fig. 2.10) gives results that best match those of the 3.125 km reference runs. The two approaches yield a similar range of temperature ramps at 12.5 and 6.25 km horizontal grid resolution, but the upscaling experiments generally favor wider temperature ramps (Table A.11 and Fig. A.27 and A.28). This is likely a consequence of the above-mentioned role of sub-grid warm-based connectivity not accounted for in the upscaling analysis. When using the resolution-dependent ramp of Eq. (2.9), the upscaling experiments provide a lower bound of $T_{\text{exp}} = 5$. Upscaling experiments with local basal hydrology lead to similar results.

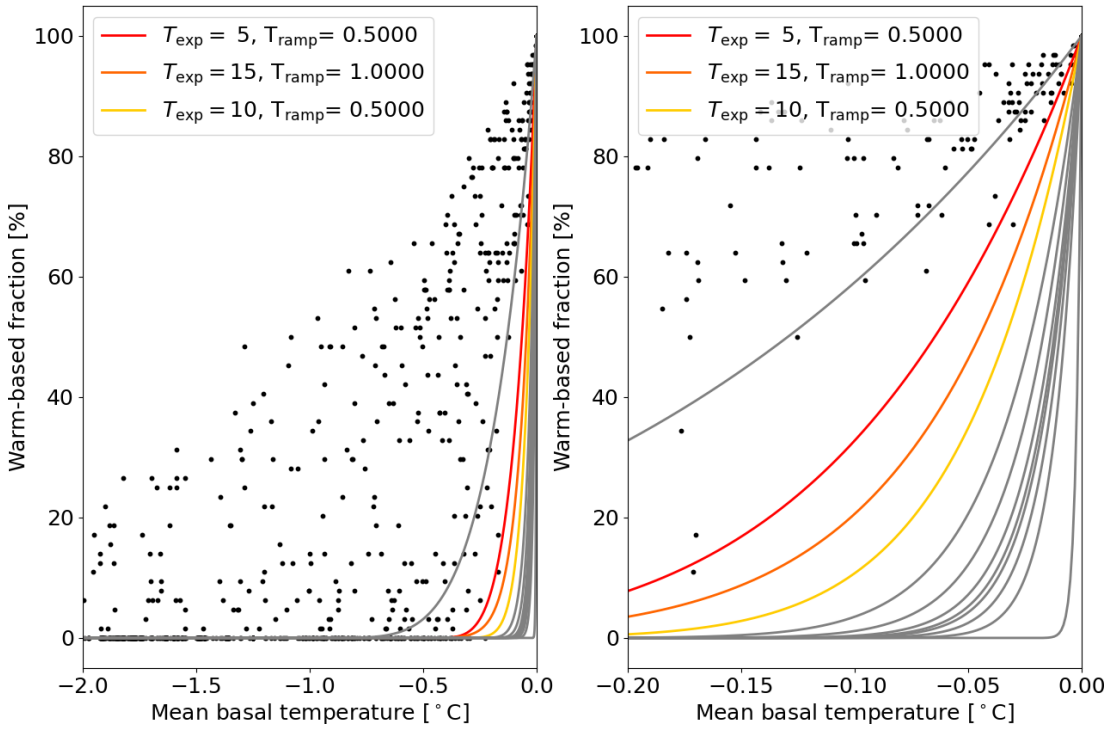

Figure 2.10: Warm-based fraction (basal temperature with respect to the pressure-melting point at 0 °C) vs. mean basal temperature with respect to the pressure-melting point when upscaling a 3.125 km run to 25 km horizontal grid resolution including all five parameter vectors using the GSM. For example, an upscaled 25 km patch (containing 64 3.125 km grid cells) with 32 3.125 km grid cells at the pressure-melting point and 32 3.125 km grid cells at −1 °C with respect to the pressure-melting point has a warm-based fraction of 50 % and a mean basal temperature of −0.5 °C. Only grid cells within the pseudo-Hudson Strait and time steps within the surges of the 10 kyr after the first surge are considered. The restriction to the 10 kyr after the first surge for these experiments is set by storage limitations due to the high temporal resolution of the model output fields (10 years). The colored ramps correspond to the 25 km horizontal grid resolution basal-temperature ramps in Table A.11, and the gray lines show all other ramps that were tested at this resolution.

2.3.3.4 Smooth sediment transition zone and non-flat topography

The effects of a smooth sediment transition zone (instead of an abrupt transition from hard bedrock (0 % sediment cover) to 100 % (soft) sediment cover) and a non-flat topography on surge characteristics are examined here.

The abrupt transition from hard bedrock to soft sediment (pseudo-Hudson Bay

and Hudson Strait) in the GSM reference setup and the corresponding difference in basal-sliding coefficient provide an additional heating source due to shearing between slow- and fast-moving ice. This additional heat appears to foster the propagation of small surges along the transition zone (e.g., 6 to 6.3 kyr in the upper row of video 03 of Hank, 2023b). Incorporating a smooth transition zone (3.125 km or 25 km wide) affects the location of the small-scale surges (not considered in surge characteristics) but shows only minor differences for the major surges ($< 7.5\,\%$ for all surge characteristics, Fig. 2.6). The mean bias for both widths is $< 1\,\%$, indicating only minor differences in ice volume between an abrupt and smooth transition. However, the timing of surges varies for different transition zones (RMSE $\leq 8\,\%$, Fig. 2.11). A wider transition zone (more sediment surrounding the pseudo-Hudson Strait and Hudson Bay) generally favors an earlier sliding onset (e.g., Fig. 2.11), but the details depend on the parameter vector in question.

Similarly to the GSM results, the PISM percentage differences between a smooth (reference setup) and abrupt sediment transition show no significant effect except for a 22 % increase in surge duration (Fig. 2.7).

Adding a 200 m deep pseudo-Hudson Strait and Hudson Bay with a smooth transition zone and 500 m deep ocean to the GSM setup displaces the origin of surges slightly further inland. Due to both the resultant warmer basal temperature and depressed pressure-melting point, the surges propagate faster, last longer, and evacuate more ice volume (Fig. 2.6). The topography slopes down towards the pseudo-Hudson Strait, increasing the ice inflow from the surroundings. The ice sheet recovers faster from the previous surge, decreasing the mean period. Note that Fig. 2.6 shows an increase in the mean period, but this is somewhat misleading due to the now early

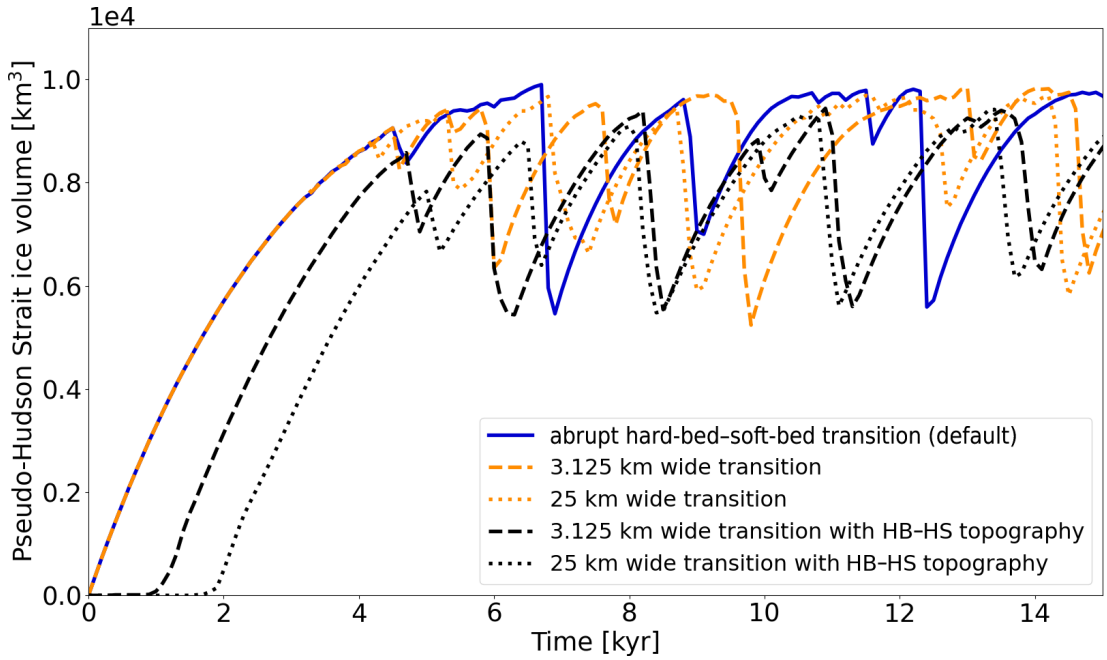

Figure 2.11: Pseudo-Hudson Strait ice volume for GSM parameter vector 1 and three different bed configurations. The horizontal grid resolution is 3.125 km. Note that the width of the topographical transition zone matches the width of the soft-bed–hard-bed transition zone. In experiments with a pseudo-Hudson Bay and Hudson Strait (HB–HS) topography, the pseudo-Hudson Strait topography is below sea level, increasing the time required for glaciation. A wider transition zone (larger area below sea level) leads to a later glaciation.

surges for parameter vector 0 and the subsequent large increase in the mean period ($\sim 100\,\%$ – no surges in the middle part of the run due to cold surface temperatures, Fig. A.29). All other parameter vectors show a decrease in the mean period for both widths of the transition zone. The mean bias indicates a decrease in ice volume of $\sim 6.5\,\%$ for runs with a non-flat topography caused by the larger surges. The pseudo-Hudson Strait topography also suppresses the small surges otherwise observed in the vicinity of the pseudo-Hudson Strait. A detailed comparison of an individual run is presented in Sec. A.7.4.

Comparing the results for two different widths of the topographic transition zone

(−200 m to sea level) indicates fewer but stronger surges (increase of mean pseudo-Hudson Strait ice volume change by 9 %, Fig. 2.6) for a wider transition zone. The gentler slope increases the width of the ice stream and, thereby, the ice flux out of the pseudo-Hudson Strait (video 04 of Hank, 2023b). The increased flux leads to a decreased pseudo-Hudson Strait ice volume at the end of the surge. The stronger surges for a wider transition zone increase the recovery time, leading to a smaller increase in the number of surges than for the narrow transition zone (difference of 16 %, Fig. 2.6).

While imposing a non-flat topography fosters surges in both models, the increase in mean ice volume change is much larger in PISM (390 %) than in the GSM (maximum $\sim$ 17 %), leading to a longer regrowth phase (79 % increase in mean period) and overall less ice volume (mean bias −30 %, Table A.13). The longer recovery times in PISM outweigh the effect of earlier sliding onsets, which lead to more surges in the GSM (see above). Therefore, the number of surges decreases in PISM (while increasing in the GSM) when using a non-flat topography (Fig. 2.7).

Since the topography will vary from ice stream to ice stream, we stick to a flat topography for the remaining experiments.

2.3.3.5 Basal hydrology

The effects of adding a simple local basal-hydrology model to the GSM are examined here. The local basal hydrology sets the basal water thickness by calculating the difference between the basal-melt rate and a constant basal-drainage rate (rBedDrainRate in Table 2.1). This sub-glacial hydrology provides a simple and computationally efficient way to capture changes in basal-sliding velocities due to effective-pressure

variations (Drew and Tarasov, 2022). However, it does not account for basal-ice accumulation, englacial or supraglacial water input, or horizontal water transport.

The basal water thickness (h_{wb}) and an estimated effective bed roughness scale ($h_{\mathrm{wb,Crit}}$ in Table 2.1) determine the effective-pressure coefficient:

$$N_{\mathrm{C,eff}} = 1 - \min\left(\frac{h_{\mathrm{wb}}}{h_{\mathrm{wb,Crit}}}, 1.0\right)^{3.5}. \tag{2.19}$$

The basal water thickness is limited to $h_{\mathrm{wb,Crit}} = 10\,\mathrm{m}$ and is set to $h_{\mathrm{wb}} = 0\,\mathrm{m}$ where the ice thickness is less than 10 m and where the temperature with respect to the pressure-melting point is below $-0.1\,^{\circ}\mathrm{C}$. Experiments with $h_{\mathrm{wb,Crit}} = 5\,\mathrm{m}$ yield the same results, and removing all the water for $H < 1\,\mathrm{m}$, $H < 50\,\mathrm{m}$, and $T_{\mathrm{bp}} < -0.5\,^{\circ}\mathrm{C}$ does not significantly (according to the MNEEs, Table 2.5) affect the model results. The effective pressure at the grid cell interface is then

$$N_{\mathrm{eff}} = g\rho_{\mathrm{ice}} \cdot 0.5\left(H_{\mathrm{L}} N_{\mathrm{C,eff,L}} + H_{\mathrm{R}} N_{\mathrm{C,eff,R}}\right), \tag{2.20}$$

where $g = 9.81\,\mathrm{m\,s^{-2}}$ is the acceleration due to gravity; $\rho_{\mathrm{ice}} = 910\,\mathrm{kg\,m^{-3}}$ is the ice density; H is the ice thickness; and the subscripts L and R denote the adjacent grid cells to the left and right of the interface, respectively (this is similarly the case for upper and lower grid cells adjacent to a horizontally aligned interface). We enforce that N_{eff} never falls below $N_{\mathrm{eff,min}} = 10\,\mathrm{kPa}$ (denominator in Eq. 2.21; similar results are found for $N_{\mathrm{eff,min}} = 5\,\mathrm{kPa}$). Finally, the effective pressure of each grid cell alters

the basal-sliding coefficient in the sliding law (Eq. 2.6a) according to

$$C_\mathrm{b} = C_\mathrm{b} \cdot \min\left(10, \max\left(0.5, \frac{N_\mathrm{eff,Fact}}{N_\mathrm{eff} + N_\mathrm{eff,min}}\right)\right), \tag{2.21}$$

where $N_\mathrm{eff,Fact}$ is the effective-pressure factor (Table 2.1). The change of the basal-sliding coefficient C_b is, therefore, limited to $C_\mathrm{b} \cdot 0.2$ to $C_\mathrm{b} \cdot 10$. Allowing a larger change of $C_\mathrm{b} \cdot 0.1$ to $C_\mathrm{b} \cdot 20$ does not significantly change the model results.

When running the GSM with the local sub-glacial hydrology model, intermediate values are used for all three parameters (the effective bed roughness scale $h_\mathrm{wb,Crit} = 0.1\,\mathrm{m}$, Eq. 2.19; the constant bed drainage rate rBedDrainRate $\simeq 0.003\,\mathrm{m\,yr^{-1}}$; and the effective-pressure factor $N_\mathrm{eff,Fact} \simeq 63\,246\,\mathrm{Pa}$, Eq. 2.21) for all five parameter vectors. However, different values were tested for all three parameters (not shown). In general, a larger $N_\mathrm{eff,Fact}$ increases the basal-sliding coefficient (Eq. 2.21) and, therefore, leads to fewer but stronger surges. The results for $h_\mathrm{wb,Crit}$ and rBedDrainRate are not as straightforward to interpret. The model response varies for the two tested parameter vectors, and the changes are generally smaller than the MNEEs.

Adding the local basal hydrology model to the GSM increases the mean ice volume change and duration by 20 % and 12 %, respectively (Fig. 2.6, exceeding the MNEEs). The stronger surges are due to the reduction of effective pressure and, thus, increased sliding (Eq. 2.21 and 2.6a). The mean period increases (17 %), while the number of surges decreases (−4 %), but the standard deviations are large.

Since the local hydrology model effectively increases the basal-sliding coefficient, we test if this impact can be replicated simply by increasing the sliding coefficients (Table 2.1) in a GSM configuration without basal hydrology. Doubling the soft-bed-

sliding coefficient leads to similar or larger maximum basal-sliding velocities and, consequently, maximum ice fluxes but a smaller increase in the mean period (12 % vs. 17 %) and mean pseudo-Hudson Strait ice volume change (11 % vs. 20 %) than that of the local hydrology model. Increasing the hard-bed-sliding coefficient has no significant effect on the surge characteristics (pseudo-Hudson Bay and Hudson Strait are soft-bedded – Fig. 2.6). Intermediate increases in the basal-sliding coefficients (not shown) also do not capture the surge characteristics of the basal-hydrology model. Therefore, simply changing the basal-sliding coefficients cannot replace the basal-hydrology model.

2.3.3.6 Sensitivity experiments without a significant effect

The effect of an experiment is considered to be insignificant when the change in surge characteristics is smaller than the MNEEs (Sec. 2.3.2). This is the case for different weights of the adjacent minimum basal temperature when calculating the basal interface temperature (Q_6) for different implementations of the basal hydrology (Q_9) and when using basal hydrology instead of the basal-temperature ramp as the primary smoothing mechanism (Q_{10}). The details of these experiments are presented in Sec. A.8.1, A.8.2, and A.8.3, respectively. We want to emphasize that experiments without a significant effect can still have physical relevance, but it is currently hidden within the numerical sensitivities.

2.3.4 Convergence study

In this section, we examine the horizontal grid resolution dependence of the GSM and PISM model results. Model results are considered to be converging when the

differences in surge characteristics decrease with increasing horizontal grid resolutions.

2.3.4.1 GSM convergence study

Significant differences in surge characteristics occur when changing the horizontal grid resolution. These differences can be as large as a highly oscillatory behavior at 3.125 km and no oscillations at 25 km horizontal grid resolution (Fig. A.23). Changing the basal-temperature ramp can somewhat counteract this discrepancy by enabling basal sliding at lower basal temperatures for coarser grid resolutions (Fig. A.24 and video 05 of Hank, 2023b). Further details on discrepancies between horizontal grid resolutions for individual parameter vectors are discussed in Sec. A.9.1.

We compare the differences in surge characteristics for different basal-temperature ramps at each resolution (Fig. 2.12). We examine a constant ramp ($T_{\text{ramp}} = 0.0625$, $T_{\text{exp}} = 28$), a resolution-dependent temperature ramp ($T_{\text{exp}} = 28$, Fig. 2.2), and the ramp with the smallest differences in surge characteristics (bold mean score in Table A.11). Note that the large differences in mean period at 25 km resolution are caused by long time intervals without any oscillations in the coarse-resolution runs (Table A.18). The 25, 12.5, and 6.25 km runs show progressively smaller differences for the constant and resolution-dependent ramp, indicating model convergence. Convergence of the GSM results with increasing grid resolutions is further supported by successively smaller pseudo-Hudson Strait ice volume RMSE and mean bias values (Table A.19). RMSE and mean bias are smaller across all resolutions when using a resolution-dependent ramp instead of a constant temperature ramp (except for the RMSE at 12.5 km horizontal grid resolution).

All three basal-temperature ramps lead to similar differences in surge character-

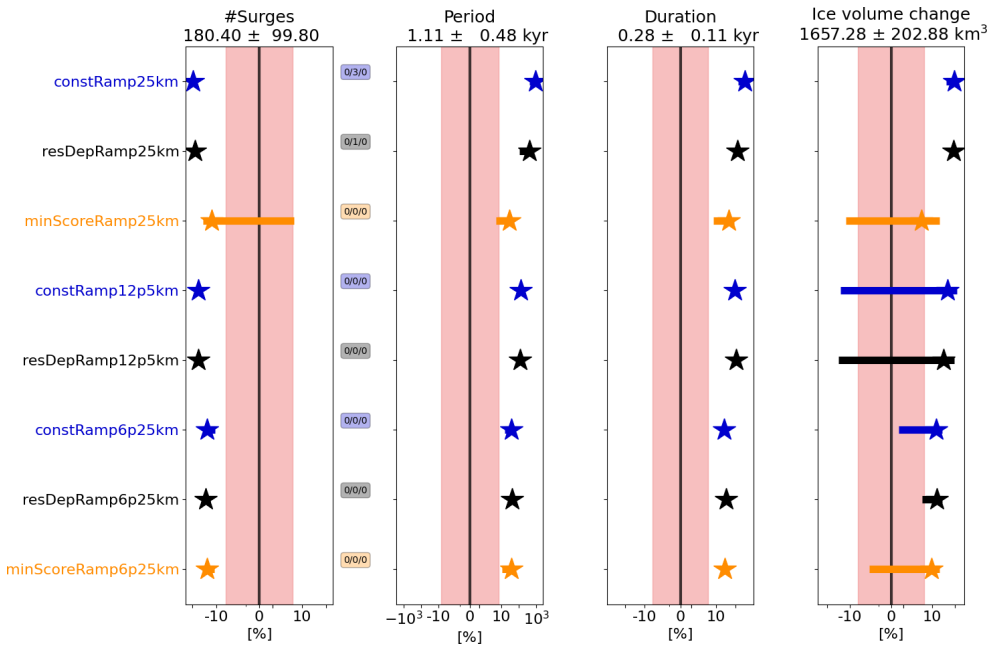

Figure 2.12: Percentage differences in surge characteristics compared to the GSM reference setup (3.125 km horizontal grid resolution) for model setups with coarser (25, 12.5, and 6.25 km) horizontal grid resolutions (average of the five parameter vectors). The different colors were added for visual alignment of the individual model setups and mark model setups with constant (blue), resolution-dependent (black), and minimum-score (orange, Sec. A.7.3) basal-temperature ramps. The resolution-dependent ramps ($T_{\text{exp}} = 28$) and constant ramps (black line, $T_{\text{ramp}} = 0.0625$, $T_{\text{exp}} = 28$) are shown in Fig. 2.2. The minimum-score basal-temperature ramps are $T_{\text{ramp}} = 0.5$, $T_{\text{exp}} = 5$ at 25 km and $T_{\text{ramp}} = 0.125$, $T_{\text{exp}} = 45$ at 6.25 km horizontal grid resolution. At 12.5 km, the minimum-score ramp is the same as the resolution-dependent ramp. Otherwise the same as Fig. 2.6. Further details of each individual experiment are provided in Sec. 2.3.4.1 and the Supplement.

istics at 6.25 and 12.5 km horizontal grid resolution (Fig. 2.12). At 25 km resolution, the ramp with the minimum differences in surge characteristics significantly improves the agreement with the 3.125 km runs, with differences that are smaller than for any other ramp or resolution. This could be a coincidence, or it could indicate that, despite thorough testing, the best ramp has not been found at 6.25 and 12.5 km horizontal grid resolution. Since other ramps at 25 km horizontal grid resolution show only slightly larger differences in surge characteristics (e.g., difference of 0.23 in the

mean score, Table A.11), it is unlikely that it is just a coincidence. However, the sensitivity of the surge characteristics to grid refinement remains, no matter the choice of the temperature ramp, with differences significantly exceeding the MNEEs from Sec. 2.3.2. Since including a sub-glacial hydrology model significantly affects the surge characteristics, we also examine the horizontal grid resolution scaling with a local-basal hydrology model (Sec. A.9.2). The results show overall smaller differences (relative to the 3.125 km reference simulations) in surge characteristics than without a sub-glacial hydrology model (Table A.22 vs. Table A.18). The analysis of the convergence study (with and without basal hydrology) and the upscaling experiments in Sec. 2.3.3.3, therefore, suggest a resolution-dependent temperature ramp with T_{exp} between 5 and 10.

2.3.4.2 PISM convergence study

Similarly to the results presented for the GSM, the ice volume RMSE and mean bias show convergence under systematic grid refinement (Table A.26). However, for the three resolutions examined here, the PISM surge characteristics show convergence for the mean duration and ice volume change but not the number of surges and mean period (Table A.25). Note that four out of nine runs at 12.5 km horizontal grid resolution did not finish within the time limit of the computational cluster and are considered to be crashed runs (potentially skewing the statistics). Additionally, one run at 12.5 km resolution did not show any surges and was also excluded from the analysis. The differences in surge characteristics for different grid resolutions are, in general, larger than the MNEEs but can be smaller (mean ice volume change of the 25 km runs).

2.4 Results summary and discussion

This section summarizes our modeling results in the context of the research questions outlined in Sec. 2.1.2 and previous modeling studies.

2.4.1 Minimum numerical error estimates

Q_1 What is the threshold of MNEEs in the two models?

The MNEEs can be as large as 16 % (Tables 2.5 and 2.6). Given the non-linearities in the SSA (or higher-approximation) ice sheet system, there is no a priori reason to confidently assume other ice sheet models will have ignorable MNEEs for unstable contexts such as surge cycling and grounding-line response. Therefore, it is crucial to determine MNEEs (or a comparable threshold) to minimize the possibility of interpreting numerical errors as a physical response to a change in model setup.

In contrast to the findings of Souček and Martinec (2011), adding low levels of surface temperature noise does not significantly affect the GSM and PISM results (Tables A.3 and A.6). Potential reasons for the different model responses are the use of an Arakawa A grid (velocities and temperatures are calculated on the same node – Arakawa and Lamb, 1977) and the JOSH (JOint Shallow-ice/Higher-order model) ice sheet dynamics in Souček and Martinec (2011).

2.4.2 Sensitivity experiments with a significant effect

Q_2 Is the inclusion of a bed thermal model a controlling factor for surge activity?

Including a 1 km deep bed thermal model significantly (according to the MNEEs) affects the surge characteristics in the GSM and PISM. The additional heat stored in the bed changes the thermal conditions at the ice–bed boundary, dampening the ice volume change during a surge (Fig. 2.6 and 2.7). Models with similar setups but without a bed thermal model likely overestimate the ice volume change during a surge (e.g., Calov et al., 2010; Brinkerhoff and Johnson, 2015). Therefore, the inclusion of a bed thermal model is a key aspect of modeling ice stream surge cycling.

Q_3 Do different approaches for determining the grid cell interface basal temperature significantly affect surge behavior, and if yes, which one should be implemented?

The choice of approach for determining the basal temperature at the grid cell interface significantly changes the surge characteristics. Without considering additional heat transfer to the grid cell interface (as an attempt to represent heat contributions from sub-glacial hydrology and sub-grid ice advection), the number of surges decreases by at least 75 %. The additional heat is, therefore, an essential component for modeling surges in the GSM.

This additional heat transfer to the grid cell interface is comparable to spreading 50 % of the basal-heating effect from sliding in a grid cell to the surrounding grid cells used in mPISM (latest version based on PISM v0.7.3, e.g., Ziemen et al., 2014, 2019; Schannwell et al., 2023). This spreading of basal heating warms the grid cells adjacent to an ice stream and was necessary to model Heinrich-event-like surges (Florian Ziemen, personal communication, 19 May 2022). While no additional heat transfer was added to PISM v2.0.2 used within this study, the

till friction angles had to be reduced to model surges.

Q_4 How different are the model results for different basal-temperature ramps? And what ramp should be used?

Similarly to Souček and Martinec (2011), we find significant differences in the period and amplitude of surges at all tested resolutions when using different implementations for thermal activation of basal sliding (the basal-temperature ramp). In the GSM, a wider temperature ramp enables sliding onset at lower temperatures, fostering more extensive surge propagation and leading to stronger surges. However, the choice of the most appropriate temperature ramp at the finest resolution tested (3.125 km, Fig. 2.9) is unclear, and identifying a single best ramp (fit of coarse-resolution runs to 3.125 km runs) is challenging (Table A.11). In general, a resolution-dependent ramp with T_{exp} between 5 and 10 (Eq. 2.8 and 2.9) yields the smallest differences between fine- and low-resolution simulations. However, given potential dependencies on the particular ice sheet model, we recommend resolution testing to determine the optimal basal-temperature ramp. Nevertheless, a basal-temperature ramp (or similar mechanism) should be implemented in all ice sheet models for contexts where surge onset and/or termination are important.

Q_5 Does the abrupt transition between a soft and hard bed significantly affect surge characteristics?

Incorporating a smooth transition zone with two different widths (3.125 and 25 km) in the GSM does affect the location of proximal small-scale ice streams (video 03 of Hank, 2023b). However, the abrupt transition is not the cause

of the major surges in the GSM (Fig. 2.6) and PISM experiments (Fig. 2.7). Since the sediment cover can change within a few kilometers (e.g., Andrews and MacLean, 2003), we conclude that, despite the minor differences, an abrupt transition between soft and hard beds is a reasonable simplification, especially considering horizontal grid cell dimensions of 25 km or larger.

Q_6 How does a non-flat topography affect the surge behavior?

Imposing a non-flat topography leads to significantly longer and stronger surges (Fig. 2.6 and 2.7). As such, and in agreement with previous modeling studies (e.g., Winsborrow et al., 2010, and references within), ice streaming is sensitive to the basal topography.

Q_7 What is the effect of a simplified basal hydrology on surge characteristics?

Activating the local basal-hydrology model (including the addition of effective-pressure dependence into the sliding law) in the GSM significantly increases the surge duration and amplitude (Fig. 2.6). Somewhat stronger surges are expected due to the reduction in effective pressure introduced by the sub-glacial water. Model runs without sub-glacial hydrology will therefore tend to underestimate the strength of surges. In general, this also holds for subglacial hydrology models with higher complexity (Drew and Tarasov, 2022). The importance of sub-glacial hydrology has also been shown in several other studies examining the effects of ice sheet surges and ice streaming within a continuum model approach (e.g., Fowler and Johnson, 1995; Fowler and Schiavi, 1998; Benn et al., 2019).

2.4.3 Sensitivity experiments without a significant effect

Q_8 How much of the ice flow should be blocked by upstream or downstream cold-based ice, or equivalently, what weight should be given to the adjacent minimum basal temperature?

Changing the weight of the adjacent minimum basal temperature for the basal-sliding temperature ramp in the GSM yields a maximum difference of 15 % (Table A.15). These somewhat small effects on surge characteristics are likely due to the fact that most surges propagate upstream (from the ocean to the pseudo-Hudson Bay), and the adjacent minimum basal temperatures (almost exclusively located upstream) have little potential to affect (e.g., partly block) the ice flow.

Q_9 How significant are the details of the basal-hydrology model to surge characteristics in PISM?

Incorporating a mass-conserving horizontal-transport hydrology model does not significantly change the surge characteristics in PISM (Fig. 2.7), indicating that the computationally much cheaper local hydrology model is a reasonable simplification for this context. More nuanced results, depending on the surge characteristics examined, are observed for the GSM (Drew and Tarasov, 2022).

Q_{10} What are the differences (if any) in surge characteristics between local basal hydrology and a basal-temperature ramp as the primary smoothing mechanism at the warm-based–cold-based transition zone?

Once included, the local basal hydrology is the primary smoothing mechanism.

However, since the two smoothing mechanisms operate in different temperature regimes, a basal-temperature ramp (representing sub-temperate sliding) cannot be replaced by a basal-hydrology scheme (as in, e.g., Robel et al., 2013; Kyrke-Smith et al., 2014; Brinkerhoff and Johnson, 2015). The differences in surge characteristics are smaller than the MNEEs, preventing further analysis.

2.4.4 Convergence study

Q_{11} Do model results converge (decreasing differences when increasing horizontal grid resolution)?

In general, both models exhibit convergence under systematic horizontal grid refinement for the overall ice volume (mean bias, Tables A.19+A.23 and A.26), but the solution is not fully converged at the finest resolutions tested. However, while all surge characteristics converge for the GSM (Table A.18), PISM results do not show convergence for the number of surges and mean period (Table A.25). This clearly illustrates that mean ice volume and, consequently, mean ice thickness, as presented, e.g., in Van Pelt and Oerlemans (2012), are insufficient metrics to determine whether cyclic model results exhibit a resolution dependency.

While other studies examining thermally induced ice streaming do not find a strong resolution dependence (Hindmarsh, 2009; Brinkerhoff and Johnson, 2015), these studies are not directly comparable. The different results are likely due to differences in the experimental design. For example, neither Hindmarsh (2009) nor Brinkerhoff and Johnson (2015) consider a bed thermal model. While

Hindmarsh (2009) considers sub-temperate sliding, his model allows sliding far below the pressure-melting point (order of $\delta = 1$ compared to $\delta = 0.01$ within this study – Eq. 2.10) and focuses on steady ice streaming and not ice stream surge cycling. Both of the above studies analyze just one parameter vector, and there are some parameter vectors for which, e.g., the GSM exhibits only a minor resolution dependence.

Even though the studies are not directly comparable, the results of Brinkerhoff and Johnson (2015) offer some insight relevant to this study. For example, they suggest that membrane stresses are necessary for convergence under horizontal grid refinement. The hybrid SIA–SSA ice dynamics used in the GSM and PISM might be insufficiently higher order and lead to a stronger resolution dependence than the schemes used in Hindmarsh (2009) and Brinkerhoff and Johnson (2015). However, GSM experiments with the SSA active everywhere show a resolution dependence comparable to the velocity-dependent SSA activation criteria (Table A.24 and A.18, respectively), indicating that the hybrid SIA–SSA ice dynamics are not the sole reason for the strong resolution dependence.

Conclusions

Within the limitations of hybrid SIA–SSA ice dynamics, we investigate the effect of ice sheet model numerics and discretization choices on surge characteristics often neglected in ice sheet modeling studies. We show how to reduce numerical and discretization sensitivities given finite computational resources and then how to de-

termine the significance of model results given residual computationally unavoidable numerical sensitivities for surge cycling contexts. In particular, our analyses offer guidance on minimizing the resolution dependency by implementing a resolution-dependent basal-temperature ramp for basal-sliding thermal activation and increasing confidence in model results by determining minimum numerical error estimates (MNEEs). Based on these MNEEs, our results indicate that surge characteristics are significantly affected by the inclusion of a basal-hydrology model. Not including the dampening effect of a bed thermal model on basal-temperature changes, as has been the tendency in idealized process studies, overestimates the surge amplitude. The key takeaways of this study are the physical modeling choices and numerical sensitivities that must be considered when numerically modeling ice stream surge oscillations.

Preface to Chapter 3: "The comparative role of system processes in Hudson Strait ice stream cycling: a comprehensive model-based test of Heinrich event hypotheses"

This manuscript is intended for submission to Climate of the Past. The GSM is now run with a realistic North American geometry, a transient last glacial cycle climate forcing, and a global visco-elastic GIA model. This chapter assesses the significance of relevant physical system processes in a HE context, particularly concerning the HE hypotheses outlined in Sec. 1.2.3.

Chapter 3

P2: The comparative role of system processes in Hudson Strait ice stream cycling: a comprehensive model-based test of Heinrich event hypotheses

Abstract

Despite their recognized significance on global climate and extensive research efforts, the mechanism(s) driving Heinrich Events remain(s) a subject of debate. Here, we use the 3D thermo-mechanically coupled Glacial Systems Model (GSM) to examine Hudson Strait ice stream surge cycling as well as the role of 3 factors previously

hypothesized to play a critical role in Heinrich events: ice shelves, glacial isostatic adjustment, and sub-surface ocean temperature forcings. In contrast to all previous modeling studies examining HEs, the GSM uses a transient last glacial cycle climate forcing, global visco-elastic glacial isostatic adjustment model, and sub-glacial hydrology model. The results presented here are based on a high-variance sub-ensemble retrieved from North American history matching for the last glacial cycle.

Over our comparatively wide sampling of the potential parameter space (48 ensemble parameters for climate forcing and process uncertainties), we find two modes of Hudson Strait ice streaming: classic binge-purge versus near continuous ice streaming with occasional shutdowns and subsequent surge onset overshoot. Our model results indicate that large ice shelves covering the Labrador Sea during the last glacial cycle only occur when extreme calving restrictions are applied. The otherwise minor ice shelves provide insignificant buttressing for the Hudson Strait ice stream. While sub-surface ocean temperature forcing leads to minor differences regarding surge characteristics, glacial isostatic adjustment does have a significant impact. Given input uncertainties, the strongest control on ice stream surge cycling is the poorly constrained deep geothermal heat flux under the Hudson Bay and Hudson Strait. Increasing the geothermal heat flux within constraints leads to a shift from the binge-purge mode to the near continuous streaming mode.

3.1 Introduction

Heinrich Events (HEs) offer a near unique opportunity to explore a coupled ice-climate-ocean instability that operates on the order of centuries to millennia. HEs

are generally attributed to large armadas of icebergs drifting from the Hudson Strait across the North Atlantic (40° - 55°N) while depositing sediment layers of Ice-Rafted Debris (IRD). At least six of these Heinrich Layers have been identified between 60 kyr BP (before present) and 15 kyr BP, but there is evidence for earlier events (Table 6.3 in Bradley, 2014, and references therein). Heinrich Layers are usually characterized by high detrital carbonate concentration, low abundance of organic carbon and terrigenous lipids, and high magnetic susceptibility (Hemming, 2004). Mineralogical inferences from IRD records indicate a Hudson Strait/Hudson Bay provenance, but there is also evidence for Icelandic and European source regions (Grousset et al., 1993; Gwiazda et al., 1996a; Hemming, 2004). HEs generally coincide with the coldest phases of the Dansgaard-Oeschger (DO) cycles, followed by a sharp temperature increase (e.g., Hemming, 2004; Clement and Peterson, 2008; Hodell et al., 2010). Proxy records further indicate a weakening of the Atlantic Meridional Overturning Circulation (AMOC) and an increase in sub-surface ocean temperatures leading up to HEs (Marcott et al., 2011).

Despite over 50 years of research, the exact mechanism behind HEs remains unclear. The proposed hypotheses include an internally driven binge-purge model (MacAyeal, 1993), an ice shelf buildup-collapse mechanism (Hulbe, 1997; Hulbe et al., 2004), and a hypothesis encompassing underwater melt modulated by glacial isostatic adjustment (GIA, Bassis et al., 2017). However, an extensive study simultaneously investigating the relative role of each proposed HE hypothesis is still missing.

Here we run sensitivity experiments with the 3D thermo-mechanically coupled glacial systems model (GSM, Tarasov et al., 2024, in preparation) and a high-variance (with respect to ensemble parameters and ice sheet configuration) ensemble-based ap-

proach to determine the role that physical system processes play in HEs. A challenge in this context is the robust modeling of ice stream cycling associated with 2 of the 3 hypotheses discussed herein. This challenge is largely due to the abrupt changes with ice stream activation/de-activation, resulting in potentially high sensitivity to the implementation and discretization of the relevant dynamical equations (Hank et al., 2023). As a step towards addressing this, we use **M**inimum **N**umerical **E**rror **E**stimates (MNEEs) as a threshold for the numerical significance of model results.

In particular, we address the following research questions.

Q_1 *What are the characteristics of Hudson Strait ice stream surges?*

Q_2 *Can the sudden reduction of the buttressing effect of ice shelves trigger Hudson Strait ice stream surging?*

A 2°C increase in the sub-surface ocean temperature has been shown to cause a 6 fold increase in the ice shelf basal melt rates in front of the Hudson Strait ($\sim$ 6 $\frac{\text{m}}{\text{yr}}$ to 35-40 $\frac{\text{m}}{\text{yr}}$) in simulations with an ocean/ice-shelf model (Marcott et al., 2011). Such an increase can significantly degrade the buttressing effect of a confined ice shelf and, thereby, potentially trigger ice stream activation or surging. To test this scenario, forced ocean warming experiments are carried out with forcing timing set to that of the HE record (timing based on average of Table 6.3 in Bradley (2014), "HE shelf forcing").

Q_3 *Can a sudden breakup of fringing ice shelves along the Canadian coast explain the IRD records (without the need for surges)?*

HEs occurred during extremely cold climates. Hulbe et al. (2004) propose that

these cold conditions led to the formation of fringing ice shelves along the Canadian coast. A sudden disintegration of the ice shelves would provide a source for Canadian-source icebergs (Hulbe, 1997) and could potentially explain the IRD records found in ocean sediment cores from the North Atlantic.

Q_4 *What is the role of GIA in a HE context?*

Due to its effect on, e.g., relative sea level changes and ice sheet mass balance (e.g., Book et al., 2022), GIA has long been known to have a significant impact on ice sheet evolution (e.g., Tarasov and Peltier, 1997).

Q_5 *How does sub-surface ocean warming affect HEs?*

In the HE mechanism proposed by Bassis et al. (2017), a glacial isostatic uplifted bed topography at the Hudson Strait mouth protects the retreated ice sheet front from sub-surface ocean warmings (SSOWs) attributed to Dansgaard–Oeschger events (DO events). The ice sheet grows, eventually depressing the bed topography. Once the bed topography is depressed below the upper limit of the SSOW, the ice sheet front is vulnerable to ocean forcing. Due to a retrograde sloping bed, the ice sheet rapidly retreats during the next SSOW, allowing the bed topography to rise and isolate the ice sheet front from ocean forcing.

Due to the numerous differences in the model setup (e.g., model domain considered, grid discretization near the grounding line, GIA model, calving and sub-shelf melt implementations, and the lack of ice thermodynamics in Bassis et al. (2017)), we do not aim to directly replicate the experiments in Bassis et al.

(2017). Instead, we examine the role of SSOW in a HE context by applying a sub-surface ocean temperature increase for every DO event.

3.2 Methods

3.2.1 Modeling approach

All experiments within this study are conducted with the glacial systems model (GSM Tarasov and Peltier, 1999, 2007; Pollard and DeConto, 2012; Tarasov et al., 2024, in preparation). The GSM is initialized from ice-free conditions at 122 kyr BP and is run to present day with a maximum ice dynamics time step size of 1 yr (automatically decreased to meet CFL constraint or when numerical solver fails to converge). The reference setup has a horizontal grid resolution of $\Delta_{\text{lon}} = 0.5°$, $\Delta_{\text{lat}} = 0.25°$ (finer horizontal grid resolutions are currently computationally unfeasible in the context of this study). The topography and sediment cover of the entire model domain are shown in Fig. B.1. To facilitate correspondence with geological reconstructions of North American ice sheet extent over time (Dalton et al., 2022), the GSM can be subject to ice margin nudging via physically-bounded changes to grid cell melt or accumulation (under the control of 2 ensemble parameters as detailed in Tarasov et al., 2024, in preparation).

Modeling sensitivities and numerical requirements for a model configuration that had reduced grid resolution dependence in an ice stream surge cycling context were determined based on an slightly earlier version of the GSM (Hank et al., 2023). The inclusion of basal sliding at sub-freezing temperatures, a basal hydrology representa-

tion, and the dampening effect of a bed thermal model on basal-temperature changes significantly affect the surge characteristics. To account for these modeling aspects, the GSM version used within this study is run with a resolution-dependent basal temperature ramp, a local basal hydrology model (Drew and Tarasov, 2022), and a 4 km deep bed thermal model.

Additionally, the GSM incorporates, among other components, an asynchronously coupled global visco-elastic GIA solver (Tarasov and Peltier, 1997) and an asynchronously coupled geographically-resolved energy balance climate model (Deblonde et al., 1992). Instead of a constant climate forcing (e.g., Roberts et al., 2016) or only varying the ocean forcing (e.g., Alvarez-Solas et al., 2013; Bassis et al., 2017), we apply a transient last glacial cycle climate forcing. Furthermore, we use a high-variance ensemble (with respect to ensemble parameters and ice sheet configuration, 20 runs) instead of just a single parameter vector to partly address potential non-linear dependencies of model results on ensemble parameters.

3.2.2 Ensemble parameter vectors

The initial parameter vector ensemble is based on a North American history-matching for 51 GSM parameters (Tarasov et al., in preparation, Tarasov and Goldstein, 2021). $\sim$ 15000 coarse resolution ($\Delta_{\mathrm{lon}} = 1^{\circ}$, $\Delta_{\mathrm{lat}} = 0.5^{\circ}$) GSM runs from the history matching are sieved for total North American ice volume (V_{tot}) and area (A_{tot}) at specific time steps, the last time the center of the Hudson Bay (lat = 61.25°N, lon = 84.5°W) became free of grounded ice ($t_{\mathrm{ice,HB}}$), the southernmost ice extent between 94.7°W and 80.3°W ($\mathrm{lat}_{\mathrm{ice}}$), and the southernmost ice extent at 69.7°W ($\mathrm{lat}_{\mathrm{ice,Q}}$).

The exact sieves are $V_{\text{tot,110}} > 0.29 \cdot 10^7$ km^3, $V_{\text{tot,100}} < (V_{\text{tot,110}} - 0.15 \cdot 10^7$ km^3), $V_{\text{tot,60}} > 0.6 \cdot 10^7$ km^3, $V_{\text{tot,30}} < (V_{\text{tot,20}} - 0.1 \cdot 10^7$ km^3), $A_{\text{tot,20}} > 12 \cdot 10^3$ km^2, 9.0 kyr BP $> t_{\text{ice,HB}} >$ 7.8 kyr BP, $\text{lat}_{\text{ice}} < 39°$N, and $\text{lat}_{\text{ice,Q}} < 45.6°$N (Tarasov, 2024, in preparation). The numbers in the sub-scripts indicate the time step in kyr BP.

For the remaining $\sim$ 10000 runs, we use a peak prominence algorithm to determine surges (*SciPy* version 1.6.3, Virtanen et al., 2020). This is similar to the approach used in (Hank et al., 2023). However, due to the more realistic model domain used herein, not every increase in mid-Hudson Strait ice flux corresponds to a decrease in Hudson Strait ice thickness and vice versa. Since we are most interested in ice flux changes, the algorithm is applied directly to mid-Hudson Strait ice flux (minimum threshold of 0.0035 Sv) instead of the mean Hudson Strait ice thickness time series (as in Hank et al., 2023). We use mid-Hudson Strait ice flux instead of, e.g., the ice flux across the Hudson Strait grounding line, as it is less noisy and a more reliable indicator of large-scale surges. 2 different sieves are then applied to the surge characteristics. The runs pass if at least one of the following conditions is met:

1. $3 \leq$ #surges ≤ 10, 0.2 kyr $\leq$ mean surge duration, 5.0 kyr $\leq$ mean periodicity $\leq$ 11.0 kyr (for surges between 100 kyr BP and 15 kyr BP), and/or

2. $3 \leq$ #surges ≤ 10 (for surges between 65 kyr BP and 10 kyr BP).

The second sieve is added to increase the number of runs that show surges within the period set by HE proxy records (e.g., Hemming, 2004). The bounds for the mean duration and period are based on the literature HE estimates in Table 3.1.

The remaining $\sim$ 200 runs are re-submitted at a finer horizontal grid resolution

($\Delta_{\text{lon}} = 0.5°$, $\Delta_{\text{lat}} = 0.25°$). As for the coarse resolution runs, we apply the peak prominence algorithm to mid-Hudson Strait ice flux to determine surges. Since we are now most interested in surges that could explain the IRD layers observed in the North Atlantic (rather than simply sieving for runs that show surges), we reject surges for which one of the following conditions is fulfilled:

1. change in mid-Hudson Strait ice flux < 0.0025 Sv (previously 0.0035 Sv, across black vertical line (*HS*) in Fig. 3.2)

2. surge duration > 3 kyr (maxium estimated duration of 2.3 kyr in Hemming, 2004)

3. change in Hudson Strait ice volume $> -5 \cdot 10^3$ km^3 (only within area outlined by the *Hudson Strait mask* in Fig. 3.2)

Note that no proxy record can directly estimate the change in mid-Hudson Strait ice flux or Hudson Strait ice volume during HEs. For example, HE ice volume estimates based on the IRD records require assumptions about the sediment concentration in icebergs. However, different values were tested, and the above thresholds led to the most consistent (with respect to the surge mode across all runs) detection of surges while ensuring that mid-Hudson Strait ice flux increases and the Hudson Strait ice volume decreases.

Based on the remaining surges in the fine resolution runs, we hand-pick a high variance (with respect to the surge characteristics) sub-ensemble of 10 runs with #surges ≤ 2 and 10 runs with #surges > 2 (between 100 kyr BP and 10 kyr BP). The ensemble members that show ≤ 2 surges at the fine resolution (but > 2 surges

at the coarse resolution) are considered as *likely to surge* and are included to test if, e.g., the repetitive removal of the buttressing effect of an ice shelf can cause ice stream surge cycling in the Hudson Strait.

3.2.3 Model description

The GSM uses hybrid shallow shelf/ice physics based on the ice dynamical core originally developed by Pollard and DeConto (2012). The hybrid ice dynamics are activated once the shallow-ice approximation velocity within a grid cell exceeds 30 m yr^{-1} over soft sediments and 200 m yr^{-1} over hard bedrock. Except for the grounding line, a Weertman-type power law is used

$$u_\mathrm{b} = C_\mathrm{b} \left|\tau_\mathrm{b}\right|^{n_\mathrm{b}-1} \tau_\mathrm{b}, \tag{3.1}$$

where u_b is the basal sliding velocity, τ_b the basal stress, and n_b the bed power strength. In contrast to the version used in Hank et al. (2023) and depending on the sediment cover, two different values are used for n_b (change around 50 % sediment cover, exact n_b values are parameter-dependent). To indirectly account for subtemperate sliding, the basal sliding coefficient C_b is calculated according to

$$C_\mathrm{b} = (1 - F_\mathrm{warm})\, C_\mathrm{froz} + F_\mathrm{warm} C_\mathrm{warm}, \tag{3.2}$$

where F_warm is the estimated warm-based fraction of a grid cell (Hank et al., 2023). C_froz and C_warm are the fully cold-based (needed for numerical regularization) and fully warm-based sliding coefficients, respectively.

The calculation of the ice flux across the grounding line depends on the ensemble parameter for the friction coefficient and resultant basal drag (Tarasov et al., 2024, in preparation). It can take either a Weertman-type analytical constraint (Eq. (29) in Schoof, 2007) or Coulomb plastic grounding line parameterization (Eq. (38) in Tsai et al., 2015). The basal shear stresses for the two grounding line parameterizations are calculated according to

$$\tau_{\mathrm{b,weert}} = C_{\mathrm{b}} u_{\mathrm{b}}^{\frac{1}{n_{\mathrm{b}}}} \tag{3.3a}$$

$$\tau_{\mathrm{b,coul}} = f_{\mathrm{cl}} \rho g \cdot (H - H_{\mathrm{f}}), \tag{3.3b}$$

where f_{cl} is the Coulomb plastic friction coefficient, H the ice sheet thickness, and H_{f} the ice thickness at flotation. For grid cells with $\tau_{\mathrm{b,weert}} > \tau_{\mathrm{b,coul}}$, the Coulomb plastic instead of the Weertman-type grounding line parameterization is used.

3.2.4 Geothermal heat flux

The deep geothermal heat flux (GHF) input used in the GSM is constant in time but varies spatially (left panel in Fig. 3.1). It provides the lower boundary flux condition for a 4 km deep bed thermodynamic model fully embedded in the ice thermodynamic solver. The default GHF input field is from Davies (2013) and represents an upper bound of the literature estimates. However, GHF data in the Hudson Bay and Hudson Strait are sparse, and the estimated values differ significantly (Fig. B.2 and, e.g., Pollack et al., 1993; Shapiro and Ritzwoller, 2004; Goutorbe et al., 2011; Lucazeau, 2019; Cuesta-Valero et al., 2021). To determine the sensitivity of model results to the GHF, we weigh the default GHF field $\mathrm{GHF}_{\mathrm{def}}$ against a modified input $\mathrm{GHF}_{\mathrm{mod}}$

(right panel in Fig. 3.1 given the lower regional values in Blackwell and Richards, 2004))

$$\mathrm{GHF} = w_{\mathrm{GHF}} \cdot \mathrm{GHF}_{\mathrm{def}} + (1 - w_{\mathrm{GHF}}) \cdot \mathrm{GHF}_{\mathrm{mod}}, \tag{3.4}$$

where w_{GHF} is the weight ranging from 0 to 1. The reference GSM setup uses $w_{\mathrm{GHF}} = 1$. We run sensitivity experiments for $w_{\mathrm{GHF}} = [0, 0.2, 0.4, 0.6, 0.8]$ applied to the Hudson Bay and Hudson Strait as well as $w_{\mathrm{GHF}} = 0$ applied separately to the Hudson Strait (Fig. B.3) and Hudson Bay area (Fig. B.4). When only considering grid cells affected by the GHF modifications (Fig. 3.1), the w_{GHF} values for the combined Hudson Bay and Hudson Strait experiments correspond to a mean GHF of $\mathrm{GHF}_{\mathrm{ave}} \approx [15, 26, 37, 48, 59]$ $\frac{\mathrm{mW}}{\mathrm{m}^2}$ ($\mathrm{GHF}_{\mathrm{ave}} \approx 70$ $\frac{\mathrm{mW}}{\mathrm{m}^2}$ for reference setup). Additionally, we determine the effects of a smaller GHF when applied to a larger area (Fig. B.5).

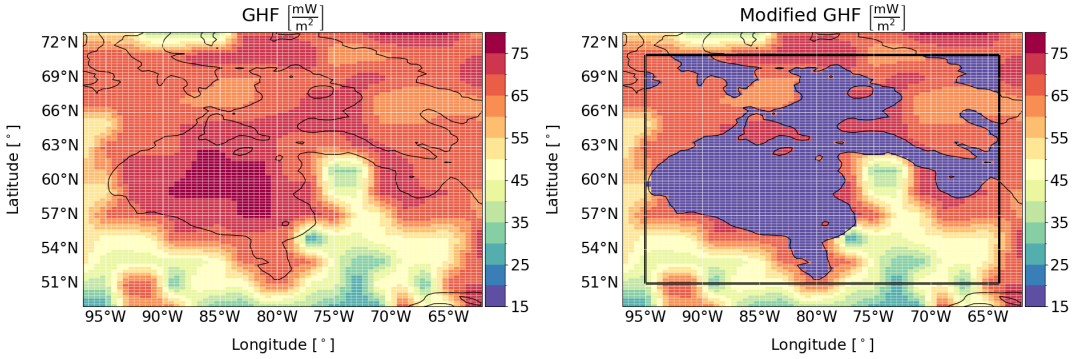

Figure 3.1: GSM input geothermal heat flux (GHF) applied at 4 km depth. The left panel shows the default input field (Davies, 2013), whereas the right panel shows the modified map used for the GHF sensitivity experiments (Sec. 3.2.4). In the modified field, we set GHF= 15 $\frac{\mathrm{mW}}{\mathrm{m}^2}$ for all grid cells below present-day sea level and within the black square.

3.2.5 Ocean temperature forcing

This section describes the additional (only applied for the ocean forcing experiments) ocean temperature forcings (added to the default ocean temperature in the GSM) used to determine the effects of ice shelves (HE ocean forcing, Sec. 3.2.5.1) and sub-surface ocean warmings attributed to DO events in a HE context (Sec. 3.2.5.2). To bound the effects of these ocean forcings, we also examine extreme scenarios (Sec. 3.2.5.3). However, in order to understand the ice-ocean interactions in the GSM, we first describe the implementation of relevant processes.

The ocean temperature T_{ocean} in the GSM is based on the summer weighted ocean temperature field $(0.5 \cdot (T_{\text{ave,Jul:Oct}} + T_{\text{ave,Jan:Dec}}))$ derived from the TraCE deglacial simulation run with the Community Climate System Model Version 3 (CCSM3, Liu et al., 2009). Using a glacial index approach, the ocean temperature chronology is interpolated between full glacial (last glacial maximum) and present day conditions for all other time slices (Tarasov et al., 2024, in preparation). Within a limited *ocean forcing area* (Fig. 3.2) and below the upper depth limit of d_{OF}, the 2 types of ocean temperature forcing T_{OF} described below are added to the background ocean temperature for grid cells with floating ice.

The ocean temperature at the relevant depth is then used to calculate the sub-shelf melt M_{SSM} and face melt M_{face}. The GSM determines M_{SSM} based on a parametrization of buoyant meltwater plumes (Lazeroms et al., 2018) and parameter ranges set so that computed melt brackets present-day observations (e.g., Depoorter et al., 2013; Enderlin and Howat, 2013; Alley et al., 2015). For a floating ice grid cell, the sub-shelf

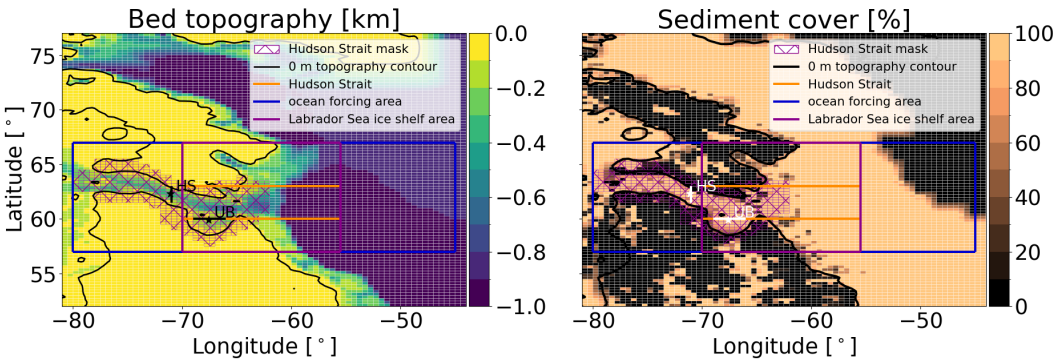

Figure 3.2: GSM input present-day bed topography and sediment cover. The black (left) and white (right) asterisks and lines indicate the location of the Hudson Strait (*HS*) and Ungava Bay (*UB*) ice thickness calculation and flux gate, respectively. The *Hudson Strait mask* is used to determine the Hudson Strait ice volume, mean and max basal ice velocity, and warm-based area. The black contour line shows the present-day sea level (coastline) used in the GSM. The *Hudson Strait* area is used to calculate the Hudson Strait ice shelf area, ice shelf volume, and the backstress exerted by the floating ice on the Hudson Strait ice stream. The *ocean forcing area* outlines the region affected by the ocean temperature increases discussed in Sec. 3.2.5. Finally, the magenta box outlines the area within which the Labrador Sea ice shelf area and volume are calculated. To prevent ice sheet growth beyond a stub North-West Greenland, the surface elevation in the corresponding area has been set to well below sea level.

melt is given by:

$$M_{\mathrm{SSM}} = \left(C_{\mathrm{SSM}} + d \cdot A_{\mathrm{WF}} \cdot \left(f_{\mathrm{SGWF}}\right)^{0.39}\right) \cdot T_{\mathrm{ocean,SSM}} \cdot F_{\mathrm{slope}}(\mathrm{SL}) \cdot f_{\mathrm{SSM,slope}} \qquad (3.5)$$

and 0 $\frac{\mathrm{m}}{\mathrm{yr}}$ otherwise. C_{SSM} is the scaled ensemble parameter for the sub-shelf melt, f_{SGWF} the basal meltwater flux into the sub-shelf melt convection cell, A_{WF} is a scaling coefficient for the meltwater dependence, and d is the depth. $T_{\mathrm{ocean,SSM}}$ is the ocean temperature at the depth of the ice shelf base and $f_{\mathrm{SSM,slope}}$ is an overall scaling coefficient (Tarasov et al., 2024, in preparation). F_{slope} is a nonlinear function of the maximum lower ice surface slope SL (across the grid cell interfaces with adjacent ice).

Face melt is determined only at the marine ice margin. It is calculated according to

$$M_{\text{face}} = \left(C_{\text{face}} \cdot H_{\text{eff}} + d \cdot A_{\text{WF}} \cdot \left(f_{\text{SGWF}}\right)^{0.39}\right) \cdot T_{\text{ocean,face}}, \tag{3.6}$$

where C_{face} is the scaled ensemble parameter for the face melt. $T_{\text{ocean,face}}$ is the ocean temperature adjacent to the ice face when assuming that the face melt water consists of equal parts of local water and shelf water. H_{eff} is the effective terminal ice thickness defined as $H_{\text{eff}} = \max\left[0.95 \cdot H, 200 \text{ m}\right]$.

Calving in the GSM is based on a crevass propagation parameterization (Pollard et al., 2015). To account for the impact of land-fast perennial sea ice, calving is inhibited when the 2 m summer (JJA) surface temperature falls below $-2.0°\text{C}$ (Tarasov et al., 2024, in preparation). The ocean temperature forcing does not affect the 2 m summer surface temperature. However, calving has no temperature control once the ice shelf extends beyond the continental shelf break (present-day depth > 860 m).

3.2.5.1 Ice shelf removal

To remove the floating ice near the Hudson Strait, we increase the ocean temperature during HEs (Fig. 3.3). We apply the ocean forcing to either the entire water column ($d_{\text{OF}} = 0$ m) or to an upper ocean forcing limit of $d_{\text{OF}} = 250$ m. The ocean temperature forcing for the ith HE is calculated according to

$$T_{\text{HE,i}} = \begin{cases} T_{\text{max,HE}} & \text{if} \quad t_{\text{HE,i,start}} \leq t \leq t_{\text{HE,i,end}} \\ 0 & \text{otherwise,} \end{cases} \tag{3.7}$$

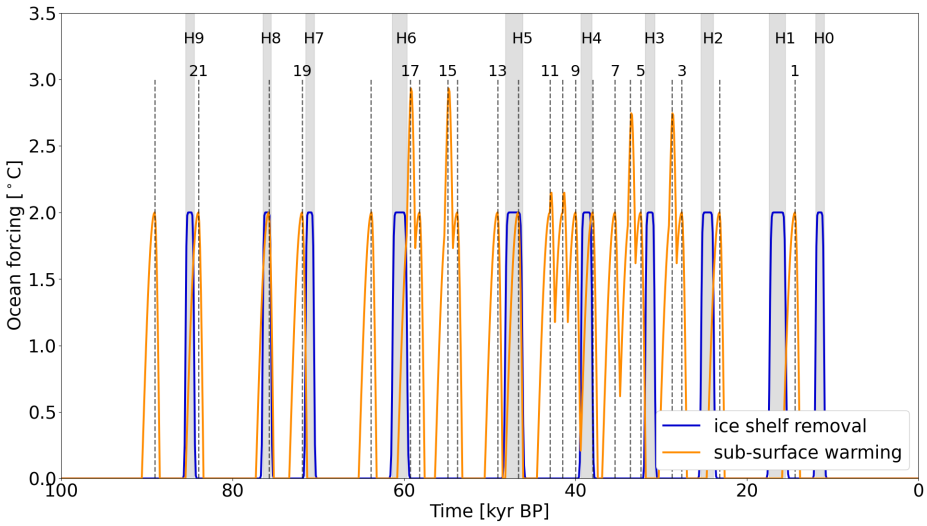

Figure 3.3: $T_{\mathrm{OF}} = 2°\mathrm{C}$ ocean temperature forcing used to remove the ice shelves (entire water column) and for the sub-surface ocean warming (below depth $d_{\mathrm{OF}} = 250$ m in reference setup). The shaded gray areas represent the timing of HEs based on the average of Table 6.3 in Bradley (2014). The vertical dashed lines indicate the timing of DO events based on peaks in the NGRIP $\delta^{18}\mathrm{O}$ time series (Bazin et al., 2013; Veres et al., 2013).

where $T_{\mathrm{max,HE}} = [1, 2, 3]°\mathrm{C}$ are the maximum ocean temperature increases tested (amplitudes based on Gibb et al., 2014) and t the time ranging from 0 to 100 kyr with a 100 yr increment. To test for a potential warm bias of the GSM ocean temperatures, we also run an experiment with a maximum ocean temperature decrease $T_{\mathrm{max,HE}} = -2°\mathrm{C}$ during HEs. $t_{\mathrm{HE,i,start}}$ and $t_{\mathrm{HE,i,end}}$ are the start and end time of the ith HE. The timing and duration of HEs are based on the average of Table 6.3 in Bradley (2014). For HE time estimates without a duration, we use the estimated time ± 0.5 kyr. To get a more gradual ocean temperature increase and decrease, we convolute $T_{\mathrm{HE,i}}$ with

a Gaussian function of the form

$$y_{\mathrm{Gauss,i,tmp}} = \exp\left(\frac{-x^2_{\mathrm{Gauss,i}}}{2}\right) \tag{3.8a}$$

$$y_{\mathrm{Gauss,i}} = \frac{y_{\mathrm{Gauss,i,tmp}}}{\max\left(y_{\mathrm{Gauss,i,tmp}}\right)} \cdot T_{\mathrm{max,HE}}, \tag{3.8b}$$

where $x_{\mathrm{Gauss,i}}$ ranges from -10π to 10π over the duration of the ith HE and is 0 otherwise. The convoluted time series of the ith HE is then

$$T_{\mathrm{HE,i,conv}} = \begin{cases} T_{\mathrm{HE,i}} * y_{\mathrm{Gauss,i}} & \text{if} \quad t_{\mathrm{HE,i,start}} \leq t \leq t_{\mathrm{HE,i,end}} \\ 0 & \text{otherwise.} \end{cases} \tag{3.9}$$

The final ocean temperature forcing time series is obtained by adding the contributions of all individual HEs.

$$T_{\mathrm{HE,tot}} = \sum_i T_{\mathrm{HE,i,conv}}. \tag{3.10}$$

Since individual HEs do not overlap, the maximum ocean temperature increase does not exceed $T_{\mathrm{max,HE}}$.

3.2.5.2 Sub-surface ocean warming

Similar to the preceding ice shelf removal experiments, the sub-surface warming preceding DO events is implemented as ocean temperature anomalies (OTAs, Fig. 3.3). The specifics of the OTAs are based on proxies from cores in the North Atlantic and the Nordic Seas at mid depths (Rasmussen and Thomsen, 2004; Marcott et al., 2011). In the reference setup, the maximum increase of sub-surface (below depth

$d_{\mathrm{OF}} = 250$ m) temperatures of a single OTA is set to $T_{\mathrm{max,DO}} = 2°\mathrm{C}$, but experiments are conducted for different sub-surface warming depths ($d_{\mathrm{OF}} = [100, 500]$ m) and maximum temperature increases ($T_{\mathrm{max,DO}} = [1, 3]°\mathrm{C}$). The OTAs last for a total of $t_{\mathrm{D,tot}} = 2200$ yr, with an $t_{\mathrm{Inc}} = 1600$ yr long temperature increase and $t_{\mathrm{Dec}} = 600$ yr decrease. According to Rasmussen and Thomsen (2004), the rapid DO warmings occur when the water column destabilizes and the warm sub-surface water rises to the surface. Since the warm sub-surface water is then mixed with the cold surface water (decreasing the sub-surface temperature), we align the maximum temperature increase of the OTAs with the DO event time estimates (Fig. 3.3). Following the above, the OTA attributed to the ith DO event is calculated according to

$$T_{DO,i} = \begin{cases} T_{\mathrm{max,DO}} \cdot \sin\left(\frac{\pi}{2} \frac{t_{\mathrm{Inc}} - (t - t_{\mathrm{DO,i}})}{t_{\mathrm{Inc}}}\right) & \text{if} \quad t_{\mathrm{DO,i}} \leq t \leq t_{\mathrm{DO,i}} + t_{\mathrm{Inc}} \\ T_{\mathrm{max,DO}} \cdot \sin\left(\frac{\pi}{2} \frac{t_{\mathrm{Dec}} - (t_{\mathrm{DO,i}} - t)}{t_{\mathrm{Dec}}}\right) & \text{if} \quad t_{\mathrm{DO,i}} - t_{\mathrm{Dec}} \leq t < t_{\mathrm{DO,i}} \\ 0 & \text{otherwise,} \end{cases} \tag{3.11}$$

where $t_{\mathrm{DO,i}}$ is the time of the ith DO event. Note that due to the implementation of the OTAs in Eq. (3.11), the first and last values of $T_{DO,i}$ are 0°C. For a time step of 100 yr, the actual duration of increased sub-surface water temperature is, therefore, $t_{\mathrm{D}} = 2000$ yr. Following Bassis et al. (2017), the contributions of overlapping OTAs are added

$$T_{\mathrm{DO,tot}} = \sum_i T_{\mathrm{DO,i}} \tag{3.12}$$

Therefore, $T_{\mathrm{DO,tot}}$ can exceed $T_{\mathrm{max,DO}}$ (Fig. 3.3).

3.2.5.3 Bounding experiments

To increase confidence in our model results and bound the effects of ocean forcings in a HE context (Sec. 3.2.5.1 and 3.2.5.2), we run additional experiments with more extreme scenarios. For all experiments within this section, the ocean forcing is applied to the whole water column ($d_{\mathrm{OF}} = 0$ m) and for all grid cells within the *ocean forcing area* (Fig. 3.2, not only the grid cells with floating ice). The experiments are:

BE_1: DO event ocean forcing ($T_{\mathrm{DO,tot}}$, $T_{\mathrm{max,DO}} = 2°\mathrm{C}$)

BE_2: HE shelf forcing ($T_{\mathrm{HE,tot}}$, $T_{\mathrm{max,HE}} = 2°\mathrm{C}$)

BE_3: $-2°\mathrm{C}$ ocean forcing applied after 100 kyr BP

BE_4: no calving after 100 kyr BP

BE_5: HE shelf forcing ($T_{\mathrm{HE,tot}}$, $T_{\mathrm{max,HE}} = 2°\mathrm{C}$) with $-2°\mathrm{C}$ ocean forcing applied outside of HEs and after 100 kyr BP

BE_6: HE shelf forcing ($T_{\mathrm{HE,tot}}$, $T_{\mathrm{max,HE}} = 2°\mathrm{C}$) with no calving outside of HEs and after 100 kyr BP

Experiments BE_1 and BE_2 examine the effect of the ocean forcing restriction to grid cells with floating ice. Experiment BE_3 aims to decrease sub-shelf melt, face melt, and calving to enable the growth of larger ice shelves. In the more extreme experiment BE_4, the growth of larger ice shelves is enabled by inhibiting calving entirely. Experiments BE_5 and BE_6 target the collapse of larger ice shelves, with experiment BE_6 being the more extreme scenario.

3.2.6 Run comparison

Ensemble members with ≤ 2 and > 2 surges are analyzed separately. For runs with > 2 surges, we determine the surge characteristics (number of surges, mean surge duration, mean period between surges, mean increase in Hudson Strait ice flux, and mean Hudson Strait ice volume change during a surge) of the reference setup and calculate the percentage difference with the comparison setups (Hank et al., 2023). We first calculate the percentage difference for every run individually and then average over all runs. MNEEs are computed by imposing stricter (than default) numerical convergence criteria in the ice dynamics solver. As in Hank et al. (2023), the final MNEEs (shaded grey regions in Fig. 3.6) are the maximum percentage difference for the metric in question of a setup with stricter numerical convergence and a setup with stricter numerical convergence with increased maximum iterations for the outer Picard loop (from 2 to 3, solving for the ice thickness) and the non-linear elliptic SSA (Shallow-Shelf Approximation) equation (from 2 to 4, solving for horizontal ice velocities). These MNEEs are then used as a threshold to determine if a change in model configuration leads to numerically significant differences in the surge characteristics. Differences smaller than the MNEEs should be interpreted as model response not resolvable given the numerical sensitivities.

For runs with ≤ 2 surges, the percentage differences in surge characteristics are large due to the small number of surges or impossible to determine for reference runs with #surges= 0. Therefore, we use alternative approaches (e.g., kernel density and time series plots) to determine the effects of physical system processes for the ≤ 2 #surges sub-ensemble.

3.3 Results

3.3.1 Hudson Strait ice stream surges

The Hudson Strait ice stream is active for most of the last glacial cycle when using the default GHF map (e.g., Fig. 3.4). This is in contrast to the idea of long quiescent intervals interspersed by short-lived surges proposed by, e.g., MacAyeal (1993); Payne (1995); Calov et al. (2002). Instead, the surges are preceded by a reduction (e.g., surges S0, S7 to S9 for parameter vector 1 shown in Fig. 3.4) or complete de-activation (S1 to S6) of the Hudson Strait ice stream. Depending on the background ice flux before the surge, the following ice flux increase occurs either rapidly (S0 to S7) or more gradually (S8 and S9). As per the definition (Sec. 3.2.2), all surges show a decrease in the Hudson Strait ice volume. The change is especially pronounced for surges preceded by a complete de-activation of the Hudson Strait ice stream. Times of complete Hudson Strait ice stream de-activation generally coincide with increased buttressing (shown as fraction of the grounding line longitudinal stress, Fig. 3.4). The decreased ice shelf volume indicates that this is due to a decrease in the longitudinal stress rather than an increase in the back stress. Therefore, the changes in buttressing are a consequence of the small Hudson Strait ice flux and not the cause. Instead, the de-activation of the Hudson Strait ice stream is caused by a decrease in the warm-based area (Fig. 3.4).

The more gradual increases in Hudson Strait ice flux (S8 and S9) are linked to surges in Ungava Bay (Fig. 3.4 and B.6). Due to the rapid increase in ice flux in Ungava Bay, these surges are still in line with the concept of rapid surge onset, although the resultant increase in Hudson Strait ice flux is more gradual.

Furthermore, some of the detected surges show an increase in Hudson Strait ice flux without a significant change in the effective pressure or the warm-based area in the Hudson Strait (e.g., S1 to S3 in Fig. B.7). During these surges, ice transport from Hudson Bay and Foxe Basin through the Hudson Strait (and other outlets) towards the ice sheet margin increases, decreasing the overall North American ice sheet volume (Fig. B.8). The increased downstream ice transport and consequential increase in driving stress eventually increase the ice flux in the Hudson Strait itself. Therefore, these surges originate further upstream and are initiated by ice and climate dynamics outside the Hudson Strait.

Surges, particularly those preceded by a complete de-activation of the Hudson Strait ice stream, tend to occur before 65 kyr BP (e.g., Fig. 3.4). The absence of complete cessation of ice streaming during marine isotope stage 3 (MIS3, $\sim$ 57 to 27 kyrBP, Lisiecki and Raymo, 2005) when using the default deep GHF map is due to increased basal temperatures. This is a result of the growing ice volume and, thereby, thicker ice and larger supply of warm-based upstream ice. The increased basal temperatures also lead to longer surges with reduced ice volume change (Fig. B.9).

To get a better understanding of the physical mechanism behind Hudson Strait surges, we analyze surge S1 of parameter vector 1 in greater detail (Fig. 3.5 and video 01 of Hank, 2023a). At 87.5 kyr BP, the ice sheet in the Hudson Strait is warm-based, enabling basal melting. Basal water thicknesses reach up to 10 m (upper limit of local sub-glacial hydrology model), leading to small effective pressures and, consequently, high basal ice velocities. Due to a combination of cold ice advection from further upstream or the ice stream margins, thinning of the ice stream, and flattening of the ice sheet surface (hence reduced gravitational driving), the basal temperature

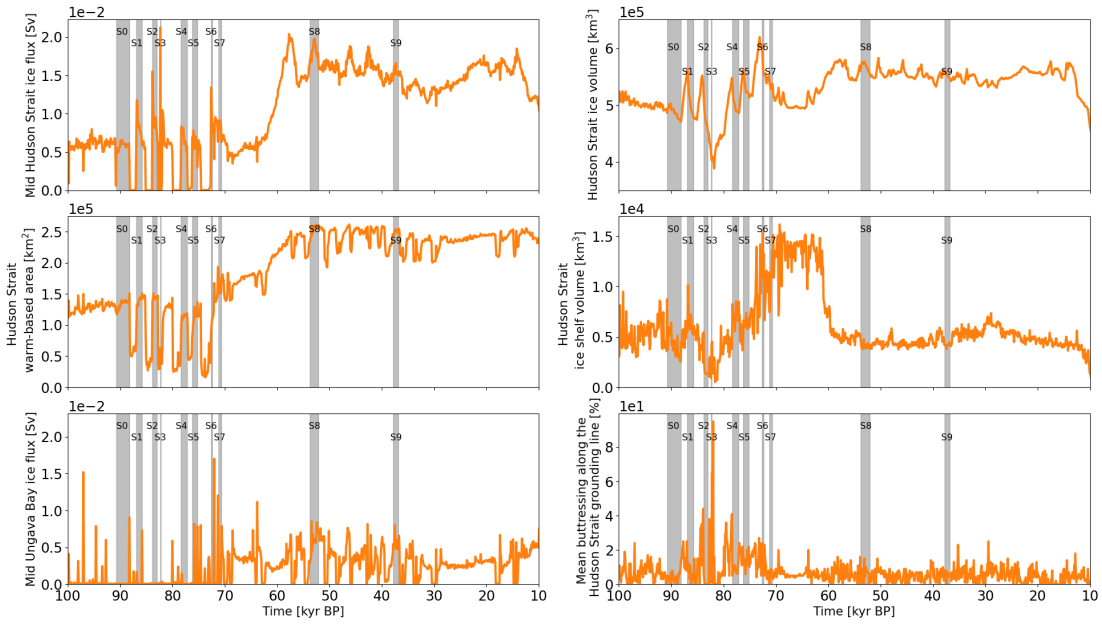

Figure 3.4: Time series of parameter vector 1. The shaded gray areas and black numbers mark the Hudson Strait ice stream surges as determined by the automated detection algorithm (Sec. 3.2.2). Hudson Strait ice flux is determined at the flux gate marked with *HS* in Fig. 3.2. The Hudson Strait ice volume and warm-based area are calculated within the *Hudson Strait mask* (Fig. 3.2). The Hudson Strait ice shelf volume is determined within the *Hudson Strait* area (Fig. 3.2). The mean buttressing along the Hudson Strait grounding line (only within *Hudson Strait* area in Fig. 3.2) is given as fraction of the grounding line longitudinal stress ($\left(\frac{\tau_{xx}}{\tau_f}\right)^{\frac{n}{m_s+1}}$ in Pollard and DeConto (2012)). The last panel shows the northward Ungava Bay ice flux determined at the flux gate marked with *UB* in Fig. 3.2. Note that the automated detection algorithm does not identify all smaller increases in mid-Hudson Strait ice flux (e.g., between 50 and 40 kyr BP) due to the additional requirement of a Hudson Strait ice volume decrease of at least $5 \cdot 10^3$ km^3 (Sec. 3.2.2).

eventually falls below the pressure melting point. The basal water refreezes and the effective pressure increases by an order of magnitude, increasing the basal drag (87.0 kyr BP). The ice streaming ceases, allowing the ice thickness to increase.

Due to increased insulation from the cold surface temperatures (thicker ice sheet) and heat contribution from the deformation work, the upstream basal temperature increases (video 02 of Hank, 2023a). Once the basal temperature is close to the

pressure melting point, basal sliding contributes further heat and the warm-based area starts to extend downstream (video 02 of Hank, 2023a). Basal melting then leads to the build-up of a sub-glacial water layer, decreasing the effective pressure and enabling high basal ice velocities. Due to the built-up ice, Hudson Strait ice flux initially increases beyond the pre-ice stream de-activation values before gradually returning to similar ice fluxes, and completing the cycle (86.1 kyr BP).

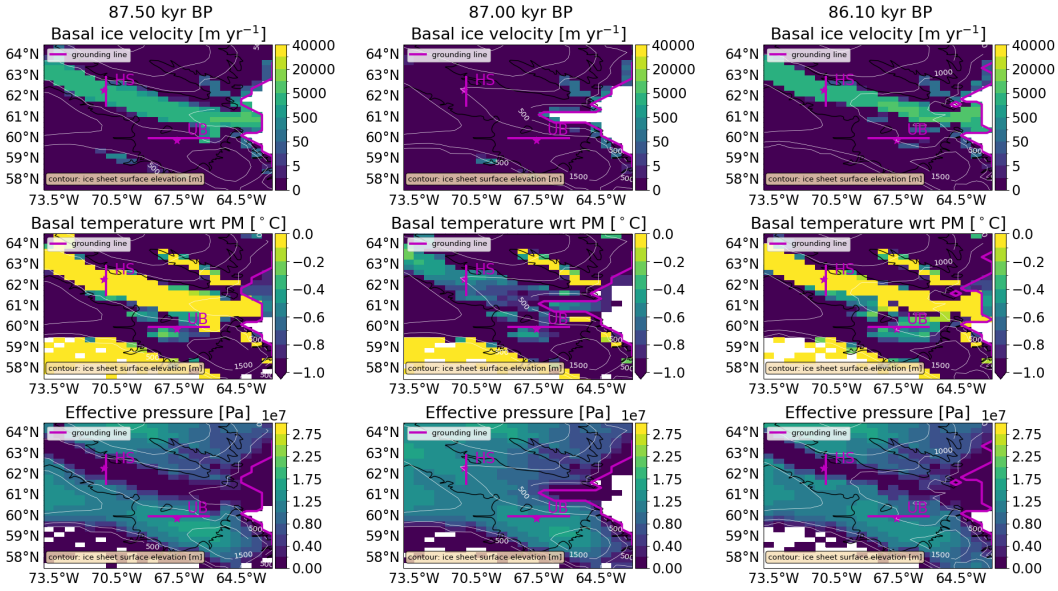

Figure 3.5: Basal ice velocity, basal temperature with respect to the pressure melting point, and effective pressure for surge S1 of parameter vector 1 (Fig. 3.4). The 3 time slices show the active ice stream before the surge (87.5 kyr BP), the quiescent period (87.0 kyr BP), and the surge at its maximum ice flux (86.1 kyr BP). The black contour is the present-day coastline provided by *cartopy* (Met Office, 2010 - 2015).

Overall, the mean surge characteristics of the reference setup for the #surges $>$ 2 sub-ensemble are in agreement with the HE estimates in the literature (Table 3.1). However, the predominance of complete de-activation surges (generally the

surges with the largest ice volume change) prior to 65 kyr BP is a major discrepancy (Fig. B.9). One inferential caveat is that proxy records can provide only indirect bounds on Hudson Strait ice flux and ice volume change. A comparison to other ice sheet modeling studies (e.g., Schannwell et al., 2023) is not straightforward, as the considered metrics vary significantly (e.g., Hudson Strait area). As the automated detection algorithm determines the increase in mid-Hudson Strait ice flux (not the total flux) and the change in Hudson Strait ice volume (not the total discharge), we refrain from providing literature estimates for these two metrics in Table 3.1. However, using an intermediate mid-Hudson Strait ice flux during a surge (1.0 Sv, e.g., Fig. 3.4) and the mean surge duration (1.4 kyr, Table. 3.1) yields an ice volume discharge of $\sim 44 \cdot 10^4$ km^3. This value is well within the range set by modeling and proxy estimates in the literature ($3 \cdot 10^4$ to $946 \cdot 10^4$ km^3, Roberts et al., 2014, and references therein).

Metric	reference setup (mean $\pm$ SD)	literature HE estimate
number of surges	5.4 ± 2.5	6 to 10 (Table 6.3 in Bradley, 2014)
period	13.6 ± 8.8 kyr	4 to 15 kyr, mean= 8.0$\pm$2.7 kyr (Table 6.3 in Bradley, 2014)
duration	1.4 ± 0.4 kyr	0.2 to 2.3 kyr (Hemming, 2004)
Hudson Strait ice flux increase	$4.9 \pm 2.0 \cdot 10^{-3}$ Sv	-
Hudson Strait ice volume change	$-3.6 \pm 2.3 \cdot 10^4$ km^3	-

Table 3.1: Surge characteristics of the reference setup compared to literature estimates. Only runs with #surges > 2 (between 100 kyr BP and 10 kyr BP) are considered. The literature HE estimates are also based on the time between 100 kyr BP and 10 kyr BP.

Due to the inclusion of a resolution-dependent basal temperature ramp (Hank et al., 2023), the differences in surge characteristics between the coarse resolution runs (horizontal grid resolution of $\Delta_{\text{lon}} = 1.0°$, $\Delta_{\text{lat}} = 0.5°$) and the reference runs ($\Delta_{\text{lon}} = 0.5°$, $\Delta_{\text{lat}} = 0.25°$) are generally within the MNEEs (Fig. 3.6). While finer (than the reference setup) horizontal grid resolutions are currently unfeasible in the context of this study, given the results of resolution response testing of surge cycling down to 3.125 km horizontal grid resolution in Hank et al. (2023), the differences in surge characteristics for finer resolutions are also expected to be within the MNEEs.

3.3.2 Geothermal heat flux

Since the Hudson Strait ice stream is active for most of the last glacial cycle and the GHF is poorly constrained in this area, we examine the effect of smaller average Hudson Bay/Hudson Strait GHFs (GHF_{ave}) on the surge characteristics. We run sensitivity experiments for $\text{GHF}_{\text{ave}} \approx [15, 26, 37, 48, 59]$ $\frac{\text{mW}}{\text{m}^2}$ (Sec. 3.2.4).

In general, decreasing the GHF in Hudson Strait and Hudson Bay leads to a decrease in the basal temperature, a smaller warm-based area, and, consequently, a decrease in mid-Hudson Strait ice flux. For small enough GHFs (15 $\frac{\text{mW}}{\text{m}^2}$), 9 parameter vectors have fully transitioned from an almost continuously active Hudson Strait ice stream to the classic binge-purge surge mode (e.g., Fig. 3.7). The exact transition point depends on the parameter vector in question but generally requires a Hudson Strait/Hudson Bay $\text{GHF}_{\text{ave}} \leq 37$ $\frac{\text{mW}}{\text{m}^2}$ ($w_{\text{GHF}} = 0.4$). Both the #surges > 2 and #surges ≤ 2 sub-ensemble show significant increases in the number of surges, and mean Hudson Strait ice volume change for decreasing GHFs (Fig. B.11 and B.12,

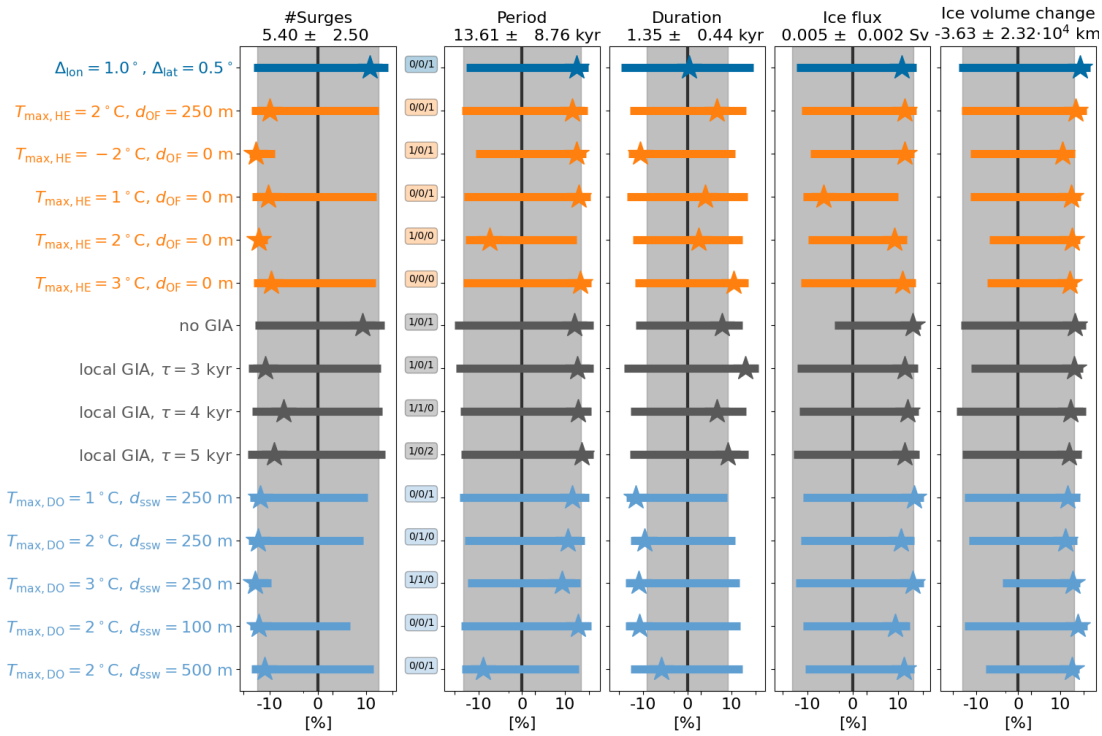

Figure 3.6: Percentage differences in surge characteristics compared to the reference setup. The shaded regions represent the MNEEs. The different colors provide visual alignment of the individual model setups. The stars and horizontal bars are the > 2 #surges sub-ensemble mean percentage differences and standard deviations, respectively. The three numbers between the first and second column show the number of crashed runs, the number of runs without a surge, and the number of runs with only one surge in the comparison setup. The x-axes are logarithmic. The model setups, from top to bottom, are: $\Delta_{\text{lon}} = 1°$, $\Delta_{\text{lat}} = 0.5°$ horizontal grid resolution, Heinrich Event shelf forcing ($T_{\text{max,HE}} = 2°\text{C}$, $d_{\text{OF}} = 250$ m), whole water column Heirich Event shelf forcing with $T_{\text{max,HE}} = [-2, 1, 2, 3]°\text{C}$ (Sec. 3.2.5.1), no GIA model, local GIA model with relaxation time constant $\tau = [3, 4, 5]$ kyr, DO event sub-surface ocean forcing with $T_{\text{max,DO}} = [1, 2, 3]°\text{C}$ and $d_{\text{OF}} = [100, 250, 500]$ m (Sec. 3.2.5.2).

Table 3.2). On the other hand, the mean surge duration significantly decreases for smaller GHFs. Therefore, the colder basal temperatures and increased Hudson Strait ice volume lead to stronger and more rapid surges (e.g., Fig. 3.7).

A key feature of the binge-purge mode is the increase of stronge Hudson Strait surges during MIS3 compared to the number of surges for the near continuous ice

streaming mode (e.g., Fig. 3.7, B.9, and B.10). This is in closer correspondence with the actual IRD record.

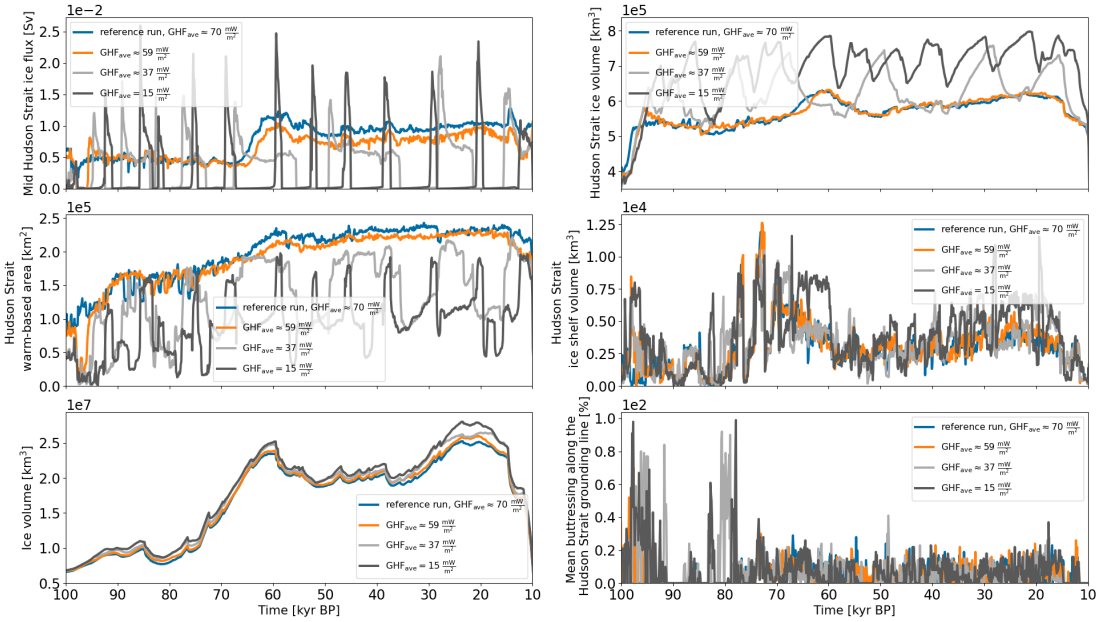

Figure 3.7: Time series of parameter vector 18 for different GHFs. The Hudson Strait ice stream surges are not highlighted for clarity. The bottom left panel shows the overall North American ice volume. Otherwise as Fig. 3.4.

Metric	reference setup (mean ± SD)	$\mathrm{GHF_{ave}} = 15\ \frac{\mathrm{mW}}{\mathrm{m^2}}$ (mean ± SD)
number of surges	5.4 ± 2.5	10.6 ± 5.3
period	13.6 ± 8.8 kyr	10.7 ± 5.5 kyr
duration	1.4 ± 0.4 kyr	0.7 ± 0.3 kyr
Hudson Strait ice flux increase	$4.9 \pm 2.0 \cdot 10^{-3}$ Sv	$23.0 \pm 13.0 \cdot 10^{-3}$ Sv
Hudson Strait ice volume change	$-3.6 \pm 2.3 \cdot 10^{4}$ km^3	$-6.6 \pm 1.1 \cdot 10^{4}$ km^3

Table 3.2: Surge characteristics of the reference setup compared to a setup with the GHF in the Hudson Bay and Hudson Strait set to 15 $\frac{\mathrm{mW}}{\mathrm{m^2}}$ (Sec. 3.2.4). Only runs with #surges > 2 (between 100 kyr BP and 10 kyr BP) are considered (10 for the reference setup, 13 for $\mathrm{GHF_{ave}} = 15\ \frac{\mathrm{mW}}{\mathrm{m^2}}$).

Separately modifying the GHF in the Hudson Strait and Hudson Bay indicates that the GHF modification in the Hudson Strait generally has a larger impact than modifications in the Hudson Bay (Fig. B.13 and B.14). However, GHF modifications in both regions are required to obtain a continuous binge-purge surge mode. GHF modifications applied to a larger region (Fig. B.5, based on Blackwell and Richards (2004)) lead to similiar conclusions, further indicating that both types of Hudson Strait ice stream surge cycling occur within available GHF constraints.

Our analyses below are based on the GSM default GHF map. However, similar conclusions are obtained when applying $\mathrm{GHF}_{\mathrm{ave}} = 25\ \frac{\mathrm{mW}}{\mathrm{m}^2}$ to the Hudson Bay and Hudson Strait (Fig. B.16, B.17, B.25, and B.26). Any differences in model response are outlined in the specific sections.

3.3.3 Ice shelf removal

Before analyzing the effects of the HE ocean forcing on the surge characteristics, we examine the ice shelf size in front of the Hudson Strait (*Hudson Strait* area) and in the Labrador Sea (both areas outlined in Fig. 3.2). The maximum area covered by an ice shelf across all reference runs is $\sim 0.5 \cdot 10^5$ and $\sim 1.0 \cdot 10^5$ km^2 (Fig. 3.9) of the *Hudson Strait* (total area of $\sim 2.6 \cdot 10^5$ km^2, Fig. B.19) and the *Labrador Sea ice shelf area* (total area of $\sim 8.7 \cdot 10^5$ km^2, Fig. 3.8), respectively. The mean ice shelf cover never exceeds $0.4 \cdot 10^5$ km^2 in the *Labrador Sea ice shelf area*. These rather small ice shelves have only limited potential to buttress the Hudson Strait ice stream.

Given system uncertainties, we examine the change in ice shelf area when decreasing the ocean temperature by 2°C (entire water column, BE_3 in Sec. 3.2.5.3)

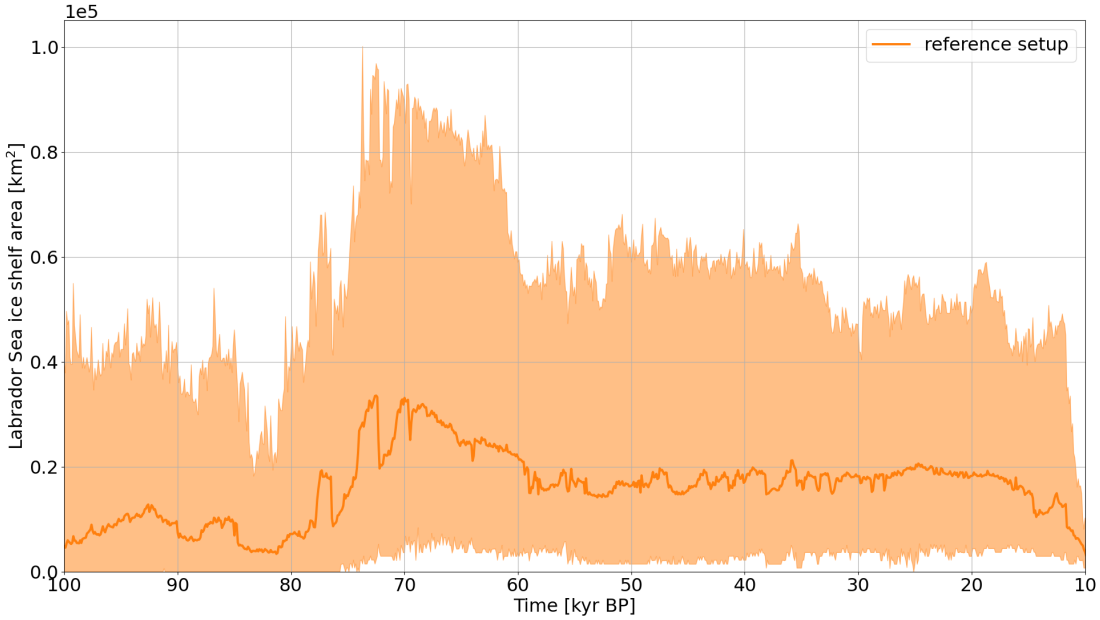

Figure 3.8: Labrador Sea ice shelf cover in the *Labrador Sea ice shelf area* outlined in Fig. 3.2 (total area of $\sim 8.7 \cdot 10^5$ km^2). The thick line represents the mean of the 20 run ensemble. The shaded area marks the minimum and maximum of the ensemble. The maximum ice shelf area at 70 kyr BP is shown in Fig. 3.9.

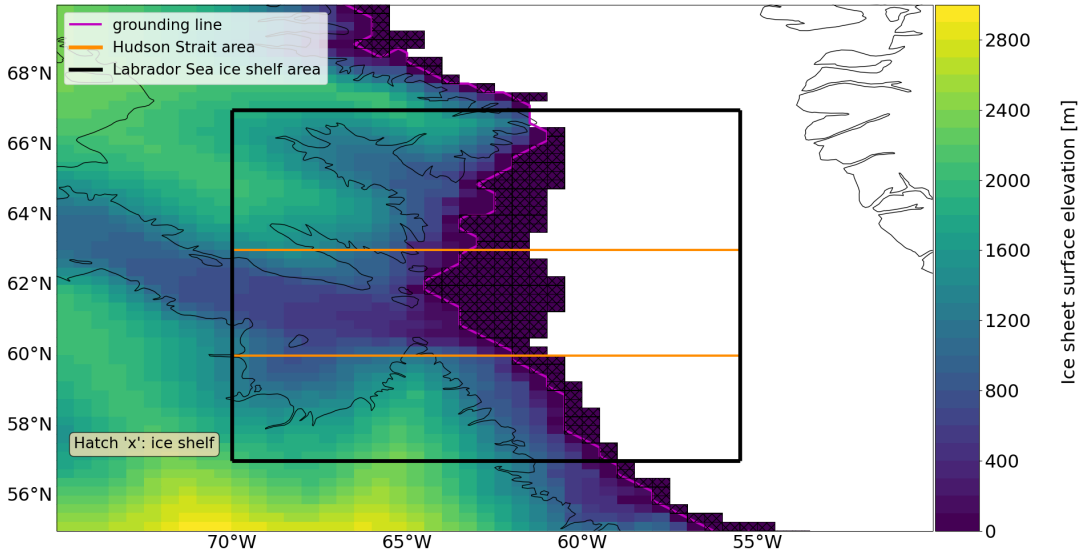

Figure 3.9: Ice sheet surface elevation at 70 kyr BP for parameter vector 1.

and inhibiting calving in the *ocean forcing area* (BE_4 in Sec. 3.2.5.3, area outlined in Fig. 3.2). Decreasing the ocean temperature leads only to a minor increase in Labrador Sea ice shelf cover (Fig. 3.10). When completely inhibiting calving, the Labrador Sea ice shelf cover increases by at least a factor of 4, at times covering all grid cells in the *Labrador Sea ice shelf area* not covered by grounded ice (maximum of $\sim 4.0 \cdot 10^5$ km^2, Fig. 3.10). However, even with this extreme calving restriction, some parameter vectors show only minor Labrador Sea ice shelves (e.g., Fig. B.20). This demonstrates the breadth of sub-shelf melt across our ensemble (maximum melt rates in BE_4 runs vary between ~ 22 $\frac{\text{m}}{\text{yr}}$ (1.6°C ocean temperature) and ~ 165 $\frac{\text{m}}{\text{yr}}$ (4.7°C ocean temperature)) and the resultant bound of process uncertainties.

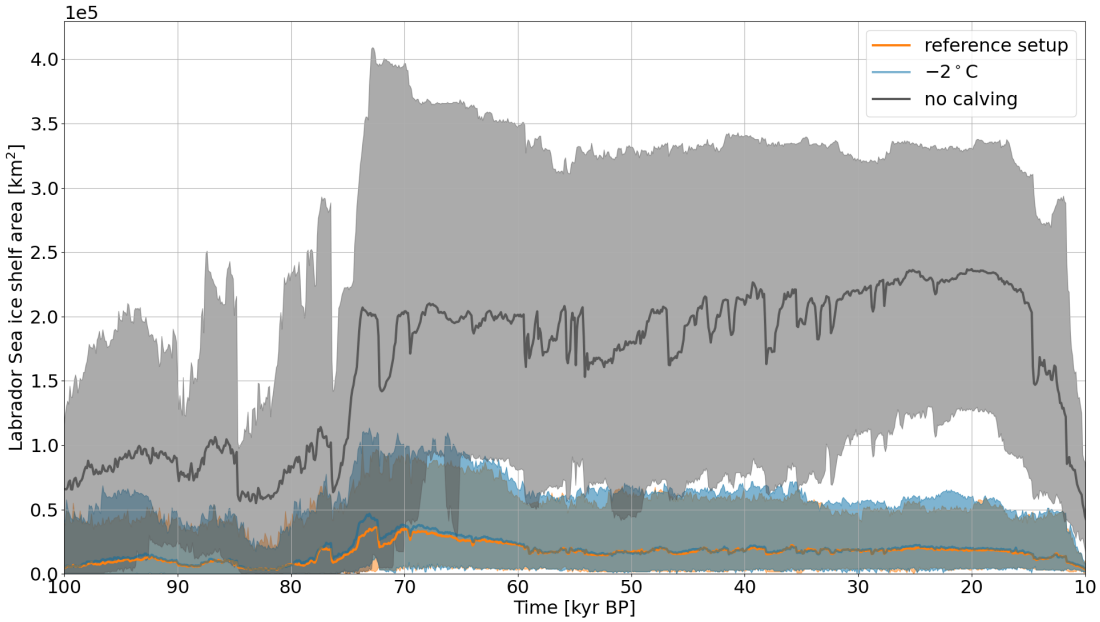

Figure 3.10: Labrador Sea ice shelf cover in the *Labrador Sea ice shelf area* for the reference setup compared to setups with 2°C colder ocean temperatures and without calving in the *ocean forcing area* (both areas outlined in Fig. 3.2). The thick line represents the mean of 18 runs (the runs for parameter vectors 8 and 15 crashed in both comparison setups and were not included). The shaded area marks the minimum and maximum of the remaining runs.

To determine the role of ice shelf buttressing in a Heinrich Event context, we apply different ocean temperature forcings (with default calving). In particular, we adjust the ocean temperature during HEs by a maximum temperature change $T_{\mathrm{max,HE}} = 2°\mathrm{C}$ below 250 m of the sea level, and $T_{\mathrm{max,HE}} = [-2, 1, 2, 3]°\mathrm{C}$ for the entire water column (Sec. 3.2.5.1 and 3.2.5.3). Except for the surge duration, none of these "HE shelf forcing" experiments significantly affects the surge characteristics of the > 2 #surges sub-ensemble (Fig. 3.6 as well as BE_2 and BE_5 in B.21). Even at $T_{\mathrm{max,HE}} = 3°\mathrm{C}$, there are only minor differences between the reference and HE shelf forcing runs (Fig. B.22).

The ≤ 2 #surges sub-ensemble generally shows only small changes in the number of surges for the "HE shelf forcing" experiments (Fig. B.23 as well as BE_2 and BE_5 in Fig. B.24). The maximum difference (increase from 2 to 7 surges across all sub-ensemble runs) occurs for $T_{\mathrm{max,HE}} = 1°\mathrm{C}$ and below depth $d_{\mathrm{OF}} = 0$ m. In comparison, the minimum increase in the total number of surges over the whole ≤ 2 #surges sub-ensemble (10 runs) for the GIA experiments is 10, and the MNEE experiments show a maximum difference of 2 (Fig. 3.13). Furthermore, the onset of the additional surges does not necessarily align with the ocean forcing (e.g., Fig. B.27). The increase in surge number is a result of slightly different ice configurations rather than a direct response to the removal of the ice shelves and their potential buttressing.

During cold climatic conditions, the 2 m summer surface temperatures near the ice shelves stay below $-2.0°\mathrm{C}$, allowing calving only where the ice shelf extends beyond the continental shelf break (e.g., Fig. B.28, see Sec. 3.2.5 for details). To ensure the minor ice shelf sensitivity to ocean temperature changes during HEs is not solely a consequence of this calving restriction, we also run an experiment with a maximum ocean temperature forcing during HEs $T_{\mathrm{max,HE}} = 3°\mathrm{C}$ applied to the whole water

column ($d_{\mathrm{OF}} = 0$ m) and without any imposed restriction on calving within the *ocean forcing area* (Fig. 3.2). This has no significant effect (Fig. B.29).

Therefore, the small effect of the ocean temperature forcing on surges of the Hudson Strait ice stream is a consequence of the relatively small ice shelf in front of the Hudson Strait, providing insignificant buttressing. While the experiments with colder ocean temperatures (-2°C only during HEs and -2°C after 100 kyr BP) slightly increase the ice shelf cover, a complete calving shutdown is required to build up large ice shelves (e.g., Fig. 3.10). The larger ice shelves provide increased buttressing, leading to more gradual changes in mid-Hudson Strait ice flux, a more stable Hudson Strait ice volume, and consequentially fewer surges (Fig. B.21 and B.30).

Using the HE ocean forcing with a maximum temperature increase of $T_{\mathrm{max,HE}} = 2$°C and no calving outside of HEs and after 100 kyr BP (BE_6) leads to a rapid collapse of the large ice shelves during HEs (due to calving and warmer ocean temperatures, Fig. 3.11). The ice shelf disintegration increases Hudson Strait ice flux, decreasing the Hudson Strait ice volume. While even in this extreme scenario, mid-Hudson Strait ice flux and Hudson Strait ice volume changes are relatively small (e.g., Fig. 3.11), the timing of at least 1 mid-Hudson Strait surge is directly affected by the ocean forcing and consequential reduction in buttressing for 10 (out of 20) parameter vectors.

3.3.4 GIA

At first, we determine the effects of GIA on the overall ice sheet by comparing the reference setup to runs without GIA. On average, GIA leads to thicker ice sheets (Fig. 3.12). The bed depression caused by the weight of the ice sheet low-

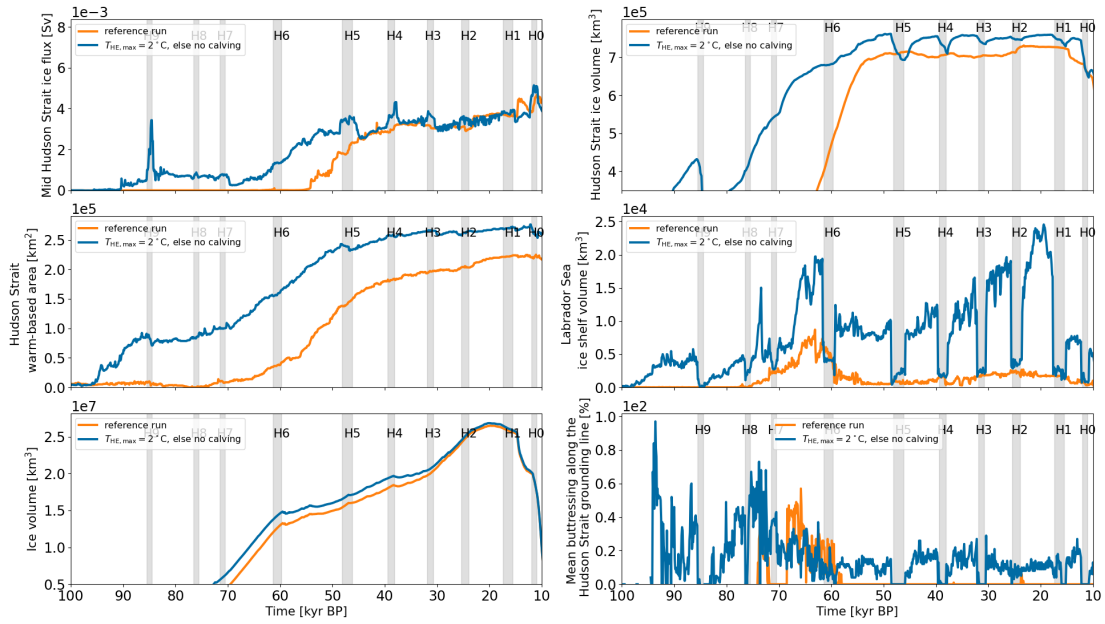

Figure 3.11: Time series of parameter vector 14 for the reference setup compared to the HE ocean forcing with a maximum temperature increase of $T_{\mathrm{max,HE}} = 2°\mathrm{C}$ (shaded grey areas) and no calving outside of HEs and after 100 kyr BP (BE_6 in Sec. 3.2.5.3). The Labrador Sea instead of the Hudson Strait ice shelf volume is shown. The bottom left panel shows the overall North American ice volume. Otherwise as Fig. 3.4.

ers the ice sheet surface elevation. Due to the atmospheric lapse rate and the Clausius–Clapeyron formula for saturation vapor pressure, accumulation generally increases for a decreasing surface elevation (except where orographic forcing is strong), allowing for a thicker ice sheet than without GIA (Fig. 3.12). Close to the ice sheet margin, a reduced ice sheet surface elevation has the potential to increase the ablation zone. However, the reduced ice sheet surface elevation could also lower the driving stress near the margin and decrease the ice flux to the ablation zone. While the bed topography under the ice sheet, including the marginal areas, is generally depressed (Fig. B.31), the total melt tends to be slightly smaller with GIA (Fig. 3.12). It is difficult to disentangle the exact underlying cause as various processes affect surface melt. As this is not our primary focus, we defer exploring the nuanced effects of GIA

on surface melt to future studies.

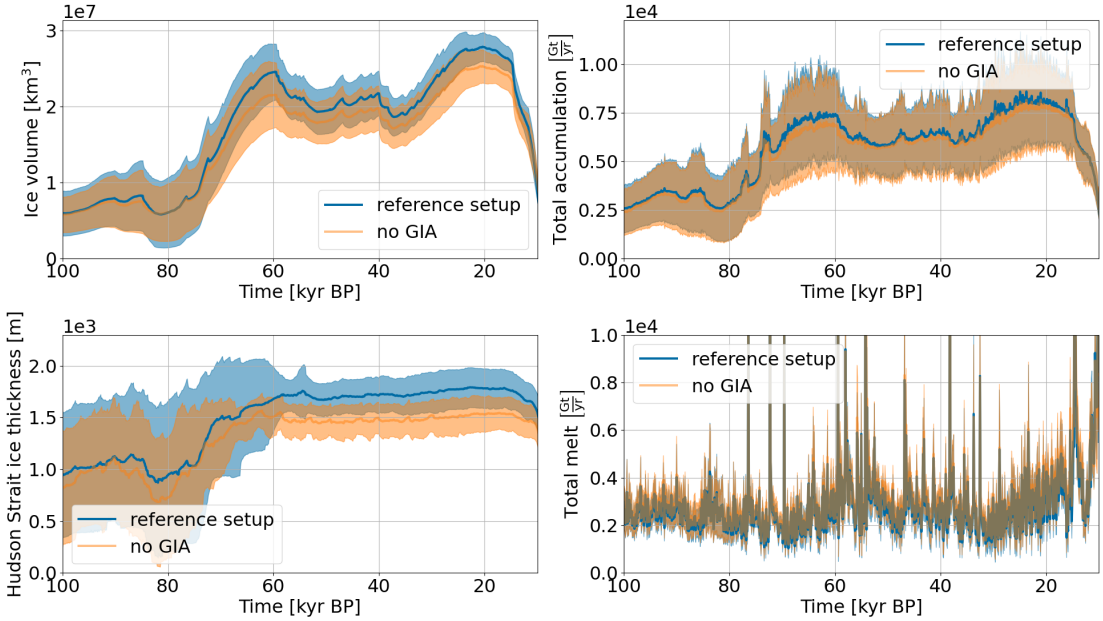

Figure 3.12: Ice sheet volume, total ice sheet accumulation, Hudson Strait ice thickness (Fig. 3.2), and total ice sheet melt for the reference setup (global GIA model) and runs without GIA. The thick lines and shaded areas represent the mean and mean±standard deviation of 18 runs, respectively (the runs for parameter vectors 8 and 15 crashed in the comparison setup and were not included).

Before analyzing the effects of GIA on the surge characteristics, we determine the ice sheet's sensitivity to different earth rheology models. All 20 parameter vectors (full ensemble) were run with 9 different earth rheologies. The rheologies differ in the thickness of the Lithosphere (d_{L}), and the viscosity of the upper and lower mantle (η_{um} and η_{lm}, respectively). The sensitivity of the mean (across all 20 parameter vectors) North American ice volume to the earth rheology is generally small. The largest differences occur between 60 and 40 kyr BP, with a maximum difference of $0.3 \cdot 10^7$ km^3 at $\sim$ 50 kyr BP (Fig. B.32). Similarly, the surge characteristics show minor sensitivities to a change in the earth rheology. However, a thinner Lithosphere

and a smaller upper mantle viscosity tend to favor shorter surges (Fig. B.33).

The number of surges in runs with ≤ 2 surges (≤ 2 #surges sub-ensemble) increases significantly for all experiments with local GIA and without GIA (Fig. 3.13). This is due to a smaller North American and Hudson Strait ice volume and the resulting change in basal temperature (Fig. B.34). The larger ice sheet in the reference setup (global GIA) leads to more stable basal temperatures and a continuously active Hudson Strait ice stream. On the other hand, the smaller ice sheet in runs with local GIA and without GIA leads to colder basal temperatures, reduced Hudson Strait warm-based area (Fig. B.35), and at times complete de-activation of the Hudson Strait ice stream. As described in Sec. 3.3.1, this de-activation eventually leads to a surge.

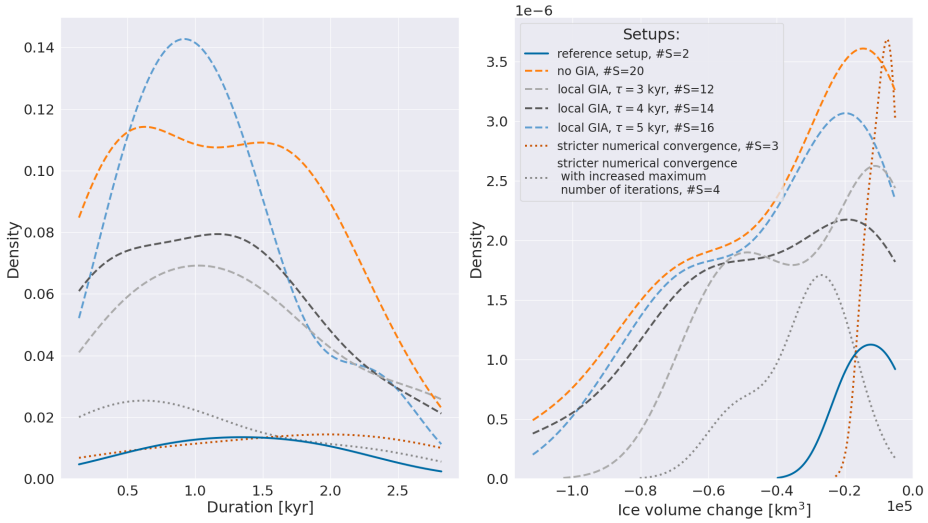

Figure 3.13: Kernel density plot for the ≤ 2 #surges sub-ensemble. The reference and MNEEs setups use a global GIA model. #S indicates the total number of surges across all runs of the sub-ensemble.

For the > 2 #surges sub-ensemble, using local GIA leads to a similar response as

completely deactivating GIA, except for the number of surges. The number of surges increases without GIA and decreases for all local GIA models, but the differences are smaller than the MNEEs (Fig. 3.6). The different response is caused by a change in ice configuration. For example, local GIA ($\tau = 4$ kyr) significantly reduces the Hudson Strait ice volume before 80 kyr BP, leading to a smaller but more stable warm-based area (e.g., no rapid changes due to advection of cold ice) and consequentially a continuously active ice stream instead of activation/de-activation cycles (Fig. B.36). Therefore, a change in ice stream behavior can be caused by differences in the Hudson Strait basal temperature due to glacial isostatically driven ice volume changes (e.g., decreased insulation due to a thinner ice sheet), indicating that surges only occur within a specific setting. The mean period, duration, increase in Hudson Strait ice flux, and mean ice volume change show an increase for experiments with local and without GIA, but most differences are smaller than the MNEEs.

In summary, the GIA experiments with the default GHF indicate that the occurrence of Hudson Strait ice stream surges is sensitive to the overall North American ice configuration. The surge characteristics, however, show only minor changes. In contrast, the experiments with local GIA and without GIA lead to more significant changes for the classic binge-purge surge mode (Fig. B.16 and B.17). The surge duration decreases, while the number of surges, increase in mid-Hudson Strait ice flux, and Hudson Strait ice volume change increase. The different model response for high and low GHFs is due to the differences in thermal conditions at the ice sheet base (e.g., Fig. B.13).

3.3.5 Adding underwater warming pulses

As for the ocean forcing associtated with HEs, the DO event sub-surface ocean warming has no significant effect on the surge characteristics, except for the surge duration (Fig. 3.6 and BE_1 in Fig. B.21). Similarly, the ≤ 2 #surges sub-ensemble show minor changes in the number of surges when applying the DO event ocean forcing (Fig. 3.14 and BE_1 Fig. B.24). The only exception is $T_{\mathrm{max,DO}} = 2°C$, $d_{\mathrm{OF}} = 250$ m, which increases the number of surges across the sub-ensemble from 2 to 11 (spread across 3 runs, maximum increase of 4 surges per run). Considering that there are 22 ocean temperature increases per run, this is still a rather small increase. Furthermore, the additional events do not necessarily align with increased ocean temperatures. As for the ice shelf removal experiments, the increase in surges is a consequence of small changes in the overall ice configuration, particularly in the Hudson Strait, rather than a direct response to the ocean forcing itself (e.g., Fig. B.18).

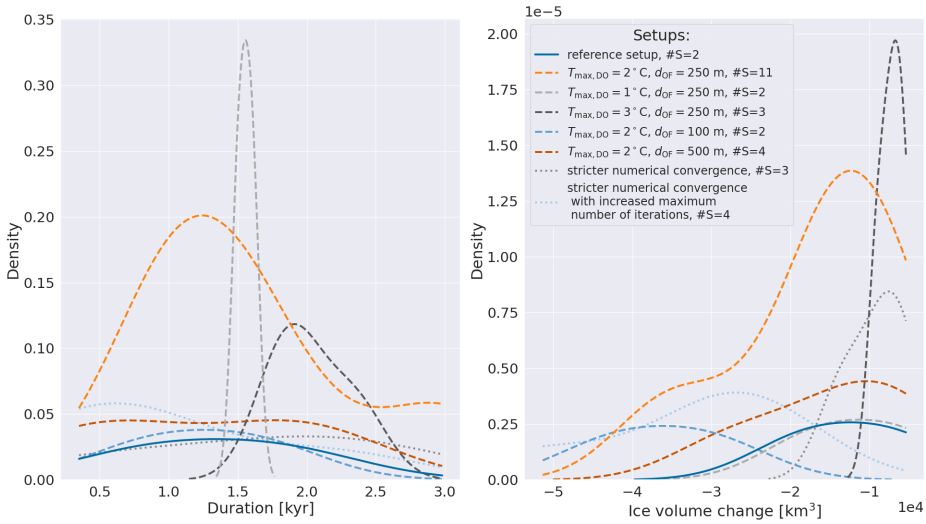

Figure 3.14: Kernel density plot for the ≤ 2 #surges sub-ensemble. The reference and MNEEs setups do not use an additional ocean forcing. #S indicates the total number of surges across all runs of the sub-ensemble.

Therefore, the ocean forcing and the consequential increase in sub-shelf melt and face melt are insufficient to significantly affect the surge characteristics (number of surges, mean surge duration, mean period between surges, mean increase in Hudson Strait ice flux, and mean Hudson Strait ice volume change during a surge) or trigger new surges. This is mainly a consequence of small ice shelves in the Labrador Sea across all runs (Fig. 3.8). However, sub-surface ocean warming can indirectly affect the overall timing of surges through changes in ice sheet evolution.

3.4 Discussion

Q_1 *What are the characteristics of Hudson Strait ice stream surges?*

The surge characteristics are very sensitive to the applied GHF. For the default GHF input field, the Hudson Strait ice stream is almost continuously active throughout the last glacial cycle. Surges occur after a short quiescent period or as an increase above the background ice flux. Furthermore, the strongest surges (preceded by a complete de-activation of the Hudson Strait ice stream) occur before MIS3. While there is evidence for pre-MIS3 HEs (e.g., Table 6.3 in Bradley, 2014), HEs are usually associated with MIS3. The limited number of strong surges within MIS3 is a consequence of increased basal temperatures (increased insulation due to a thicker ice sheet), leading to a continuously active ice stream (no ice build-up before surge).

Decreasing the GHF in the Hudson Bay/Hudson Strait below $\sim 37\ \frac{\mathrm{mW}}{\mathrm{m}^2}$ leads to a surge mode consistent with the originally proposed binge-purge mechanism (long quiescent periods interspersed with short surges, MacAyeal, 1993).

Depending on the parameter vector, the surges can now occur continuously between $\sim$ 110 and $\sim$ 10 kyr BP (surges before 100 kyr BP are not considered in the surge characteristics). Critically, the binge-purge mode increases the number of strong surges during MIS3 (compared to the near continuous ice streaming mode), which is more in accord with the timing of Heinrich Layers in sediment cores (e.g., Hemming, 2004).

During a surge, both GHF scenarios lead to a Hudson Strait ice flux and ice volume discharge consistent with literature estimates (Roberts et al., 2014, and references therein). As HEs are identified by IRD layers, the applied GHF must enable the entrainment of enough sediment. However, depending on the mechanism considered, sediment can be entrained for a cold-based (e.g., Meyer et al., 2019) as well as warm-based Hudson Bay/Hudson Strait (Drew, 2023). What ultimately controls the sediment discharge during a surge is the sediment availability. Furthermore, depending on the study and method used, GHF estimates in the Hudson Bay and Hudson Strait vary between 20 and 80 $\frac{\mathrm{mW}}{\mathrm{m}^2}$ (e.g., Pollack et al., 1993; Shapiro and Ritzwoller, 2004; Blackwell and Richards, 2004; Davies, 2013; Lucazeau, 2019). Therefore, both surge modes occur within GHF constraints and are consistent with proposed sediment entrainment mechanisms.

When using the default GHF, the GSM temperatures in the bed are colder or similar to borehole measurements south of the Hudson Bay (Fig. B.37 and B.38). While these boreholes indicate a negative GHF gradient toward the North and older bedrock material tends to be colder (less radioactive decay, Matthew Drew, personal communication, 1 December 2023), no deep boreholes are available in

the Hudson Bay and Hudson Strait. Therefore, better constraints on the GHF in the Hudson Bay and Hudson Strait as well as the inclusion of a fully coupled sediment model are required to determine the most likely surge mode.

Q_2 *Can the sudden reduction of the buttressing effect of ice shelves trigger Hudson Strait ice stream surging?*

In line with proxy data indicating ice shelf free conditions during most of the last glacial cycle (Hillaire-Marcel et al., 1994; Hesse et al., 1999; De Vernal et al., 2000; Gibb et al., 2014) and other modeling studies (Schannwell et al., 2023), there is no significant Labrador Sea ice shelf in the GSM runs. This conclusion still holds even when running the GSM with a full North American and Greenland ice sheet configuration (instead of just the stub North-West Greenland shown in Fig. B.1).

The relatively small ice shelves in front of the Hudson Strait provide only minor buttressing and are barely affected by the applied ocean temperature forcing. Reducing the ocean temperature by $-2°C$ leads to minor ice shelf growth. Even when completely inhibiting calving in front of the Hudson Strait, not all parameter vectors yield large ice shelves. Ice shelf collapse in runs that have large ice shelves leads to minor increases in mid-Hudson Strait ice flux. In summary, our results indicate that buttressing ice shelves are likely not the main trigger of Hudson Strait ice stream surging but, depending on the parameter vector, can affect the timing of surges.

This is in contrast to the findings of Alvarez-Solas et al. (2013, Hudson Strait surge induced by collapse of buttressing ice shelf), which use fixed glacial cli-

matic boundary conditions except for changes in the sub-surface ocean temperature. However, the ice shelf in their simulation covers the entire area between the Hudson Strait and Greenland, significantly increasing the buttressing and enabling a larger Hudson Strait ice volume (larger surges when removing the buttressing). As discussed above, this scenario is inconsistent with available marine records. Furthermore, this scenario is arguably ruled out by the bounding experiments within this study along with the range of sub-shelf melt rates across the ensemble.

Q_3 *Can a sudden breakup of fringing ice shelves along the Canadian coast explain the IRD records (without the need for surges)?*

Based on assumptions about the terrigenous material transported by floating ice during HEs (100 km^3, Alley and MacAyeal, 1994), the debris concentration in basal glacier ice (5 to 35 %, Lawson et al., 1998), and the accreted ice thickness (1 % of total ice thickness), Hulbe et al. (2004) estimate that a minimum ice shelf volume of $2.8 \cdot 10^4$ to $20 \cdot 10^4$ km^3 is required to explain the IRD records by disintegration of fringing ice shelves. The maximum Labrador sea ice shelf volume across all reference runs is $2.5 \cdot 10^4$ km^3 ($12.6 \cdot 10^4$ km^3 when calving is completely inhibited in the *ocean forcing area* outlined in Fig. 3.2). Therefore, it is unlikely that the IRD layers found in the North Atlantic are solely a consequence of ice shelf disintegration. However, this conclusion neglects potential contributions of other source regions with similar geological material, such as the Boothia ice stream (Sanford and Grant, 1998; Hulbe et al., 2004; Naafs et al., 2013). Future work, e.g. ice sheet modeling with a fully coupled

sediment model, is required to determine the contributions of individual source regions.

Q_4 *What is the role of GIA in a HE context?*

GIA leads to lower ice sheet surface elevations, increased accumulation, and consequently, larger ice sheets (Fig. 3.12). The reduction in overall North American and Hudson Strait ice volume when using a local or no GIA model leads to, on average, lower basal temperatures (Fig. B.35) and fosters surges in runs that otherwise show a continuous Hudson Strait ice stream.

Analyzing the surge characteristics with the default GHF shows a tendency towards longer and stronger surges for local or no GIA. The differences are caused by the change in ice configuration but are generally on the same order of magnitude as the MNEEs. Changes in the earth rheology used by the global GIA model have minor impact.

The classic binge-purge surge mechanism in the low GHF experiments is more sensitive to GIA. Due to the different thermal conditions at the ice sheet base, the experiments with local or without GIA now lead to shorter but stronger surges.

Due to its effect on the overall North American ice volume, the consequential change in basal temperatures in the Hudson Strait, and the limited range of ice sheet configurations for which Hudson Strait ice stream surges occur, global GIA plays a critical role in modeling ice stream activation/de-activation cycles. These results are especially relevant for interpreting HE modeling experiments that do not use a physically-based GIA scheme.

Q_5 *How does sub-surface ocean warming affect HEs?*

In the idealized setup of Bassis et al. (2017), underwater melt modulated by GIA leads to pseudo-Hudson Strait surges. Although not exactly replicating the experiments of Bassis et al. (2017), we examine the effect of sub-surface ocean warming in a HE context by applying sub-surface ocean forcings of different magnitudes at varying depths. In general, applying a similar sub-surface ocean forcing in the GSM does not significantly affect the surge characteristics and does not trigger new Hudson Strait surges. However, it can affect the timing of Hudson Strait surges. Depending on the sub-shelf melt coefficient and the ocean temperature (Sec. 3.2.5), the sub-shelf melt can reach up to 400 $\frac{\mathrm{m}}{\mathrm{yr}}$ in our simulations, indicating that the minor model response concerning surges is not an issue of insufficient sub-shelf melt. The different model response is likely a consequence of the less idealized model setup and the large variety of system processes affecting the surges in the GSM that are not present in the modeling of Bassis et al. (2017, such as their lack of ice thermodynamics). Different implementations of GIA and calving along with different grid resolutions further contribute to the different results.

Conclusions

Within this study, we investigate Hudson Strait ice stream surges and determine the role of geothermal heat flux (GHF), ice shelves, GIA, and sub-surface ocean temperature forcings in a HE context. The model results are based on the first HE simulations with transient last glacial cycle climate forcing, global visco-elastic

glacial isostatic adjustment model, sub-glacial hydrology model, and high-variance sub-ensemble retrieved from North American history matching for the last glacial cycle.

Consistent with proxy records, no large ice shelves develop in the Labrador Sea (unless extreme calving restrictions are applied), leading to minor buttressing effects. Even when completely inhibiting calving in the Labrador Sea, the collapse of large ice shelves leads to only minor increase in mid-Hudson Strait ice flux. Except for the exact timing of surges, sub-surface ocean warming does not significantly affect the surge characteristics. Due to its significant effect on the overall ice sheet configuration, GIA can increase the number of Hudson Strait surges but does not significantly affect the surge characteristics.

Based on our results, Hudson Strait ice stream surge cycling is the most likely Heinrich Event mechanism, but ocean forcings can affect the timing of surges and provide a means to synchronize HEs with the coldest phases of the Bond cycles. However, the surge pattern is highly sensitive to the GHF in the Hudson Bay and Hudson Strait area. The GHF estimates in this region vary by a factor of 4. While better constraints on the GHF are essential to determine the likelihood of the classic binge-purge mechanism compared to a near continuous ice stream with pre-Heinrich Event shutdowns, the increased number of strong surges during MIS3 in the binge-purge mode hints towards smaller GHFs.

A key caveat is the usual assumption that IRD flux is approximately proportional to ice flux (be it from Hudson Strait ice stream surge cycling or collapsing ice shelves). Future work incorporating a fully coupled sediment model is required to evaluate the correlation between ice and sediment discharge and better link the glacial processes

examined here to the IRD layers.

Preface to Chapter 4: "Laurentide ice sheet sediment discharge during simulated Heinrich events with a comprehensive glaciological and sediment processes model"

This manuscript is intended for submission to Nature. In addition to the setup presented in Chap. 3, the GSM is now run with a fully dynamical linked-cavity basal hydrology model and fully coupled sediment model. The HE characteristics are determined based directly on the sediment flux out of the Hudson Strait (instead of, e.g., the mid-Hudson Strait ice flux).

Chapter 4

P3: Laurentide ice sheet sediment discharge during simulated Heinrich events with a comprehensive glaciological and sediment processes model

Abstract

Layers of ice-rafted debris found in sediment cores from the North Atlantic are usually inferred to be associated with a large increase in freshwater flux due to the melting of icebergs. Ice flux or ice thickness/volume changes are, therefore, often used in paleo-ice sheet studies to identify these Heinrich Events. Here, we present the first study

incorporating a fully coupled ice sheet and sub-glacial sediment processes model, allowing the determination of Heinrich Events based directly on the sediment flux. A high-variance parameter vector ensemble is used to partly address potential non-linear dependencies of model results on model parameters. In line with provenance studies, our results indicate that the Hudson Strait ice stream is the main ice-rafted debris contributor. The sediment contributions from the Cumberland Sound and Boothia ice stream are an order of magnitude smaller. The key finding of this study is the poor correlation between the sediment and ice flux, indicating that sediment flux out of the Hudson Strait should be used as the primary metric when examining Heinrich Events. This conclusion challenges the previously hypothesized large increase in Hudson Strait calving flux (be it through ice stream activation/speed-up or ice shelf collapse) attributed to Heinrich Events.

4.1 Introduction

Ocean sediment records in the North Atlantic, particularly in the Ruddiman Belt (40° - 55°N, Ruddiman, 1977), show layers of ice-rafted debris (IRD). Depending on the location of the sediment core and the layer in question, these "Heinrich Layers" can be < 5 cm close to the European coast or > 60 cm thick in the Labrador Sea (Hemming, 2004). Based on the sediment distribution and geochemical provenance studies, the Heinrich Layers are generally attributed to large armadas of icebergs calved from the Hudson Bay-Hudson Strait region. The timing of Heinrich Events (HEs) generally coincides with oceanic and climatic changes in the Northern Hemisphere as well as on a global scale (e.g., Hemming, 2004; Srokosz et al., 2012; Lauterbach et al., 2020).

However, IRD records are noisy and do not necessarily provide a consistent interpretation across ocean sediment records. For example, Heinrich Layer thickness estimates within the same core and layer can differ by ~ 60 cm (Hemming, 2004, and references therein). Sediment volume estimates of an average Heinrich Layer range from 100 to 400 km^3 (Hemming, 2004). Additionally, it is unclear what percentage of the fine sediment (e.g., < 106 μm) in a Heinrich Layer was transported by icebergs, particularly for the thickest layers in close proximity to the Hudson Strait (e.g., Veiga-Pires and Hillaire-Marcel, 1999; Hesse and Khodabakhsh, 2016).

Another source of uncertainty when determining the sediment discharge during HEs is the poorly constrained sediment distribution across North America. Even for present-day, the sediment thickness estimates in, e.g., the Hudson Bay vary between < 5 and > 1500 m (e.g., Fig. 39 in Drew, 2023). Due to these large uncertainties, constraining the sediment discharge during HEs is challenging.

On the modeling side, a key challenge for improving the understanding of HEs is that processes related to sediment erosion, entrainment, and deposition, as well as iceberg melt processes, are generally highly parameterized in numerical models (e.g., Meyer et al., 2019; Drew, 2023; Fendrock et al., 2023). For example, there is no consensus on the englacial sediment distribution, including the limits of englacial sediment thickness terrestrial ice can transport. The maximum sediment thickness in a frozen-fringe model is 15 m (Meyer et al., 2019). In contrast, results of a coupled ocean-iceberg model indicate that icebergs with an isolated basal sediment layer cannot reproduce the observed Heinrich Layer distribution, even when considering capsized icebergs (Fendrock et al., 2023). The authors conclude that sediment needs to be distributed throughout the entire volume of a 260 m thick iceberg to capture

the sediment distribution pattern of a Heinrich Layer.

In this study, we re-analyze the sediment thickness data in Table 1 of Hemming (2004) to provide revised estimates of the sediment discharge during HEs. We use various interpolation methods and Heinrich Layer thickness estimates to partly address the associated uncertainties. The new sediment discharge estimates are then used as bounds to interpret the results of subglacial/englacial sediment resolving glaciological simulations of North American ice stream cycling.

Based on recent modeling studies, the most likely driving mechanism for Heinrich Events is Hudson Strait ice stream surge cycling synchronized to the coldest phases of Dansgaard-Oeschger (DO) cycles by ocean forcings (Hank and Tarasov, 2023, in preparation). However, other ice streams may have contributed to Heinrich Layers (e.g., Hulbe et al., 2004; Andrews et al., 2012). Therefore, we use the glacial systems model (GSM, Tarasov et al., 2024, in preparation) to simulate sediment discharge of the Hudson Strait, Cumberland Sound, and Boothia ice stream. This is the first glaciological simulation of HEs that incorporates all the following components: fully coupled sediment model, asynchronously coupled global visco-elastic glacial isostatic adjustment (GIA) solver, linked-cavity basal hydrology model, and transient last glacial cycle climate forcing. The GSM, including the basal hydrology and sediment model, has been thoroughly tested in a HE context (Drew and Tarasov, 2022; Drew, 2023; Hank et al., 2023; Hank and Tarasov, 2023, in preparation). A high-variance (with respect to the ensemble parameters) ensemble and minimum numerical error estimates (MNEEs, Hank et al., 2023) are used to partly address parametric uncertainties and determine the numerical significance of model results, respectively.

We are particularly interested in the following research questions.

Q_1 *How does the sediment distribution in the Hudson Strait ice drainage basin change throughout the last glacial cycle?*

Q_2 *How is the sediment distributed within the ice column?*

Q_3 *What are likely bounds on the englacial sediment discharge out of the Hudson Strait, Cumberland Sound, and Boothia ice stream?*

Q_4 *How well does sediment discharge correlate with ice stream flux?*

4.2 Methods

4.2.1 Sediment discharge estimation

The Heinrich Layer thickness estimates in this study are based on Table 1 in Hemming (2004). The thickness estimates can vary significantly between different studies, even when examining the same layer in the same core. The causes of such differences are multifaceted but are generally related to the definition of a Heinrich Layer and the methods used. For example, Heinrich Layer 2 in core *CH69-K09* (lat = 41.75°N, lon = 47.35°W) has sediment thickness estimates of 3 and 62 cm (Hemming, 2004, and references therein).

In a first step, we replace duplicate entries with the average sediment thickness (32.5 cm in the above case). We then remove all cores that do not provide a sediment thickness estimate for any of the 6 Heinrich Layers (note that the data includes 0 cm thickness estimates). Finally, we calculate the mean sediment thickness ($d_{\mathrm{sed,ave}}$) in all remaining cores (ignoring Heinrich Layers for which no thickness estimate is

available). However, we also calculate a sediment volume estimate for each Heinrich Layer individually.

While we do not consider the above difference of 59 cm to be representative of the general uncertainty of Heinrich Layer thickness estimates (for the same layer and core), differences of 5 to 10 cm occur frequently (Hemming, 2004, and references therein). To incorporate this uncertainty and provide lower/upper bounds, we use the minimum/maximum sediment layer thickness in each core and further subtract/add 10 cm ($d_{\mathrm{sed,min}}/d_{\mathrm{sed,max}}$). However, we ensure the sediment thickness is at least 1 cm ($\min\left[d_{\mathrm{sed,ave}}\right] = 1.5$ cm).

To estimate the total sediment volume transported during a HE, we interpolate the sediment thickness between the core locations. The interpolation grid covers the area between 37.8°N to 61.5°N and 58.7°W to 9.5°W ($\sim$ min/max lat/lon core location) with a latitudinal and longitudinal increment of 0.1°. To bound the data set and extract a more realistic sediment distribution, we added 8 data points with 0 cm sediment thickness at the minimum and maximum latitudinal extent (magenta circles in Fig. 4.2). Various different interpolation methods are available. Here we compare the piecewise-linear, nearest-neighbor, and Clough-Tocher interpolation schemes provided by the Python module *SciPy* (version 1.5.2, Virtanen et al., 2020). Negative values from the Clough-Tocher interpolation are replaced by 0 m sediment thickness in a post-processing step. Multiplying the interpolated sediment thickness with the corresponding interpolation grid cell area and summing the result yields the final sediment discharge estimate.

4.2.2 Model description

All experiments within this study are conducted with the 3D thermo-mechanically coupled glacial systems model (GSM, Tarasov and Peltier, 1999, 2007; Pollard and DeConto, 2012; Tarasov et al., 2024, in preparation). The GSM setup is similar to the one in Hank and Tarasov (2023, in preparation). It incorporates an asynchronously coupled global visco-elastic GIA solver (Tarasov and Peltier, 1997), an asynchronously coupled geographically-resolved energy balance climate model (Deblonde et al., 1992), and a transient last glacial cycle climate forcing. However, we now use a fully dynamical linked-cavity basal hydrology model (instead of a local basal hydrology model Drew and Tarasov, 2022). Additionally, the GSM setup includes a fully coupled sediment model, enabling the determination of the sediment discharge for the Hudson Strait, Cumberland Sound, and Boothia ice streams (Drew, 2023). As in Hank and Tarasov (2023, in preparation), we use a transient last glacial cycle climate forcing.

Numerical modeling of instabilities such as ice stream surge cycling is challenging due to the highly non-linear response and rapid changes involved. For this reason, the GSM numerics, including the effects of grid discretization, have been tested explicitly in a HE context (Hank et al., 2023). Furthermore, numerous sensitivity experiments have been conducted within the framework of HEs to determine the effects of various system processes (Drew and Tarasov, 2022; Drew, 2023; Hank et al., 2023; Hank and Tarasov, 2023, in preparation). As a result of these tests, the model setup incorporates sub-temperate basal sliding, global visco-elastic GIA, and different geothermal heat flux (GHF) boundary conditions.

The GSM is initialized from ice-free conditions at 122 kyr BP (Eemian) and is run

to present day with a maximum ice dynamics time step size of 1 yr (automatically decreased to meet CFL constraint or when numerical solver convergence fails) at a horizontal grid resolution of $\Delta_{\text{lon}} = 0.5°$, $\Delta_{\text{lat}} = 0.25°$. The full model domain is shown in Fig. C.1.

4.2.3 Sediment model

The sediment model in the GSM accounts for abrasion, quarrying, as well as subglacial and englacial sediment transport (Drew, 2023). However, sediment entrainment is currently only possible under warm-based conditions. A frozen-fringe model (as, e.g., in Meyer et al., 2019) has not yet been implemented.

An exponential vertical grid with the finest resolution near the ice-sediment interface is used for modeling sediment entrainment as well as englacial mixing and advection (Drew, 2023). The gris is uniform in ξ and transformed according to:

$$z_{\text{ice}} = \frac{z_{\max}}{\sum \left[e^{\xi/z_0}\right]} e^{\xi/z_0}, \tag{4.1}$$

where the exponential grid spacing $z_0 = 15$ and the maximum height of the englacial entrainment grid $z_{\max} = 23$ m.

Englacial sediment transport is controlled by horizontal velocities $\mathbf{v}$, vertical mixing V_{mix} (diffusion of sediment concentration between layers), and the entrainment/deposition rate v_{net} (Melanson et al., 2013; Drew, 2023)

$$\frac{\partial C}{\partial t} = -\nabla \cdot C\mathbf{v} - \frac{\partial \left(C\dot{V}_{\text{net}}\right)}{\partial z} + V_{\text{mix}}, \tag{4.2}$$

where C is the englacial sediment concentration. The vertical mixing is

$$V_{\text{mix}} = \frac{\partial}{\partial z}\left(D\frac{\partial C}{\partial z}\right), \tag{4.3}$$

where D is a diffusion coefficient (Drew, 2023). The net of sediment entrainment and deposition due to basal melt follows

$$v_{\text{net}} = v_r - \frac{\dot{b}_{\text{melt}} C_0}{1-\Phi}, \tag{4.4}$$

where $\dot{b}_{\text{melt}}$ is the basal melt rate, C_0 the englacial sediment concentration at the ice sheet base, and Φ the porosity with which the englacial sediment is deposited (Drew, 2023). The entrainment rate v_r (regelation) is calculated according to

$$v_r = K_s \frac{N_{\text{eff}}}{l_a}, \tag{4.5}$$

where K_s is the conductivity of ice into the sediment layer, N_{eff} the effective pressure, and l_a the englacial array depth modifier (Drew, 2023). l_a incorporates the negative feedback between englacial sediment concentration and entrainment rate. Following Eqs. 4.4 and 4.5, the largest net sediment entrainment occurs for high effective pressures and low basal melt rates.

4.2.4 Ensemble parameter vectors

We use a high-variance ensemble of parameter vectors to partly address parametric uncertainties. The parameter vectors for the initial ensemble are from combining each

of the 20 GSM parameter vectors used in Hank and Tarasov (2023, in preparation) with 3 different linked-cavity basal hydrology and sediment parameter vectors (Drew, 2023). The 20 GSM parameter vectors are from a North American history-matching [Tarasov et al., in preparation] and have passed several HE sieves in line with proxy constraints (Hank and Tarasov, 2023, in preparation). The 3 linked-cavity basal hydrology and sediment parameter vectors are based on whole Pleistocene glacial systems modeling sieved on last glacial maximum and deglaciation constraints (Drew, 2023).

For all 60 runs, we determine the sediment flux across the Hudson Strait grounding line to identify nominal HEs (Fig. 4.1). However, the sediment flux time series (100 yr output) is noisy, hindering such HE identification. Therefore, we smooth the time series by applying a running mean with 1 kyr window length (e.g., Fig. C.3). The same running mean is also applied to the sediment flux across the Cumberland Sound and Boothia grounding line (Fig. 4.1).

A peak prominence algorithm is then applied to the smoothed Hudson Strait sediment flux to determine sediment discharge peaks between 100 and 10 kyr BP (*SciPy* version 1.5.2, Virtanen et al., 2020). The minimum threshold (increase in sediment flux of 0.01 $\frac{\text{km}^3}{\text{yr}}$) is based on estimates of the minimum IRD volume in the North Atlantic (100 km^3 Hemming, 2004) and a maximum HE duration of $<$ 3 kyr (maxium estimated duration of 2.3 kyr in Hemming, 2004). Additionally, we consider the possibility of a small continuous background sediment flux and multiple provenance regions (e.g., Cumberland Sound and Boothia ice stream). To minimize overlap, we ensure a minimum time separation of 1.5 kyr (half of maximum HE duration) between sediment flux peaks. We then remove sediment flux peaks with a

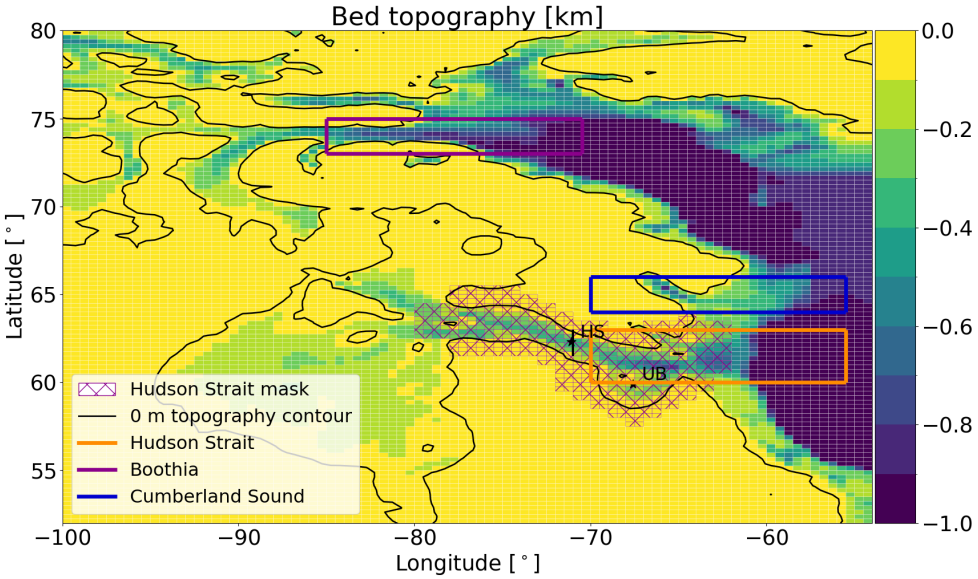

Figure 4.1: GSM input present-day bed topography. The black asterisks and line indicate the location of the mid-Hudson Strait (HS) and Ungava Bay (UB) ice thickness calculation and the HS flux gate, respectively. The Hudson Strait mask is used to determine the Hudson Strait ice volume, warm-based area, sub- and englacial sediment thickness and volume. The orange, blue, and magenta boxes outline the areas of the Hudson Strait, Cumberland Sound, and Boothia ice stream, respectively. Within these areas, we determine the sediment and ice flux across the grounding line. The black contour line shows the present-day sea level (coastline) used in the GSM. To prevent ice sheet growth over Greenland, the landmask in the corresponding area has been set to below sea level aside from a North-West Greenland stub to enable ice growth across Nares Strait.

duration < 0.2 kyr (Hemming, 2004) and > 3 kyr. Since we are mostly interested in the sediment discharge in a HE context, we reject runs with < 3 peaks and > 15 peaks. The sediment discharge for all 3 ice streams is calculated as the integral of the grounding line sediment flux during a sediment flux peak. The analysis is then conducted on the remaining 9 reference runs.

We tested different values for the running mean window length and sediment flux prominence threshold. In general, shorter window lengths (less smoothing) lead to

more and shorter sediment peaks with a larger Hudson Strait sediment flux. Due to the removal of small sediment peaks, a larger prominence threshold results in fewer and longer peaks with a larger Hudson Strait sediment flux. Increasing the model output frequency to every 10 yr leads to no significant differences.

4.2.5 Run comparison

Similar to Hank and Tarasov (2023, in preparation), we also apply a peak prominence algorithm to the smoothed (1 kyr running mean) mid-Hudson Strait ice flux (minimum threshold of 0.0015 Sv, Fig. 4.1) to determine large-scale Hudson Strait surges. We filter the surges with the same sieves as the sediment flux peaks (Sec. 4.2.4). The results are then used to determine the overlap between sediment flux peaks and Hudson Strait ice stream surges.

The sediment flux characteristics (Fig. 4.4 and Table C.2) and surge characteristics (Fig. C.6) are determined for all reference runs. The percentage differences to the comparison experiment in question are obtained by calculating the percentage differences for every run individually and then averaging over all runs (Hank et al., 2023). **M**inimum **N**umerical **E**rror **E**stimates (MNEEs) are determined for all sediment flux characteristics based on their percentage difference between runs with the reference GSM setup and runs with stricter numerical convergence thresholds (Hank et al., 2023). Differences smaller than the MNEEs are considered numerically insignificant. However, that does not necessarily mean the differences have no physical relevance.

4.3 Results

4.3.1 Sediment discharge estimates

The sediment discharge estimates between different interpolation methods vary significantly (Table 4.1, based on the sediment thickness estimates in ocean sediment cores). Due to large areas with thick sediment in 3 corners of the interpolation area (Fig. C.5), the nearest-neighbor scheme yields the largest estimates. Piecewise-linear interpolation slightly reduces the estimates, but the Clough-Tocher method returns the smallest estimates. Overall, the sediment discharge estimates vary between 187 and 2078 km^3, with a mean of 953 ± 673 km^3 ($\pm$ indicates the standard deviation, Table 4.1).

Metric	piecewise-linear [km^3]	nearest-neighbor [km^3]	Clough-Tocher [km^3]
ave	800	939	753
min	212	226	187
max	1732	2078	1646

Table 4.1: Sediment discharge estimates for an average Heinrich Layer using different interpolation methods. The mean, minimum, and maximum estimates are based on the sediment thickness estimates $d_{\text{sed,ave}}$, $d_{\text{sed,min}}$, and $d_{\text{sed,max}}$. respectively (Sec. 4.2.1). The sediment distributions for $d_{\text{sed,ave}}$ are shown in Fig. C.4, C.5, and 4.2.

When using the Clough-Tocher interpolation scheme, the estimates for individual HEs vary between 199 km^3 for Heinrich Layer 6 and 1325 km^3 for Heinrich Layer 2. The piecewise-linear and nearest-neighbor methods lead to larger estimates, with maxima of 1089 km^3 and 1268 km^3 for Heinrich Layer 2, respectively.

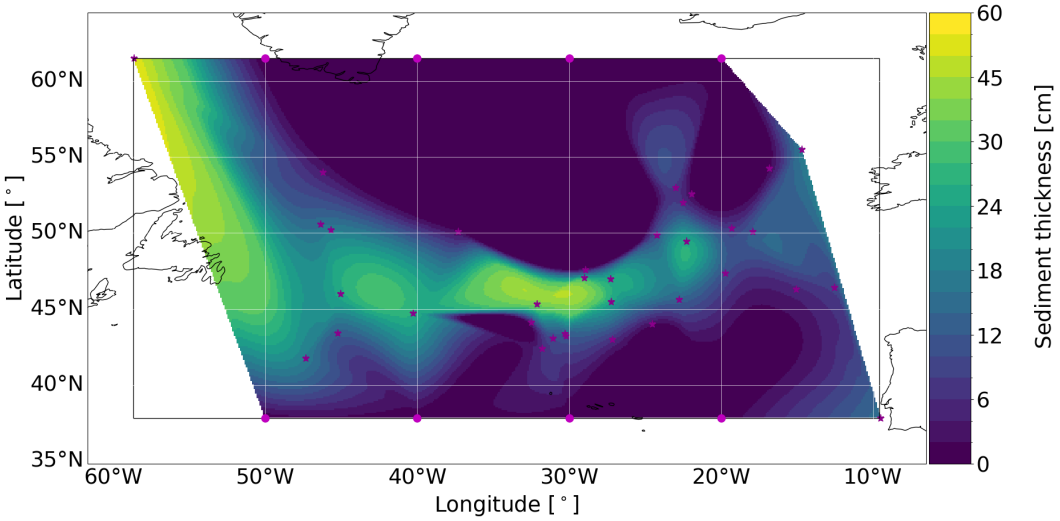

Figure 4.2: Sediment thickness distribution for an average Heinrich Layer based on the Clough-Tocher interpolation and the mean sediment thickness estimates $d_{\mathrm{sed,ave}}$ (Sec. 4.2.1). The magenta asterisks and circles mark the location of the cores and the data points that were added to bound the data set (0 cm sediment thickness, Sec. 4.2.1), respectively. The thin black line outlines the interpolation area. The black contour is the present-day coastline provided by *cartopy* (Met Office, 2010 - 2015). Note the change in the color bar step at 30 cm.

4.3.2 Initial sediment distribution

Since the North American sediment distribution during the Eemian (GSM initialization time) is poorly constrained, we first examine the effect of various uniform sediment distributions with an inital sediment thickness of $d_{\mathrm{sed,in}} = [0, 10, 20, 30, 40]$ m. Furthermore, two present-day sediment distributions ($d_{\mathrm{sed,PDlow}}$ and $d_{\mathrm{sed,PDhigh}}$ in Fig. C.2, Geological Survey of Canada, 2014; Laske and Masters, 1997) are used to bound model results within literature estimates. For the set of experiments with initial sediment thickness < 20 m), a thicker initial layer increases the mean englacial sediment thickness in Hudson Strait for the interval before $\sim$ 70 kyr BP (Fig. 4.3).

Due to the production of new sediment by abrasion and quarrying, the differences in englacial sediment thickness decrease over time. The englacial sediment thickness is then controlled by englacial sediment transport as well as the net of sediment entrainment and deposition due to basal melt v_{net} (Eq. 4.4) rather than the sediment availability. Increasing the initial sediment layer thickness beyond 20 m has only minor effects on the Hudson Strait englacial sediment thickness (Fig. 4.3).

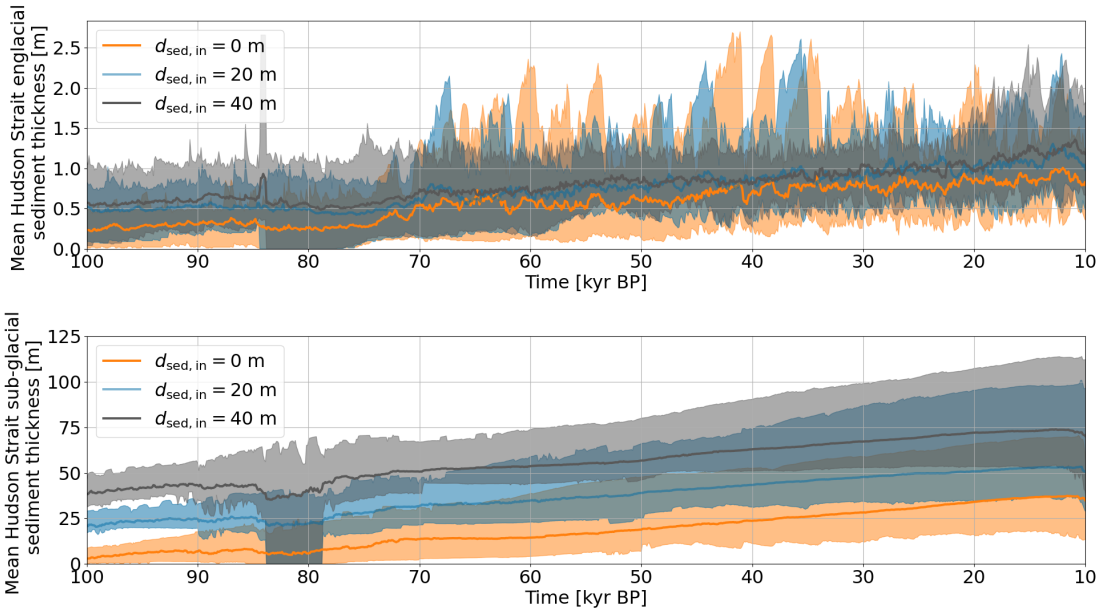

Figure 4.3: Mean Hudson Strait englacial and subglacial sediment thickness for various uniform initial sediment thicknesses $d_{\mathrm{sed,in}}$. The thick lines represent the ensemble mean of the different model setups. The shaded areas mark the ensemble minimum and maximum of the corresponding setup. The Hudson Strait area considered is outlined in Fig. 4.1.

Changes in sediment flux characteristics (shown in Fig. 4.4) are considered numerically significant when they exceed the MNEEs (Sec. 4.2.5). In general, the changes in sediment flux characteristics due to different initial sediment thickness distributions are on the same order of magnitude as the MNEEs (Fig. 4.4). Considering the

standard deviations, the sediment flux characteristics are not significantly affected by the initial sediment distribution. Note that all runs with $d_{\text{sed,PDhigh}}$ (Fig. C.2) crashed and the results are, therefore, not shown in Fig. 4.4. Based on the minor effects of the initial sediment thickness distribution and the large uncertainties involved, we use the GSM setup with medium uniform initial sediment thickness $d_{\text{sed,in}} = 20$ m as our reference setup.

4.3.3 North-East American sediment distribution

Due to sediment production and transport, the North-East American sediment distribution evolves continuously over the last glacial cycle. The sediment thickness on topographic highs remains relatively unchanged due to the generally low basal temperatures (lack of sedimentary processes under cold based ice, e.g., Fig. C.7). The largest differences occur within warm-based topographic troughs and along the ice sheet margin, where effective pressures are low and basal temperatures high (Eqs. 4.4 and 4.5).

The Hudson Bay and the catchment basins of other ice streams experience a decrease in sub-glacial sediment thickness (e.g., Fig. C.7). Due to the prevailing basal water thickness, effective pressure, and basal melt rate in these areas, sediment entrainment and transport out of the region outweigh sediment production and melt out (Fig. C.8). The removed sub-glacial sediment then accumulates further downstream in the Hudson Strait, Cumberland Sound, and Boothia ice streams as well as along the Canadian coast.

The present-day sediment distribution in the GSM is generally within the bounds

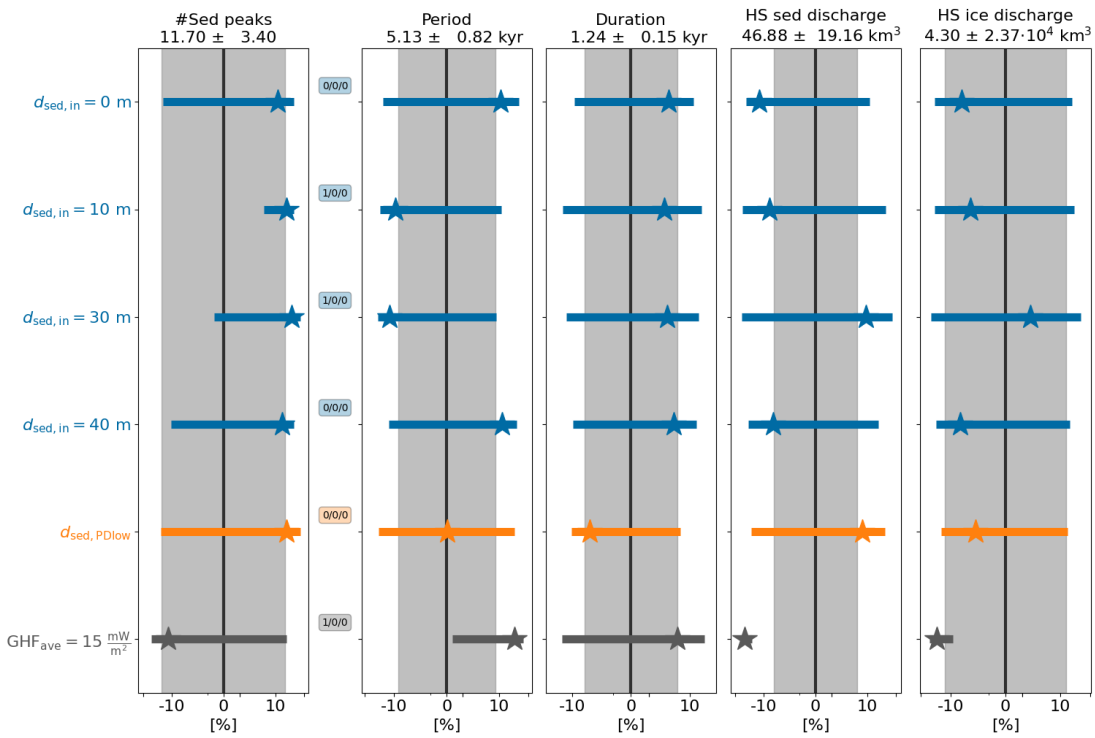

Figure 4.4: Percentage differences in sediment flux characteristics compared to the reference setup ($d_{\text{sed,in}} = 20$ m). The shaded regions represent the MNEEs. HS sed discharge and HS ice discharge represent the sediment and ice discharge across the Hudson Strait grounding line during a sediment flux peak, respectively. The different colors provide visual alignment of the individual model setups. The stars and horizontal bars are the ensemble mean percentage differences and standard deviations, respectively. The three numbers between the first and second column show the number of crashed runs, the number of runs without a sediment discharge peak, and the number of runs with only one sediment discharge peak in the comparison setup. The x-axes are logarithmic. The model setups, from top to bottom, are: $d_{\text{sed,in}} = [0, 10, 30, 40]$ m, present-day sediment distribution based on Geological Survey of Canada (2014), and average geothermal heat flux in the Hudson Bay and Hudson Strait GHF$_{\text{ave}} = 15\ \frac{\text{mW}}{\text{m}^2}$ ($d_{\text{sed,in}} = 20$ m, Hank and Tarasov, 2023, in preparation). Note that $d_{\text{sed,in}}$ experiments with GHF$_{\text{ave}} = 15\ \frac{\text{mW}}{\text{m}^2}$ lead to similar results (Fig. C.13).

set by literature estimates (e.g., compare Fig. C.7 and Fig. 39 in Drew, 2023). However, due to the large uncertainties associated with the present-day sediment distribution (differences $>$ 1500 m), a more precise/detailed validation is currently not possible.

4.3.4 Englacial sediment concentration

Here, we examine the sediment distribution within the ice column for 8 diagnostic sediment stations along and across the Hudson Strait ice stream (Fig. 4.6 and C.9). In general, the englacial sediment thickness during the last glacial cycle increases until deglaciation (Fig. C.10). The sediment concentration is highest in the basal layer and continuously decreases towards higher layers. However, due to the limited total englacial sediment height in the model (23 m, Eq. 4.1), sediment can accumulate in the uppermost layer, and the concentration, at times, can then be higher than that of some lower layers.

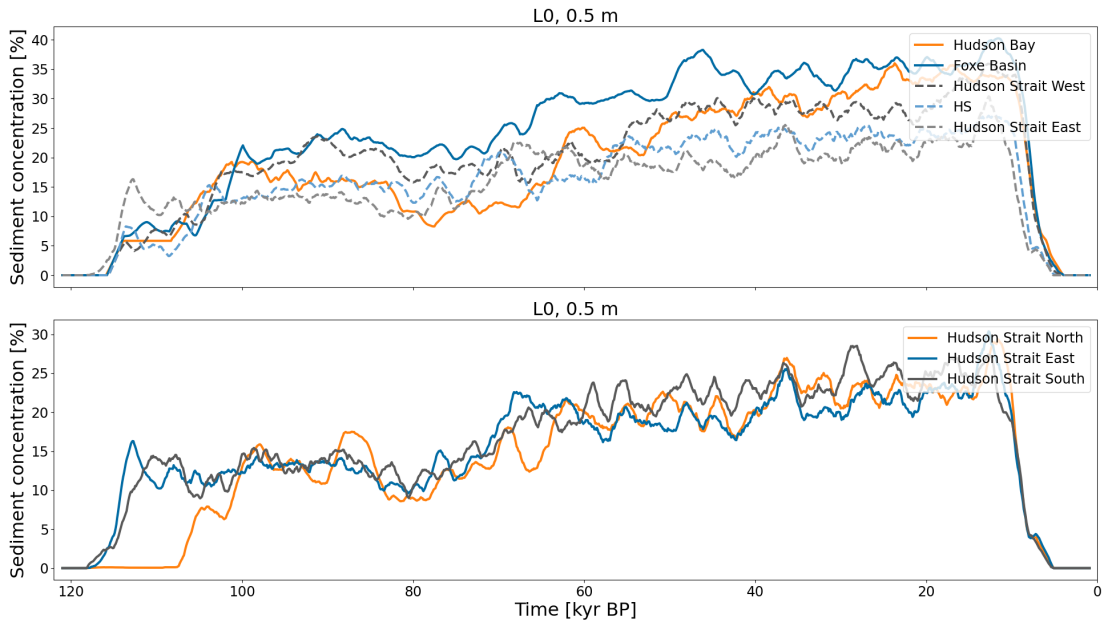

Figure 4.5: Englacial sediment concentrations within the bottom layer (L0, 0.5 m center height) for sediment stations along (upper panel) and across the Hudson Strait ice stream (lower panel). All lines represent the ensemble mean of the stations. The time series were smoothed with a 2 kyr running mean. The exact locations of the sediment stations are shown in Fig. C.9.

The englacial sediment concentration in the basal layer is higher for the Foxe

Basin outlet than for the Hudson Bay outlet (Fig. 4.5). The Hudson Bay station is generally located at the margin of the warm-based area (Fig. 4.6). Depending on the parameter vector and time in question, the Hudson Bay station does not experience continuous sediment entrainment (sediment entrainment over cold-based areas is not included in the GSM reference setup). Conversely, the Foxe Basin station is situated well within the warm-based area, enabling continuous sediment entrainment and increased englacial sediment concentrations. As a consequence of englacial sediment transport and deposition due to sediment meltout (increased basal melt rate within ice stream), the sediment concentration further downstream (Hudson Strait (HS) West, Hudson Strait, and Hudson Strait East) continuously decreases towards the ice margin (Fig. 4.5 and 4.6). In contrast, there is limited cross flow variation of sediment concentration.

4.3.5 Ice and sediment fluxes

HEs are ultimately defined by sediment layers but are often attributed to a large increase in freshwater flux caused by, e.g., a Hudson Strait ice stream surge. In this section, we compare the sediment flux and mid-Hudson Strait surge characteristics. Additionally, the effects of a lower GHF (averge GHF in Hudson Bay and Hudson Strait $\mathrm{GHF}_{\mathrm{ave}} = 15\ \frac{\mathrm{mW}}{\mathrm{m}^2}$) on the sediment flux and surge characteristics are examined.

Synchronized sediment peaks across the grounding line of the Hudson Strait, Cumberland Sound, and Boothia ice stream, as previously postulated for surges of the Mackenzie and Hudson ice stream (Schannwell et al., 2023), are scarce and show no indication of a connected system. The apparent synchronized timing is, therefore,

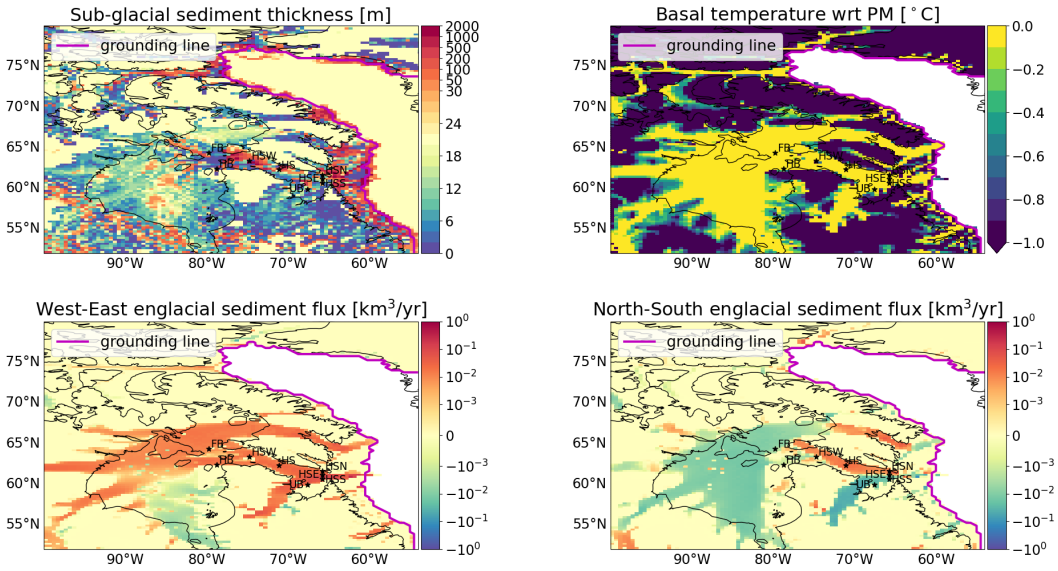

Figure 4.6: Sub-glacial sediment thickness, basal temperature with respect to the pressure melting point, West to East englacial sediment flux, and North to South englacial sediment flux for parameter vector 1, all at 20 kyr BP. The initial sediment thickness is 20 m. The black asterisks mark the sediment stations for which the englacial sediment concentration is examined: Hudson Bay (HB), Foxe Basin (FB), Hudson Strait West (HSW), Hudson Strait (HS), Ungava Bay (UB), Hudson Strait East (HSE), Hudson Strait South (HSS), Hudson Strait North (HSN). The black contour is the present-day coastline provided by *cartopy*.

likely a coincidence. As an added dynamical complication, the ice streams can draw sediments from the same catchment (e.g., Hudson Strait and Cumberland Sound ice stream in Fig. 4.6).

On average, there are 13.4 ± 6.2 Hudson Strait ice stream surges and 11.7 ± 3.4 Hudson Strait sediment flux peaks per run (between 100 and 10 kyr BP). The duration and periodicity of the sediment flux peaks and surges differ by only 0.1 kyr (Table C.1). However, not all increases in Hudson Strait sediment flux correspond to an increase in mid-Hudson Strait ice flux (e.g., Fig. 4.7). Only ~ 48 % of sediment peaks overlap with at least one surge, and the total overlap (duration of mid-Hudson

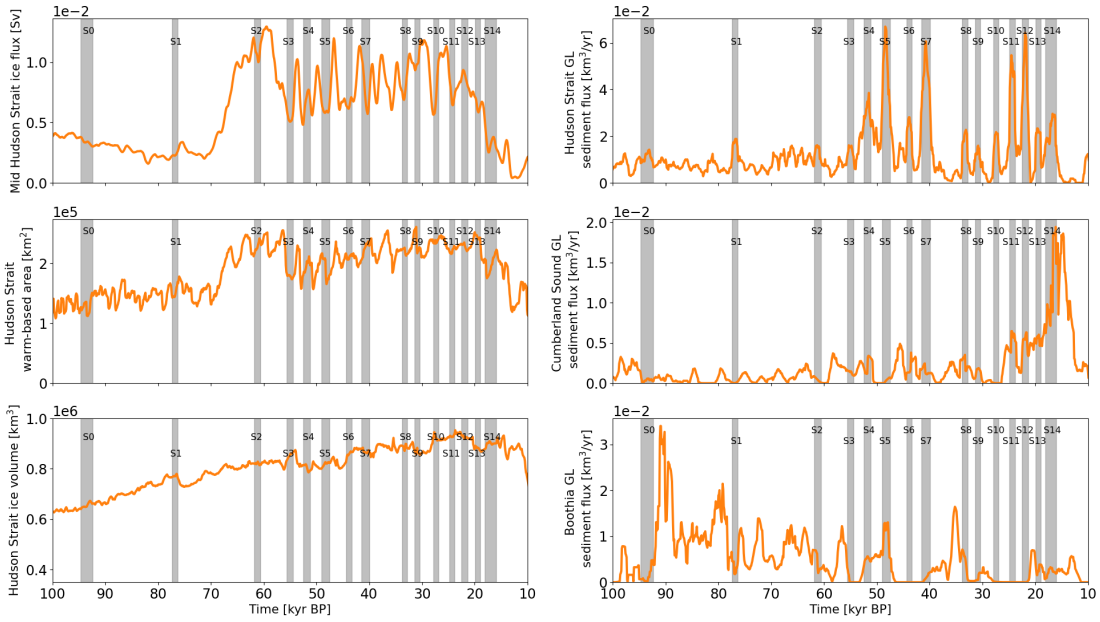

Figure 4.7: Time series of parameter vector 0. The shaded gray areas and black numbers mark the Hudson Strait sediment peaks as determined by the automated detection algorithm (Sec. 4.2.4). The Hudson Strait ice flux is determined at the flux gate marked with *HS* in Fig. 4.1. The Hudson Strait warm-based area and ice volume are calculated within the Hudson Strait mask (Fig. 4.1). The sediment fluxes shown in the 3 panels on the right represent the mean sediment flux across the grounding line within the corresponding areas in Fig. 4.1.

Strait ice velocity peaks and sediment peaks over duration of sediment peaks) is ~ 29 % (e.g., Fig. C.11). The delay between the ice flux increase in the mid-Hudson Strait and the Hudson Strait grounding line (order of centuries) can not explain this weak correlation between ice and sediment flux (order of millennia).

While at least a minimum grounding line ice flux is a prerequisite for sediment discharge, not every increase corresponds to a sediment flux peak (e.g., Fig. 4.8). Similarly, not every peak in englacial sediment thickness (controlled by englacial sediment transport and net sediment entrainment, which in turn depends on the effective pressure and the basal melt rate (Sec. 4.2.3)) leads to an increase in sediment flux (vertical lines in Fig. 4.8). Only the combination of increased englacial sediment thickness and

minimum grounding line ice flux leads to a significant sediment discharge.

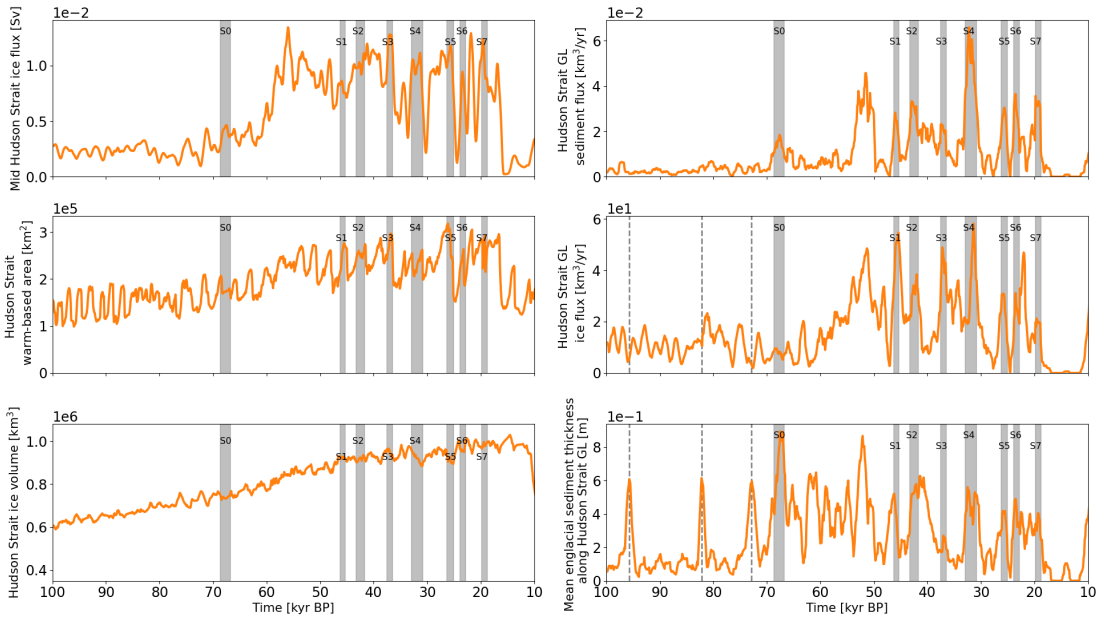

Figure 4.8: Time series of parameter vector 2. The ice flux across the Hudson Strait grounding line and the englacial sediment thickness along the Hudson Strait grounding line are calculated within the Hudson Strait area in Fig. 4.1. The dashed vertical lines are added for visual alignment. Otherwise as Fig. 4.7.

In general, the englacial sediment concentration along the Hudson Strait ice stream decreases due to sediment melt out (Fig. 4.5 and 4.6). Hudson Strait surges generally increase the thermal input from deformation work and basal sliding (Hank and Tarasov, 2023, in preparation). If the resulting increase in sediment melt out (Eq. 4.4) sufficiently reduces the englacial sediment thickness before the ice reaches the Hudson Strait grounding line, an increase in ice discharge occurs without a corresponding sediment flux peak. Therefore, our results indicate that determining HEs based on the mid-Hudson Strait ice flux will lead to flawed statistics.

As discussed in detail in Hank and Tarasov (2023, in preparation), a lower GHF

leads to the classic binge-purge surge pattern of the Hudson Strait ice stream (e.g., Fig. C.12). Since neither a near continuous ice stream with pre-Heinrich Event shutdowns nor the classic binge-purge mechanism can be ruled out, we also examine the sediment characteristics for a lower GHF. Overall, the lower GHF leads to fewer ($\sim$ 28 % of reference setup) but stronger Hudson Strait ice stream surges ($\sim$ 750 % increase in Hudson Strait ice volume change during a surge, Fig. C.6 and C.14).

Conversely, the number of sediment peaks, mean period, and mean duration based on the Hudson Strait sediment flux for the lower GHF are similar to the values of the GSM reference setup (Table C.2, Fig. 4.4 and C.13). Due to the smaller GHF, the warm-based area decreases (Fig. C.12), slightly reducing the overall englacial sediment volume in the Hudson Strait (the model has no sediment entrainment over cold-based regions) and the mean ice flux across the Hudson Strait grounding line (Fig. C.15). Consequently, the total sediment and ice discharge decrease for the smaller GHF (Table C.2). The total overlap between Hudson Strait surges and sediment peaks reduces to $\sim$ 13 %.

4.4 Discussion

Based on the results presented in Sec. 4.3, we discuss the research questions in the context of proxy constraints and previous modeling attempts.

Q_1 *How does the sediment distribution in the Hudson Strait ice drainage basin change throughout the last glacial cycle?*

Maps for present-day sediment thickness differ significantly, especially in Canada where data is sparse, and the associated uncertainties are large (Drew, 2023,

and references therein). For example, sediment thickness estimates in the Hudson Bay vary between < 5 and > 1500 m, prohibiting the validation of model results. We partially account for this uncertainty by analyzing the results of different initial sediment distributions and an ensemble with different sediment parameter values instead of just one parameter vector. While the initial sediment distribution has only minor effects on the englacial sediment thickness and sediment flux characteristics, better constraints on the present-day North American sediment distribution are required to minimize associated uncertainties.

In general, the sediment thickness decreases over time during the course of a glaciation in the Hudson Bay, Ungava Bay, and the catchment regions of ice streams. The sediment is transported from these regions and deposited along the ice streams and the ice sheet margin. Depending on the parameter vector in question, the sediment thickness at the Hudson Strait mouth can exceed 2 km by the end of the run, which is within the large bounds provided by the literature estimates.

Q_2 *How is the sediment distributed within the ice column?*

The englacial sediment concentration is highest within the basal layer (up to 50 %) and reduces significantly further up. The top layer (20.9 m center height) has generally < 5 %. The englacial sediment distribution modeled in the GSM is consistent with sediment thickness and concentration studies (Herron et al., 1979; Dowdeswell and Dowdeswell, 1989; Lawson et al., 1998; Knight et al., 2000). A constant 4 % sediment concentration throughout the whole ice column

(or iceberg), as, e.g., postulated in Fendrock et al. (2023), is very unlikely.

Better constraints on the present-day sediment discharge out of ice streams with comparable glaciological conditions and high-quality data of the sediment distribution within icebergs are required to improve sediment flux estimates during HEs.

Q_3 *What are likely bounds on the englacial sediment discharge out of the Hudson Strait, Cumberland Sound, and Boothia ice stream?*

On average, the mean Hudson Strait sediment flux peak duration and period agree with the literature estimates (Table C.2). However, the number of peaks is slightly too high. The sediment discharge out of the Cumberland Sound and Boothia ice stream is an order of magnitude smaller than the Hudson Strait sediment discharge. In line with sediment provenance studies (Hemming, 2004, and references therein) and the size of the ice drainage basins, the Hudson Strait ice stream is the main North American IRD provenance ($\sim$ 84 % of total sediment discharge, Table C.2). The average Hudson Strait sediment discharge in the GSM is $\sim$ 47 km^3, with minimum and maximum values of $\sim$ 9 and $\sim$ 329 km^3.

In comparison, the sediment volume based on Heinrich Layer thickness estimates varies between 187 and 2078 km^3 (831 ± 79 km^3 for an average Heinrich Layer, Sec. 4.3.1). Due to the different approaches used (constant sediment thickness within square box(es) vs. interpolation methods) and areas considered (especially regarding the cores with the thickest Heinrich Layers in the Labrador Sea), these estimates generally exceed the previously proposed 100 to

400 km^3 (Hemming, 2004).

While the largest modeled Hudson Strait sediment discharges are within proxy constraints (12 % of all peaks > 100 km^3), the average sediment discharge is an order of magnitude smaller. However, the Heinrich Layer sediment volume estimates are based on the assumption that all of the sediment within a Heinrich Layer is IRD (Heinrich Layer thickness estimates are based on top and bottom layer core depths). In sediment cores close to the Hudson Strait (generally containing the thickest Heinrich Layers), this is likely not the case (e.g., non-englacially transported sediments, Veiga-Pires and Hillaire-Marcel, 1999; Gibb et al., 2014; Hesse and Khodabakhsh, 2016). Therefore, the provided estimates might significantly overestimate the actual IRD volume. Different methods for identifying and quantifying IRD further complicate the interpretation (McKay et al., 2022).

Furthermore, the small sediment discharges ($\sim$ 9 km^3) identified by the automated detection algorithm used within this study decrease the modeled average sediment discharge but might not be recorded in sediment records from the North Atlantic. While there is some evidence for small events between HEs (e.g., Andrews and Barber, 2002), they are usually not considered in HE IRD volume estimates. Additionally, 5 sediment discharges are within proxy constraints for one parameter vector, demonstrating the breadth of sediment discharge across our ensemble and the resultant bound of process uncertainties. Acquiring additional high-quality ocean sediment data in the North Atlantic and a better understanding of the sediment entrainment, transport, and preser-

vation in icebergs is crucial for minimizing associated uncertainties.

Q_4 *How well does sediment discharge correlate with ice stream flux?*

In general, Hudson Strait ice stream surges occur more frequently and have a shorter duration than Hudson Strait sediment flux peaks. Due to the increased sediment melt out during surges, the total overlap between surges and sediment flux peaks is only ~ 29 %. Therefore, Hudson Strait ice stream surges in our experiments are not well correlated with sediment discharge and IRD deposition.

The average total ice discharge (Hudson Strait, Cumberland Sound, and Boothia ice stream) during a sediment peak is at the very lower end of literature estimates (Roberts et al., 2014, and references therein). Even the maximum total ice discharge during a sediment flux peak across the whole ensemble ($\sim 34.5 \cdot 10^4$ km^3) is well below the median of $75.0 \cdot 10^4$ km^3 in Roberts et al. (2014). However, proxy records do not necessarily show changes in sea surface salinity aligned with HEs (e.g., Hillaire-Marcel and de Vernal, 2008; Gibb et al., 2014). As such, the common association of IRD deposition in the North Atlantic with a large release of freshwater has unclear paleo data support. Furthermore, the small ice discharge during sediment peaks indicates that the timing of HEs within the coldest phases of the Dansgaard-Oeschger (DO) cycles is more complex than previously thought and needs further investigation.

Conclusions

The present study is the first modeling approach to directly determine HEs based on the sediment flux instead of the commonly used ice flux or ice thickness/volume. The duration and reoccurrence period of the identified HEs are within proxy constraints. The modeled sediment discharge during HEs ($\sim$ 56 km^3) tends to be smaller than IRD volume estimates but clearly identifies the Hudson Strait as the primary North American provenance ($\sim$ 84 % of total sediment discharge). The bulk of the englacial sediment is situated within a thin ($<$ 10 m) basal ice layer. While poorly constrained, different initial sediment distributions do not significantly affect the HE characteristics.

Our most significant result is that the timing of Hudson Strait ice stream surges is poorly correlated with Hudson Strait sediment flux peaks. Therefore, future HE modeling studies should refrain from using, e.g., the mid-Hudson Strait ice flux as a metric to identify HEs. This lack of correlation implies that the deposition of IRD in the North Atlantic is not representative of a large release of freshwater caused by a Hudson Strait surge.

Chapter 5

Conclusions

5.1 Summary

The present study aims to comprehensively determine the role of relevant system processes in a HE context, including but not limited to the processes involved in the theories discussed in Sec. 1.2.3. The numerical modeling was conducted with careful consideration and testing of numerical aspects and implementations. Model results are based on high-variance (with respect to ensemble parameters and surge characteristics) ensembles to partly address potential non-linear dependencies on ensemble parameters. Furthermore, this work incorporates the first HE experiments with a transient LGC climate forcing, global visco-elastic GIA solver, fully dynamical linked-cavity basal hydrology model, and fully coupled sediment model (Drew and Tarasov, 2022; Drew, 2023; Tarasov et al., 2024, in preparation). Here, the results presented in this study are discussed within the context of the research questions outlined in Sec. 1.4.

5.1.1 Numerical and discretization sensitivities

Instabilities within the glacial system, such as HEs, are challenging to robustly model given the highly non-linear processes involved. Therefore, differentiating numerical and discretization sensitivities from a physical response of the system is a key aspect of this work. Numerical sensitivities due to different convergence criteria are used to determine **M**inimum **N**umerical **E**rror **E**stimates (MNEEs). The MNEEs are then used as a threshold to determine the numerical significance of model results. However, this does not necessarily mean that the effect of system processes that lead to differences smaller than the MNEEs have no physical relevance, but rather that the physical response of the system might be hidden within the numerical sensitivities.

Even for an idealized North American geometry and climate representation, the MNEEs range up to 7 % for the GSM and 16 % for PISM. Since these numerical sensitivities occur in both the GSM and PISM, they are likely present (though with model-specific values) in other ice sheet models with similar approximations. Therefore, the determination of MNEEs or a comparable metric is essential to increase confidence in model results when modeling highly non-linear processes.

Discretization sensitivities are evident in the GSM and PISM. In general, the model results show a strong resolution dependence with convergence under systematic horizontal grid refinement. Incorporating an appropriate resolution-dependent basal temperature ramp that enables sub-freezing basal sliding reduces the resolution dependence and also has observational, experimental, theoretical and numerical motivation (e.g., Barnes et al., 1971; Shreve, 1984; Echelmeyer and Zhongxiang, 1987; Cuffey et al., 1999; McCarthy et al., 2017; Mantelli et al., 2019). It should therefore

be a standard part of ice sheet models. However, significant differences in surge characteristics remain between the two finest resolutions tested (6.25 and 3.15 km) even when using the resolution-dependent ramp.

5.1.2 Role of relevant system processes in a HE context

Considering the numerical and discretization sensitivities outlined above, this study examines the physical significance of relevant system processes on the HE duration, periodicity, and ice discharge (sediment discharge is discussed separately in Sec. 5.1.4).

The system processes discussed in the HE hypotheses (Sec. 1.2.3) include ice stream surge cycling, ice shelf dynamics (buttressing as well as ice shelf disintegration as IRD source), GIA, and sub-surface ocean warming. In line with proxy evidence suggesting an ice-free Labrador Sea during HEs (Hillaire-Marcel et al., 1994; Hesse et al., 1999; De Vernal et al., 2000; Gibb et al., 2014) and other modeling studies (e.g., Schannwell et al., 2023), no large ice shelves develop in the Labrador Sea, leading to minor buttressing. Furthermore, the small ice shelves imply only limited ice and IRD fluxes are possible under ice shelf disintegration. Similarly, sub-surface ocean warming pulses do not significantly affect the HE characteristics. As the GSM does not include an ocean circulation and sea ice model, further sensitivity experiments with respect to the ice shelf size were conducted. Model results indicate that extreme calving restrictions are required to consistently obtain large ice shelves in the Labrador Sea.

By a process of elimination, ice stream surge cycling is therefore the most likely mechanism of the individual hypotheses discussed for driving HEs (Sec. 1.2.3). However, ice stream surge cycling alone can not explain the apparent approximate syn-

chronization of HEs with the coldest part of the Bond cycles. The modeling experiments show that the exact timing of ice stream surging has some sensitivity to the presence/absence of fringing ice shelves and sub-surface ocean warming. However, an increase in mid-Hudson Strait ice flux directly linked to ocean forcings is only apparent when applying a 2°C increase in ocean temperature during HEs and otherwise completely inhibiting calving. The exact timing of Hudson Strait surges for less extreme ocean forcing experiments is only indirectly affected by the ocean forcing through changes in ice sheet evolution (as a consequence of the ocean forcing).

While surge characteristics are generally not sensitive to different GIA models, the resultant change in overall ice configuration can foster new surges.

The largest differences in surge characteristics, however, occur for processes affecting the basal friction. For example, the inclusion of basal hydrology increases the surge duration and ice volume change. The largest physical control of basal friction is the thermal energy balance at the bed, which controls whether the ice is frozen to the bed or able to slide along it with or without subglacial till deformation. In line with this (especially given input uncertainties), a key takeaway of this study (that has to date not been raised in published literature) is the high sensitivity of surge characteristics to changes in the poorly constrained GHF in the Hudson Bay and Hudson Strait. The overall surge pattern changes from the classic binge-purge mechanism to an almost continuously active ice stream when increasing the GHF within inferential bounds. For the binge-purge mode, the number of strong surges during MIS3 increases, which more closely resembles the timing of Heinrich Layers in sediment cores.

5.1.3 Correlation between sediment and ice flux

All HE hypotheses discussed within this study (Sec. 1.2.3) rely on the assumption that ice flux correlates reasonably well with the sediment flux. While internally driven ice stream surges are generally capable of reproducing the HE duration, periodicity, and ice discharge within proxy constraints, they only show a weak correlation to the sediment flux in the numerical experiments with the fully coupled sub-glacial sediment processes model. Furthermore, sediment flux peaks only occur when there is at least a minimum Hudson Strait grounding line ice flux and a significant englacial sediment thickness along the Hudson Strait grounding line. A high ice flux across the grounding line alone is not indicative of the sediment discharge. Therefore, another key takeaway is that the Hudson Strait sediment flux instead of the ice flux and/or ice thickness/volume should be used to determine HEs in future HE modeling studies.

The average ice discharge during HEs (identified based on the sediment flux) is at the very lower end of literature estimates (Roberts et al., 2014, and references therein). As such, the implications of the weak correlation between ice and sediment flux on the climatic impact of HEs and their occurrence within the coldest phases of DO cycles needs further examination.

5.1.4 Sediment discharge

Since HEs are identified by layers of IRD in the North Atlantic, the simulated sediment discharge during a sediment flux peak is of key interest. Based on geological provenance studies (Hemming, 2004, and references therein) and the size of the drainage basins, the primary North American provenance is usually inferred to be

the Hudson Strait. In line with this rational, the modeled average Hudson Strait sediment discharge is an order of magnitude larger than the contributions from the Cumberland Sound and Boothia ice streams. The modeled Hudson Strait sediment discharge during HEs varies between ~ 9 and ~ 329 km^3 with an average discharge of ~ 47 km^3.

Previous IRD volume estimates range from 100 to 400 km^3 (Hemming, 2004). Due to the different interpolation methods used and the large uncertainties associated with Heinrich Layer thickness estimates (up to 60 cm for the same core and layer), the IRD volume estimates presented within this study range from 187 to 2078 km^3 (based on minimum and maximum sediment layer thickness estimates and 3 different interpolation methods).

The average total (Hudson Strait, Cumberland Sound, and Boothia ice stream) sediment discharge modeled in the GSM (~ 56 km^3) differs significantly from the IRD volume estimate (mean of 3 different interpolation methods when using an average sediment layer thickness is 831 ± 79 km^3). Part of this difference might be explained by IRD contributions from European provenances and an overestimation of the actual IRD concentration in the Heinrich Layers (especially for the thickest layers just off the Hudson Strait). Additionally, the automated sediment flux detection algorithm also detects small events that decrease the modeled average sediment discharge but might not be recorded in sediment records in the North Atlantic. While there is some evidence supporting the occurrence of small events between HEs (e.g., Andrews and Barber, 2002), these events are typically not taken into account in HE IRD volume estimates. Further research, in particular with respect to high-quality IRD records and the representation of sedimentary processes in ice sheet models (e.g., the inclusion

of a frozen-fringe mechanism, Meyer et al., 2019)), is required to determine the exact cause of this mismatch.

5.2 Key findings

This section summarizes the key findings of this thesis outlined in Sec. 5.1 by directly addressing the research questions (Sec. 1.4).

RQ_1 How accurately can a numerical ice sheet model (North American model domain, transient LGC climate forcing, no additional HE triggers) capture the HE characteristics observed in proxy records?

A key takeaway of this thesis are the numerical and discretization sensitivities that must be considered when modeling ice sheet instabilities such as HEs. Uncertainties related to boundary conditions (e.g., GHF) further complicate the interpretation of model results. Nevertheless, the GSM is able to capture the duration and periodicity of HEs within proxy constraints. However, depending on the model setup, HEs tend to occur earlier than indicated by the IRD layers.

RQ_2 What are the relative roles of different aspects of the interconnected glacial system in HEs?

Based on the results presented here, ice stream surge cycling synchronized to the coldest phases of Bond cycles by ocean forcings is the most likely HE mechanism. Furthermore, HEs are sensitive to topography, GIA, basal hydrology, and thermal processes at the ice sheet bed (e.g., sub-temperate basal sliding).

RQ_3 How much sediment is discharged during an average HE, and what are the key North American provenances?

Model results indicate the Hudson Strait as primary North American provenance with an average sediment discharge of ~ 47 km^3.

RQ_4 How well correlated is sediment discharge with the occurrence of ice stream surge cycling?

The occurrence of Heinrich Layers within the coldest phases of the Bond cycles is usually attributed to a change in freshwater flux and the consequential climatic change. However, this argument is based on the assumption that the sediment and ice discharge are well correlated. Therefore, the final and arguably most important takeaway is the weak correlation between the ice and sediment flux (~ 29 % overlap) and its implications on the climatic footprint of HEs.

5.3 Future work

The next steps required to advance the understanding of HEs are discussed here. On the data side, better constraints on the North American sediment distribution and GHF, in particular in the Hudson Bay and Hudson Strait are essential to validate model results (e.g., comparison of present day sediment distrubtions and deep (> 3 km) borehole measurements). High-quality ocean sediment cores from the North Atlantic are required to better constrain the sediment volume deposited during individual HEs. Observations of sediment discharge out of ice streams with comparable glaciological conditions and sediment distribution within icebergs are needed to im-

prove confidence in the modeled sediment flux.

To improve the understanding of englacial sediment transport (in icebergs) to the North Atlantic, an ice sheet model with a fully dynamical sediment model (such as the GSM) would ideally be coupled to an ocean/iceberg model. However, as coupling of an ice sheet and ocean model likely remains computationally unfeasible for ensemble-based LGC sensitivity experiments in the foreseeable future, the sediment discharge and englacial sediment concentration of individual HEs modeled by, e.g., the GSM can be used as input for an ocean/iceberg model.

Concerning the ice sheet model, determining discretization sensitivities remains important. Therefore, future validation work, e.g., increasing the horizontal grid resolution below 3.125 km (once computationally feasible), is required to increase the confidence in model results.

While the consideration of MNEEs is useful for the purpose of this study and marks a significant step forward, MNEEs fail to capture uncertainties due to physical processes not included in the models. As the largest source of differences in surge characteristics is from processes affecting the basal friction, additional sensitivity experiments to determine the effect of various basal sliding laws are required to increase confidence in model results and advance the understanding of HEs. To resolve any issues concerning grounding line stability, tests are needed with a dynamic grid discretization (e.g., Cornford et al., 2013) and different approximations of the Stokes equations.

Overall, the results presented in this study indicate a critical need to better understand the controls on sediment discharge in the Hudson Strait. Due to the weak correlation between Hudson Strait surges (examined in detail in this study) and sedi-

ment discharge, a study comprehensively examining the effects of relevant system processes (e.g., through sensitivity experiments), including the proposed HE hypotheses (Sec. 1.2.3) and cold-based sediment entrainment mechanisms currently not implemented in the GSM (e.g., frozen-fringe, Meyer et al., 2019), on sediment discharge out of the Hudson Strait is required. However, the key outstanding research question is the dynamical source of the synchronization of North American and European sediment provenances and the timing of high sediment discharge within the coldest phases of the DO cycles.

Bibliography

Alley, R. B. and MacAyeal, D. R.: Ice-rafted debris associated with binge/purge oscillations of the Laurentide Ice Sheet, Paleoceanography, 9, 503–511, https://doi.org/https://doi.org/10.1029/94PA01008, 1994.

Alley, R. B., Anandakrishnan, S., Christianson, K., Horgan, H. J., Muto, A., Parizek, B. R., Pollard, D., and Walker, R. T.: Oceanic forcing of ice-sheet retreat: West Antarctica and more, Annual Review of Earth and Planetary Sciences, 43, 207–231, https://doi.org/10.1146/annurev-earth-060614-105344, 2015.

Alvarez-Solas, J., Robinson, A., Montoya, M., and Ritz, C.: Iceberg discharges of the last glacial period driven by oceanic circulation changes, Proceedings of the National Academy of Sciences of the United States of America, 110, 16 350–16 354, https://doi.org/10.1073/pnas.1306622110, 2013.

Andrews, J. T.: Icebergs and iceberg rafted detritus (IRD) in the North Atlantic: Facts and assumptions, Oceanography, 13, 100–108, https://doi.org/10.5670/oceanog.2000.19, 2000.

Andrews, J. T. and Barber, D. C.: Dansgaard-oeschger events: Is there a signal off the hudson strait ice stream?, Quaternary Science Reviews, 21, 443–454, https://doi.org/10.1016/S0277-3791(01)00073-7, 2002.

Andrews, J. T. and MacLean, B.: Hudson Strait ice streams: A review of stratigraphy, chronology and links with North Atlantic Heinrich events, Boreas, 32, 4–17, https://doi.org/10.1080/03009480310001010, 2003.

Andrews, J. T. and Voelker, A. H.: "Heinrich events" (& sediments): A history of terminology and recommendations for future usage, Quaternary Science Reviews, 187, 31–40, https://doi.org/10.1016/j.quascirev.2018.03.017, 2018.

Andrews, J. T., Barber, D. C., Jennings, A. E., Eberl, D. D., Maclean, B., Kirby, M. E., and Stoner, J. S.: Varying sediment sources (Hudson Strait, Cumberland Sound, Baffin Bay) to the NW Labrador Sea slope between and during Heinrich events 0 to 4, Journal of Quaternary Science, 27, 475–484, https://doi.org/10.1002/jqs.2535, 2012.

Arakawa, A. and Lamb, V. R.: Computational Design of the Basic Dynamical Processes of the UCLA General Circulation Model, in: General Circulation Models of the Atmosphere, edited by CHANG, J., vol. 17 of *Methods*

in Computational Physics: Advances in Research and Applications, pp. 173–265, Elsevier, https://doi.org/https://doi.org/10.1016/B978-0-12-460817-7.50009-4, 1977.

Bahadory, T. and Tarasov, L.: LCice 1.0-a generalized Ice Sheet System Model coupler for LOVECLIM version 1.3: Description, sensitivities, and validation with the Glacial Systems Model (GSM version D2017.aug17), Geoscientific Model Development, 11, 3883–3902, https://doi.org/10.5194/gmd-11-3883-2018, 2018.

Barnes, P., Tabor, D., and Walker, J. C. F.: The Friction and Creep of Polycrystalline Ice, Proceedings of the Royal Society of London. Series A, Mathematical and Physical Sciences, 324, 127–155, URL `http://www.jstor.org/stable/77933`, 1971.

Bassis, J. N., Petersen, S. V., and Mac Cathles, L.: Heinrich events triggered by ocean forcing and modulated by isostatic adjustment, Nature, 542, 332—334, https://doi.org/10.1038/nature21069, 2017.

Bazin, L., Landais, A., Lemieux-Dudon, B., Toyé Mahamadou Kele, H., Veres, D., Parrenin, F., Martinerie, P., Ritz, C., Capron, E., Lipenkov, V., Loutre, M.-F., Raynaud, D., Vinther, B., Svensson, A., Rasmussen, S. O., Severi, M., Blunier, T., Leuenberger, M., Fischer, H., Masson-Delmotte, V., Chappellaz, J., and Wolff, E.: An optimized multi-proxy, multi-site Antarctic ice and gas orbital chronology (AICC2012): 120 - 800 ka, Climate of the Past, 9, 1715–1731, https://doi.org/10.5194/cp-9-1715-2013, 2013.

Benn, D. I., Fowler, A. C., Hewitt, I., and Sevestre, H.: A general theory of glacier surges, Journal of Glaciology, 65, 701–716, https://doi.org/10.1017/jog.2019.62, 2019.

Blackwell, D. and Richards, M.: Geothermal Map of North America, AAPG Map, scale 1:6,500,000, Product Code 423, URL `https://www.smu.edu/-/media/Site/Dedman/Academics/Programs/Geothermal-Lab/Graphics/Geothermal_MapNA_7x10in.gif`, 2004.

Blunier, T. and Brook, E. J.: Timing of Millennial-Scale Climate Change in Antarctica and Greenland During the Last Glacial Period, Science, 291, 109–112, https://doi.org/10.1126/science.291.5501.109, 2001.

Bond, G., Heinricht, H., Broecker, W., Labeyrie, L., Mcmanus, J., Andrews, J., Huonll, S., Jantschik, R., Clasen, S., Simet, C., Tedesco, K., Klas, M., Bonanitt, G., and Ivy, S.: Evidence for massive discharges of icebergs into the North Atlantic ocean during the last glacial period, 360, 1668–1672, https://doi.org/https://doi.org/10.1038/360245a0, 1992.

Bond, G., Broecker, W., Johnsen, S., McManus, J., Labeyrie, L., Jouzel, J., and Bonani, G.: Correlations between Climate Records from North Atlantic Sediments and Greenland Ice, Nature, 365, 143–147, https://doi.org/10.1038/365143a0, 1993.

Bond, G. C. and Lotti, R.: Iceberg Discharges Into the North Atlantic on Millennial Time Scales During the Last Glaciation, Science, 267, 1005–1010, URL `http://www.jstor.org/stable/2886290`, 1995.

Book, C., Hoffman, M. J., Kachuck, S. B., Hillebrand, T. R., Price, S. F., Perego, M., and Bassis, J. N.: Stabilizing effect of bedrock uplift on retreat of Thwaites Glacier, Antarctica, at centennial timescales, Earth and Planetary Science Letters, 597, 117 798, https://doi.org/10.1016/j.epsl.2022.117798, 2022.

Bradley, R.: PALEOCLIMATOLOGY (3rd edition), 2014.

Bramlette, M. N. and Bradley, W. H.: Geology and Biology of North Atlantic Deep-Sea Cores: Lithology and geologic interpretations, Geological Survey Professional Paper, 196-A, 1940.

Brinkerhoff, D. J. and Johnson, J. V.: Dynamics of thermally induced ice streams simulated with a higher-order flow model, Journal of Geophysical Research F: Earth Surface, 120, 1743–1770, https://doi.org/10.1002/2015JF003499, 2015.

Broecker, W., Bond, G., Klas, M., Clark, E., and McManus, J.: Origin of the northern Atlantic's Heinrich events, Climate Dynamics, 6, 265–273, https://doi.org/10.1007/BF00193540, 1992.

Bueler, E. and Brown, J.: Shallow shelf approximation as a "sliding law" in a thermomechanically coupled ice sheet model, Journal of Geophysical Research: Earth Surface, 114, https://doi.org/https://doi.org/10.1029/2008JF001179, 2009.

Bueler, E. and Van Pelt, W.: Mass-conserving subglacial hydrology in the Parallel Ice Sheet Model version 0.6, Geoscientific Model Development, 8, 1613–1635, https://doi.org/10.5194/gmd-8-1613-2015, 2015.

Buizert, C. and Schmittner, A.: Southern Ocean control of glacial AMOC stability and Dansgaard-Oeschger interstadial duration, Paleoceanography, 30, 1595–1612, https://doi.org/10.1002/2015PA002795, 2015.

Buizert, C., Sigl, M., Severi, M., Markle, B. R., Wettstein, J. J., McConnell, J. R., Pedro, J. B., Sodemann, H., Goto-Azuma, K., Kawamura, K., Fujita, S., Motoyama, H., Hirabayashi, M., Uemura, R., Stenni, B., Parrenin, F. r., He, F., Fudge, T. J., and Steig, E. J.: Abrupt ice-age shifts in southern westerly winds and Antarctic climate forced from the north, Nature, 563, 681–685, https://doi.org/10.1038/s41586-018-0727-5, 2018.

Calov, R. and Greve, R.: ISMIP HEINO. Ice Sheet Model Intercomparison Project - Heinrich Event INtercOmparison, pp. 1–15, URL `http://www.pik-potsdam.de/~calov/heino/he_setup_2006_11_02.pdf`, 2006.

Calov, R., Ganopolski, A., Petoukhov, V., Claussen, M., and Greve, R.: Large-scale instabilities of the Laurentide ice sheet simulated in a fully coupled climate-system model, Geophysical Research Letters, 29, 1–4, https://doi.org/10.1029/2002GL016078, 2002.

Calov, R., Greve, R., Abe-Ouchi, A., Bueler, E., Huybrechts, P., Johnson, J. V., Pattyn, F., Pollard, D., Ritz, C., Saito, F., and Tarasov, L.: Results from the Ice-Sheet Model Intercomparison Project-Heinrich Event INtercOmparison (ISMIP HEINO), Journal of Glaciology, 56, 371–383, https://doi.org/10.3189/002214310792447789, 2010.

Chapman, M. R. and Shackleton, N. J.: Global ice-volume fluctuations, North Atlantic ice-rafting events, and deep-ocean circulation changes between 130 and 70 ka, Geology, 27, 795–798, https://doi.org/10.1130/0091-7613(1999)027⟨0795:GIVFNA⟩2.3.CO;2, 1999.

Clement, A. C. and Peterson, L. C.: Mechanisms of abrupt climate change of the last glacial period, Reviews of Geophysics, 46, https://doi.org/10.1029/2006RG000204, 2008.

Cornford, S. L., Martin, D. F., Graves, D. T., Ranken, D. F., Le Brocq, A. M., Gladstone, R. M., Payne, A. J., Ng, E. G., and Lipscomb, W. H.: Adaptive mesh, finite volume modeling of marine ice sheets, Journal of Computational Physics, 232, 529–549, https://doi.org/https://doi.org/10.1016/j.jcp.2012.08.037, 2013.

Courant, R., Friedrichs, K., and Lewy, H.: Über die partiellen Differenzengleichungen der mathematischen Physik, Mathematische Annalen, 100, 32–74, https://doi.org/10.1007/BF01448839, 1928.

Cuesta-Valero, F. J., García-García, A., Beltrami, H., González-Rouco, J. F., and García-Bustamante, E.: Long-term global ground heat flux and continental heat storage from geothermal data, Climate of the Past, 17, 451–468, https://doi.org/10.5194/cp-17-451-2021, 2021.

Cuffey, K. M., Conway, H., Hallet, B., Gades, A. M., and Raymond, C. F.: Interfacial water in polar glaciers and glacier sliding at -17 °C, Geophysical Research Letters, 26, 751–754, https://doi.org/10.1029/1999GL900096, 1999.

Dalton, A. S., Stokes, C. R., and Batchelor, C. L.: Evolution of the Laurentide and Innuitian ice sheets prior to the Last Glacial Maximum (115 ka to 25 ka), Earth-Science Reviews, 224, 103 875, https://doi.org/10.1016/j.earscirev.2021.103875, 2022.

Davies, J. H.: Global map of solid Earth surface heat flow, Geochemistry, Geophysics, Geosystems, 14, 4608–4622, https://doi.org/10.1002/ggge.20271, 2013.

De Vernal, A., Hillaire-Marcel, C., Turon, J. L., and Matthiessen, J.: Reconstruction of sea-surface temperature, salinity, and sea-ice cover in the northern North Atlantic during the last glacial maximum based on dinocyst assemblages, Canadian Journal of Earth Sciences, 37, 725–750, https://doi.org/10.1139/cjes-37-5-725, 2000.

Deblonde, G., Peltier, W. R., and Hyde, W. T.: Simulations of continental ice sheet growth over the last glacial-interglacial cycle: Experiments with a one level seasonal energy balance model including seasonal ice albedo feedback, 98, 37–55, 1992.

Depoorter, M. A., Bamber, J. L., Griggs, J. A., Lenaerts, J. T., Ligtenberg, S. R., Van Den Broeke, M. R., and Moholdt, G.: Calving fluxes and basal melt rates of Antarctic ice shelves, Nature, 502, 89–92, https://doi.org/10.1038/nature12567, 2013.

Dowdeswell, J. A. and Dowdeswell, E. K.: Debris in icebergs and rates of glaci-marine sedimentation: observations from Spitsbergen and a simple model, Journal of Geology, 97, 221–231, https://doi.org/10.1086/629296, 1989.

Drew, M.: The role of fully coupled ice sheet basal processes in quaternary glacial cycles, Ph.D. thesis, https://doi.org/10.48336/74Z6-9585, 2023.

Drew, M. and Tarasov, L.: Surging of a Hudson Strait Scale Ice Stream: Subglacial hydrology matters but the process details don't, The Cryosphere Discussions, 2022, 1–41, https://doi.org/10.5194/tc-2022-226, 2022.

Dutton, A., Carlson, A. E., Long, A. J., Milne, G. A., Clark, P. U., DeConto, R., Horton, B. P., Rahmstorf, S., and Raymo, M. E.: Sea-level rise due to polar ice-sheet mass loss during past warm periods, Science, 349, https://doi.org/10.1126/science.aaa4019, 2015.

Echelmeyer, K. and Zhongxiang, W.: Direct Observation of Basal Sliding and Deformation of Basal Drift at Sub-Freezing Temperatures, Journal of Glaciology, 33, 83–98, https://doi.org/10.3189/s0022143000005396, 1987.

Enderlin, E. M. and Howat, I. M.: Submarine melt rate estimates for floating termini of Greenland outlet glaciers (2000-2010), Journal of Glaciology, 59, 67–75, https://doi.org/10.3189/2013JoG12J049, 2013.

Fairbridge, R. W.: Climatology of a glacial cycle, Quaternary Research, 2, 283 – 302, https://doi.org/https://doi.org/10.1016/0033-5894(72)90049-X, 1972.

Fendrock, M., Condron, A., and McGee, D.: Modeling the Production of Heinrich Layers With a Sediment-Enabled Iceberg Model, Paleoceanography and Paleoclimatology, 38, 1–12, https://doi.org/10.1029/2022pa004583, 2023.

Flowers, G. E., Björnsson, H., and Pálsson, F.: New insights into the subglacial and periglacial hydrology of Vatnajökull, Iceland, from a distributed physical model, Journal of Glaciology, 49, 257–270, https://doi.org/10.3189/172756503781830827, 2003.

Fowler, A. C.: Sub-Temperate Basal Sliding, Journal of Glaciology, 32, 3–5, https://doi.org/10.3189/S0022143000006808, 1986.

Fowler, A. C. and Johnson, C.: Hydraulic run-away: a mechanism for thermally regulated surges of ice sheets, Journal of Glaciology, 41, 554–561, https://doi.org/10.3189/S002214300003478X, 1995.

Fowler, A. C. and Schiavi, E.: A theory of ice-sheet surges, Journal of Glaciology, 44, 104–118, https://doi.org/10.3189/s0022143000002409, 1998.

Gandy, N., Gregoire, L. J., Ely, J. C., Cornford, S. L., Clark, C. D., and Hodgson, D. M.: Exploring the ingredients required to successfully model the placement, generation, and evolution of ice streams in the British-Irish Ice Sheet, Quaternary Science Reviews, 223, 105 915, https://doi.org/10.1016/j.quascirev.2019.105915, 2019.

Geological Survey of Canada: Surficial Geology of Canada / Géologie des Formations Superficielles du Canada, https://doi.org/10.4095/295462, https://doi.org/10.4095/295462, open Access, 2014.

Gibb, O. T., Hillaire-Marcel, C., and de Vernal, A.: Oceanographic regimes in the northwest Labrador Sea since Marine Isotope Stage 3 based on dinocyst and stable isotope proxy records, Quaternary Science Reviews, 92, 269–279, https://doi.org/10.1016/j.quascirev.2013.12.010, 2014.

Goutorbe, B., Poort, J., Lucazeau, F., and Raillard, S.: Global heat flow trends resolved from multiple geological and geophysical proxies, Geophysical Journal International, 187, 1405–1419, https://doi.org/10.1111/j.1365-246X.2011.05228.x, 2011.

Greve, R., Takahama, R., and Calov, R.: Simulation of large-scale ice-sheet surges: The ISMIP HEINO experiments, Polar Meteorology and Glaciology, pp. 1–15, URL http://hdl.handle.net/2115/30205, 2006.

Grousset, F. E., Labeyrie, L., Sinko, J. a., Bond, G., Duprat, J., and Cortijo, E.: Patterns of Ice-Rafted Detritus in the Glacial North Atlantic (40-55°N), Atlantic, 8, 175–192, https://doi.org/10.1029/92PA02923, 1993.

Gwiazda, R., Hemming, S., and Broecker, W.: Provenance of icebergs during Heinrich Event 3 and the contrast to their sources during other Heinrich episodes, Paleoceanography, 11, 371–378, https://doi.org/10.1029/96PA01022, 1996a.

Gwiazda, R., Hemming, S., and Broecker, W.: Provenance of icebergs during Heinrich Event 3 and the contrast to their sources during other Heinrich episodes, Paleoceanography, 11, 371–378, https://doi.org/10.1029/96PA01022, 1996b.

Hank, K.: Supplementary material for "The comparative role of system processes in Hudson Strait ice stream cycling: a comprehensive model-based test of Heinrich event hypotheses", https://doi.org/10.5281/zenodo.10214928, 2023a.

Hank, K.: Supplementary material for "Numerical issues in modeling thermally and hydraulically driven ice stream surge cycling", https://doi.org/10.5281/zenodo.7905404, 2023b.

Hank, K. and Tarasov, L.: The comparative role of system processes in a Heinrich Event context: a comprehensive model-based test of Heinrich event hypotheses, 2023.

Hank, K., Tarasov, L., and Mantelli, E.: Modeling sensitivities of thermally and hydraulically driven ice stream surge cycling, Geoscientific Model Development, 16, 5627–5652, https://doi.org/10.5194/gmd-16-5627-2023, 2023.

Heinrich, H.: Origin and consequences of cyclic ice rafting in the Northeast Atlantic Ocean during the past 130,000 years, Quaternary Research, 29, 142–152, https://doi.org/10.1016/0033-5894(88)90057-9, 1988.

Hemming, S.: Heinrich events: Massive late Pleistocene detritus layers of the North Atlantic and their global climate imprint, Reviews of Geophysics - REV GEOPHYS, 42, https://doi.org/10.1029/2003RG000128, 2004.

Herron, S., Hoar, and Langway, C. C.: The Debris-Laden Ice at the Bottom of the Greenland Ice Sheet, Journal of Glaciology, 23, 193–207, https://doi.org/10.3189/S002214300002983X, 1979.

Hesse, R. and Khodabakhsh, S.: Anatomy of Labrador Sea Heinrich layers, Marine Geology, 380, 44–66, https://doi.org/10.1016/j.margeo.2016.05.019, 2016.

Hesse, R., Klauck, I., Khodabakhsh, S., and Piper, D.: Continental slope sedimentation adjacent to an ice margin. III. The upper Labrador Slope, Marine Geology, 155, 249–276, https://doi.org/10.1016/S0025-3227(98)00054-1, 1999.

Hicock, S. R., Lian, O. B., and Mathewes, R. W.: 'Bond cycles' recorded in terrestrial Pleistocene sediments of southwestern British Columbia, Canada, Journal of Quaternary Science, 14, 443–449, https://doi.org/10.1002/(SICI)1099-1417(199908)14:5⟨443::AID-JQS459⟩3.0.CO;2-6, 1999.

Hillaire-Marcel, C. and de Vernal, A.: Stable isotope clue to episodic sea ice formation in the glacial North Atlantic, Earth and Planetary Science Letters, 268, 143–150, https://doi.org/10.1016/j.epsl.2008.01.012, 2008.

Hillaire-Marcel, C., De Vernal, A., Bilodeau, G., and Wu, G.: Isotope stratigraphy, sedimentation rates, deep circulation, and carbonate events in the Labrador Sea during the last ˜200 ka, Canadian Journal of Earth Sciences, 31, 63–89, https://doi.org/10.1139/e94-007, 1994.

Hindmarsh, R. C.: Consistent generation of ice-streams via thermo-viscous instabilities modulated by membrane stresses, Geophysical Research Letters, 36, 1–6, https://doi.org/10.1029/2008GL036877, 2009.

Hodell, D. and Channell, J.: Mode transitions in Northern Hemisphere glaciation: Co-evolution of millennial and orbital variability in Quaternary climate, Climate of the Past, 12, 1805–1828, https://doi.org/10.5194/cp-12-1805-2016, 2016.

Hodell, D. and Curtis, J.: Oxygen and carbon isotopes of detrital carbonate in North Atlantic Heinrich Events, Marine Geology - MAR GEOLOGY, 256, 30–35, https://doi.org/10.1016/j.margeo.2008.09.010, 2008.

Hodell, D., Evans, H., Channell, J., and Curtis, J.: Phase relationships of North Atlantic ice-rafted debris and surface-deep climate proxies during the last glacial period, Quaternary Science Reviews, 29, 3875–3886, https://doi.org/10.1016/j.quascirev.2010.09.006, 2010.

Hulbe, C.: An ice shelf mechanism for Heinrich layer production, Paleoceanography, 12, 711–717, https://doi.org/10.1029/97PA02014, 1997.

Hulbe, C. L., MacAyeal, D. R., Denton, G. H., Kleman, J., and Lowell, T. V.: Catastrophic ice shelf breakup as the source of Heinrich event icebergs, Paleoceanography, 19, n/a–n/a, https://doi.org/10.1029/2003pa000890, 2004.

IPCC: IPCC, 2023: Climate Change 2023: Synthesis Report, Summary for Policymakers. Contribution of Working Groups I, II and III to the Sixth Assessment Report of the Intergovernmental Panel on Climate Change [Core Writing Team, H. Lee and J. Romero (eds.)]. IPCC, Geneva, Switzerland., https://doi.org/10.59327/ipcc/ar6-9789291691647.001, 2023.

Jones, R. W.: Foraminifera and their applications, https://doi.org/10.1017/CBO9781139567619, 2014.

Joughin, I., Smith, B. E., Howat, I. M., Floricioiu, D., Alley, R. B., Truffer, M., and Fahnestock, M.: Seasonal to decadal scale variations in the surface velocity of Jakobshavn Isbrae, Greenland: Observation and model-based analysis, Journal of Geophysical Research: Earth Surface, 117, 1–20, https://doi.org/10.1029/2011JF002110, 2012.

Joughin, I., Smith, B. E., Shean, D. E., and Floricioiu, D.: Brief communication: Further summer speedup of Jakobshavn Isbræ, Cryosphere, 8, 209–214, https://doi.org/10.5194/tc-8-209-2014, 2014.

Kaspi, Y., Sayag, R., and Tziperman, E.: A "triple sea-ice state" mechanism for the abrupt warming and synchronous ice sheet collapses during Heinrich events, Paleoceanography, 19, 1–12, https://doi.org/10.1029/2004PA001009, 2004.

K.M. Cuffey and W.S.B. Paterson.: The Physics of Glaciers, Butterworth-Heinemann/Elsevier, Burlington, MA, 4th edn., 2010.

Knight, P. G., Patterson, C. J., Waller, R. I., Jones, A. P., and Robinson, Z. P.: Preservation of basal-ice sediment texture in ice-sheet moraines, Quaternary Science Reviews, 19, 1255–1258, https://doi.org/10.1016/S0277-3791(00)00091-3, 2000.

Kyrke-Smith, T. M., Katz, R. F., and Fowler, A. C.: Subglacial hydrology and the formation of ice streams, Proceedings of the Royal Society A: Mathematical, Physical and Engineering Sciences, 470, 20130 494, https://doi.org/10.1098/rspa.2013.0494, 2014.

Larour, E., Rignot, E., Seroussi, H., and Morlighem, M.: Ice sheet modeling, URL `https://issm.jpl.nasa.gov/documentation/icesheetmodeling/`, 2020.

Laske, G. and Masters, G.: A Global Digital Map of Sediment Thickness, EOS Trans., 78, F483, 1997.

Lauterbach, S., Andersen, N., Wang, Y. V., Blanz, T., Larsen, T., and Schneider, R. R.: An ˜130 kyr Record of Surface Water Temperature and δ18O From the Northern Bay of Bengal: Investigating the Linkage Between Heinrich Events and Weak Monsoon Intervals in Asia, Paleoceanography and Paleoclimatology, 35, 1–17, https://doi.org/10.1029/2019PA003646, 2020.

Lawson, D. E., Strasser, J. C., Evenson, E. B., Alley, R. B., Larson, G. J., and Arcone, S. A.: Glaciohydraulic supercooling: a freeze-on mechanism to create stratified, debris-rich basal ice: I. Field evidence, Journal of Glaciology, 44, 547–562, https://doi.org/10.3189/S0022143000002069, 1998.

Lazeroms, W. M., Jenkins, A., Hilmar Gudmundsson, G., and Van De Wal, R. S.: Modelling present-day basal melt rates for Antarctic ice shelves using a parametrization of buoyant meltwater plumes, Cryosphere, 12, 49–70, https://doi.org/10.5194/tc-12-49-2018, 2018.

Lehman, S. J.: Ice sheets, wayward winds and sea change, Nature, https://doi.org/10.1038/365108a0, 1993.

Li, C. and Born, A.: Coupled atmosphere-ice-ocean dynamics in Dansgaard-Oeschger events, Quaternary Science Reviews, 203, 1–20, https://doi.org/10.1016/j.quascirev.2018.10.031, 2019.

Lisiecki, L. E. and Raymo, M. E.: A Pliocene-Pleistocene stack of 57 globally distributed benthic d18O records, Paleoceanography, 20, https://doi.org/10.1029/2004PA001071, 2005.

Liu, Z., Otto-Bliesner, B. L., He, F., Brady, E. C., Tomas, R., Clark, P. U., Carlson, A. E., Lynch-Stieglitz, J., Curry, W., Brook, E., and et al.: Transient Simulation of Last Deglaciation with a New Mechanism for Bolling-Allerod Warming, Science, 325, 310 314, https://doi.org/10.1126/science.1171041, 2009.

Lucazeau, F.: Analysis and Mapping of an Updated Terrestrial Heat Flow Data Set, Geochemistry, Geophysics, Geosystems, 20, 4001–4024, https://doi.org/10.1029/2019GC008389, 2019.

MacAyeal, D. R.: Binge/purge oscillations of the Laurentide Ice Sheet as a cause of the North Atlantic's Heinrich events, Paleoceanography, 8, 775–784, https://doi.org/10.1029/93PA02200, 1993.

Mantelli, E., Bertagni, M. B., and Ridolfi, L.: Stochastic ice stream dynamics, Proceedings of the National Academy of Sciences, 113, E4594–E4600, https://doi.org/10.1073/pnas.1600362113, 2016.

Mantelli, E., Haseloff, M., and Schoof, C.: Ice sheet flow with thermally activated sliding. Part 1: the role of advection, Proceedings of the Royal Society A: Mathematical, Physical and Engineering Sciences, 475, 20190 410, https://doi.org/10.1098/rspa.2019.0410, 2019.

Marcott, S. A., Clark, P. U., Padman, L., Klinkhammer, G. P., Springer, S. R., Liu, Z., Otto-Bliesner, B. L., Carlson, A. E., Ungerer, A., Padman, J., He, F., Cheng, J., and Schmittner, A.: Ice-shelf collapse from subsurface warming as a trigger for Heinrich events, Proceedings of the National Academy of Sciences of the United States of America, 108, 13 415–13 419, https://doi.org/10.1073/pnas.1104772108, 2011.

McCarthy, C., Savage, H., and Nettles, M.: Temperature dependence of ice-on-rock friction at realistic glacier conditions, Philosophical Transactions of the Royal Society A: Mathematical, Physical and Engineering Sciences, 375, 20150 348, https://doi.org/10.1098/rsta.2015.0348, 2017.

McKay, R., Albot, O., Dunbar, G. B., Lee, J. I., Lee, M. K., Yoo, K. C., Kim, S., Turton, N., Kulhanek, D., P̃atterson, M., and Levy, R.: A Comparison of Methods for Identifying and Quantifying Ice Rafted Debris on the Antarctic Margin, Paleoceanography and Paleoclimatology, 37, https://doi.org/10.1029/2021PA004404, 2022.

McManus, J. F., Bond, G. C., Broecker, W. S., Johnsen, S., Labeyrie, L., and Higginš, S.: High-resolution climate records from the North Atlantic during the last interglacial, Nature, 371, 326–329, https://doi.org/10.1038/371326a0, 1994.

McManus, J. F., Anderson, R. F., Broecker, W. S., Fleisher, M. Q., and Higgins, S. M.: Radiometrically determined sedimentary fluxes in the sub-polar North Atlantic during the last 140,000 years, Earth and Planetary Science Letters, 155, 29–43, https://doi.org/10.1016/s0012-821x(97)00201-x, 1998.

Melanson, A., Bell, T., and Tarasov, L.: Numerical modelling of subglacial erosion and sediment transport and its application to the North American ice sheets over the Last Glacial cycle, Quaternary Science Reviews, 68, 154–174, https://doi.org/10.1016/j.quascirev.2013.02.017, 2013.

Met Office: Cartopy: a cartographic python library with a Matplotlib interface, Exeter, Devon, URL `https://scitools.org.uk/cartopy`, 2010 - 2015.

Meyer, C. R., Robel, A. A., and Rempel, A. W.: Frozen fringe explains sediment freeze-on during Heinrich events, Earth and Planetary Science Letters, 524, 115 725, https://doi.org/10.1016/j.epsl.2019.115725, 2019.

Milanković, M.: Kanon der Erdbestrahlung und seine Anwendung auf das Eiszeitenproblem, Académie royale serbe. Éditions speciales, Königlich Serbische Akademie, URL `https://books.google.ca/books?id=oN0iQgAACAAJ`, 1941.

Mitchell, J. and Soga, K.: Fundamentals of Soil Behavior, John Wiley & Sons, Inc., 3ed edn., 2005.

Naafs, B. D., Hefter, J., and Stein, R.: Millennial-scale ice rafting events and Hudson Strait Heinrich(-like) Events during the late Pliocene and Pleistocene: A review, Quaternary Science Reviews, 80, 1–28, https://doi.org/10.1016/j.quascirev.2013.08.014, 2013.

Payne, A. J.: Limit cycles in the basal thermal regime of ice sheets, 1995.

Payne, A. J. and Dongelmans, P. W.: Self-organization in the thermomechanical flow of ice sheets, Journal of Geophysical Research: Solid Earth, 102, 12 219–12 233, https://doi.org/10.1029/97jb00513, 1997.

Payne, A. J., Huybrechts, P., Abe-Ouchi, A., Calov, R., Fastook, J. L., Greve, R., Marshall, S. J., Marsiat, I., Ritz, C., Tarasov, L., and Thomassen, M. P.: Results from the EISMINT model intercomparison: The effects of thermomechanical coupling, Journal of Glaciology, 46, 227–238, https://doi.org/10.3189/172756500781832891, 2000.

Pedro, J. B., Andersson, C., Vettoretti, G., Voelker, A. H., Waelbroeck, C., Dokken, T. M., Jensen, M. F., Rasmussen, S. O., Sessford, E. G., Jochum, M., and Nisancioglu, K. H.: Dansgaard-Oeschger and Heinrich event temperature anomalies in the North Atlantic set by sea ice, frontal position and thermocline structure, Quaternary Science Reviews, 289, 107 599, https://doi.org/10.1016/j.quascirev.2022.107599, 2022.

PISM 2.0.6 documentation: PETSc options for PISM users, URL `https://www.pism.io/docs/manual/practical-usage/petsc-options.html`, 2023.

Pollack, H. N., Hurter, S. J., and Johnson, J. R.: Heat flow from the Earth's interior: Analysis of the global data set, Reviews of Geophysics, 31, 267–280, https://doi.org/https://doi.org/10.1029/93RG01249, 1993.

Pollard, D. and DeConto, R. M.: A Coupled Ice-Sheet/Ice-Shelf/Sediment Model Applied to a Marine-Margin Flowline: Forced and Unforced Variations, Glacial Sedimentary Processes and Products, pp. 37–52, https://doi.org/10.1002/9781444304435.ch4, 2007.

Pollard, D. and DeConto, R. M.: Description of a hybrid ice sheet-shelf model, and application to Antarctica, Geoscientific Model Development, 5, 1273–1295, https://doi.org/10.5194/gmd-5-1273-2012, 2012.

Pollard, D., DeConto, R. M., and Alley, R. B.: Potential Antarctic Ice Sheet retreat driven by hydrofracturing and ice cliff failure, Earth and Planetary Science Letters, 412, 112–121, https://doi.org/10.1016/j.epsl.2014.12.035, 2015.

Rasmussen, T., Oppo, D., Thomsen, E., and Lehman, S.: Deep sea records from the southeast Labrador Sea: Ocean circulation changes and ice-rafting events during the last 160,000 years, Paleoceanography, 18, https://doi.org/10.1029/2001PA000736, 2003.

Rasmussen, T. L. and Thomsen, E.: The role of the North Atlantic Drift in the millennial timescale glacial climate fluctuations, Palaeogeography, Palaeoclimatology, Palaeoecology, 210, 101–116, https://doi.org/10.1016/j.palaeo.2004.04.005, 2004.

Robel, A. A., Degiuli, E., Schoof, C., and Tziperman, E.: Dynamics of ice stream temporal variability: Modes, scales, and hysteresis, Journal of Geophysical Research: Earth Surface, 118, 925–936, https://doi.org/10.1002/jgrf.20072, 2013.

Roberts, W. H., Valdes, P. J., and Payne, A. J.: A new constraint on the size of Heinrich Events from an iceberg/sediment model, Earth and Planetary Science Letters, 386, 1–9, https://doi.org/10.1016/j.epsl.2013.10.020, 2014.

Roberts, W. H., Payne, A. J., and Valdes, P. J.: The role of basal hydrology in the surging of the Laurentide Ice Sheet, Climate of the Past, 12, 1601–1617, https://doi.org/10.5194/cp-12-1601-2016, 2016.

Rolandone, F., Jaupart, C., Mareschal, J. C., Gariépy, C., Bienfait, G., Carbonne, C., and Lapointe, R.: Surface heat flow, crustal temperatures and mantle heat flow in the Proterozoic Trans-Hudson Orogen, Canadian Shield, Journal of Geophysical Research: Solid Earth, 107, ETG 7–1–ETG 7–19, https://doi.org/10.1029/2001jb000698, 2002.

Rolandone, F., Mareschal, J. C., and Jaupart, C.: Temperatures at the base of the Laurentide Ice Sheet inferred from borehole temperature data, Geophysical Research Letters, 30, 18–21, https://doi.org/10.1029/2003GL018046, 2003.

Rovere, A., Raymo, M. E., Mitrovica, J. X., Hearty, P. J., O'Leary, M. J., and Inglis, J. D.: The Mid-Pliocene sea-level conundrum: Glacial isostasy, eustasy and dynamic topography, Earth and Planetary Science Letters, 387, 27–33, https://doi.org/10.1016/j.epsl.2013.10.030, 2014.

Ruddiman, W. F.: Late Quaternary deposition of ice-rafted sand in the subpolar North Atlantic (lat 40 degree to 65 degree N), Bulletin of the Geological Society of America, 88, 1813–1827, https://doi.org/10.1130/0016-7606(1977)88⟨1813:LQDOIS⟩2.0.CO;2, 1977.

Sanchez Goñi, M. F. and Harrison, S. P.: Millennial-scale climate variability and vegetation changes during the Last Glacial: Concepts and terminology, Quaternary Science Reviews, 29, 2823–2827, https://doi.org/10.1016/j.quascirev.2009.11.014, 2010.

Sanchez Goñi, M., Bard, E., Landais, A., Rossignol, L., and d'Errico, F.: Air-sea temperature decoupling in western Europe during the last interglacial-glacial transition, Nature Geoscience, 6, 837–841, https://doi.org/10.1038/ngeo1924, 2013.

Sanford, B. and Grant, A.: Paleozoic and Mesozoic geology of the Hudson and southeast Arctic Platforms, Geological Survey of Canada, 1998.

Sauer, E. K., Egeland, A. K., and Christiansen, E. A.: Preconsolidation of tills and intertill clays by glacial loading in southern Saskatchewan, Canada, Canadian Journal of Earth Sciences, 30, 420–433, https://doi.org/10.1139/e93-031, 1993.

Sayag, R. and Tziperman, E.: Interaction and variability of ice streams under a triple-valued sliding law and non-Newtonian rheology, Journal of Geophysical Research: Earth Surface, 116, https://doi.org/10.1029/2010JF001839, 2011.

Schannwell, C., Mikolajewicz, U., Ziemen, F., and Kapsch, M.-L.: Sensitivity of Heinrich-type ice-sheet surge characteristics to boundary forcing perturbations, Climate of the Past, 19, 179–198, https://doi.org/10.5194/cp-19-179-2023, 2023.

Schoof, C.: Ice sheet grounding line dynamics: Steady states, stability, and hysteresis, Journal of Geophysical Research: Earth Surface, 112, 1–19, https://doi.org/10.1029/2006JF000664, 2007.

Seager, R. and Battisti, D.: Challenges to Our Understanding of the General Circulation: Abrupt Climate Change, The Global Circulation of the Atmosphere, https://doi.org/10.2307/j.ctv1t1kg52.16, 2007.

Shapiro, N. M. and Ritzwoller, M. H.: Inferring surface heat flux distributions guided by a global seismic model: Particular application to Antarctica, Earth and Planetary Science Letters, 223, 213–224, https://doi.org/10.1016/j.epsl.2004.04.011, 2004.

Shreve, R. L.: Glacier sliding at subfreezing temperatures., Journal of Glaciology, 30, 341–347, https://doi.org/10.1017/S0022143000006195, 1984.

Souček, O. and Martinec, Z.: ISMIP-HEINO experiment revisited: Effect of higher-order approximation and sensitivity study, Journal of Glaciology, 57, 1158–1170, https://doi.org/10.3189/002214311798843278, 2011.

Srokosz, M., Baringer, M., Bryden, H., Cunningham, S., Delworth, T., Lozier, M., Marotzke, J., and Sutton, R.: Past, Present, and Future Changes in the Atlantic Meridional Overturning Circulation, Bulletin of the American Meteorological Society, 93, 1663–1676, https://doi.org/10.1175/BAMS-D-11-00151.1, 2012.

Takahama, R.: Heinrich Event Intercomparison with the ice-sheet model SICOPOLIS, Master's thesis, URL `http://hdl.handle.net/2115/28749`, 2006.

Tarasov, L.: 50 degree N summer half year (AMJJAS) GSM surface insolation, path: /net/glacdyn2-data/data/ltarasov/data.dir/Orbital.dir/test3.nn222, 2019.

Tarasov, L.: North American history matching, 2024.

Tarasov, L. and Goldstein, M.: Assessing uncertainty in past ice and climate evolution: overview, stepping-stones, and challenges, Climate of the Past Discussions, 2021, 1–54, https://doi.org/10.5194/cp-2021-145, 2021.

Tarasov, L. and Peltier, W. R.: A high-resolution model of the 100 ka ice-age cycle, Annals of Glaciology, 25, 58–65, https://doi.org/10.3189/s026030550001380x, 1997.

Tarasov, L. and Peltier, W. R.: Impact of thermomechanical ice sheet coupling on a model of the 100 kyr ice age cycle, Journal of Geophysical Research Atmospheres, 104, 9517–9545, https://doi.org/10.1029/1998JD200120, 1999.

Tarasov, L. and Peltier, W. R.: Coevolution of continental ice cover and permafrost extent over the last glacial-interglacial cycle in North America, Journal of Geophysical Research: Earth Surface, 112, 1–13, https://doi.org/10.1029/2006JF000661, 2007.

Tarasov, L., Dyke, A. S., Neal, R. M., and Peltier, W. R.: A data-calibrated distribution of deglacial chronologies for the North American ice complex from glaciological modeling, Earth and Planetary Science Letters, 315-316, 30–40, https://doi.org/10.1016/j.epsl.2011.09.010, 2012.

Tarasov, L., Hank, K., and Lecavalier, B. S.: GSMv01.31.2023 code archive for LISsq experiments, https://doi.org/10.5281/zenodo.7668472, 2023.

Tarasov, L., Hank, K., and Lecavalier, B. S.: The glacial systems model (GSM), 2024.

Tsai, V. C., Stewart, A. L., and Thompson, A. F.: Marine ice-sheet profiles and stability under Coulomb basal conditions, Journal of Glaciology, 61, 205–215, https://doi.org/10.3189/2015JoG14J221, 2015.

Tulaczyk, S., Kamb, W. B., and Engelhardt, H. F.: Basal mechanics of Ice Stream B, west Antarctica: 2. Undrained plastic bed model, Journal of Geophysical Research: Solid Earth, 105, 483–494, https://doi.org/https://doi.org/10.1029/1999JB900328, 2000a.

Tulaczyk, S., Kamb, W. B., and Engelhardt, H. F.: Basal mechanics of Ice Stream B, West Antarctica 1. Till mechanics, Journal of Geophysical Research: Solid Earth, 105, 463–481, https://doi.org/10.1029/1999jb900329, 2000b.

Van Pelt, W. J. and Oerlemans, J.: Numerical simulations of cyclic behaviour in the Parallel Ice Sheet Model (PISM, Journal of Glaciology, 58, 347–360, https://doi.org/10.3189/2012JoG11J217, 2012.

Veiga-Pires, C. C. and Hillaire-Marcel, C.: U and Th isotope constraints on the duration of Heinrich events H0-H4 in the southeastern Labrador Sea, Paleoceanography, 14, 187–199, https://doi.org/https://doi.org/10.1029/1998PA900003, 1999.

Veres, D., Bazin, L., Landais, A., Toyé Mahamadou Kele, H., Lemieux-Dudon, B., Parrenin, F., Martinerie, P., Blayo, E., Blunier, T., Capron, E., Chappellaz, J., Rasmussen, S. O., Severi, M., Svensson, A., Vinther, B., and Wolff, E. W.: The Antarctic ice core chronology (AICC2012): an optimized multi-parameter and multi-site dating approach for the last 120 thousand years, Climate of the Past, 9, 1733–1748, https://doi.org/10.5194/cp-9-1733-2013, 2013.

Vernal, A. d., Hillaire-Marcel, C., Turon, J.-L., and Matthiessen, J.: Reconstruction of sea-surface temperature, salinity, and sea-ice cover in the northern North Atlantic during the last glacial maximum based on dinocyst assemblages, Canadian Journal of Earth Sciences, 37, 725–750, https://doi.org/10.1139/e99-091, 2000.

Virtanen, P., Gommers, R., Oliphant, T. E., Haberland, M., Reddy, T., Cournapeau, D., Burovski, E., Peterson, P., Weckesser, W., Bright, J., van der Walt, S. J., Brett, M., Wilson, J., Millman, K. J., Mayorov, N., Nelson, A. R. J., Jones, E., Kern, R., Larson, E., Carey, C. J., Polat, I., Feng, Y., Moore, E. W., VanderPlas, J., Laxalde,

D., Perktold, J., Cimrman, R., Henriksen, I., Quintero, E. A., Harris, C. R., Archibald, A. M., Ribeiro, A. H., Pedregosa, F., van Mulbregt, P., Vijaykumar, A., Bardelli, A. P., Rothberg, A., Hilboll, A., Kloeckner, A., Scopatz, A., Lee, A., Rokem, A., Woods, C. N., Fulton, C., Masson, C., Häggström, C., Fitzgerald, C., Nicholson, D. A., Hagen, D. R., Pasechnik, D. V., Olivetti, E., Martin, E., Wieser, E., Silva, F., Lenders, F., Wilhelm, F., Young, G., Price, G. A., Ingold, G.-L., Allen, G. E., Lee, G. R., Audren, H., Probst, I., Dietrich, J. P., Silterra, J., Webber, J. T., Slavič, J., Nothman, J., Buchner, J., Kulick, J., Schönberger, J. L., de Miranda Cardoso, J. V., Reimer, J., Harrington, J., Rodríguez, J. L. C., Nunez-Iglesias, J., Kuczynski, J., Tritz, K., Thoma, M., Newville, M., Kümmerer, M., Bolingbroke, M., Tartre, M., Pak, M., Smith, N. J., Nowaczyk, N., Shebanov, N., Pavlyk, O., Brodtkorb, P. A., Lee, P., McGibbon, R. T., Feldbauer, R., Lewis, S., Tygier, S., Sievert, S., Vigna, S., Peterson, S., More, S., Pudlik, T., Oshima, T., Pingel, T. J., Robitaille, T. P., Spura, T., Jones, T. R., Cera, T., Leslie, T., Zito, T., Krauss, T., Upadhyay, U., Halchenko, Y. O., Vázquez-Baeza, Y., and Contributors, S. .: SciPy 1.0: fundamental algorithms for scientific computing in Python, Nature Methods, 17, 261–272, https://doi.org/10.1038/s41592-019-0686-2, 2020.

Werder, M. A., Hewitt, I. J., Schoof, C. G., and Flowers, G. E.: Modeling channelized and distributed subglacial drainage in two dimensions, Journal of Geophysical Research: Earth Surface, 118, 2140–2158, https://doi.org/10.1002/jgrf.20146, 2013.

Winkelmann, R., Martin, M. A., Haseloff, M., Albrecht, T., Bueler, E., Khroulev, C., and Levermann, A.: The Potsdam Parallel Ice Sheet Model (PISM-PIK) – Part 1: Model description, The Cryosphere, 5, 715–726, URL `http://www.the-cryosphere.net/5/715/2011/tc-5-715-2011.pdf`, 2011.

Winsborrow, M. C., Clark, C. D., and Stokes, C. R.: What controls the location of ice streams?, Earth-Science Reviews, 103, 45–59, https://doi.org/10.1016/j.earscirev.2010.07.003, 2010.

Wunsch, C.: What Is the Thermohaline Circulation?, Science, 298, 1179–1181, https://doi.org/10.1126/science.1079329, 2002.

Wunsch, C.: Abrupt climate change: An alternative view, Quaternary Research, 65, 191 – 203, https://doi.org/https://doi.org/10.1016/j.yqres.2005.10.006, 2006.

Zhou, Y., McManus, J. F., Jacobel, A. W., Costa, K. M., Wang, S., and Caraveo, B. A.: IRD flux and supporting data on two cores in the western North Atlantic, https://doi.org/10.1594/PANGAEA.911512, 2020.

Zhou, Y., McManus, J. F., Jacobel, A. W., Costa, K. M., Wang, S., and Alvarez Caraveo, B.: Enhanced iceberg discharge in the western North Atlantic during all Heinrich events of the last glaciation, Earth and Planetary Science Letters, 564, 116 910, https://doi.org/10.1016/j.epsl.2021.116910, 2021.

Ziemen, F. A., Rodehacke, C. B., and Mikolajewicz, U.: Coupled ice sheet-climate modeling under glacial and pre-industrial boundary conditions, Climate of the Past, 10, 1817–1836, https://doi.org/10.5194/cp-10-1817-2014, 2014.

Ziemen, F. A., Kapsch, M. L., Klockmann, M., and Mikolajewicz, U.: Heinrich events show two-stage climate response in transient glacial simulations, Climate of the Past, 15, 153–168, https://doi.org/10.5194/cp-15-153-2019, 2019.

Appendix A

Supplement for P1

A.1 GSM - Details of different model aspects

A.1.1 Climate forcing

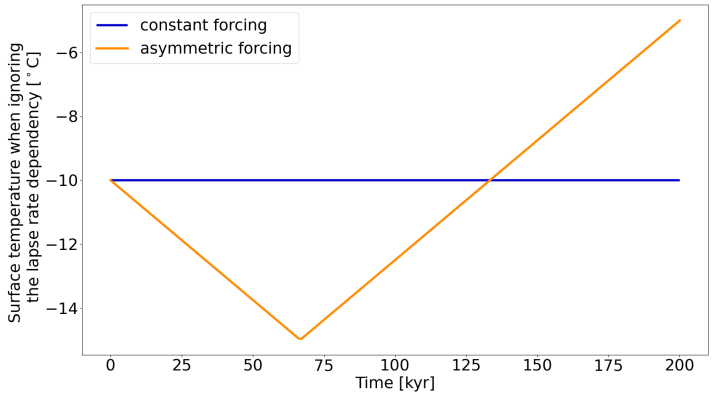

Figure A.1: Constant and asymmetric temperature forcing in the GSM. The coldest temperature is reached at 66.7 kyr. For the case shown here, the surface temperature constant is set to rTsurf= -10°C (Table 2.1). All model runs within this paper use the asymmetric forcing.

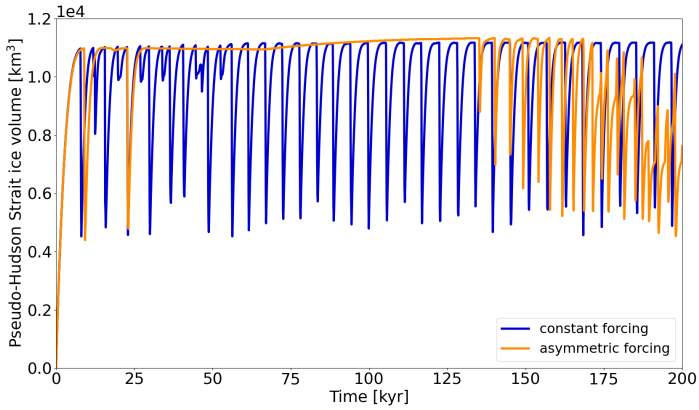

Figure A.2: Pseudo-Hudson Strait ice volume for a constant and asymmetric temperature forcing in the GSM (Fig. A.1). This plot shows parameter vector 1 with a horizontal grid resolution of 25 km.

A.1.2 SSA activation velocities

Setup	number of surges	mean duration	mean period	mean pseudo-Hudson Strait ice volume change
reference setup	180 ± 100	1.1 ± 0.5 kyr	0.3 ± 0.1 kyr	$1.7 \pm 0.2 \cdot 10^3$ km^3
$v_{\mathrm{SIA,crit}} = 20$ m yr^{-1}	-3.7 ± 7.0	3.2 ± 6.4	1.5 ± 2.1	3.2 ± 2.4
$v_{\mathrm{SIA,crit}} = 40$ m yr^{-1}	-5.5 ± 5.4	6.1 ± 6.8	2.4 ± 5.7	3.5 ± 9.0
SSA everywhere	7.3 ± 24.8	1.7 ± 27.6	-9.3 ± 14.1	-17.7 ± 29.7

Table A.1: Percentage differences (except first row) of surge characteristics between the GSM reference setup (first row) and runs with different SSA activation velocities at 3.125 km. By default, the SSA is activated once the SIA velocity exceeds $v_{\mathrm{SIA,crit}} = 30$ m yr^{-1}. No runs crashed and all runs had more than 1 surge. The first 20 kyr of each run are treated as a spin-up interval and are not considered in the above.

A.1.3 Parameter vectors

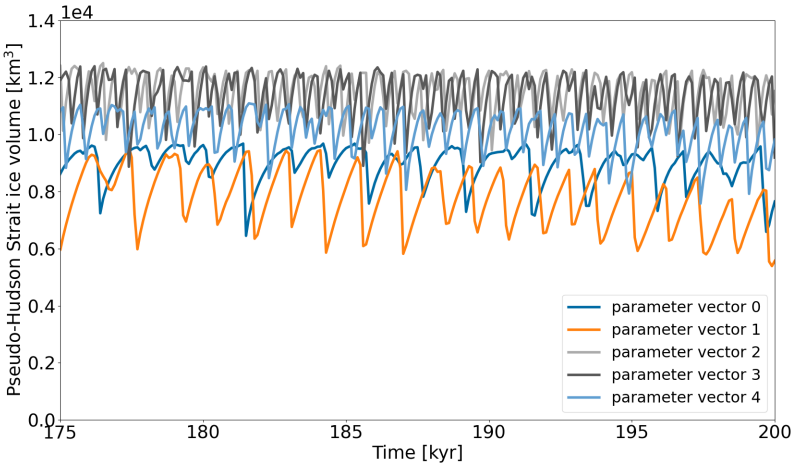

Figure A.3: Pseudo-Hudson Strait ice volume for the last 25 kyr of all 5 GSM parameter vectors when using the reference setup. Note that only the last 25 kyr are shown for better visibility of the individual oscillation pattern.

A.1.4 Bed properties

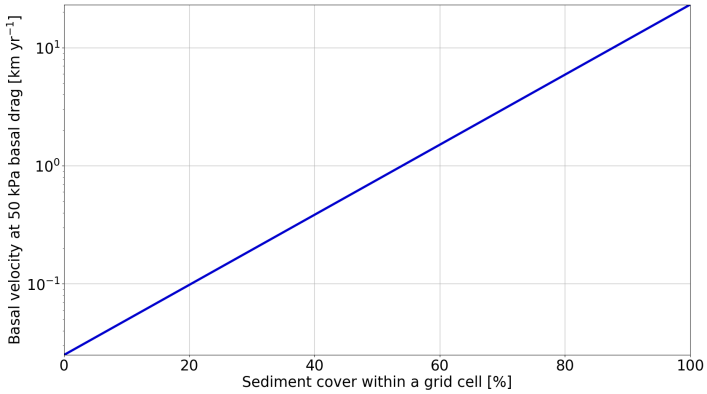

Figure A.4: Basal velocity at 50 kPa basal drag for variable sediment cover and a power-law exponent of 3 (n_b in Table 2.1).

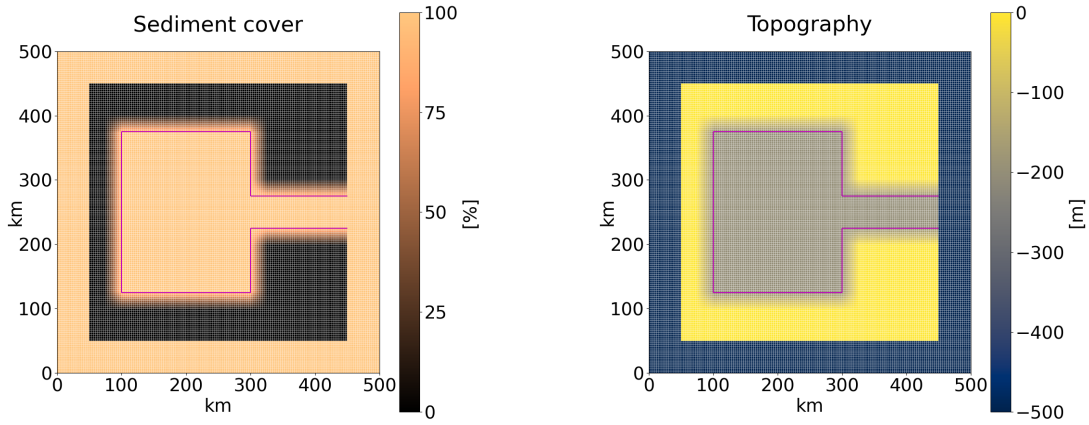

(a) (b)

Figure A.5: Sediment cover and topography map for a 25 km wide transition zone at 3.125 km horizontal grid resolution. The transition zones for topography and sediment cover are at the same locations. The magenta line outlines the 100 % soft-bedded pseudo-Hudson Bay and Hudson Strait.

The effects of an abrupt transition from hard bedrock (0 % sediment cover) to soft sediment (100 % sediment cover) are examined by adding a smooth transition zone (Fig. A.5 a)). Two widths of this transition zone (25 km and 3.125 km) are investigated. The basal velocity (or more precisely the sliding coefficient C in Eq. (2.6b)) then depends on the sediment cover within a grid cell (Fig. A.4). In the experiments with a non-flat topography, the bed of the pseudo-Hudson Bay and Hudson Strait is placed 200 m and the surrounding ocean 500 m below the sea level (Fig. A.5 b). The topographic transition zones (25 km and 3.125 km wide) align with the sediment transition zones.

A.1.5 Weighting function of the adjacent minimum basal-temperature

A weighting function takes into account the adjacent minimum basal-temperature for the basal-sliding temperature ramp.

$$T_{\mathrm{bp,I}} = W_{\mathrm{Tb,min}} \cdot \min\left[T_{\mathrm{bp,L}}, T_{\mathrm{bp,R}}\right] + T_{\mathrm{bp,I}} \cdot \left(1 - W_{\mathrm{Tb,min}}\right), \tag{A.1}$$

where $T_{\mathrm{bp,I}}$ is the basal-temperature with respect to the pressure-melting point at the grid cell interface, and $T_{\mathrm{bp,L}}$ and $T_{\mathrm{bp,R}}$ are the basal-temperatures with respect to the pressure-melting point at the adjacent grid cell centers. Note that $T_{bp,Im,L}$ and $T_{bp,Im,R}$ instead of $T_{\mathrm{bp,L}}$ and $T_{\mathrm{bp,R}}$ are used when calculating $T_{\mathrm{bp,I}}$ according to TpmTrans (Eq. (2.18)). In this way, the additional heat T_{add} is still considered even when $W_{\mathrm{Tb,min}} = 1$.

A.2 PISM - Details of different model aspects

A.2.1 Input fields

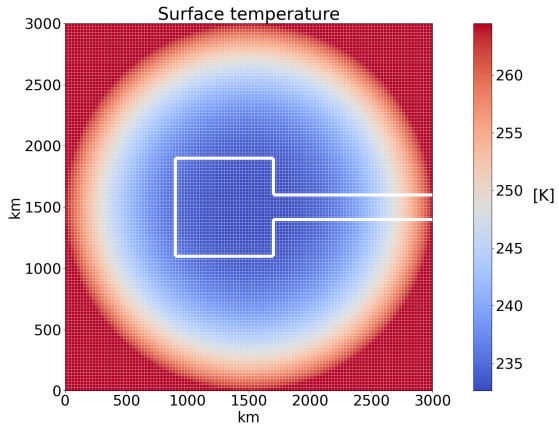

Figure A.6: PISM surface temperature input field for parameter vector 1. The corresponding parameter values of $T_{\min}$ and S_t are 232.60 K and $9.45 \cdot 10^{-9}$ K km^{-3}, respectively. Thick white lines outline the simplified soft-bedded pseudo-Hudson Bay/Hudson Strait area. The horizontal grid resolution is 25x25 km.

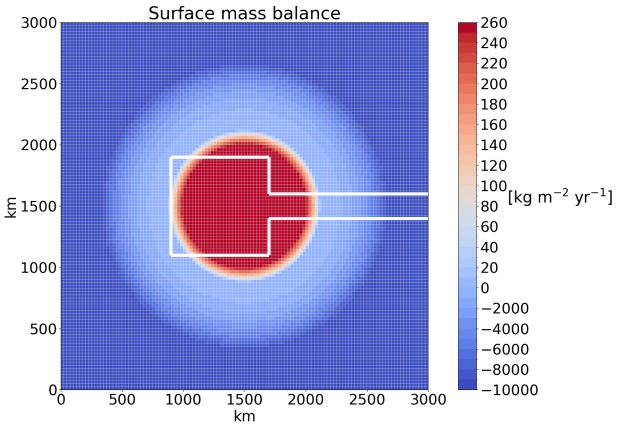

Figure A.7: PISM surface mass balance input field for parameter vector 1. The corresponding parameter values of $B_{\max}$ and S_b are 408.81 kg m^{-2} yr^{-1} and $4.55 \cdot 10^{-12}$ kg m^{-2} yr^{-1} km^{-5}, respectively. Thick white lines outline the simplified soft-bedded pseudo-Hudson Bay/Hudson Strait area. The horizontal grid resolution is 25x25 km.

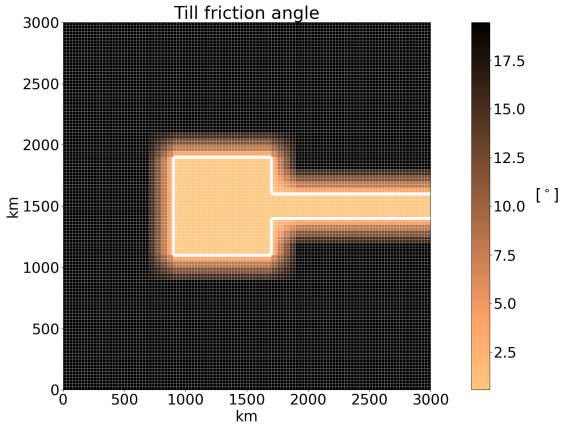

Figure A.8: PISM till friction angle input field for parameter vector 1. The corresponding parameter values of *soft* and *hard* are 0.56°C and 19.44°C, respectively. Magenta lines outline the simplified soft-bedded pseudo-Hudson Bay/Hudson Strait area. The horizontal grid resolution is 25x25 km.

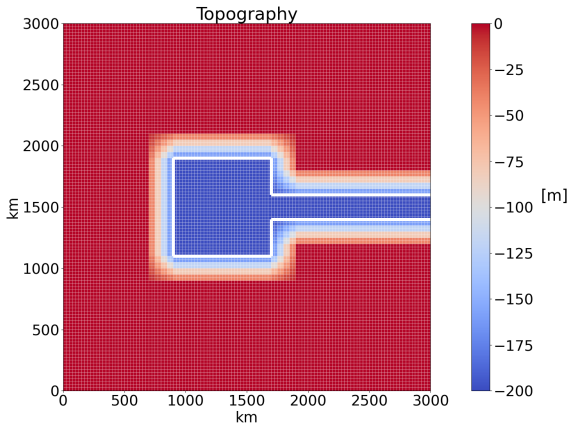

Figure A.9: PISM topography input field (same for all parameter vectors). The white lines outline the simplified soft-bedded pseudo-Hudson Bay/Hudson Strait area. The horizontal grid resolution is 25x25 km.

A.2.2 Parameter vectors

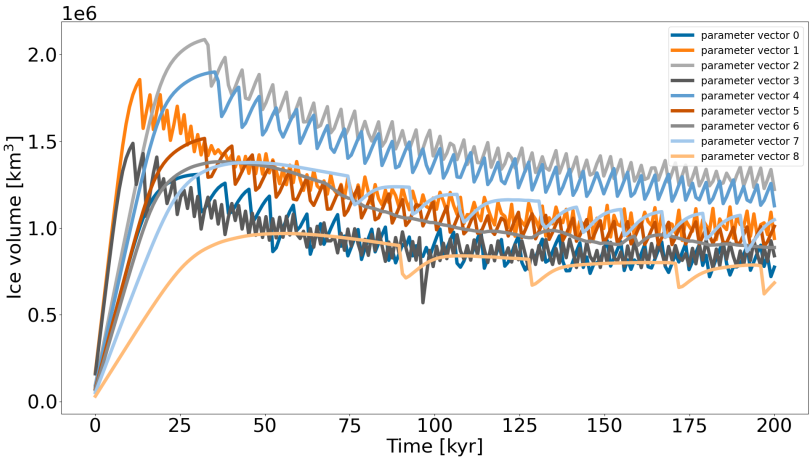

Figure A.10: Ice volume in the eastern half of the pseudo-Hudson Bay and the pseudo-Hudson Strait for all 9 PISM parameter vectors when using the reference setup.

A.2.3 Bed properties

In PISM, oscillatory behavior only occurs for small yield stresses τ_c (Eq. (2.15)). This can be achieved by either a small till friction angle Φ or low effective-pressure on the till (N_{till}) (Bueler and Van Pelt, 2015). N_{till} is given by

$$N_{\text{till}} = \min\left\{P_0, N_0\left(\frac{\delta_e P_0}{N_0}\right)^s 10^{\left(\frac{e_0}{C_c}\right)(1-s)}\right\}, \tag{A.2}$$

where P_0 is the ice overburden pressure, $N_0 = 1$ kPa is the reference effective-pressure, $e_0 = 0.69$ the void ratio at N_0, $C_c = 0.12$ the dimensionless coefficient of compressibility, δ_e the effective fraction of the overburden pressure, P_0 the ice overburden pressure, and s the ratio $\frac{W_{\text{till}}}{W_{\text{till}}^{\max}}$ (Tulaczyk et al., 2000b; Bueler and Van Pelt, 2015). W_{till} and $W_{\text{till}}^{\max} = 2$ m are the effective and maximum thickness of water in the till,

respectively. The values listed here are the PISM defaults. C_c is on the lower end of measured values (Tulaczyk et al., 2000b) with significantly larger (up to 17) values reported (Sauer et al., 1993; Mitchell and Soga, 2005). e_0 can vary between 0.45 (Tulaczyk et al., 2000b) and approximately 4 (Fig. 10.2 in Mitchell and Soga, 2005). The default value of δ_e is based on Greenland and Antarctic model runs, but δ_e is generally considered as a tuning parameter to match observed surface velocities, which are not available in a paleo context (Andy Aschwanden, personal communication, 18 October 2022).

When only changing the till friction angle (Eq. (2.15)), oscillations do not occur unless $\Phi < 1^\circ$ (Fig. A.13). This is well below the measured values of about 10 to 40° (K.M. Cuffey and W.S.B. Paterson., 2010). However, similar oscillatory results are obtained for till friction angles between 5 and 10° when slightly adjusting the values of $C_c = 0.2$, $e_0 = 0.6$, and $\delta_e = 0.01$ to favor sliding (compare Fig. A.11 and A.12). These values are all well within the ranges set by laboratory measurements.

A.2.4 Maximum magnitude of basal ice velocity

Small till friction angles (0.5 to 1.0°) lead to slippery beds and high maximum basal-sliding velocities (up to $\sim$ 600 km yr^{-1}) for a small number of time steps in some runs. A maximum of 7 out of 2000 time steps exceeds 50 km yr^{-1} (parameter vector 1 in Fig. A.11). While observed velocities can reach several hundreds of meters per day for short periods (K.M. Cuffey and W.S.B. Paterson. (2010), e.g., 300 m d^{-1} = 109.5 km yr^{-1}), high modeled velocities might lead to instabilities in the numerical matrix solver. Therefore, we set an upper limit of 40 km yr^{-1} for the SSA velocity.

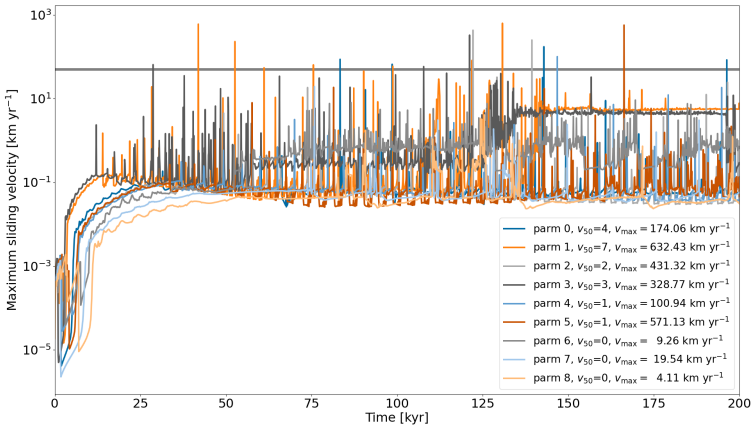

Figure A.11: Maximum sliding velocity (max(max(abs($\boldsymbol{u}$)), max(abs($\boldsymbol{v}$)))) at each time step (100 yr interval) within the whole model domain for all 9 parameter vectors using PISM without an upper limit for the SSA velocity. The black horizontal line marks 50 km yr^{-1} and v_{50} indicates the number of time steps exceeding this velocity. v_{max} is the highest maximum sliding velocity in a run.

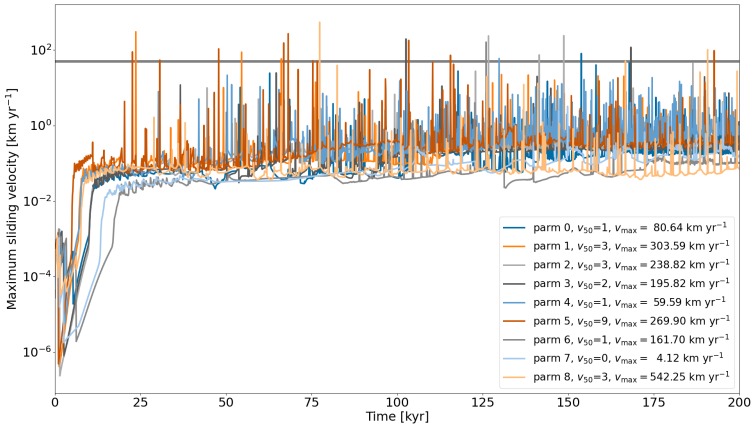

Figure A.12: Maximum sliding velocity (max(max(abs($\boldsymbol{u}$)), max(abs($\boldsymbol{v}$)))) at each time step (100 yr interval) within the whole model domain for 9 parameter vectors with till friction angles between 5 and 10° and values of $C_c = 0.2$, $e_0 = 0.6$, and $\delta_e = 0.01$ using PISM without an upper limit for the SSA velocity. The black horizontal line marks 50 km yr^{-1} and v_{50} indicates the number of time steps exceeding this velocity. v_{max} is the highest maximum sliding velocity in a run.

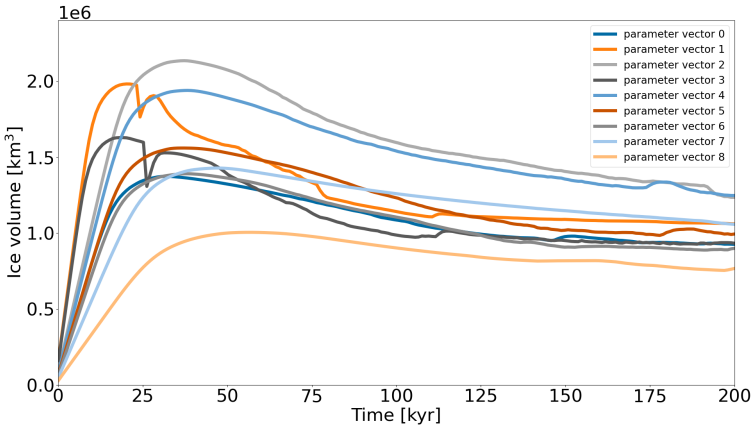

Figure A.13: Ice volume in the eastern half of the pseudo-Hudson Bay and the pseudo-Hudson Strait for all 9 PISM parameter vectors when using the reference setup but a soft-bed till friction angle of 1°.

A.2.5 Ice volume - pseudo-Hudson Strait vs. surge-affected area

During a surge, ice from the pseudo-Hudson Bay and areas surrounding the pseudo-Hudson Strait is rapidly transported into the mostly ice-free pseudo-Hudson Strait. Consequently, the ice sheet extends further to the East (increasingly stronger melting), covering almost the entire pseudo-Hudson Strait area. Due to the complex interaction between ice transport and melting area, times of minimum ice volume over the area most affected by the pseudo-Hudson Strait surge (eastern half of the pseudo-Hudson Bay and the pseudo-Hudson Strait, e.g., Fig. 2.5 and video 06 of Hank (2023b)) correspond to maxima in the pseudo-Hudson Strait ice volume for most surges (grey lines in Fig. A.14). However, some ice volume minima do not align with a maximum of the pseudo-Hudson Strait ice volume (red lines in Fig. A.14). This inconsistency hampers the detection of surges when using the pseudo-Hudson Strait ice volume and can lead to flawed statistics. To avoid this issue, we use the ice

volume in the surge-affected area, for which surges appear as minima, for all PISM results. A comparison between PISM results based on the pseudo-Hudson Strait and the surge-affected area is shown in Fig. A.15. Note that we only consider the eastern half of the pseudo-Hudson Bay because some runs also show surges on the Western side of the ice sheet (e.g., 50 km run in video 09 of Hank (2023b)).

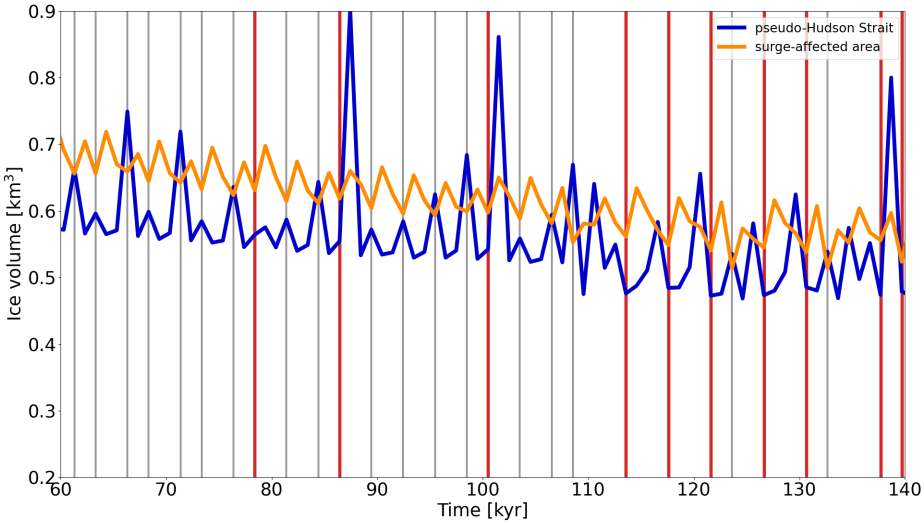

Figure A.14: Normalized pseudo-Hudson Strait and surge-affected area (eastern half of the pseudo-Hudson Bay and the pseudo-Hudson Strait) ice volume for parameter vector 1 using PISM. For most surges, the minimum ice volume over the surge-affected area aligns with a maxima in the pseudo-Hudson Strait ice volume (grey lines). This is, however, not true for all surges (thick red lines) and can lead to flawed statistics. See also video 06 of Hank (2023b).

A.3 Run analysis approach

For both models, we use the Python module *scipy* (version 1.5.2 on GSM cluster and 1.7.0 on PISM cluster, different versions due to the availability on computational clusters) and its built-in function *scipy.signal.find_peaks* on the ice volume

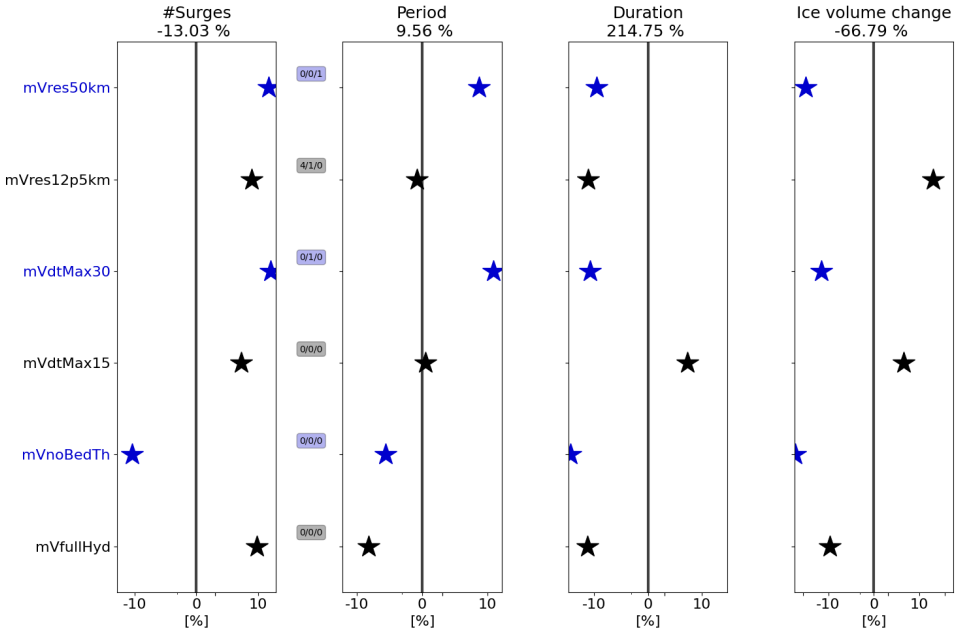

Figure A.15: Differences in the percentage differences of the mean surge characteristics (between comparison and reference setup) when using the ice volume of the surge-affected area (eastern half of the pseudo-Hudson Bay and the pseudo-Hudson Strait) compared to only the pseudo-Hudson Strait ice volume. A positive difference indicates a larger change for the analysis based on the pseudo-Hudson Strait ice volume. The different colors were added for visual alignment of the individual model setups. The 3 small numbers between the first two columns represent the number of crashed runs (nC), the number of runs without a surge (nS0), and the number of runs with only one surge (nS1), respectively. The first 20 kyr of each run are treated as a spin-up interval and are not considered in the above. The percentages in the titles of each subplot represent the percentage differences in the surge characteristics of the reference runs. For example, the mean number of surges based on the pseudo-Hudson Strait ice volume is ~ 13 % smaller than for the ice volume of the surge-affected area. Note that the surge threshold is $4 \cdot 10^4$ km^3 when using the surge-affected area ice volume and $0.5 \cdot 10^4$ km^3 for the pseudo-Hudson Strait ice volume (~ 5 % of mean ice volume across all runs). The x-axis is logarithmic. Further details of each individual experiments are provided in Fig. 2.6.

output to determine the surge characteristics. The surge duration and ice volume change during a surge are determined by the functions *scipy.signal.peak_widths* and *scipy.signal.peak_prominences*, respectively. The Python analysis scripts are provided as supplementary material.

Temporal resolution of output time series

The standard output time steps in the GSM and PISM are 0.1 and 1 kyr, respectively. Note that these time steps might not exactly capture the minimum ice volume but are generally a good compromise between storage requirements and temporal resolution (e.g., Fig. A.16 and A.17).

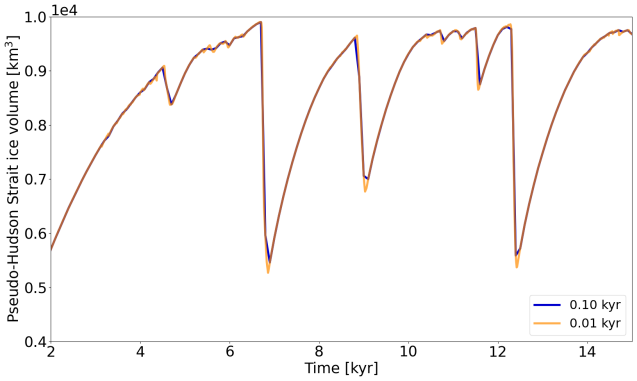

Figure A.16: Pseudo-Hudson Strait ice volume of a GSM model run (parameter vector 1) with different output time steps. The horizontal grid resolution is 3.125 km.

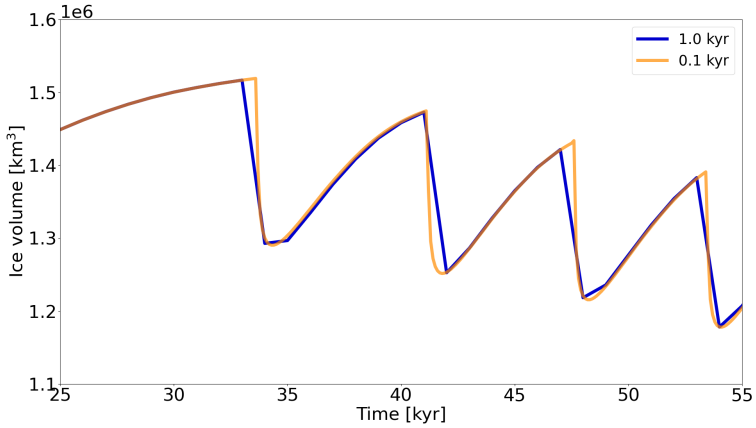

Figure A.17: Ice volume in the surge-affected area (eastern half of the pseudo-Hudson Bay and the pseudo-Hudson Strait) of a PISM model run (parameter vector 5) with different output time steps. The horizontal grid resolution is 25 km.

A.4 RMSE and mean bias

The RMSE and mean bias values presented throughout the paper are calculated according to the following equations

$$rmse = \sqrt{\frac{\sum_{t=0}^{t_{max}} (x_t - b_t)^2}{N}} \cdot \frac{100}{b_m}, \text{ and} \tag{A.3}$$

$$mean\ bias = \frac{\sum_{t=0}^{t_{max}} (x_t - b_t)}{N} \cdot \frac{100}{b_m}, \tag{A.4}$$

where x_t and b_t are the (pseudo-Hudson Strait) ice volume values at time t of the comparison setup and reference setup, respectively. t_{max} is the maximum time, N the number of time steps, and b_m the mean of the reference setup time series. These values are then averaged over all 5 parameter vectors. Crashed runs are excluded from the averaging process.

A.5 Comparison between different model setups

The analysis to compare the different model setups follows

1. run 1 parameter vector with the reference setup (Table 2.2)
2. calculate the surge characteristics for this reference run (s_{ref})
3. re-run the same parameter vector for one of the comparison setups (Sec. 2.2.1.3 and 2.2.2.4)
4. calculate the surge characteristics for the comparison run (s_{comp})

5. calculate the differences in surge characteristics between the reference run and comparison run expressed as percentage differences from the reference run (positive for increase compared to the value of the reference run): $p = \frac{s_{\mathrm{comp}} - s_{\mathrm{ref}}}{s_{\mathrm{ref}}} \cdot 100$

6. repeat steps 1) to 5) for all parameter vectors (5 for the GSM, 9 for PISM)

7. the values shown in the tables and figures are the mean and standard deviation of all percentage differences for each surge characteristic

Percentage differences for crashed comparison runs are not considered for the final average and runs with less than 2 surges require special treatment. In these cases, the period is set to a NaN value, leading to a NaN difference between that particular run and the corresponding reference run. We use Numpys *numpy.nanmean()* and *numpy.nanstd()* to ignore these NaN values when averaging over all parameter vectors. Similarly, all surge characteristics except for the number of surges are set to NaN values for runs with no surges at all. Note that the values for the reference setup stated in the tables are the mean and standard deviation of the actual surge characteristics of all reference runs, not percentage differences.

A.6 Minimum numerical error estimates

A.6.1 GSM

A.6.1.1 Minimum numerical error estimates at 12.5 km

Metric	original 12.5 km runs	stricter numerical convergence [% difference]	stricter numerical convergence with increased maximum iterations [% difference]
#Surges	81 ± 42	2.3 ± 8.5	$\mathbf{2.8 \pm 9.2}$
mean period	2.3 ± 0.8 kyr	$\mathbf{-2.1 \pm 7.5}$	-1.5 ± 9.3
mean duration	0.6 ± 0.2 kyr	-1.4 ± 9.4	$\mathbf{2.6 \pm 14.2}$
mean pseudo-Hudson Strait ice volume change	$2.2 \pm 1.1 \cdot 10^3$ km^3	$\mathbf{20.9 \pm 53.0}$	-5.1 ± 12.2

Table A.2: Percentage differences (except first column) of surge characteristics between GSM runs with regular and stricter numerical convergence and increased maximum iterations for the ice dynamics loops at 12.5 km. The values represent the average of 5 parameter vectors. No runs crashed and all runs had more than 1 surge. The first 20 kyr of each run are treated as a spin-up interval and are not considered in the above. The bold numbers mark the largest MNEE for each surge characteristic.

A.6.1.2 Adding surface temperature noise

Metric	reference setup	± 0.1°C noise	± 0.5°C noise
#Surges	180 ± 100	-4.0 ± 4.3	-4.1 ± 7.0
mean period	1.1 ± 0.5 kyr	4.8 ± 5.3	3.8 ± 6.8
mean duration	0.3 ± 0.1 kyr	1.3 ± 4.4	0.9 ± 4.3
mean pseudo-Hudson Strait ice volume change	$1.7 \pm 0.2 \cdot 10^3$ km^3	0.9 ± 4.1	2.1 ± 5.5
RMSE	-	8.0 ± 2.5	7.8 ± 2.1
Mean Bias	-	-0.1 ± 0.2	0.1 ± 0.0

Table A.3: Percentage differences (except first column) of surge characteristics, pseudo-Hudson Strait ice volume RMSE and mean bias compared to the GSM reference setup for two different amplitudes of surface temperature noise. No runs crashed and all runs had more than 1 surge. The first 20 kyr of each run are treated as a spin-up interval for the surge characteristics (not the RMSE and mean bias).

A.6.1.3 Implicit thermodynamics/ice dynamics coupling

Metric	reference setup	implicit coupling
#Surges	180 ± 100	1.1 ± 4.9
mean period	1.1 ± 0.5 kyr	-0.3 ± 5.3
mean duration	0.3 ± 0.1 kyr	-12.7 ± 9.5
mean pseudo-Hudson Strait ice volume change	$1.7 \pm 0.2 \cdot 10^3$ km^3	-25.1 ± 18.7
RMSE	-	7.3 ± 2.5
Mean Bias	-	1.8 ± 1.5

Table A.4: Percentage differences (except first column) of surge characteristics, pseudo-Hudson Strait ice volume RMSE and mean bias compared to the GSM reference setup for implicit coupling between the thermodynamics and ice dynamics in the GSM. No runs crashed and all runs had more than 1 surge. The first 20 kyr of each run are treated as a spin-up interval for the surge characteristics (not the RMSE and mean bias).

A.6.2 PISM

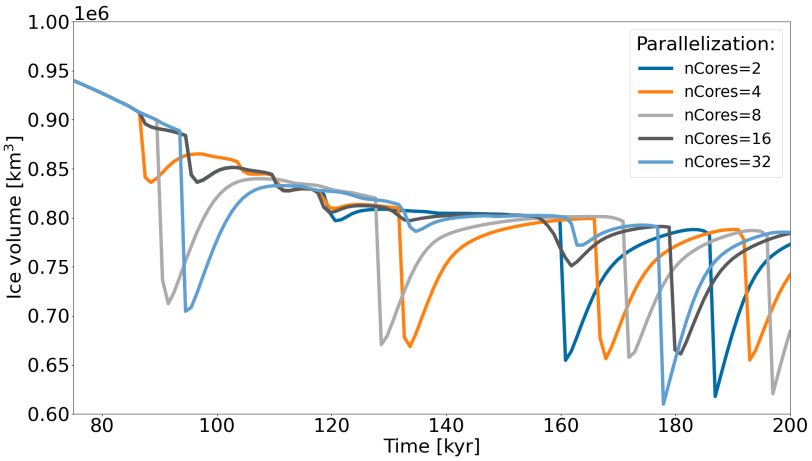

Figure A.18: Ice volume in the eastern half of the pseudo-Hudson Bay and the pseudo-Hudson Strait for parameter vector 8 and different numbers of cores/processes using PISM.

A.6.2.1 Relative tolerances

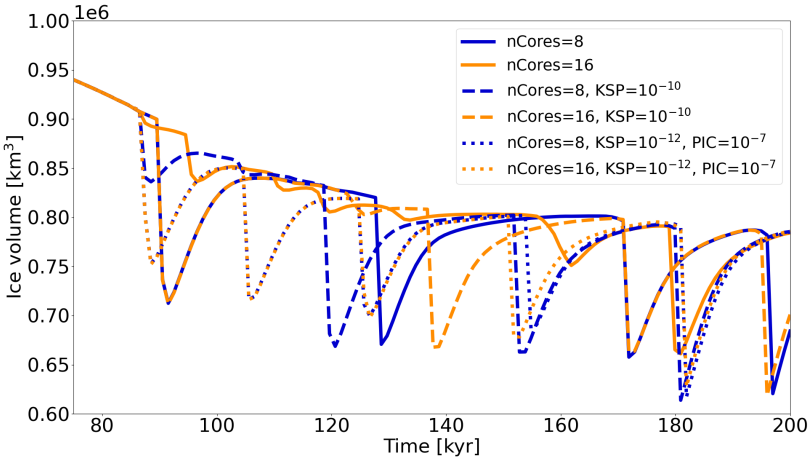

Figure A.19: Ice volume in the eastern half of the pseudo-Hudson Bay and the pseudo-Hudson Strait for parameter vector 8 and different number of cores/processes using PISM with different relative tolerances for the Picard iteration in the calculation of the vertically-averaged effective viscosity (PIC, default is 10^{-4}) and the Krylov linear solver used at each Picard iteration (KSP, default is 10^{-7}.

Setup	number of surges	mean period	mean duration	mean ice volume change	nC	nS1
25 km reference setup	35 ± 25	10 ± 10 kyr	3 ± 2 kyr	$1.1 \pm 0.3 \cdot 10^5$ km^3	0	0
nCores= 8, KSP= 10^{-10}	-10.7 ± 21.6	-1.8 ± 5.6	11.2 ± 32.8	5.3 ± 11.2	0	1
nCores= 16, KSP= 10^{-10}	-4.7 ± 22.4	-2.7 ± 4.8	0.1 ± 9.3	-0.4 ± 5.1	0	1
nCores= 32, KSP= 10^{-10}	-10.5 ± 28.7	-3.7 ± 6.2	-1.2 ± 12.4	1.2 ± 7.2	4	1
nCores= 8, KSP= 10^{-10}, PIC= 10^{-7}	8.3 ± 11.8	-28.6 ± 17.4	-17.1 ± 35.2	9.0 ± 21.5	6	0
nCores= 16, KSP= 10^{-10}, PIC= 10^{-7}	98.1 ± 135.9	-22.5 ± 10.1	-14.4 ± 24.6	15.7 ± 54.4	5	0
nCores= 32, KSP= 10^{-10}, PIC= 10^{-7}	83.8 ± 125.1	-18.2 ± 11.6	-13.9 ± 25.7	23.2 ± 56.4	5	0

Table A.5: Percentage differences (except first row) of surge characteristics compared to the PISM reference setup with different numbers of cores and adjusted relative tolerances for the Picard iteration in the calculation of the vertically-averaged effective viscosity (PIC, default is 10^{-4}) and the Krylov linear solver used at each Picard iteration (KSP, default is 10^{-7}). The values represent the average of 9 parameter vectors. Crashed runs (nC) are not considered and runs with just one surge (nS1) are ignored when calculating the change in mean period. The first 20 kyr of each run are treated as a spin-up interval and are not considered in the above. Note that more than 50 % of all runs with KSP= 10^{-10} and PIC= 10^{-7} did not finish within the time limit set by the computational cluster and are considered as crashed runs (nC). A direct comparison of runs with these tolerances can be found in Fig. A.19. Note that all test runs without preconditioning (removes processor-number-dependence of results) crashed during the spin-up phase and long before the first surge occurs.

A.6.2.2 Adding surface temperature noise

Metric	reference setup	± 0.1°C noise	± 0.5°C noise
#Surges	35 ± 25	-12.4 ± 24.2	-12.0 ± 25.2
mean period	10 ± 10 kyr	-5.6 ± 8.0	-4.0 ± 8.8
mean duration	3 ± 2 kyr	11.5 ± 37.9	2.0 ± 12.9
mean pseudo-Hudson Strait ice volume change	$1.1 \pm 0.3 \cdot 10^5$ km^3	1.9 ± 15.9	2.5 ± 8.1
RMSE	-	4.1 ± 3.5	4.3 ± 2.6
Mean Bias	-	-0.8 ± 1.9	0.1 ± 0.3
nS1	0	1	1

Table A.6: Percentage differences (except first column) of surge characteristics, ice volume RMSE and mean bias compared to the PISM reference setup for two different amplitudes of surface temperature noise. No runs crashed and all runs showed at least 1 surge. Runs with just one surge (nS1) are ignored when caluclating the change in mean period. The first 20 kyr of each run are treated as a spin-up interval for the surge characteristics (not the RMSE and mean bias).

A.7 Sensitivity experiments with a significant effect

A.7.1 Bed thermal model

Metric	reference setup	20 m deep (1 layer) bed thermal model
number of surges	180 ± 100	-31.6 ± 5.6
mean period	1.1 ± 0.5 kyr	60.2 ± 22.4
mean duration	0.3 ± 0.1 kyr	65.2 ± 24.5
mean pseudo-Hudson Strait ice volume change	$1.7 \pm 0.2 \cdot 10^3$ km^3	49.6 ± 14.6
RMSE	-	10.4 ± 2.2
Mean Bias	-	-2.3 ± 1.7

Table A.7: Percentage differences (except first column) of surge characteristics, pseudo-Hudson Strait ice volume RMSE and mean bias compared to the GSM reference setup for runs with only one bed thermal layer (20 m deep). No runs crashed and all runs had more than 1 surge. The first 20 kyr of each run are treated as a spin-up interval for the surge characteristics (not the RMSE and mean bias).

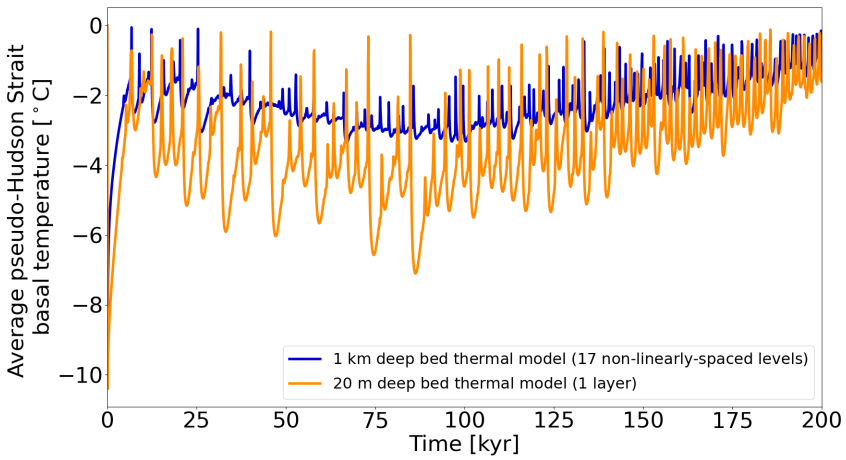

Figure A.20: Average pseudo-Hudson Strait basal ice temperature with respect to the pressure-melting point for parameter vector 1 with a 20 m and 1 km deep bed thermal model (17 non-linearly-spaced levels) using the GSM. The horizontal grid resolution is 3.125 km.

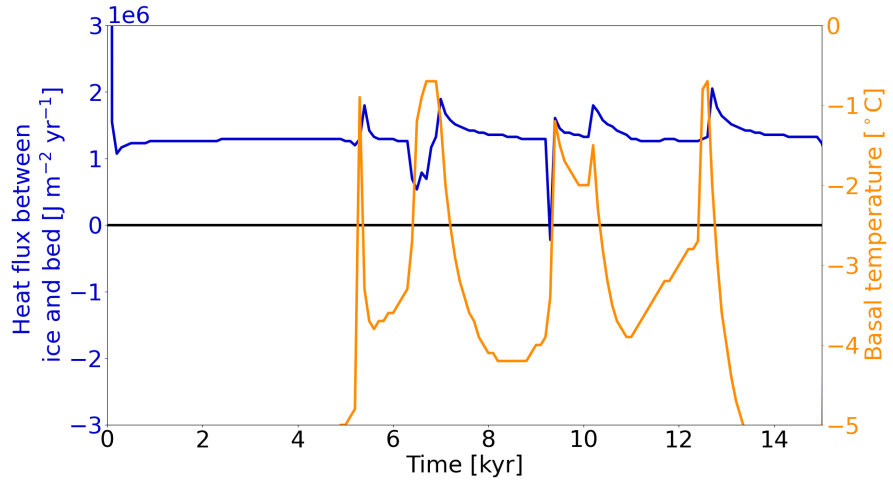

Figure A.21: Heat flux at the base of the ice sheet (positive from bed into ice) and basal ice temperature for a grid cell in the center of the pseudo-Hudson Strait (grid cell center at $x = 376.5625$ km and $y = 248.4375$ km, white star in Fig. 2.1) and parameter vector 1 with only one bed thermal layer (20 m deep) using the GSM. The horizontal grid resolution is 3.125 km.

Metric	reference setup	no bed thermal model
number of surges	35 ± 25	20.7 ± 140.5
mean period	10 ± 10 kyr	79.9 ± 80.0
mean duration	3 ± 2 kyr	69.8 ± 60.4
mean ice volume change	$1.1 \pm 0.3 \cdot 10^5$ km^3	395.8 ± 240.5
RMSE	-	36.0 ± 5.3
Mean Bias	-	-27.1 ± 5.6

Table A.8: Percentage differences (except first column) of surge characteristics, ice volume RMSE and mean bias compared to the PISM reference setup for runs without a bed thermal model. No runs crashed and all runs had more than 1 surge. The first 20 kyr of each run are treated as a spin-up interval for the surge characteristics (not the RMSE and mean bias).

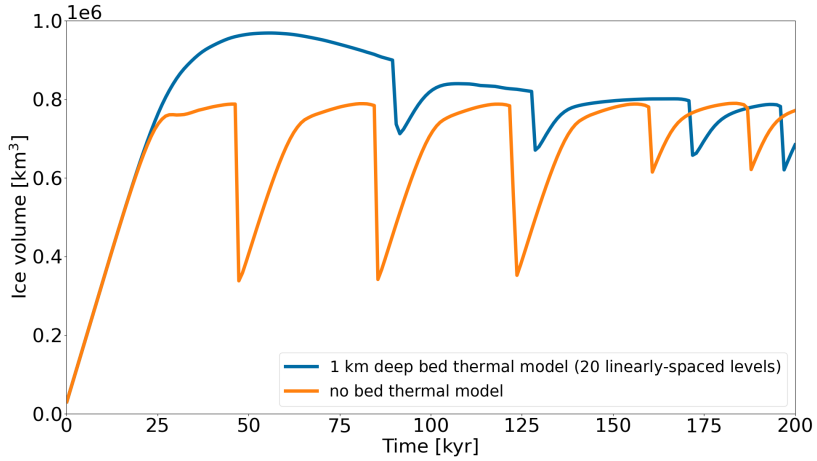

Figure A.22: Ice volume in the eastern half of the pseudo-Hudson Bay and the pseudo-Hudson Strait for parameter vector 8 with and without the 1 km deep (20 linearly-spaced levels) bed thermal model using PISM. The horizontal grid resolution is 25 km.

A.7.2 Basal-temperature at the grid cell interface

Metric	reference setup (TpmTrans)	TpmInt	TpmInt, upwind	TpmCen
nC	0	0	0	1
nS0	0	4	1	0
nS1	0	0	1	0
number of surges	180 ± 100	-96.9 ± 6.3	-90.2 ± 15.4	-74.6 ± 13.9
mean period	1.1 ± 0.5 kyr	106.2 ± 0.0	1645.4 ± 2136.8	609.4 ± 832.22
mean duration	0.3 ± 0.1 kyr	-15.9 ± 0.0	11.1 ± 17.4	43.3 ± 71.1
mean pseudo-Hudson Strait ice volume change	$1.7 \pm 0.2 \cdot 10^3$ km^3	-66.2 ± 0.0	-60.4 ± 6.5	-61.3 ± 5.6
RMSE	-	7.4 ± 2.4	9.4 ± 2.6	6.9 ± 2.5
Mean Bias	-	4.0 ± 1.6	6.7 ± 2.4	2.1 ± 2.1

Table A.9: Percentage differences (except first column) of surge characteristics, pseudo-Hudson Strait ice volume RMSE and mean bias compared to the GSM reference setup for different approaches to calculate the basal-temperature at the grid cell interface (Sec. 2.3.3.2). Crashed runs (nC) are not considered and runs without surges (nS0) only contribute to the change in surge number. Runs with only 1 surge (nS1) are excluded from the calculation of the mean period. The first 20 kyr of each run are treated as a spin-up interval for the surge characteristics (not the RMSE and mean bias).

A.7.3 Basal-temperature ramps at different resolutions

To simplify the comparison of different temperature ramps, we calculate a single value score based on all surge characteristics. The calculation steps are as follows.

1. calculate the absolute values for all surge characteristic means
2. calculate the average across all ramps for all characteristics (means and standard deviations separately, total of 4 means and 4 standard deviations)
3. for each ramp, divide all surge characteristics by their corresponding average
4. sum the values for all surge characteristics (separately for mean and std)

The above calculation combines the 4 surge characteristics to a single value for the mean and standard deviation of each ramp. We keep separate values for the mean and standard deviation since the two metrics contain different information. Smaller values indicate a better agreement with the 3.125 km reference setup.

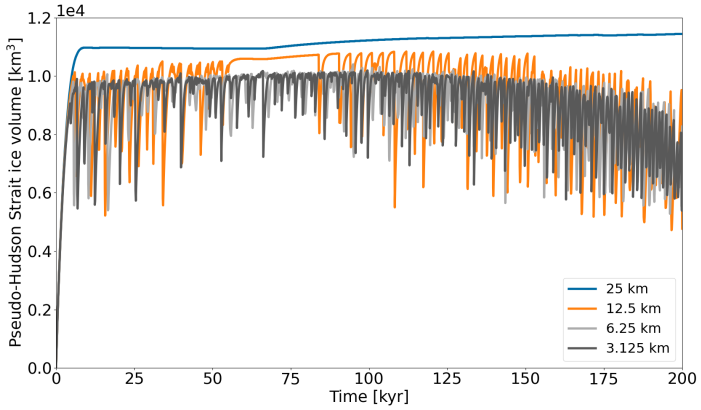

Figure A.23: Pseudo-Hudson Strait ice volume for parameter vector 1 and different horizontal grid resolutions using the GSM. A constant temperature ramp with $T_{\text{ramp}} = 0.0625°\text{C}$ and $T_{\text{exp}} = 28$ is used for all horizontal grid resolutions (magenta line in Fig. 2.2).

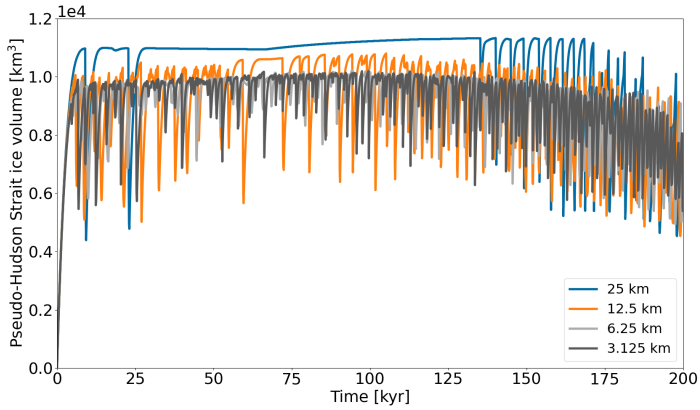

Figure A.24: Pseudo-Hudson Strait ice volume for parameter vector 1 and different horizontal grid resolutions using the GSM. A resolution-dependent temperature (Eq. (2.9)) with $P_{T_{\text{ramp}}} = 1$ and $T_{\text{exp}} = 28$ is used for all horizontal grid resolutions (matching colors in Fig. 2.2).

Metric	#Surges	mean period	mean duration	mean pseudo-Hudson Strait ice volume change	RMSE	Mean Bias
$T_{\text{exp}} = 5$, $T_{\text{ramp}} = 1$	-63.5 ± 17.1	121.7 ± 29.5	300.0 ± 116.6	95.5 ± 39.5	21.8 ± 4.8	-17.8 ± 5.6
$T_{\text{exp}} = 15$, $T_{\text{ramp}} = 1$	-39.0 ± 10.2	64.6 ± 22.8	179.2 ± 117.3	51.5 ± 35.3	17.4 ± 3.7	-11.2 ± 4.6
$T_{\text{exp}} = 28$, $T_{\text{ramp}} = 0.5$	-17.1 ± 7.1	28.6 ± 21.0	64.0 ± 54.1	18.7 ± 12.4	10.0 ± 3.3	-3.5 ± 3.2
$T_{\text{exp}} = 5$, $T_{\text{ramp}} = 0.0625$	-9.5 ± 5.1	16.5 ± 12.4	14.9 ± 12.0	3.9 ± 2.9	8.1 ± 2.4	-0.8 ± 0.6
$T_{\text{exp}} = 10$, $T_{\text{ramp}} = 0.0625$	-9.3 ± 5.0	10.1 ± 5.0	8.8 ± 7.0	3.4 ± 4.0	8.0 ± 2.4	-0.4 ± 0.3
$T_{\text{exp}} = 28$, $T_{\text{ramp}} = 0.125$	-4.6 ± 6.4	3.2 ± 4.2	4.4 ± 5.4	0.3 ± 2.1	7.9 ± 2.2	-0.3 ± 0.2
$T_{\text{exp}} = 14$, $T_{\text{ramp}} = 0.0625$	-7.1 ± 5.1	9.3 ± 7.4	7.3 ± 7.5	2.8 ± 3.4	7.8 ± 1.9	-0.2 ± 0.1
$T_{\text{exp}} = 15$, $T_{\text{ramp}} = 0.0625$	-4.9 ± 4.7	8.4 ± 10.5	4.8 ± 4.4	0.3 ± 6.3	7.8 ± 2.0	-0.2 ± 0.1
$T_{\text{exp}} = 20$, $T_{\text{ramp}} = 0.0625$	-3.0 ± 4.7	2.0 ± 3.9	-0.1 ± 2.9	1.3 ± 4.2	7.9 ± 2.4	-0.1 ± 0.1
$T_{\text{exp}} = 25$, $T_{\text{ramp}} = 0.0625$	-1.2 ± 3.5	4.1 ± 7.7	0.5 ± 1.1	-1.5 ± 3.0	7.8 ± 2.4	-0.0 ± 0.1
3.125 km reference setup	$\mathbf{180 \pm 100}$	$\mathbf{1.1 \pm 0.5}$ **kyr**	$\mathbf{0.3 \pm 0.1}$ **kyr**	$\mathbf{1.7 \pm 0.2 \cdot 10^3}$ **km^3**	-	-
$T_{\text{exp}} = 30$, $T_{\text{ramp}} = 0.0625$	-2.4 ± 3.6	2.4 ± 3.9	-0.1 ± 2.9	-0.4 ± 2.4	7.9 ± 2.2	0.0 ± 0.1
$T_{\text{exp}} = 35$, $T_{\text{ramp}} = 0.0625$	-2.6 ± 4.7	2.6 ± 4.8	0.5 ± 4.3	-0.6 ± 4.1	7.9 ± 2.3	0.1 ± 0.2
$T_{\text{exp}} = 45$, $T_{\text{ramp}} = 0.0625$	-1.3 ± 4.8	1.8 ± 4.4	-0.1 ± 1.6	-1.6 ± 4.1	7.8 ± 2.2	0.1 ± 0.1
$T_{\text{exp}} = 56$, $T_{\text{ramp}} = 0.0625$	-1.7 ± 4.7	1.3 ± 4.7	-3.2 ± 2.1	-0.4 ± 5.2	7.7 ± 2.1	0.2 ± 0.0
$T_{\text{exp}} = 28$, $T_{\text{ramp}} = 0.03125$	-0.8 ± 4.9	3.2 ± 8.0	-2.3 ± 3.1	-0.2 ± 3.8	7.8 ± 2.3	0.2 ± 0.1

Table A.10: Percentage differences (except for reference setup) of surge characteristics, pseudo-Hudson Strait ice volume RMSE and mean bias compared to the GSM reference setup ($T_{\text{ramp}} = 0.0625$, $T_{\text{exp}} = 28$) for different basal-temperature ramps. The ramps are sorted from widest (first row) to sharpest (last row, see Fig. A.25). The bold reference values in the middle of the table separate the ramps that are wider (above) and sharper (below) than the reference setup. No runs crashed and all runs had more than 1 surge. The first 20 kyr of each run are treated as a spin-up interval for the surge characteristics (not the RMSE and mean bias).

ramp	score mean	score SD	sum of scores
res= 25 km, $T_{\text{exp}} = 5$, $T_{\text{ramp}} = 0.5$	**0.85**	**2.92**	**3.77**
res= 25 km, $T_{\text{exp}} = 15$, $T_{\text{ramp}} = 1$	1.08	3.53	4.61
res= 25 km, $T_{\text{exp}} = 10$, $T_{\text{ramp}} = 0.5$	1.58	3.88	5.46
res= 12.5 km, $T_{\text{exp}} = 10$, $T_{\text{ramp}} = 0.25$	3.87	4.11	7.98
res= 12.5 km, $T_{\text{exp}} = 20$, $T_{\text{ramp}} = 0.25$	3.04	2.55	**5.59**
res= 12.5 km, $T_{\text{exp}} = 25$, $T_{\text{ramp}} = 0.25$	3.43	3.31	6.74
res= 12.5 km, $T_{\text{exp}} = 28$, $T_{\text{ramp}} = 0.25$	**2.93**	2.72	5.65
res= 12.5 km, $T_{\text{exp}} = 30$, $T_{\text{ramp}} = 0.25$	3.54	**2.45**	5.99
res= 12.5 km, $T_{\text{exp}} = 35$, $T_{\text{ramp}} = 0.25$	3.30	2.98	6.28
res= 12.5 km, $T_{\text{exp}} = 45$, $T_{\text{ramp}} = 0.25$	3.36	3.17	6.54
res= 12.5 km, $T_{\text{exp}} = 28$, $T_{\text{ramp}} = 0.0625$	3.40	2.87	6.27
res= 6.25 km, $T_{\text{exp}} = 10$, $T_{\text{ramp}} = 0.125$	2.73	1.69	4.42
res= 6.25 km, $T_{\text{exp}} = 15$, $T_{\text{ramp}} = 0.125$	2.13	**1.17**	**3.30**
res= 6.25 km, $T_{\text{exp}} = 20$, $T_{\text{ramp}} = 0.125$	1.92	2.98	4.90
res= 6.25 km, $T_{\text{exp}} = 25$, $T_{\text{ramp}} = 0.125$	2.09	2.35	4.44
res= 6.25 km, $T_{\text{exp}} = 28$, $T_{\text{ramp}} = 0.125$	2.05	2.10	4.15
res= 6.25 km, $T_{\text{exp}} = 30$, $T_{\text{ramp}} = 0.125$	1.95	1.63	3.58
res= 6.25 km, $T_{\text{exp}} = 35$, $T_{\text{ramp}} = 0.125$	1.94	1.66	3.60
res= 6.25 km, $T_{\text{exp}} = 45$, $T_{\text{ramp}} = 0.125$	**1.70**	2.67	4.37
res= 6.25 km, $T_{\text{exp}} = 28$, $T_{\text{ramp}} = 0.0625$	1.80	2.56	4.36

Table A.11: Single value scores for the mean and standard deviation of the basal-temperature ramps. The temperature ramps are shown in Fig. A.26. A total of 12, 13, and 13 ramps were tested at 25 km, 12.5 km, and 6.25 km horizontal grid resolution, respectively. Note that ramps whose sum (score mean + score SD) differ by more than 50 % from the minimum sum at the corresponding resolution are not listed here. The minimum scores for the mean, standard deviation, and sum at each resolution are marked as bold numbers. No runs crashed and all runs had more than 1 surge. Note that the sum of scores can be slightly off due to rounding (± 0.01).

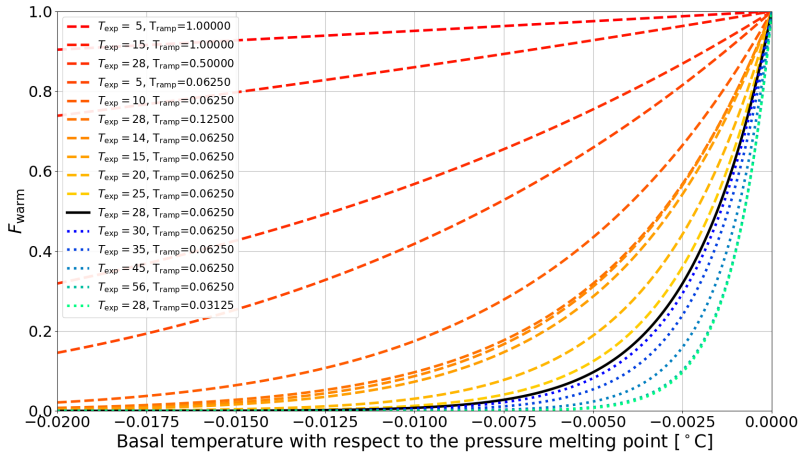

Figure A.25: Temperature ramps for different values of T_{ramp} and T_{exp}. The black solid line shows the ramp used for the 3.125 km horizontal grid resolution reference setup ($T_{\text{ramp}} = 0.0625$, $T_{\text{exp}} = 28$). The solid and dotted lines show ramps that are wider and sharper than the reference setup, respectively. The depicted temperature ramps are the same as the ones listed in Fig. 2.9 and Table A.10.

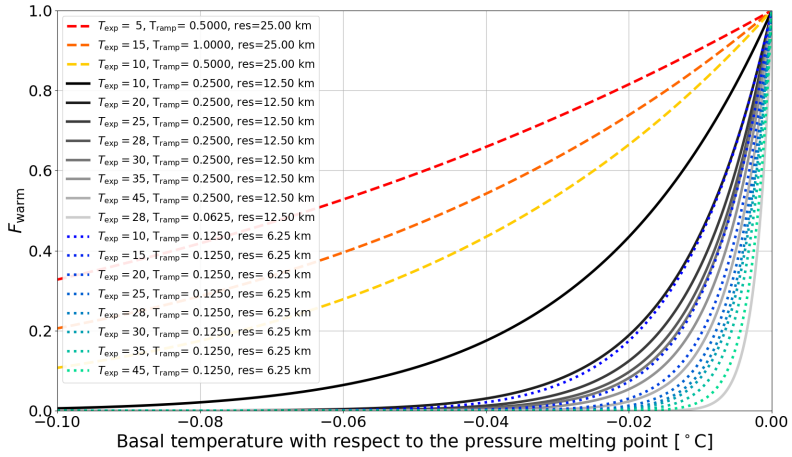

Figure A.26: Shown are the temperature ramps listed in Table A.11 at 25 km (dashed lines), 12.5 km (solid lines), and 6.25 km horizontal grid resolution (dotted lines).

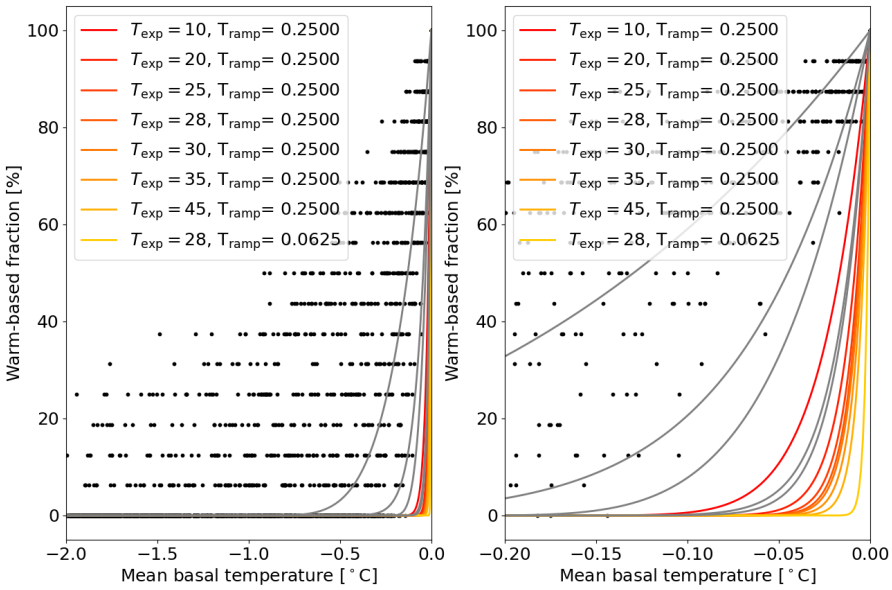

Figure A.27: Warm-based fraction (basal-temperature with respect to the pressure-melting point at 0 °C) vs. mean basal-temperature with respect to the pressure-melting point when upscaling a 3.125 km run to 12.5 km horizontal grid resolution including all 5 parameter vectors using the GSM. Only grid cells within the pseudo-Hudson Strait and time steps within the surges of the 10 kyr after the first surge are considered. The restriction to the 10 kyr after the first surge for these experiments is set by storage limitations due to the high temporal resolution of the model output fields (10 yr). The colored ramps correspond to the 12.5 km horizontal grid resolution basal-temperature ramps in Table A.11 and the gray lines show all other ramps that were tested at this resolution.

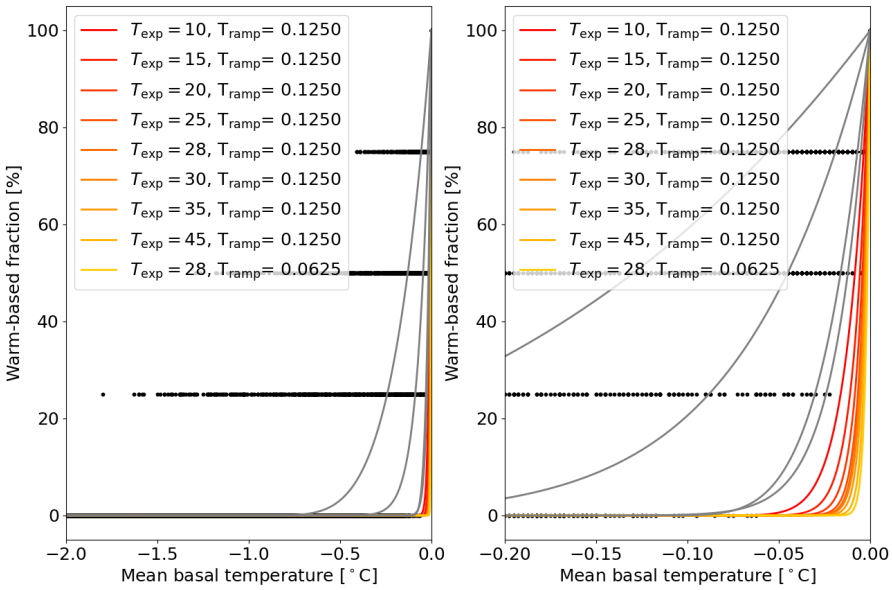

Figure A.28: Warm-based fraction (basal-temperature with respect to the pressure-melting point at 0 °C) vs. mean basal-temperature with respect to the pressure-melting point when upscaling a 3.125 km run to 6.25 km horizontal grid resolution including all 5 parameter vectors using the GSM. The colored ramps correspond to the 6.25 km horizontal grid resolution basal-temperature ramps in Table A.11 and the gray lines show all other ramps that were tested at this resolution. Otherwise same as Fig. A.27.

A.7.4 Smooth sediment transition zone and non-flat topography

Metric	reference setup (abrupt transition) reference values	3.125 km wide transition	25 km wide transition	3.125 km wide transition with HB/HS topography	25 km wide transition with HB/HS topography
number of surges	180 ± 100	-4.2 ± 8.9	1.0 ± 11.4	36.3 ± 17.3	19.9 ± 22.6
mean period	1.1 ± 0.5 kyr	4.6 ± 9.2	-0.4 ± 10.4	2.2 ± 48.0	14.5 ± 45.1
mean duration	0.3 ± 0.1 kyr	2.7 ± 3.6	7.2 ± 4.4	10.2 ± 17.5	24.3 ± 9.0
mean pseudo-Hudson Strait ice volume change	$1.7 \pm 0.2 \cdot 10^3$ km^3	0.2 ± 4.8	-1.7 ± 4.1	8.4 ± 10.0	17.3 ± 15.6
RMSE	-	7.9 ± 2.3	8.0 ± 2.2	11.2 ± 1.8	12.2 ± 2.0
Mean Bias	-	0.0 ± 0.2	-0.6 ± 0.5	-6.2 ± 1.9	-6.6 ± 2.2

Table A.12: Percentage differences (except first column) of surge characteristics, pseudo-Hudson Strait ice volume RMSE and mean bias compared to the GSM reference setup for runs with a smooth transition between hard bedrock and soft sediment, and runs with a pseudo-Hudson Bay/Hudson Strait (HB/HS) topography. No runs crashed and all runs had more than 1 surge. The first 20 kyr of each run are treated as a spin-up interval for the surge characteristics (except for the RMSE and mean bias).

Comparing the runs for parameter vector 1 more closely shows that when using a non-flat topography, the surges now start and propagate at the southernmost and northernmost end of the pseudo-Hudson Strait, where the topography is deepest and begins to slope upwards. Additionally, the surges tend to propagate faster and extend further to the West and in North-South direction than without topography (e.g., 8.0 to 8.3 kyr in the bottom row of video 07 of Hank (2023b)). This is mainly due to warmer basal conditions in the transition zone and Hudson Bay region before the start of the surge (200 m bed depression increases the heat generation at the bed (video 08 of Hank (2023b)) which, in turn, increases the average basal-temperature with respect to the pressure-melting point). Furthermore, the pressure-melting point

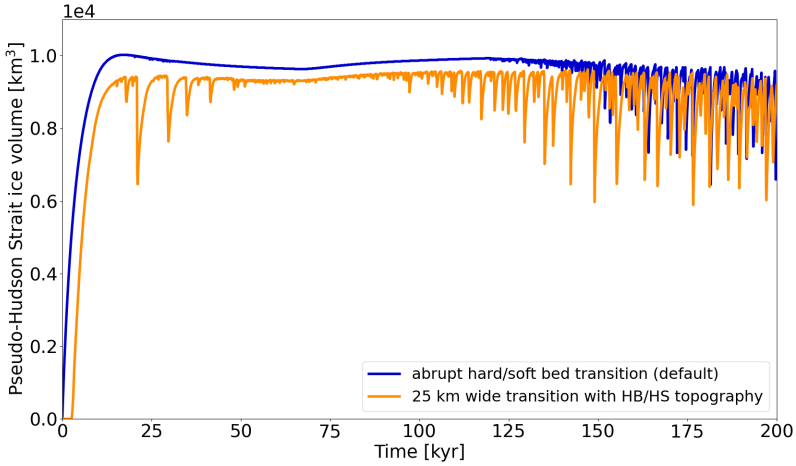

Figure A.29: Pseudo-Hudson Strait ice volume for parameter vector 0 with and without a 200 m deep topography in the pseudo-Hudson Bay and Hudson Strait region using the GSM. In runs with a non-flat topography, the initial glaciation is delayed because the pseudo-Hudson Strait topography is below sea level. The horizontal grid resolution is 3.125 km.

in the 200 m deep Hudson Strait and 500 m deep ocean setup is first reached further inland and not at the eastern end of the pseudo-Hudson Strait, as is the case for a flat topography (e.g., 7.8 to 8.1 kyr in the bottom row of video 07 of Hank (2023b)).

Metric	reference setup (smooth transition, e.g., Fig. A.8) reference values	abrupt transition	smooth transition with HB/HS topography
number of surges	35 ± 25	-4.8 ± 13.4	-0.1 ± 190
mean period	10 ± 10 kyr	7.4 ± 24.5	79.0 ± 64.1
mean duration	3 ± 2 kyr	21.5 ± 59.4	56.2 ± 53.4
mean pseudo-Hudson Strait ice volume change	$1.1 \pm 0.3 \cdot 10^5$ km^3	14.1 ± 37.8	389.5 ± 169.8
RMSE	-	4.4 ± 2.5	37.7 ± 2.5
Mean Bias	-	-0.2 ± 0.3	-30.4 ± 1.4
nS0	0	0	3

Table A.13: Percentage differences (except first column) of surge characteristics, ice volume RMSE and mean bias compared to the PISM reference setup for runs with an abrupt transition between hard bedrock and soft sediment, and runs with a pseudo-Hudson Bay/Hudson Strait (HB/HS) topography. No runs crashed and runs without surges (nS0) only contribute to the change in surge number. The first 20 kyr of each run are treated as a spin-up interval for the surge characteristics (except for the RMSE and mean bias).

A.7.5 Basal-hydrology

Metric	no hydrology	local hydrology	no hydrology, double C_{rmu}	no hydrology, double C_{fslid}
number of surges	180 ± 100	-3.8 ± 23.8	-9.5 ± 3.9	-3.0 ± 8.8
mean period	1.1 ± 0.5 kyr	17.4 ± 44.9	12.4 ± 4.1	4.5 ± 10.3
mean duration	0.3 ± 0.1 kyr	11.6 ± 19.1	3.1 ± 5.6	2.3 ± 3.5
mean ice volume change	$1.7 \pm 0.2 \cdot 10^3$ km^3	20.2 ± 44.7	10.5 ± 5.9	-0.9 ± 5.8
RMSE	-	8.7 ± 2.6	8.5 ± 2.7	7.8 ± 2.2
Mean Bias	-	-0.9 ± 0.8	-0.4 ± 0.4	-0.1 ± 0.1

Table A.14: Percentage differences (except first column) of surge characteristics, ice volume RMSE and mean bias of GSM runs with a local basal-hydrology model compared to runs without sub-glacial hydrology. Additionally shown are the changes in surge characteristics when doubling the values of the soft and hard-bed-sliding coefficient (C_{rmu} and C_{fslid} in Table 2.1, respectively). No runs crashed and all runs had more than 1 surge. The first 20 kyr of each run are treated as a spin-up interval for the surge characteristics (not the RMSE and mean bias).

A.8 Sensitivity experiments without a significant effect

A.8.1 Weight of adjacent minimum basal-temperature

Depending on the location of the adjacent minimum grid cell center basal-temperature, either the ice flow (when the adjacent minimum basal-temperature is downstream) or upstream propagation of the surge should be affected (decreasing basal interface temperature with increasing weight). For the large-scale surges, the adjacent minimum basal-temperature is almost exclusively located upstream (e.g., video 02 of Hank (2023b)). Changing the weight of the adjacent minimum basal-temperature, therefore, affects the surge propagation rather than blocking parts of the ice flow.

Here we compare the effect of three different weights on the GSM surge characteristics (Eq. (A.1)): no consideration of adjacent minimum basal-temperature ($W_{\mathrm{Tb,min}} = 0.0$), basal-temperature at the interface depends to 50 % on the adjacent minimum basal-temperature at the grid cell center (reference setup, $W_{\mathrm{Tb,min}} = 0.5$), and basal-temperature at the interface is equal to the adjacent minimum basal-temperature at the grid cell center ($W_{\mathrm{Tb,min}} = 1.0$).

The surge cycling response to changes in $W_{\mathrm{Tb,min}}$ is not coherent (Table A.15). For instance, the mean surge period increases for both $W_{\mathrm{Tb,min}} = 0.$ and $W_{\mathrm{Tb,min}} = 1.0$ compared to the reference $W_{\mathrm{Tb,min}} = 0.5$. However, standard deviations are large, indicating a different model response for different parameter vectors.

Metric	reference setup	$W_{\mathrm{Tb,min}} = 0.0$	$W_{\mathrm{Tb,min}} = 1.0$
#Surges	180 ± 100	-9.6 ± 6.5	-3.7 ± 7.8
mean period	1.1 ± 0.5 kyr	14.7 ± 13.5	3.0 ± 0.8
mean duration	0.3 ± 0.1 kyr	5.1 ± 4.9	-2.6 ± 3.3
mean pseudo-Hudson Strait ice volume change	$1.7 \pm 0.2 \cdot 10^3$ km^3	-1.9 ± 4.0	4.0 ± 6.7
RMSE	-	7.8 ± 2.5	8.0 ± 2.5
Mean Bias	-	-0.1 ± 0.1	0.3 ± 0.1

Table A.15: Percentage differences (except first column) of surge characteristics, pseudo-Hudson Strait ice volume RMSE and mean bias compared to the GSM reference setup ($W_{\mathrm{Tb,min}} = 0.5$) for different weights of the adjacent minimum basal-temperature for the basal-sliding temperature ramp. No runs crashed and all runs had more than 1 surge. The first 20 kyr of each run are treated as a spin-up interval for the surge characteristics (not the RMSE and mean bias).

A.8.2 Different approaches to basal-hydrology

Here we compare the effects on surge characteristics when using a horizontal transport model in PISM instead of a simple local basal-hydrology. In general, PISM experiments with a mass-conserving horizontal transport hydrology model yield similar results to the local hydrology model (Fig. 2.7 and Table A.16). The mean duration, period, and ice volume change increase (11 %, 10 %, and 7 %, respectively), while the number of surges decreases (5 %). These differences are on the same level as the MNEEs (Table 2.6) and show large standard deviations, indicating a different model response for different parameter vectors. The ice volume RMSE and mean bias are also small (+3.9 % and −0.1 %, respectively).

Metric	local hydrology	horizontal transport
number of surges	35 ± 25	-4.6 ± 14.5
mean period	10 ± 10 kyr	10.8 ± 27.8
mean duration	3 ± 2 kyr	10.5 ± 35.4
mean ice volume change	$1.1 \pm 0.3 \cdot 10^5$ km^3	6.8 ± 17.9
RMSE	-	3.9 ± 2.5
Mean Bias	-	-0.1 ± 0.3

Table A.16: Percentage differences (except first column) of surge characteristics, ice volume (eastern half of pseudo-Hudson Bay and the pseudo-Hudson Strait) RMSE and mean bias of PISM runs with a mass-conserving horizontal transport hydrology model compared to the local hydrology model. No runs crashed and all runs had more than 1 surge. The first 20 kyr of each run are treated as a spin-up interval for the surge characteristics (not the RMSE and mean bias).

A.8.3 Basal-hydrology instead of basal-temperature ramp as the primary smoothing mechanism

We examine the effects of a local basal-hydrology as main smoothing mechanism for basal-sliding (compared to a basal-temperature ramp) by using a very sharp ramp ($T_{\text{ramp}} = 0.001$, $T_{\text{exp}} = 28$), minimizing the smoothing effect of the basal-temperature ramp. The change in surge characteristics between runs with local basal-hydrology and the sharp temperature ramp and the GSM reference setup is similar (maximum difference of 3 %; compare Tables A.14 and A.17) to the runs with local basal-hydrology and the reference basal-temperature ramp ($T_{\text{ramp}} = 0.0625$, $T_{\text{exp}} = 28$), indicating that the local basal-hydrology is the primary smoothing mechanism in both cases. The differences in the change of surge characteristics between the reference and the sharper ramp are smaller than the MNEEs, preventing further analysis.

Metric	reference setup	sharper ramp ($T_{\text{ramp}} = 0.001$, $T_{\text{exp}} = 28$), local hydrology
#Surges	180 ± 100	-3.8 ± 24.6
mean period	1.1 ± 0.5 kyr	16.0 ± 42.0
mean duration	0.3 ± 0.1 kyr	8.7 ± 17.0
mean pseudo-Hudson Strait ice volume change	$1.7 \pm 0.2 \cdot 10^3$ km^3	21.5 ± 43.3
RMSE	-	8.9 ± 3.2
Mean Bias	-	-0.6 ± 0.9

Table A.17: Percentage differences (except first column) of surge characteristics, pseudo-Hudson Strait ice volume RMSE and mean bias compared to the GSM reference setup with local basal-hydrology instead of a basal-temperature ramp as the primary smoothing mechanism. No runs crashed and all runs had more than 1 surge. The first 20 kyr of each run are treated as a spin-up interval for the surge characteristics (not the RMSE and mean bias).

A.9 Convergence study

A.9.1 GSM convergence study without basal-hydrology

Analyzing individual GSM parameter vectors in detail shows that some discrepancies prevail even when using a resolution-dependent temperature ramp. In the case of parameter vector 1, for example, surges do still not occur for the coldest temperatures (Fig. A.30). Note the asymmetry in termination and onset of surge cyclicity ($\Delta t_1 < \Delta t_2$). For increasing temperatures after the minimum surface temperature $T_{\text{min}} = -15°\text{C}$ at $t_{\text{min}} = 66.7$ kyr, the first surge occurs at a surface temperature slightly higher than the initial temperature T_{init}, for which oscillations occur. The difference between Δt_1 and Δt_2 is ~ 25 kyr and closely resembles the lag of the average pseudo-Hudson Strait basal-temperature with respect to the pressure-melting point behind the surface temperature changes. For example, the minimum average

pseudo-Hudson Strait basal-temperature with respect to the pressure-melting point ($T_{\mathrm{bpm}} = -3.2°\mathrm{C}$) occurs 23 kyr after the minimum surface temperature (not shown). The period without oscillations in the 25 km run corresponds to a period of somewhat smaller and less frequent oscillations in the finer resolution runs (Fig. A.24).

Setup	number of surges	mean period	mean duration	mean pseudo-Hudson Strait ice volume change	nS0
3.125 km reference setup	180 ± 100	1.1 ± 0.5 kyr	0.3 ± 0.1 kyr	$1.7 \pm 0.2 \cdot 10^3$ km^3	0
25 km, constant ramp	-95.1 ± 7.4	942.3 ± 517.70	300.0 ± 172.22	95.9 ± 52.6	3
25 km, resolution-dependent ramp	-78.1 ± 18.2	414.5 ± 309.0	119.5 ± 17.6	91.9 ± 23.6	1
25 km, $T_{\mathrm{ramp}} = 0.5$, $T_{\mathrm{exp}} = 5$	-15.9 ± 20.4	29.7 ± 24.6	43.8 ± 36.6	3.5 ± 18.7	0
12.5 km, constant ramp	-59.2 ± 16.5	129.0 ± 41.8	90.3 ± 17.9	50.3 ± 76.5	0
12.5 km, resolution-dependent ramp, also minimum mean score	-56.5 ± 15.1	115.7 ± 46.8	101.1 ± 20.5	33.0 ± 66.3	0
6.25 km, constant ramp	-24.2 ± 13.1	36.4 ± 20.9	24.8 ± 8.5	14.9 ± 14.2	0
6.25 km, resolution-dependent ramp	-27.9 ± 9.9	42.2 ± 18.9	32.1 ± 6.3	15.9 ± 12.3	0
6.25 km, $T_{\mathrm{ramp}} = 0.125$, $T_{\mathrm{exp}} = 45$	-25.3 ± 13.6	37.9 ± 26.7	28.2 ± 7.0	9.8 ± 11.6	0

Table A.18: Percentage differences (except first row) of surge characteristics compared to the 3.125 km GSM reference setup. The values represent the average of 5 parameter vectors. No runs crashed and runs without surges (nS0) only contribute to the change in surge numbers. The first 20 kyr of each run are treated as a spin-up interval and are not considered in the above. The resolution-dependent ramps ($T_{\mathrm{exp}} = 28$) and constant ramp (black line, $T_{\mathrm{ramp}} = 0.0625$, $T_{\mathrm{exp}} = 28$) are shown in Fig. 2.2. The third ramp listed for each resolution is the ramp with the smallest mean score (Table A.11).

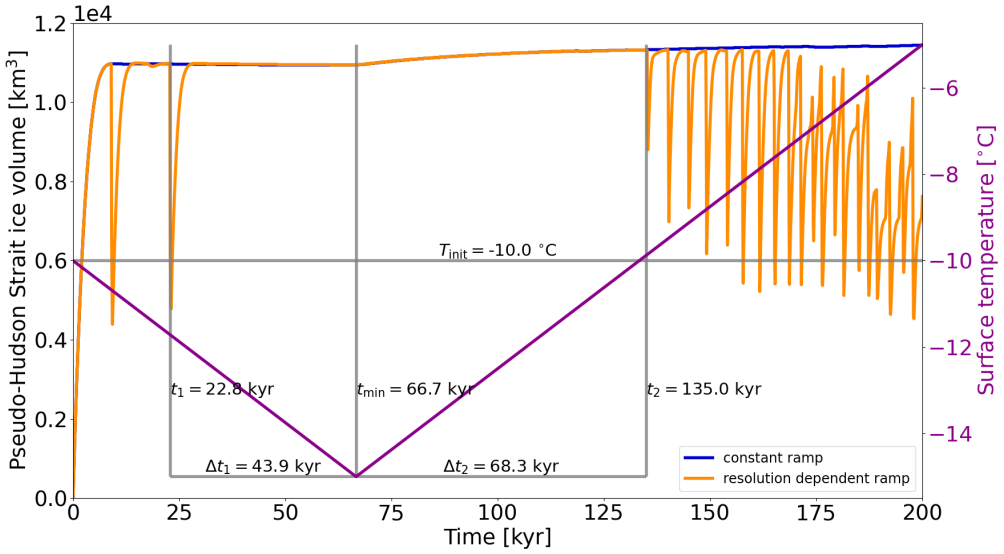

Figure A.30: Pseudo-Hudson Strait ice volume for parameter vector 1 and different basal-temperature ramps using the GSM (constant ramp: $T_{\text{ramp}} = 0.0625°\text{C}$ and $T_{\text{exp}} = 28$; resolution-dependent ramp: $T_{\text{ramp}} = 0.5°\text{C}$ and $T_{\text{exp}} = 28$, see Fig. 2.2). The right axis shows the surface temperature when ignoring the lapse rate dependency. t_{min}, t_1, and t_2 mark the time of the minimum surface temperature, the start of the last surge before t_{min}, and the start of the first surge after t_{min}, respectively. Δt_1 and Δt_2 represent the time difference between t_{min} and t_1 and t_2, respectively. T_{init} indicates the surface temperature at the beginning of the run.

Setup	mean RMSE	mean Bias
25 km, constant ramp	17.1 ± 4.7	14.6 ± 4.4
12.5 km, constant ramp	10.3 ± 2.5	4.0 ± 1.1
6.25 km, constant ramp	8.7 ± 2.2	0.4 ± 0.5
25 km, resolution-dependent ramp	15.3 ± 3.0	10.3 ± 2.5
12.5 km, resolution-dependent ramp	10.3 ± 2.8	3.0 ± 2.3
6.25 km, resolution-dependent ramp	8.5 ± 2.3	0.2 ± 0.6
25 km, $T_{\text{ramp}} = 0.5$, $T_{\text{exp}} = 5$	12.8 ± 2.4	6.4 ± 1.7
12.5 km, $T_{\text{ramp}} = 0.25$, $T_{\text{exp}} = 28$, same as resolution-dependent ramp	10.3 ± 2.8	3.0 ± 2.3
6.25 km, $T_{\text{ramp}} = 0.125$, $T_{\text{exp}} = 45$	8.5 ± 2.0	0.6 ± 0.5

Table A.19: Pseudo-Hudson Strait ice volume RMSE and mean bias compared to the 3.125 km GSM reference setup in percent. The values represent the average of 5 parameter vectors. No runs crashed and the entire 200 kyr run time is used (no spin-up interval).

A.9.2 GSM convergence study with basal-hydrology

Based on the results without basal-hydrology (Sec. 2.3.4.1), 5 basal-temperature ramps ($T_{\text{exp}} = [5, 10, 15, 20, 28]$) with a resolution-dependent T_{ramp} (Eq. (2.9)) are tested for all resolutions. As it is unclear which basal-temperature ramp should be used at the finest horizontal grid resolution (3.125 km), we test two different ramps ($T_{\text{exp}} = [5, 28]$). The experiments that yield the smallest differences in surge characteristics (smallest mean score in Tables A.20 and A.21) compared to the corresponding 3.125 km reference runs (bold rows) are presented in Table A.22.

Similar to the results without a basal-hydrology model, the smallest differences in surge characteristics (except the mean pseudo-Hudson Strait ice volume change) occur for the coarsest horizontal grid resolution (25 km, Table A.22). This likely indicates that the optimal ramps at 12.5 and 6.25 km horizontal grid resolution have

not been found.

In general, the resolution-dependent ramp with $T_{\text{exp}} = 5$ leads to the smallest differences between coarse- and fine-resolution runs. The differences in surge characteristics are significantly smaller than for a resolution-dependent temperature ramp without local basal-hydrology (except for the mean pseudo-Hudson Strait ice volume change, Tables A.18 vs. A.22), further underlining the importance of the basal-hydrology.

Except for 12.5 km horizontal grid resolution, the resolution-dependent ramp with $T_{\text{exp}} = 5$ yields a self-consistent response across all resolutions. At 12.5 km, the next closest exponent ($T_{\text{exp}} = 10$) has the minimum mean score. However, given that there is no single best ramp across all resolutions, we assess different ramps as to whether differences are within inferred numerical errors (DWINE). To this end, we calculate the differences between the ramp with the minimum mean score and all other ramps at each resolution and for all surge characteristics (Tables A.20 and A.21). We rule out ramps for which the differences exceed the maximum MNEEs (maximum of Tables 2.5 and A.2) for more than one surge characteristic (DWINE failures).

Under these criteria and when using $T_{\text{exp}} = 5$ at 3.125 km horizontal grid resolution, the resolution-dependent ramp with $T_{\text{exp}} = 10$ remains within the DWINE ensemble for all resolutions (Table A.21). The results for $T_{\text{exp}} = 28$ at 3.125 km horizontal grid resolution do not yield a single ramp that remains within the DWINE ensemble at all resolutions (Table A.20). However, except for 6.25 km, for which the differences between the tested basal-temperature ramps are the smallest, $T_{\text{exp}} = 5$ yields the minimum mean-score.

The pseudo-Hudson Strait ice volume RMSE and mean bias show convergence

(smaller differences) for both 3.125 km horizontal grid resolution setups (Table A.23).

ramp	score mean	score SD	sum of scores	DWINE failures
res= 25 km, $T_{\text{exp}} = 5$, $T_{\text{ramp}} = 0.5$	**0.99**	4.31	**5.31**	0
res= 25 km, $T_{\text{exp}} = 10$, $T_{\text{ramp}} = 0.5$	1.44	5.29	6.74	2
res= 25 km, $T_{\text{exp}} = 15$, $T_{\text{ramp}} = 0.5$	4.80	**3.05**	7.85	4
res= 25 km, $T_{\text{exp}} = 20$, $T_{\text{ramp}} = 0.5$	5.65	3.47	9.11	4
res= 25 km, $T_{\text{exp}} = 28$, $T_{\text{ramp}} = 0.5$	7.11	3.88	11.00	4
res= 12.5 km, $T_{\text{exp}} = 5$, $T_{\text{ramp}} = 0.25$	**3.69**	4.60	8.29	0
res= 12.5 km, $T_{\text{exp}} = 10$, $T_{\text{ramp}} = 0.25$	3.81	5.07	8.88	2
res= 12.5 km, $T_{\text{exp}} = 15$, $T_{\text{ramp}} = 0.25$	3.82	4.11	7.93	2
res= 12.5 km, $T_{\text{exp}} = 20$, $T_{\text{ramp}} = 0.25$	4.21	3.42	7.63	3
res= 12.5 km, $T_{\text{exp}} = 28$, $T_{\text{ramp}} = 0.25$	4.47	**2.81**	**7.28**	4
res= 6.25 km, $T_{\text{exp}} = 5$, $T_{\text{ramp}} = 0.125$	4.03	4.29	8.33	3
res= 6.25 km, $T_{\text{exp}} = 10$, $T_{\text{ramp}} = 0.125$	3.94	**3.76**	7.70	3
res= 6.25 km, $T_{\text{exp}} = 15$, $T_{\text{ramp}} = 0.125$	4.65	3.90	8.55	1
res= 6.25 km, $T_{\text{exp}} = 20$, $T_{\text{ramp}} = 0.125$	3.79	3.82	**7.60**	1
res= 6.25 km, $T_{\text{exp}} = 28$, $T_{\text{ramp}} = 0.125$	**3.59**	4.23	7.82	0

Table A.20: Single value scores for the mean and standard deviation of the basal-temperature ramps and the number of DWINE failures (maximum 4) for a resolution-dependent reference temperature ramp with $T_{\text{exp}} = 28$ in the GSM. The minimum scores for the mean, standard deviation, and sum at each resolution are marked as bold numbers. At = 25 km, 1 run crashed for $T_{\text{exp}} = 10$ and 1 run showed no surges for $T_{\text{exp}} = [15, 20, 28]$. Note that the sum of scores can be slightly off due to rounding (± 0.01).

ramp	score mean	score SD	sum of scores	DWINE failures
res= 25 km, $T_{\text{exp}} = 5$, $T_{\text{ramp}} = 0.5$	**0.84**	3.91	**4.75**	0
res= 25 km, $T_{\text{exp}} = 10$, $T_{\text{ramp}} = 0.5$	1.21	5.04	6.25	1
res= 25 km, $T_{\text{exp}} = 15$, $T_{\text{ramp}} = 0.5$	4.89	**3.29**	8.18	4
res= 25 km, $T_{\text{exp}} = 20$, $T_{\text{ramp}} = 0.5$	5.76	3.63	9.40	4
res= 25 km, $T_{\text{exp}} = 28$, $T_{\text{ramp}} = 0.5$	7.30	4.13	11.43	4
res= 12.5 km, $T_{\text{exp}} = 5$, $T_{\text{ramp}} = 0.25$	3.97	4.49	8.45	2
res= 12.5 km, $T_{\text{exp}} = 10$, $T_{\text{ramp}} = 0.25$	**3.77**	4.60	8.37	0
res= 12.5 km, $T_{\text{exp}} = 15$, $T_{\text{ramp}} = 0.25$	3.79	4.13	7.93	1
res= 12.5 km, $T_{\text{exp}} = 20$, $T_{\text{ramp}} = 0.25$	4.10	3.50	**7.59**	1
res= 12.5 km, $T_{\text{exp}} = 28$, $T_{\text{ramp}} = 0.25$	4.37	**3.28**	7.65	2
res= 6.25 km, $T_{\text{exp}} = 5$, $T_{\text{ramp}} = 0.125$	**3.53**	4.44	7.97	0
res= 6.25 km, $T_{\text{exp}} = 10$, $T_{\text{ramp}} = 0.125$	4.27	3.77	8.04	0
res= 6.25 km, $T_{\text{exp}} = 15$, $T_{\text{ramp}} = 0.125$	4.59	3.82	8.42	1
res= 6.25 km, $T_{\text{exp}} = 20$, $T_{\text{ramp}} = 0.125$	3.91	**3.64**	**7.55**	1
res= 6.25 km, $T_{\text{exp}} = 28$, $T_{\text{ramp}} = 0.125$	3.70	4.33	8.03	3

Table A.21: Single value scores for the mean and standard deviation of the basal-temperature ramps and the number of DWINE failures (maximum 4) for a resolution-dependent reference temperature ramp with $T_{\text{exp}} = 5$ in the GSM. The minimum scores for the mean, standard deviation, and sum at each resolution are marked as bold numbers. At = 25 km, 1 run crashed for $T_{\text{exp}} = 10$ and 1 run showed no surges for $T_{\text{exp}} = [15, 20, 28]$. Note that the sum of scores can be slightly off due to rounding (± 0.01).

Setup	number of surges	mean period	mean duration	mean pseudo-Hudson Strait ice volume change
3.125 km, $T_{\mathrm{ramp}} = 0.0625$, $T_{\mathrm{exp}} = 28$	**197 ± 131**	**1.5 ± 1.1 kyr**	**0.3 ± 0.2 kyr**	**$2.0 \pm 0.7 \cdot 10^3$ km^3**
25 km, $T_{\mathrm{ramp}} = 0.5$, $T_{\mathrm{exp}} = 5$	9.7 ± 59.9	15.5 ± 42.3	24.3 ± 36.1	13.6 ± 46.7
12.5 km, $T_{\mathrm{ramp}} = 0.25$, $T_{\mathrm{exp}} = 5$	-36.1 ± 17.6	68.0 ± 49.8	97.1 ± 60.3	3.0 ± 26.4
6.25 km, $T_{\mathrm{ramp}} = 0.125$, $T_{\mathrm{exp}} = 28$	-13.2 ± 31.1	27.0 ± 40.6	25.7 ± 25.2	5.6 ± 27.5
3.125 km, $T_{\mathrm{ramp}} = 0.0625$, $T_{\mathrm{exp}} = 5$	**190 ± 118**	**1.3 ± 0.7 kyr**	**0.3 ± 0.2 kyr**	**$1.8 \pm 0.4 \cdot 10^3$ km^3**
25 km, $T_{\mathrm{ramp}} = 0.5$, $T_{\mathrm{exp}} = 5$	-2.4 ± 35.8	16.1 ± 31.4	20.7 ± 30.3	14.3 ± 35.8
12.5 km, $T_{\mathrm{ramp}} = 0.25$, $T_{\mathrm{exp}} = 10$	-37.7 ± 12.1	61.7 ± 44.1	63.4 ± 34.8	20.5 ± 39.0
6.25 km, $T_{\mathrm{ramp}} = 0.125$, $T_{\mathrm{exp}} = 5$	-25.6 ± 13.9	37.8 ± 23.8	41.1 ± 21.3	0.3 ± 19.8

Table A.22: Percentage differences (except bold rows) of surge characteristics compared to the 3.125 km GSM setups with local basal-hydrology (bold rows, $T_{\mathrm{exp}} = [5, 28]$) for the ramps with the smallest mean score (analysis steps described in Sec. A.7.3). The values represent the average of 5 parameter vectors. No runs crashed and all runs had more than 1 surge. The first 20 kyr of each run are treated as a spin-up interval and are not considered in the above.

Setup	mean RMSE	mean Bias
25 km, $T_{\mathrm{ramp}} = 0.5$, $T_{\mathrm{exp}} = 5$	14.3 ± 3.2	6.0 ± 0.9
12.5 km, $T_{\mathrm{ramp}} = 0.25$, $T_{\mathrm{exp}} = 5$	11.2 ± 4.2	0.6 ± 2.4
6.25 km, $T_{\mathrm{ramp}} = 0.125$, $T_{\mathrm{exp}} = 28$	10.0 ± 3.0	0.5 ± 0.6
25 km, $T_{\mathrm{ramp}} = 0.5$, $T_{\mathrm{exp}} = 5$	14.5 ± 3.2	6.8 ± 0.4
12.5 km, $T_{\mathrm{ramp}} = 0.25$, $T_{\mathrm{exp}} = 10$	11.7 ± 4.2	1.6 ± 2.5
6.25 km, $T_{\mathrm{ramp}} = 0.125$, $T_{\mathrm{exp}} = 5$	10.1 ± 1.8	0.6 ± 0.8

Table A.23: Resolution scaling of pseudo-Hudson Strait ice volume RMSE and mean bias with local basal-hydrology in percent. The three upper ramps are compared to the 3.125 km GSM setup with $T_{\mathrm{exp}} = 28$, the lower three to $T_{\mathrm{exp}} = 5$. The values represent the average of 5 parameter vectors. No runs crashed and the entire 200 kyr run time is used (no spin-up interval).

A.9.3 GSM convergence study with active SSA everywhere (no basal-hydrology)

Setup	number of surges	mean period	mean duration	mean pseudo-Hudson Strait ice volume change	nS0
3.125 km reference setup	216 ± 146	1.3 ± 0.8 kyr	0.3 ± 0.1 kyr	$1.4 \pm 0.6 \cdot 10^3$ km^3	0
25 km	-76.9 ± 17.9	432.2 ± 384.3	151.7 ± 49.0	163.8 ± 65.9	1
12.5 km	-61.3 ± 23.8	179.8 ± 127.1	154.3 ± 79.3	40.1 ± 54.4	0
6.25 km	-46.2 ± 11.6	66.7 ± 12.9	59.8 ± 19.5	75.1 ± 42.9	0

Table A.24: Percentage differences (except first row) of surge characteristics compared to the 3.125 km GSM reference setup with a resolution-dependent basal-temperature ramp ($T_{\text{exp}} = 28$, Fig. 2.2) and active SSA everywhere. The values represent the average of 5 parameter vectors. No runs crashed and runs without surges (nS0) only contribute to the change in surge numbers. The first 20 kyr of each run are treated as a spin-up interval and are not considered in the above.

A.9.4 PISM convergence study

Similar to the results presented for the GSM (Sec. A.9.1 and A.9.2), analyzing individual parameter vectors for PISM shows significant differences in surge behavior for different horizontal grid resolutions. Parameter vector 8 at 25 km horizontal grid resolution, for example, only shows 4 oscillations (Fig. A.31). In contrast, more oscillations occur for both the 12.5 km and 50 km horizontal grid resolution run. Additionally, most of the 50 km surges transport ice toward the West, whereas the 25 and 12.5 km runs almost exclusively surge through the pseudo-Hudson Strait (video 09 of Hank (2023b)).

Setup	number of surges	mean period	mean duration	mean ice volume change	nC	nS0	nS1
12.5 km reference setup	**22 ± 19**	**9 ± 6 kyr**	**3 ± 1 kyr**	**$1.3 \pm 0.2 \cdot 10^5$ km^3**	**4**	**1**	**0**
50 km	4.1 ± 46.0	15.3 ± 47.4	11.9 ± 33.7	30.6 ± 39.6	0	0	1
25 km	-28.3 ± 12.0	46.5 ± 31.9	6.3 ± 13.8	4.0 ± 20.3	0	0	0

Table A.25: Percentage differences (except bold row) of PISM surge characteristics due to different horizontal grid resolutions. Note that the 12.5 km (finest resolution tested) is used as a reference for the grid resolution convergence study. 4 of the 12.5 km runs crashed after $\sim$ 50 kyr because they hit the run-time limit on the computational cluster (7 days) and one 12.5 km run does not show a surge (nS0). Crashed runs (nC) are not considered and runs without surges in the comparison setup only contribute to the change in surge numbers. Runs without surges in the reference setup are not considered. The first 20 kyr of each run are treated as a spin-up interval and are not considered in the above.

Setup	nC	mean RMSE	mean Bias
50 km	0	11.1 ± 2.6	6.5 ± 4.1
25 km	0	7.4 ± 1.4	3.7 ± 0.8

Table A.26: Ice volume RMSE and mean bias (in percent) due to different horizontal grid resolutions. Note that the 12.5 km (finest resolution tested) is used as a reference for the grid resolution convergence study. 4 of the 12.5 km runs crashed after $\sim$ 50 kyr because they hit the run-time limit on the computational cluster (7 days) and one 12.5 km run does not show a surge (nS0). Crashed runs (nC) are not considered. The entire 200 kyr run time is used (no spin-up interval).

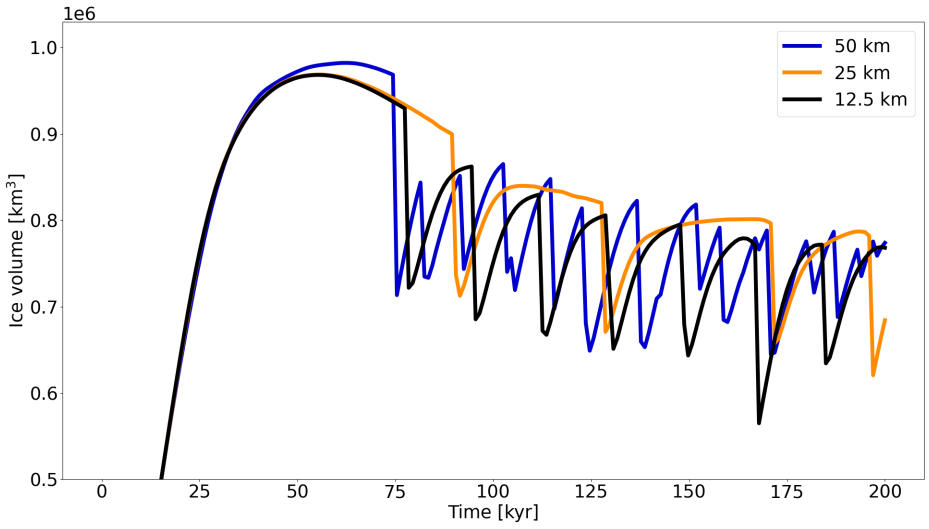

Figure A.31: Ice Volume in the eastern half of the pseudo-Hudson Bay and the pseudo-Hudson Strait for parameter vector 8 and different horizontal grid resolutions using PISM. See also video 09 of Hank (2023b).

Appendix B

Supplement for P2

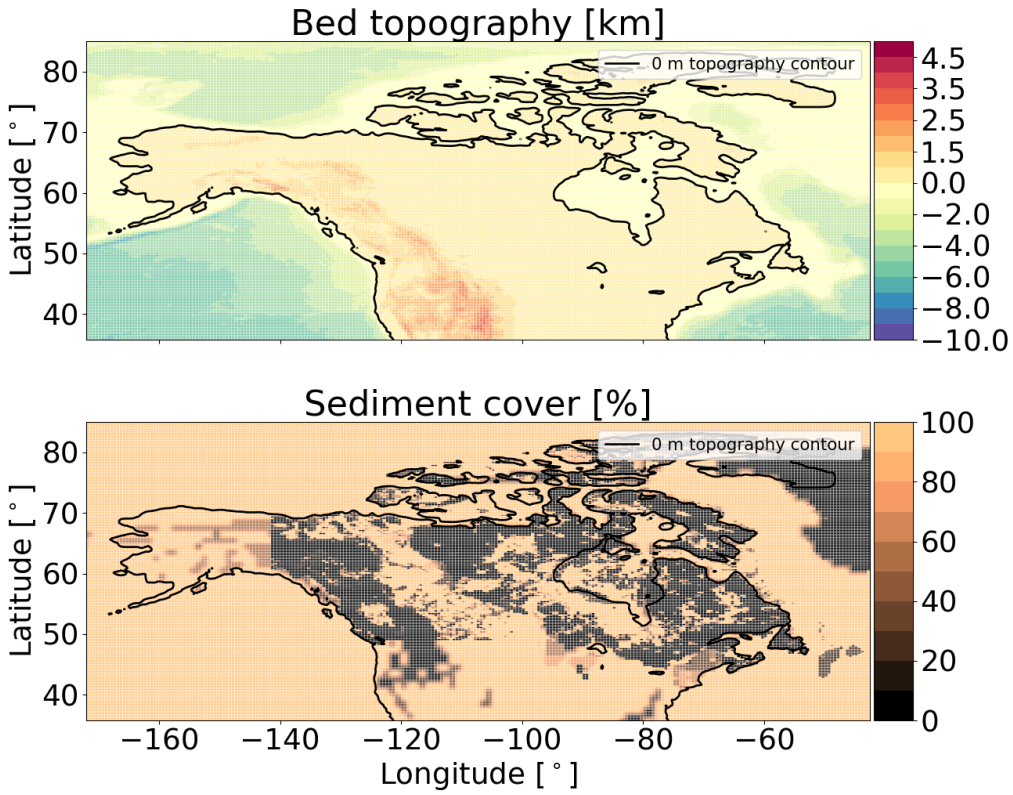

Figure B.1: GSM input present-day bed topography and sediment cover for the full model domain. The black contour line shows the present-day sea level (coastline) used in the GSM. Note the change in the color bar step at 0 km.

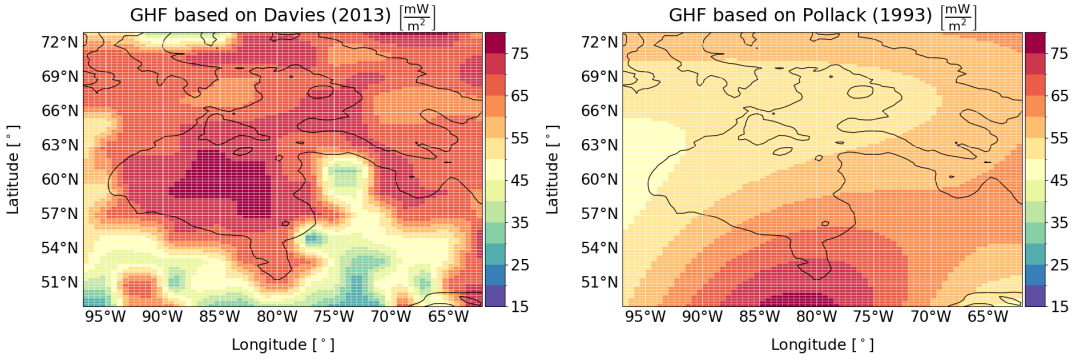

Figure B.2: GSM input geothermal heat flux (GHF) applied at 4 km depth. The left panel shows the default input field (Davies, 2013), whereas the right panel shows the GHF based on Pollack et al. (1993). The black contour line shows the present-day sea level used in the GSM.

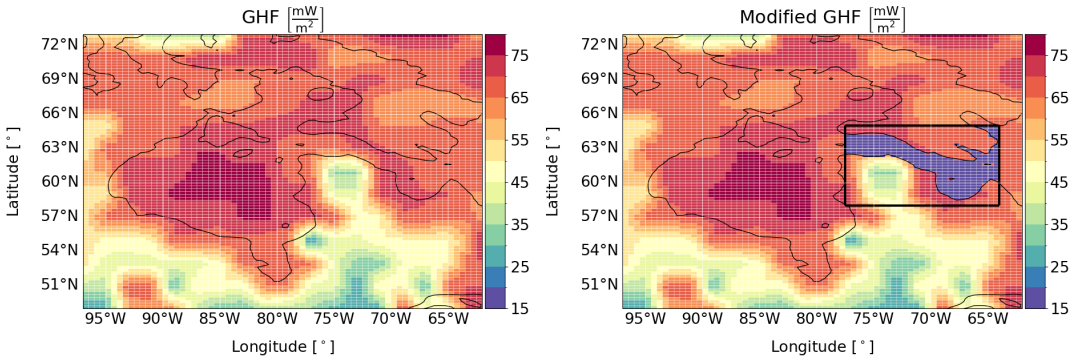

Figure B.3: GSM input geothermal heat flux modification for the Hudson Strait area only. Otherwise as Fig. 3.1.

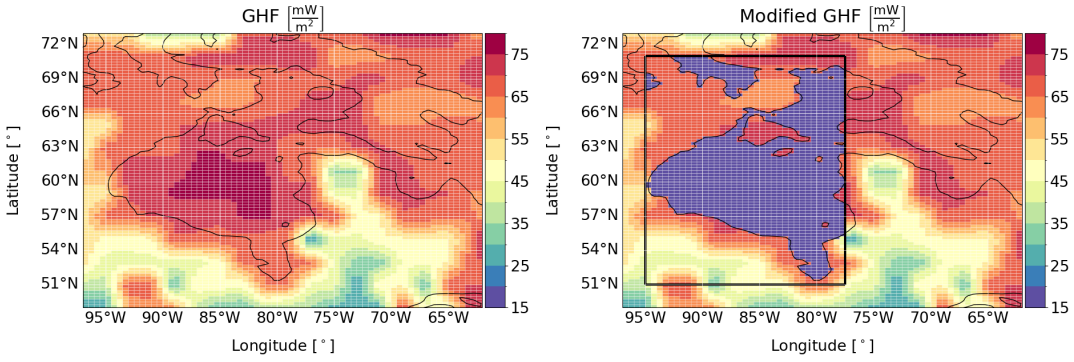

Figure B.4: GSM input geothermal heat flux modification for the Hudson Bay area only. Otherwise as Fig. 3.1.

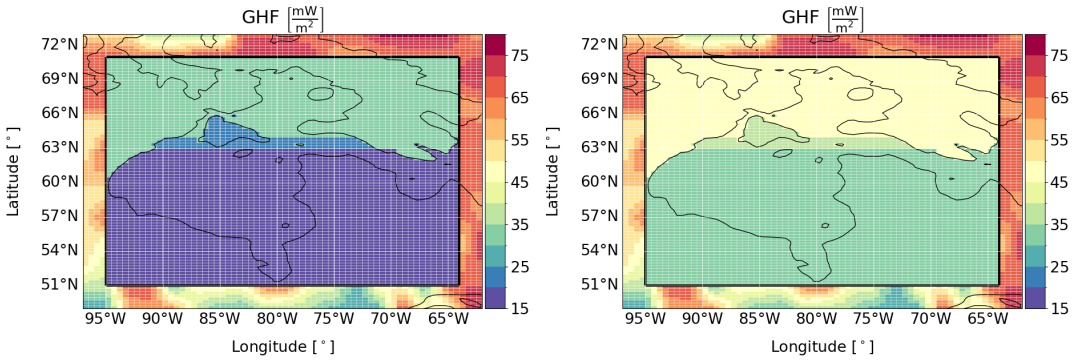

Figure B.5: GSM input geothermal heat flux (GHF) applied at 4 km depth. Both panels show GHF maps used to determine the effect of a lower GHF ($\mathrm{GHF_{ave}} \approx 20\ \frac{\mathrm{mW}}{\mathrm{m^2}}$ and $\mathrm{GHF_{ave}} \approx 35\ \frac{\mathrm{mW}}{\mathrm{m^2}}$ in the left and right panel, respectively) when applied to a larger regional area. The GHF was modified based on the GHF map of Blackwell and Richards (2004, reduced values in left panel). Otherwise as Fig. 3.1.

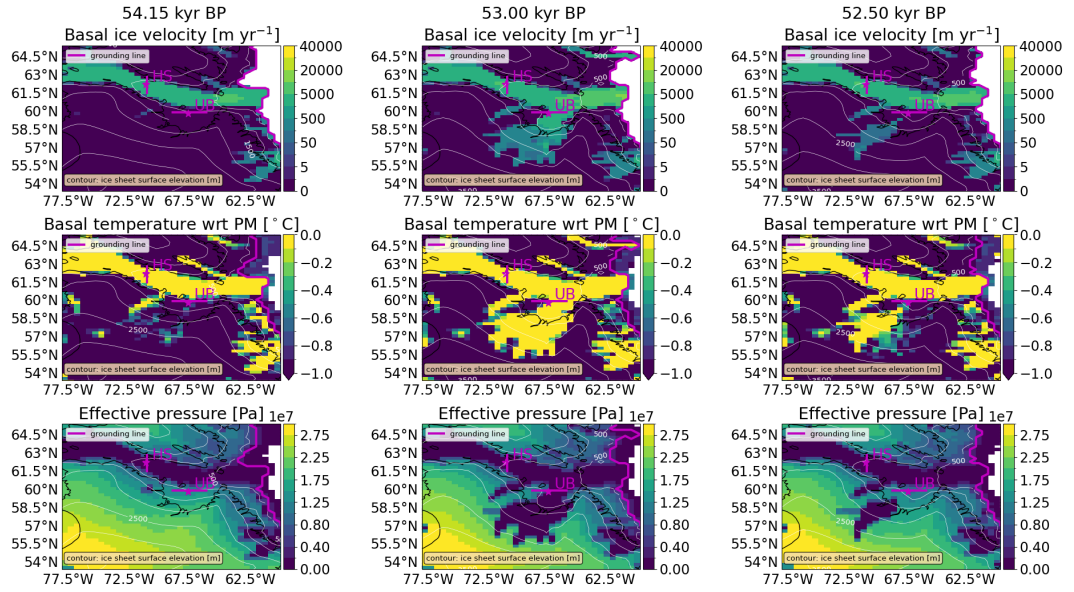

Figure B.6: Basal ice velocity, basal temperature with respect to the pressure melting point, and effective pressure for a surge in Ungava Bay. The 3 time slices show the active Hudson Strait ice stream before the Ungava Bay surge (54.15 kyr BP), the Ungava Bay surge (53.00 kyr BP), and the active Hudson Strait ice stream after the Ungava Bay surge (52.50 kyr BP). The black contour is the present-day coastline provided by *cartopy* (Met Office, 2010 - 2015).

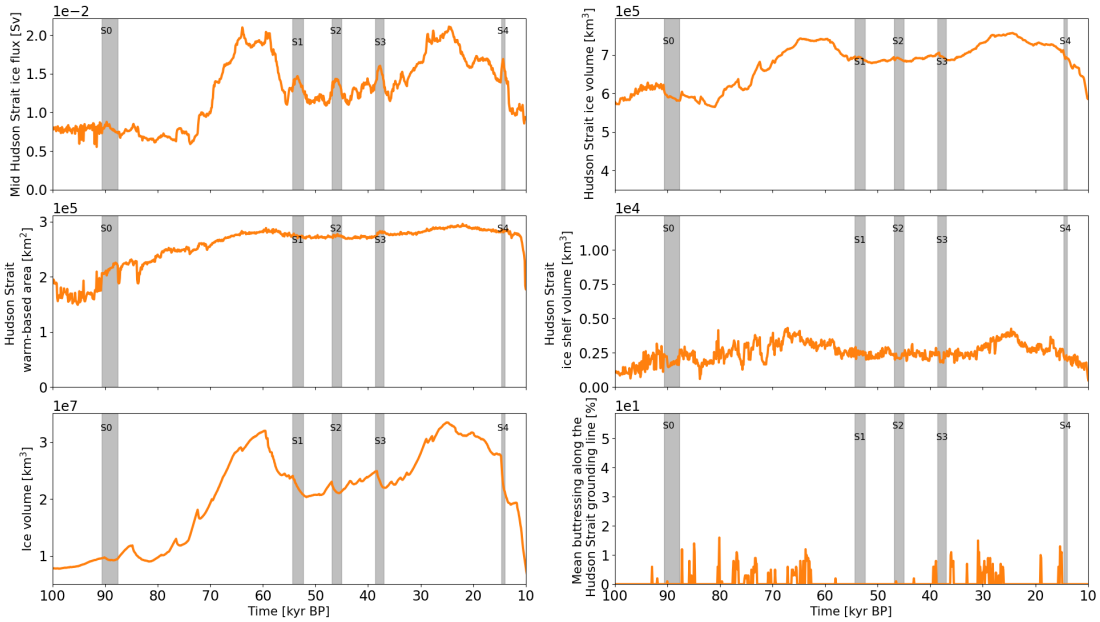

Figure B.7: Time series of parameter vector 11. The bottom left panel shows the overall North American ice volume. Otherwise as Fig. 3.4.

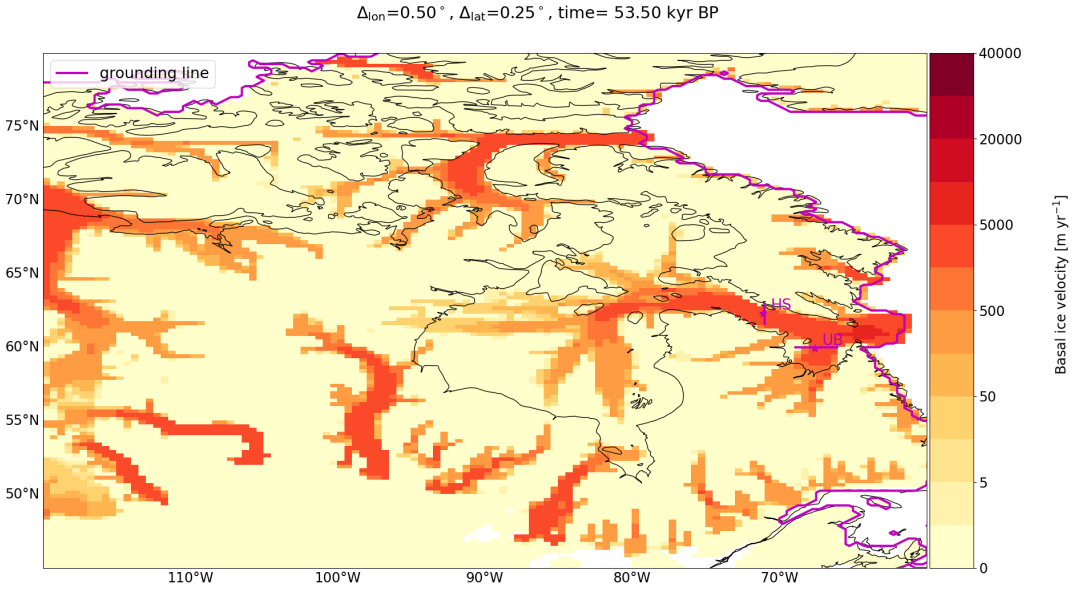

Figure B.8: Basal ice velocity during surge S1 in Fig. B.7. The black contour is the present-day coastline provided by *cartopy* (Met Office, 2010 - 2015).

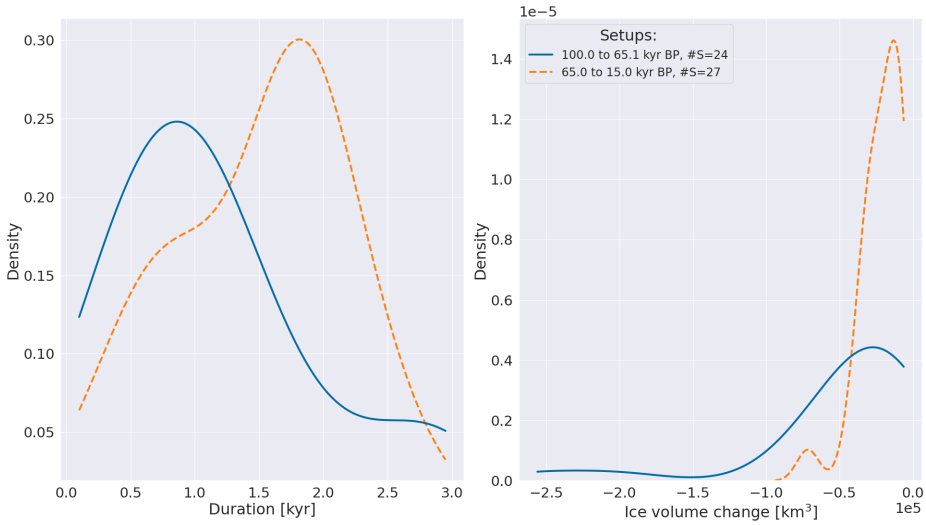

Figure B.9: Kernel density plot for the full ensemble and 2 different periods. #S indicates the total number of surges across all runs of the ensemble.

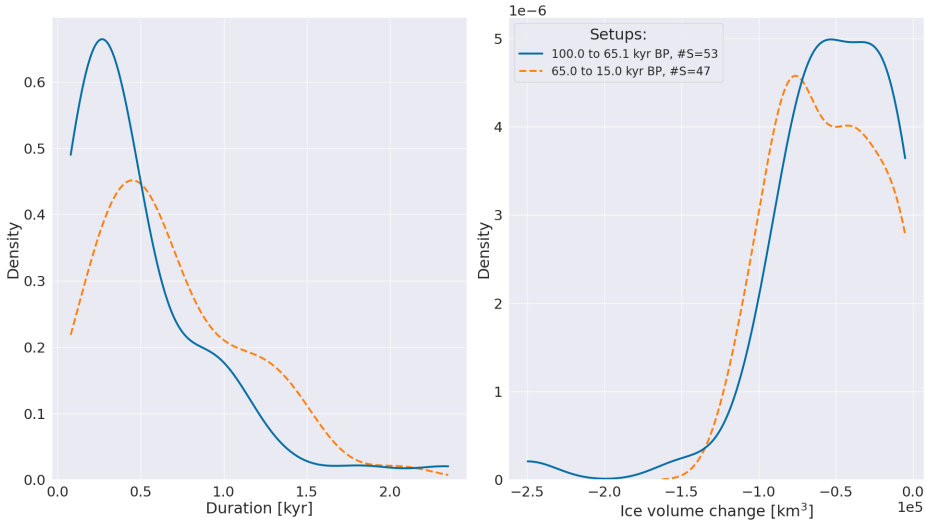

Figure B.10: Kernel density plot for the full ensemble of the $\mathrm{GHF}_{\mathrm{ave}} = 25\ \frac{\mathrm{mW}}{\mathrm{m}^2}$ experiments and 2 different periods. #S indicates the total number of surges across all runs of the ensemble.

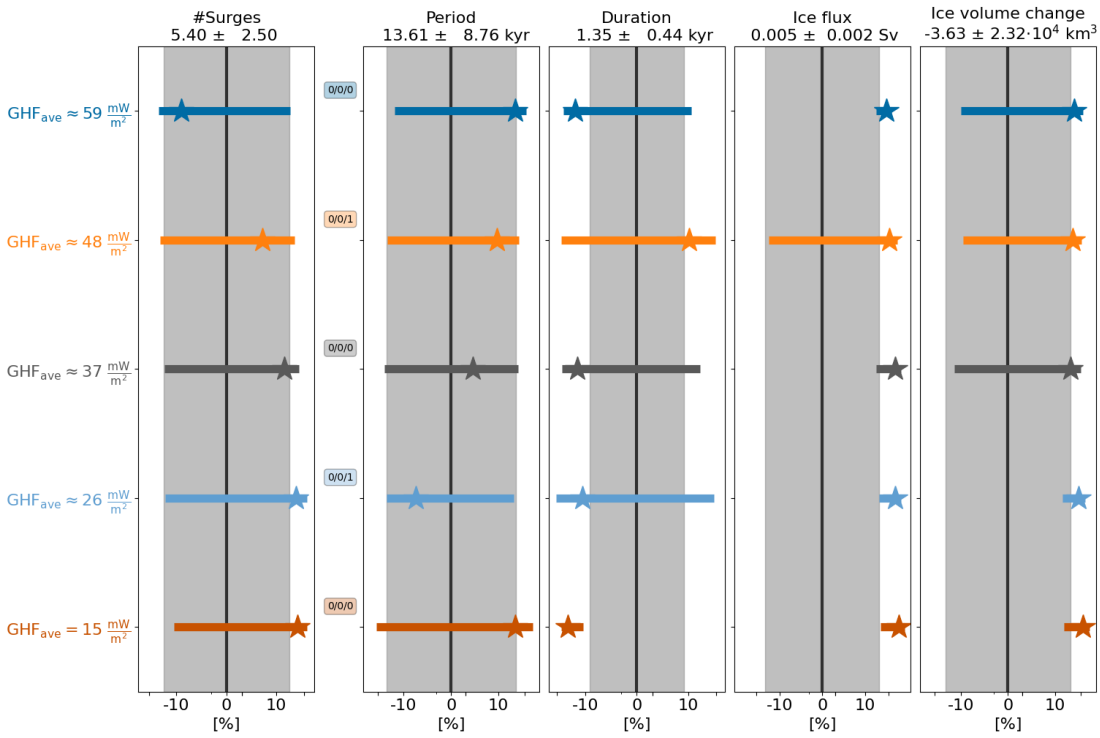

Figure B.11: Percentage differences in surge characteristics compared to the reference setup. Only parameter vectors within the > 2 #surges sub-ensemble are considered. The model setups, from top to bottom, are $\mathrm{GHF}_{\mathrm{ave}} \approx [15, 26, 37, 48, 59]$ $\frac{\mathrm{mW}}{\mathrm{m}^2}$ (Sec. 3.2.4). Otherwise as Fig. 3.6

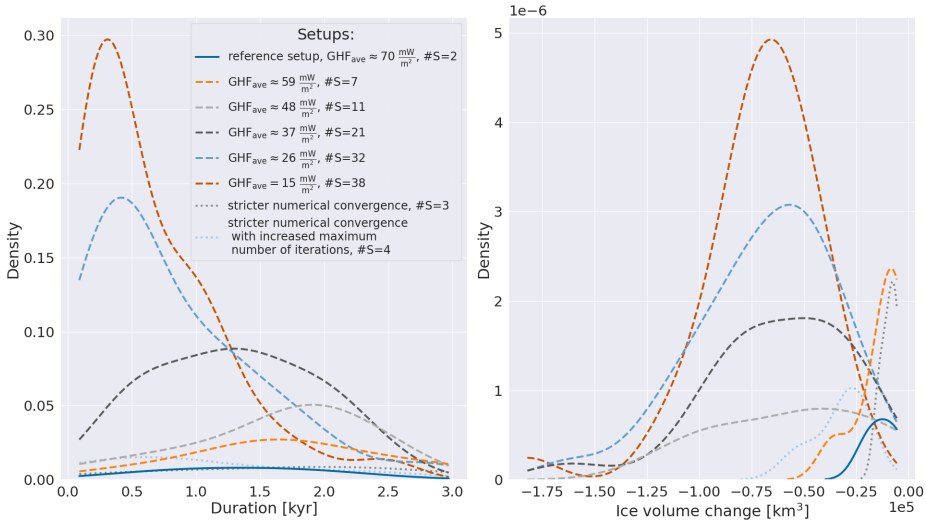

Figure B.12: Kernel density plot for the ≤ 2 #surges sub-ensemble. The reference and MNEEs setups use $\mathrm{GHF}_{\mathrm{ave}} \approx 70$ $\frac{\mathrm{mW}}{\mathrm{m}^2}$. #S indicates the total number of surges across all runs of the sub-ensemble.

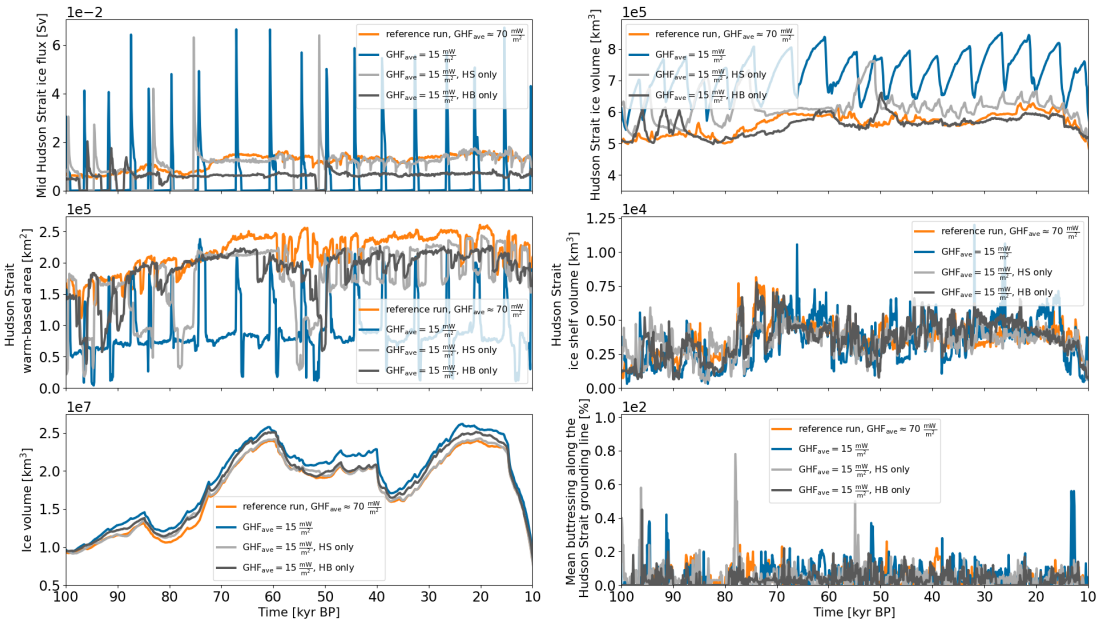

Figure B.13: Time series of parameter vector 16 for different GHF modification regions (Sec. 3.2.4 and Fig. 3.1, B.3, and B.4). The Hudson Strait ice stream surges are not highlighted for clarity. The bottom left panel shows the overall North American ice volume. Otherwise as Fig. 3.4.

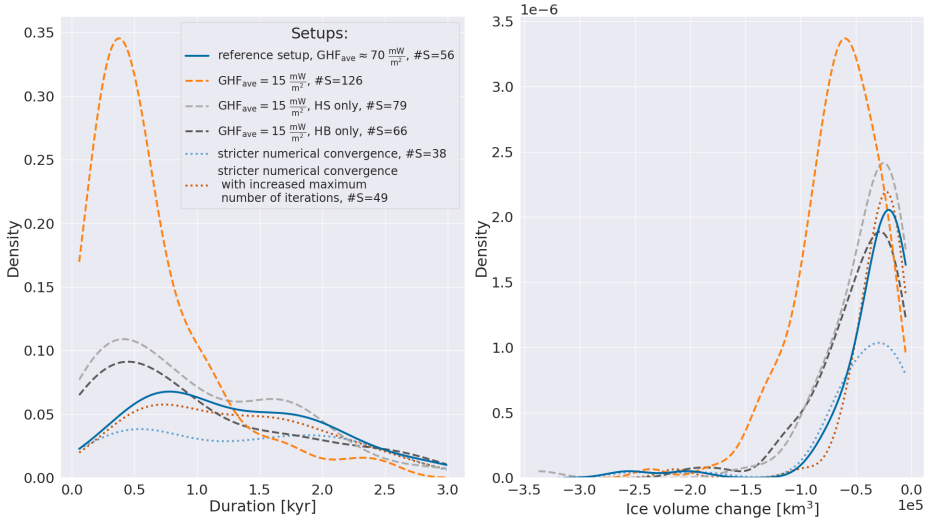

Figure B.14: Kernel density plot for the full ensemble. The reference and MNEEs setups use $\mathrm{GHF}_{\mathrm{ave}} \approx 70\ \frac{\mathrm{mW}}{\mathrm{m}^2}$. The GHF modification is applied separately to the Hudson Strait (Fig. B.3) and Hudson Bay (Fig. B.4) for the *HS only* and *HB only* setup, respectively. #S indicates the total number of surges across all runs of the ensemble.

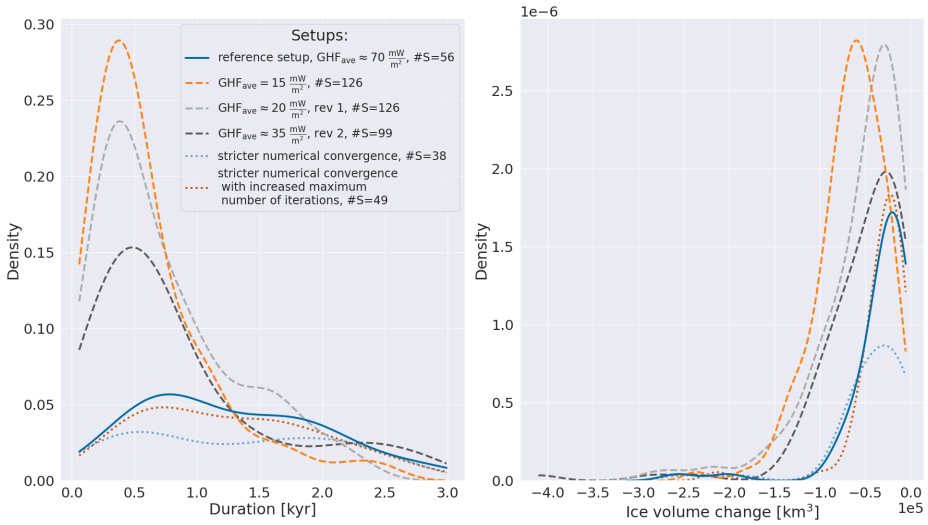

Figure B.15: Kernel density plot for the full ensemble. The reference and MNEEs setups use GHF$_{\text{ave}} \approx 70$ $\frac{\text{mW}}{\text{m}^2}$. The GHF modification for GHF$_{\text{ave}} = 15$ $\frac{\text{mW}}{\text{m}^2}$ is applied to the Hudson Strait and Hudson Bay (Fig. 3.1). GHF$_{\text{ave}} \approx 20$ $\frac{\text{mW}}{\text{m}^2}$, rev 1 and GHF$_{\text{ave}} \approx 35$ $\frac{\text{mW}}{\text{m}^2}$, rev 2 use the GHF maps shown in the left and right panels of Fig. B.5, respectively. #S indicates the total number of surges across all runs of the ensemble.

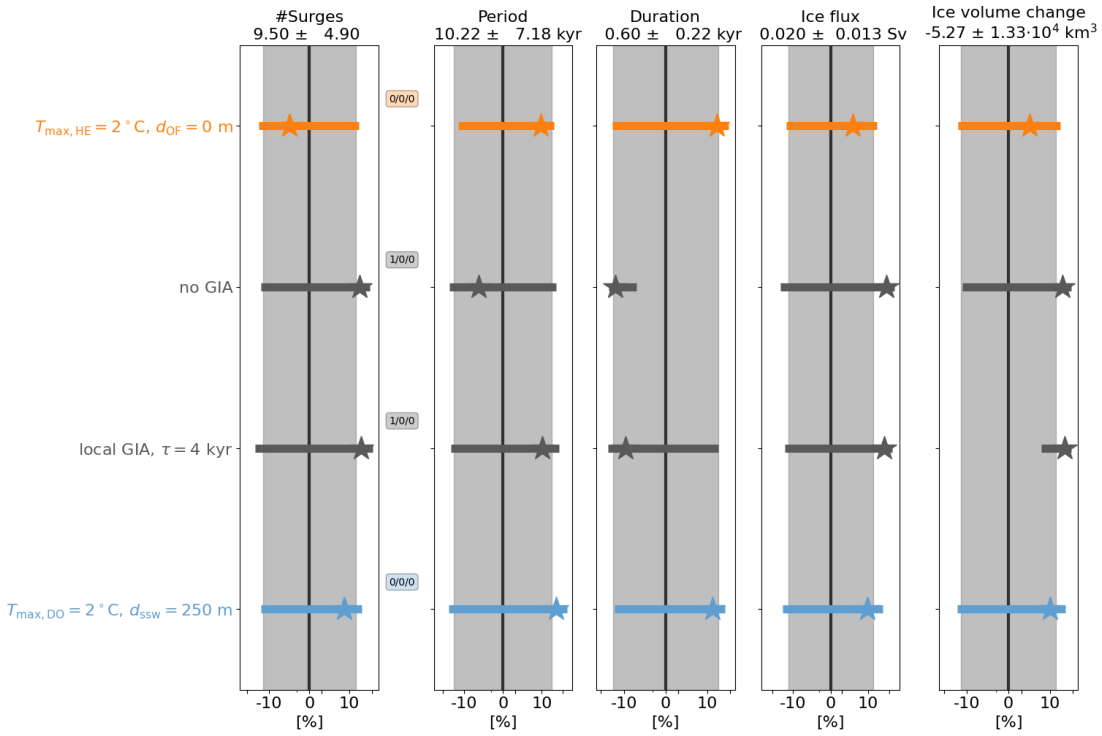

Figure B.16: Percentage differences in surge characteristics compared to the $\mathrm{GHF}_{\mathrm{ave}} = 25\ \frac{\mathrm{mW}}{\mathrm{m}^2}$ setup for the > 2 #surges sub-ensemble (11 parameter vectors). All comparison setups also use $\mathrm{GHF}_{\mathrm{ave}} = 25\ \frac{\mathrm{mW}}{\mathrm{m}^2}$. The model setups, from top to bottom, are: Heinrich Event ocean forcing ($T_{\mathrm{max,HE}} = 2°\mathrm{C}$, $d_{\mathrm{OF}} = 250$ m), no GIA model, local GIA model with relaxation time constant $\tau = 4$ kyr, DO event sub-surface ocean forcing with $T_{\mathrm{max,DO}} = 2°\mathrm{C}$. Otherwise as Fig. 3.6.

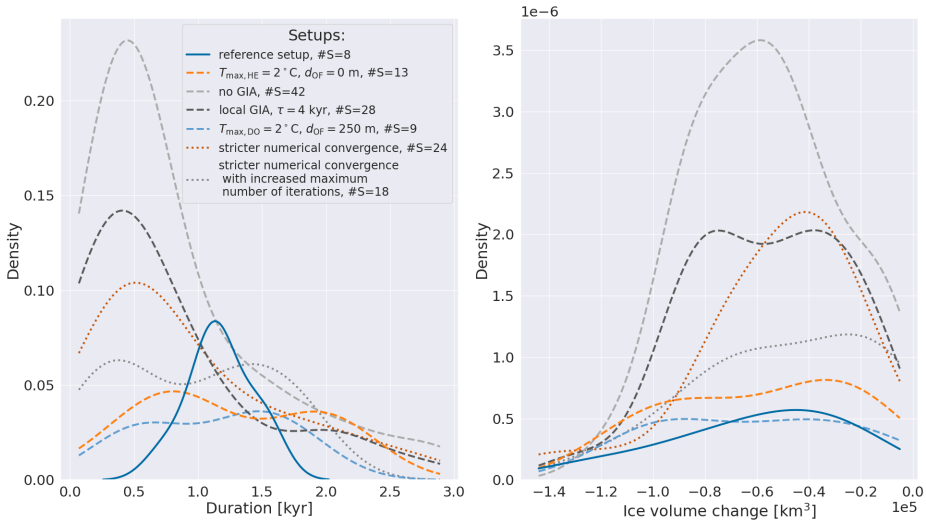

Figure B.17: Kernel density plot for the ≤ 2 #surges sub-ensemble (9 parameter vectors) of the $\text{GHF}_{\text{ave}} = 25\ \frac{\text{mW}}{\text{m}^2}$ experiments. #S indicates the total number of surges across all runs of the sub-ensemble.

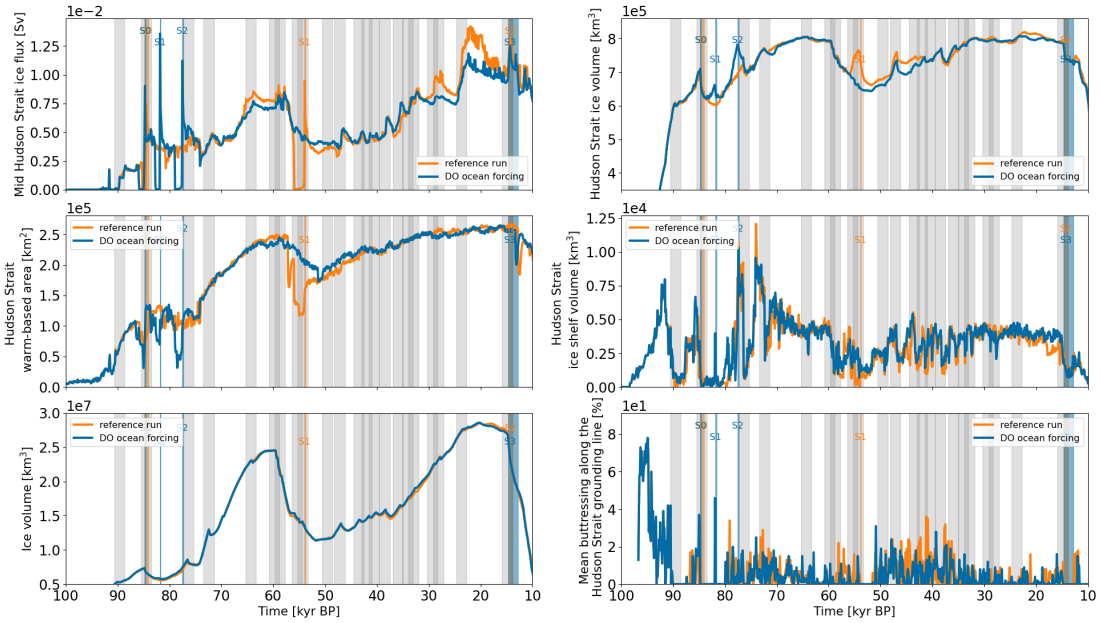

Figure B.18: Time series of parameter vector 0 for the reference setup and the sub-surface ocean forcing (Sec. 3.2.5.2). The shaded gray areas mark the DO event time estimates based on peaks in the NGRIP δ^{18}O time series (Bazin et al., 2013; Veres et al., 2013) with a total duration of $t_{\text{D,tot}} = 2200$ yr (Sec. 3.2.5.2). The darker gray areas indicate an overlap of sub-surface ocean warmings. The ocean forcing was applied below a water depth $d_{\text{OF}} = 250$ m and with a maximum temperature increase of $T_{\text{max,DO}} = 2°\text{C}$. Otherwise as Fig. 3.4.

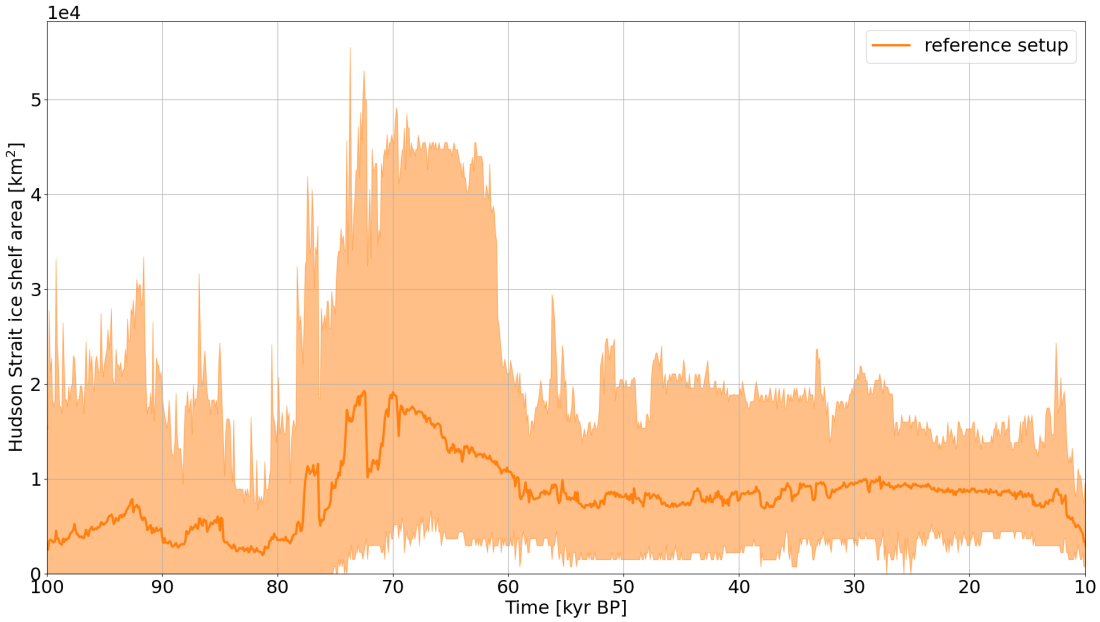

Figure B.19: Hudson Strait ice shelf cover in the *Hudson Strait* area outline in Fig. 3.2 (total area of $\sim 2.6 \cdot 10^5$ km^2). The thick line represents the mean of the 20 run ensemble. The shaded area marks the minimum and maximum of the ensemble.

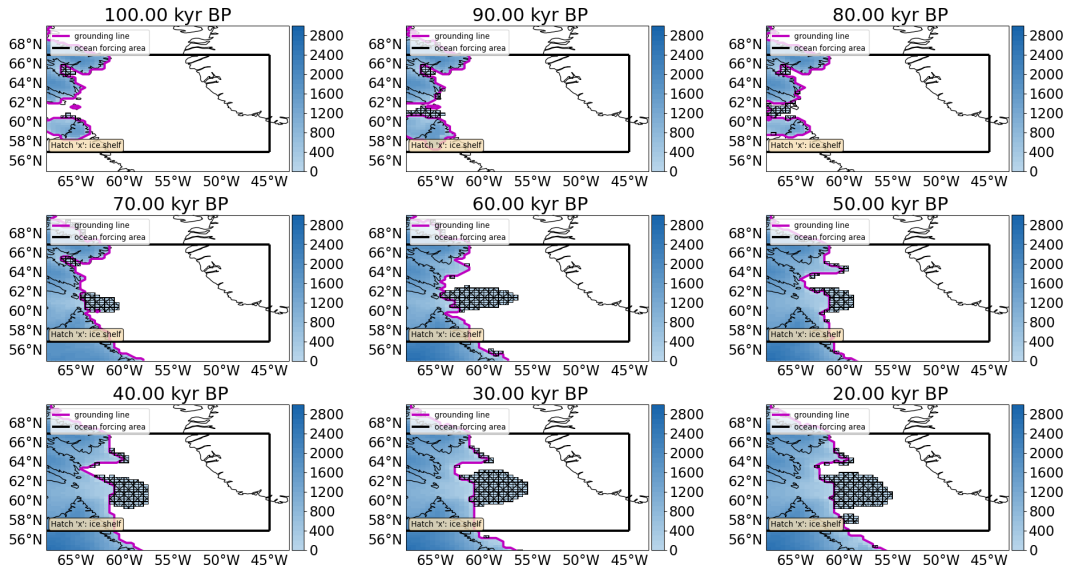

Figure B.20: Ice surface elevation in meters for parameter vector 14 and no calving in the *ocean forcing area* (black box, see also Fig. 3.2). The black contour is the present-day coastline provided by *cartopy* (Met Office, 2010 - 2015).

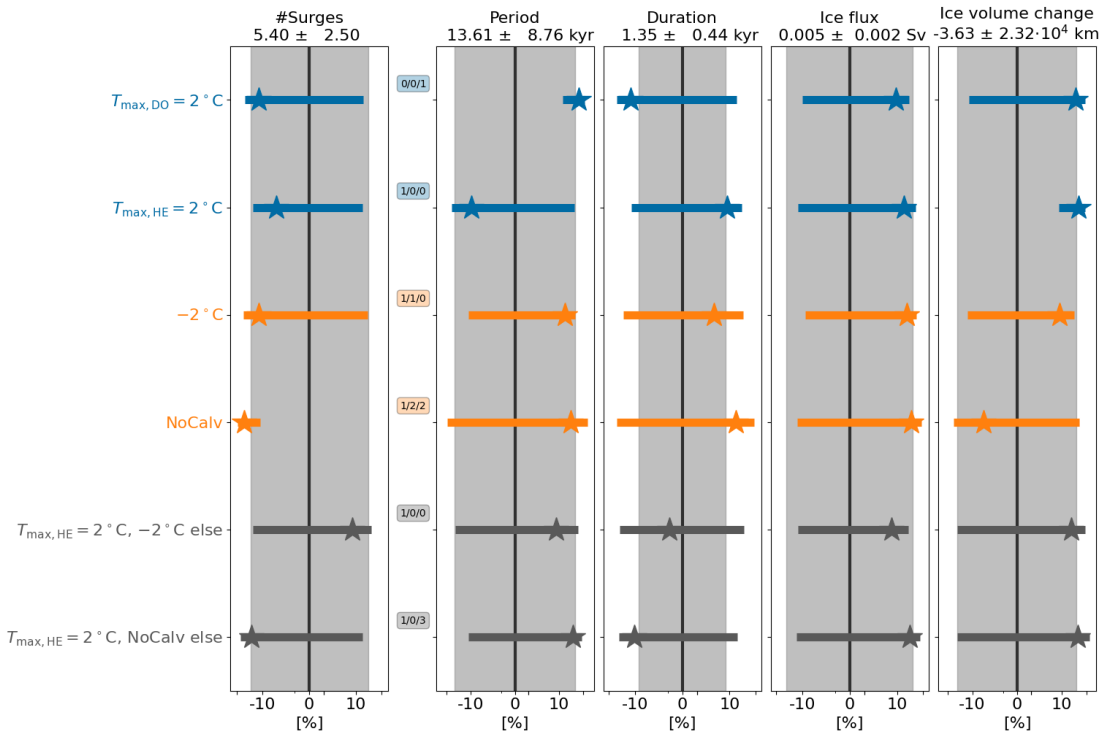

Figure B.21: Percentage differences in surge characteristics compared to the reference setup. Only parameter vectors within the > 2 #surges sub-ensemble are considered. The model setups, from top to bottom, are the bounding experiments (Sec. 3.2.5.3): DO event ocean forcing with maximum temperature increase $T_{\mathrm{max,DO}} = 2°\mathrm{C}$ (BE_1), HE ocean forcing with maximum temperature increase $T_{\mathrm{max,HE}} = 2°\mathrm{C}$ (BE_2), $-2°\mathrm{C}$ ocean temperature decrease applied after 100 kyr BP (BE_3), no calving after 100 kyr BP (BE_4), HE ocean forcing ($T_{\mathrm{max,HE}} = 2°\mathrm{C}$) with $-2°\mathrm{C}$ ocean forcing applied outside of HEs and after 100 kyr BP (BE_5), and HE ocean forcing ($T_{\mathrm{max,HE}} = 2°\mathrm{C}$) with no calving outside of HEs and after 100 kyr BP (BE_6). The ocean forcings are applied for the entire water column and all grid cells within the *ocean forcing area* (not only the ones containing floating ice, Sec. 3.2.5.3). Otherwise as Fig. 3.6.

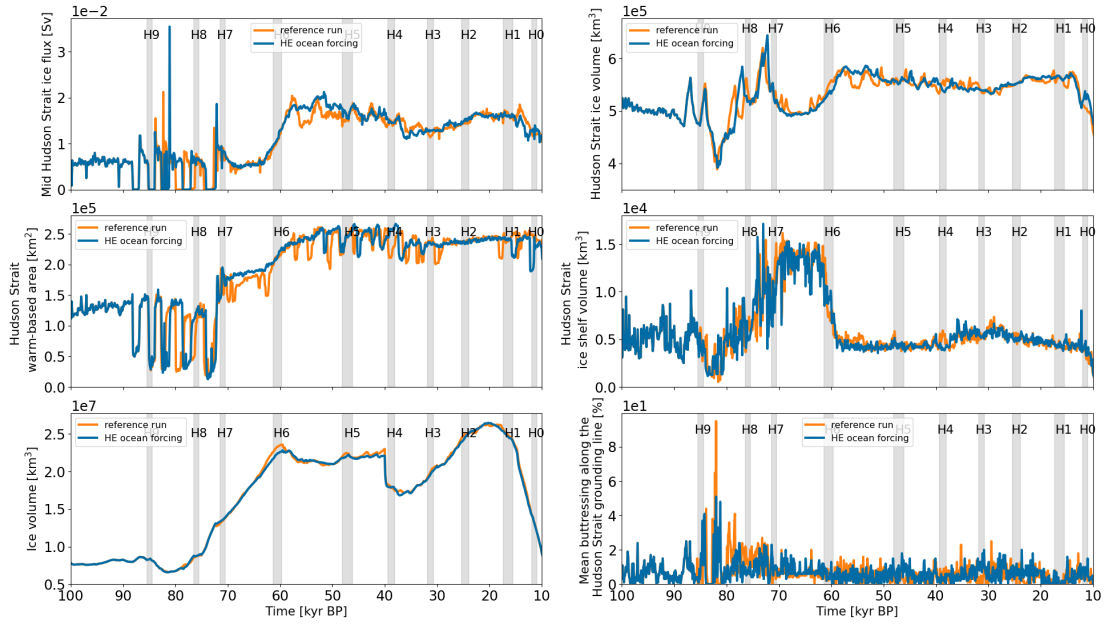

Figure B.22: Time series of parameter vector 1 for the reference setup and the ice shelf removal ocean forcing (Sec. 3.2.5.1). The shaded gray areas mark the HE time estimates based on the average of Table 6.3 in Bradley (2014). The ocean forcing was applied to the whole water column and with a maximum temperature increase of $T_{\mathrm{max,HE}} = 3°\mathrm{C}$. Otherwise as Fig. 3.4.

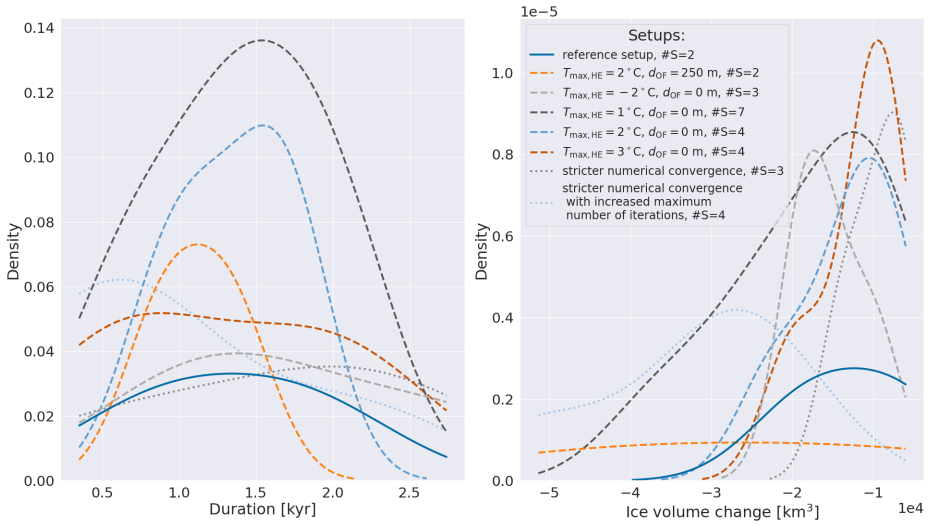

Figure B.23: Kernel density plot for the $\leq$ 2 #surges sub-ensemble. The model setups, from top to bottom, are the reference setup, Heinrich Event ocean forcings (maximum temperature increase $T_{\mathrm{max,HE}} = 2°\mathrm{C}$, $d_{\mathrm{OF}} = 250$ m), whole water column Heirich Event ocean forcing with $T_{\mathrm{max,HE}} = [-2, 1, 2, 3]°\mathrm{C}$ (Sec. 3.2.5.1) and the 2 MNEE experiments. #S indicates the total number of surges across all runs of the sub-ensemble.

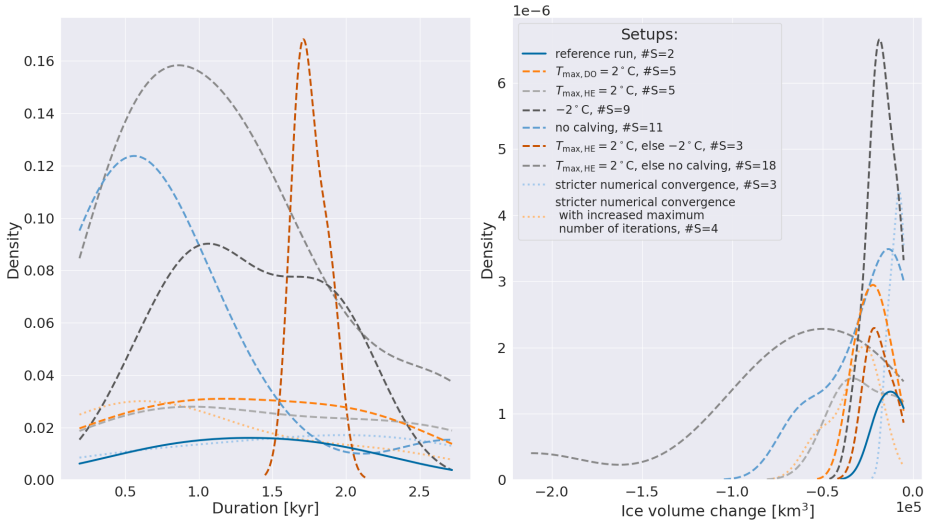

Figure B.24: Kernel density plot for the $\leq$ 2 #surges sub-ensemble. The model setups, from top to bottom, are the reference setup, DO event ocean forcing with maximum temperature increase $T_{\mathrm{max,DO}} = 2°\mathrm{C}$ (BE_1), HE ocean forcing with maximum temperature increase $T_{\mathrm{max,HE}} = 2°\mathrm{C}$ (BE_2), $-2°\mathrm{C}$ ocean temperature decrease applied after 100 kyr BP (BE_3), no calving after 100 kyr BP (BE_4), HE ocean forcing ($T_{\mathrm{max,HE}} = 2°\mathrm{C}$) with $-2°\mathrm{C}$ ocean forcing applied outside of HEs and after 100 kyr BP (BE_5), HE ocean forcing ($T_{\mathrm{max,HE}} = 2°\mathrm{C}$) with no calving outside of HEs and after 100 kyr BP (BE_6), and the 2 MNEE experiments. The ocean forcings are applied for the entire water column and all grid cells within the *ocean forcing area* (not only the ones containing floating ice, Sec. 3.2.5.3). #S indicates the total number of surges across all runs of the sub-ensemble.

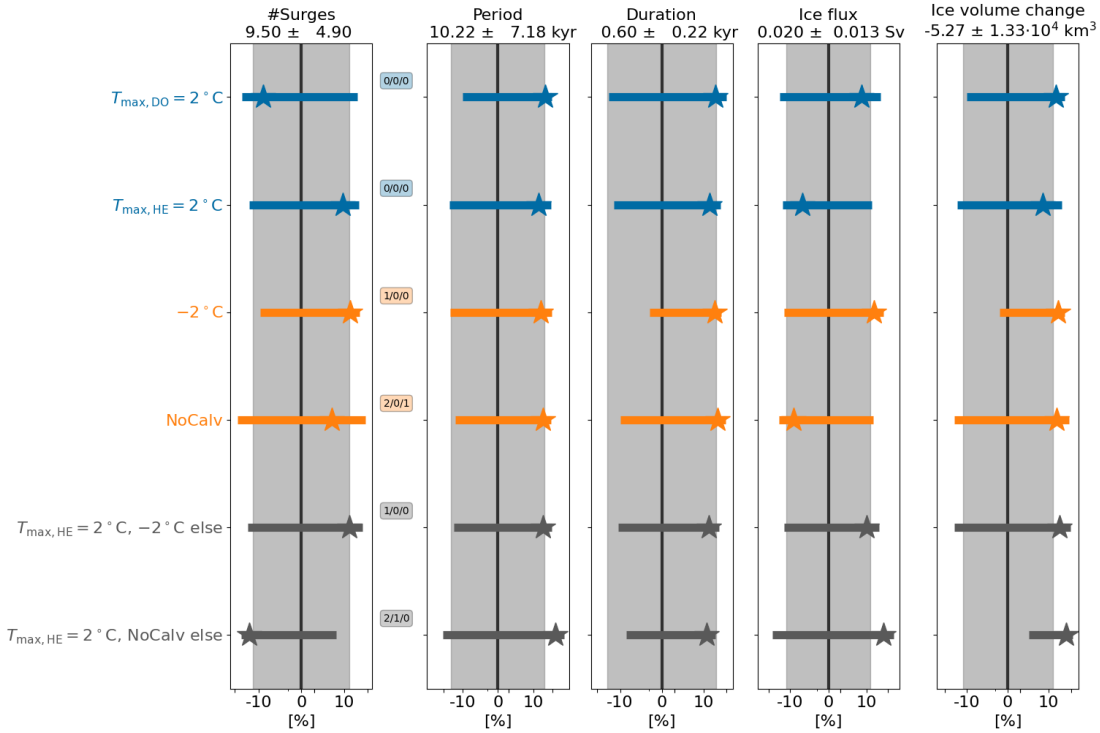

Figure B.25: Percentage differences in surge characteristics compared to the $\mathrm{GHF}_{\mathrm{ave}} = 25\ \frac{\mathrm{mW}}{\mathrm{m}^2}$ setup for the > 2 #surges sub-ensemble (11 parameter vectors). All comparison setups also use $\mathrm{GHF}_{\mathrm{ave}} = 25\ \frac{\mathrm{mW}}{\mathrm{m}^2}$. The model setups, from top to bottom, are the bounding experiments (Sec. 3.2.5.3): DO event ocean forcing with maximum temperature increase $T_{\mathrm{max,DO}} = 2°\mathrm{C}$ (BE_1), HE ocean forcing with maximum temperature increase $T_{\mathrm{max,HE}} = 2°\mathrm{C}$ (BE_2), $-2°\mathrm{C}$ ocean temperature decrease applied after 100 kyr BP (BE_3), no calving after 100 kyr BP (BE_4), HE ocean forcing ($T_{\mathrm{max,HE}} = 2°\mathrm{C}$) with $-2°\mathrm{C}$ ocean forcing applied outside of HEs and after 100 kyr BP (BE_5), and HE ocean forcing ($T_{\mathrm{max,HE}} = 2°\mathrm{C}$) with no calving outside of HEs and after 100 kyr BP (BE_6). The ocean forcings are applied for the entire water column and all grid cells within the *ocean forcing area* (not only the ones containing floating ice, Sec. 3.2.5.3). Otherwise as Fig. 3.6.

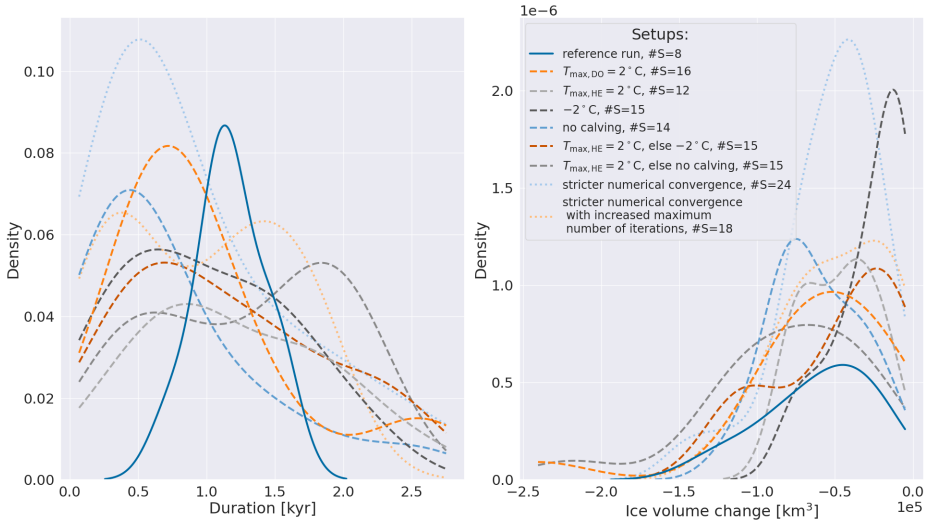

Figure B.26: Kernel density plot for the ≤ 2 #surges sub-ensemble with $\mathrm{GHF}_{\mathrm{ave}} = 25\ \frac{\mathrm{mW}}{\mathrm{m}^2}$ (9 parameter vectors). The model setups, from top to bottom, are the reference setup, DO event ocean forcing with maximum temperature increase $T_{\mathrm{max,DO}} = 2°\mathrm{C}$ (BE_1), HE ocean forcing with maximum temperature increase $T_{\mathrm{max,HE}} = 2°\mathrm{C}$ (BE_2), $-2°\mathrm{C}$ ocean temperature decrease applied after 100 kyr BP (BE_3), no calving after 100 kyr BP (BE_4), HE ocean forcing ($T_{\mathrm{max,HE}} = 2°\mathrm{C}$) with $-2°\mathrm{C}$ ocean forcing applied outside of HEs and after 100 kyr BP (BE_5), HE ocean forcing ($T_{\mathrm{max,HE}} = 2°\mathrm{C}$) with no calving outside of HEs and after 100 kyr BP (BE_6), and the 2 MNEE experiments. The ocean forcings are applied for the entire water column and all grid cells within the *ocean forcing area* (not only the ones containing floating ice, Sec. 3.2.5.3). #S indicates the total number of surges across all runs of the sub-ensemble.

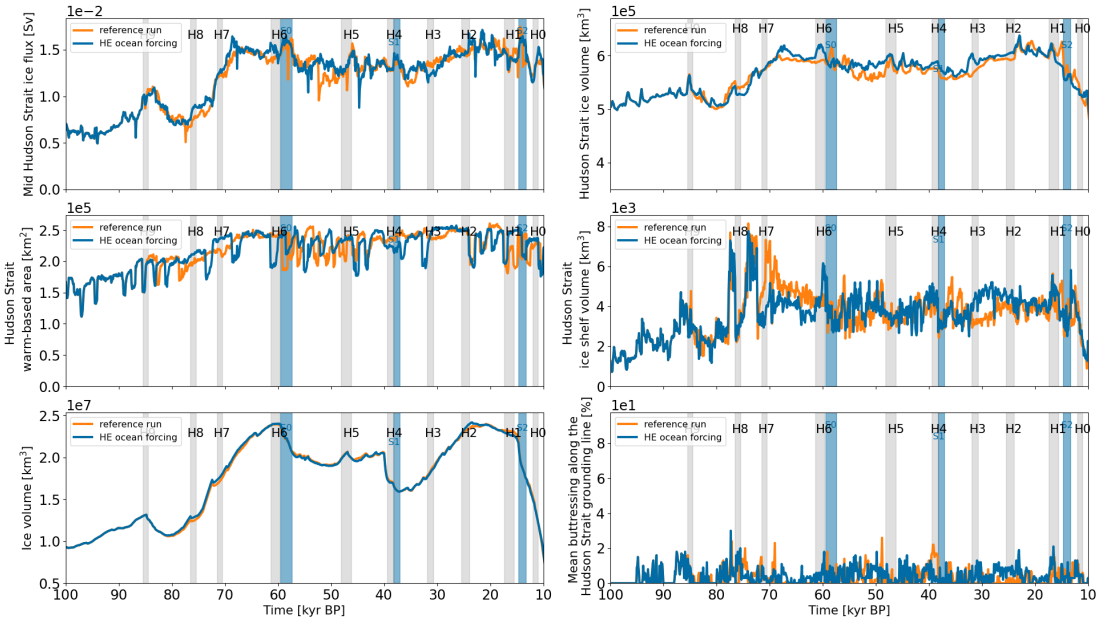

Figure B.27: Time series of parameter vector 16 for the reference setup and the ice shelf removal ocean forcing (Sec. 3.2.5.1). The shaded gray areas mark the HE time estimates based on the average of Table 6.3 in Bradley (2014). The ocean forcing was applied to the whole water column and with a maximum temperature increase of $T_{\mathrm{max,HE}} = 1°\mathrm{C}$. Otherwise as Fig. 3.4.

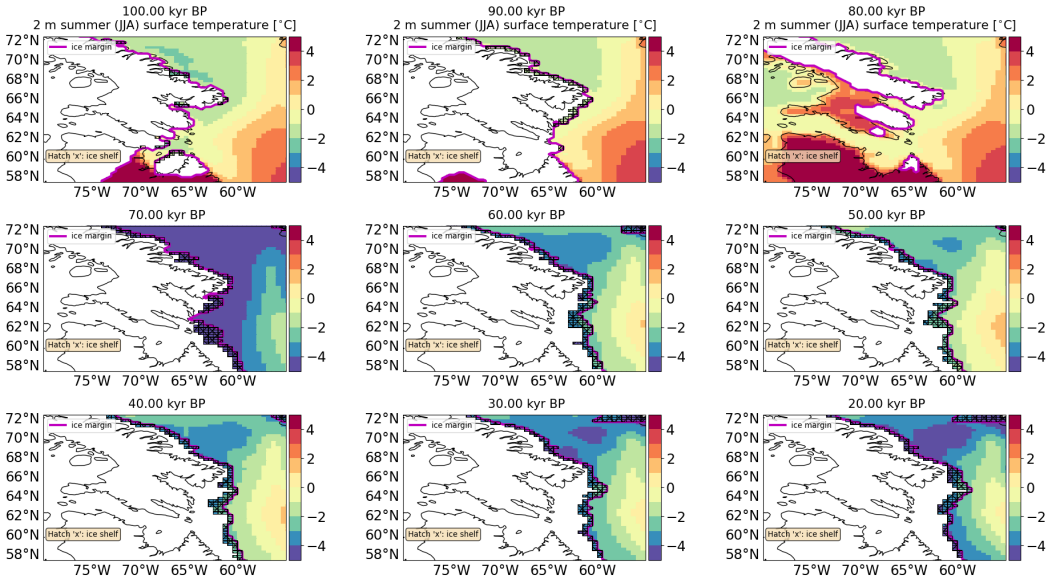

Figure B.28: 2 m summer surface temperature for parameter vector 2 (not shown for grid cells with grounded ice). The black contour is the present-day coastline provided by *cartopy* (Met Office, 2010 - 2015).

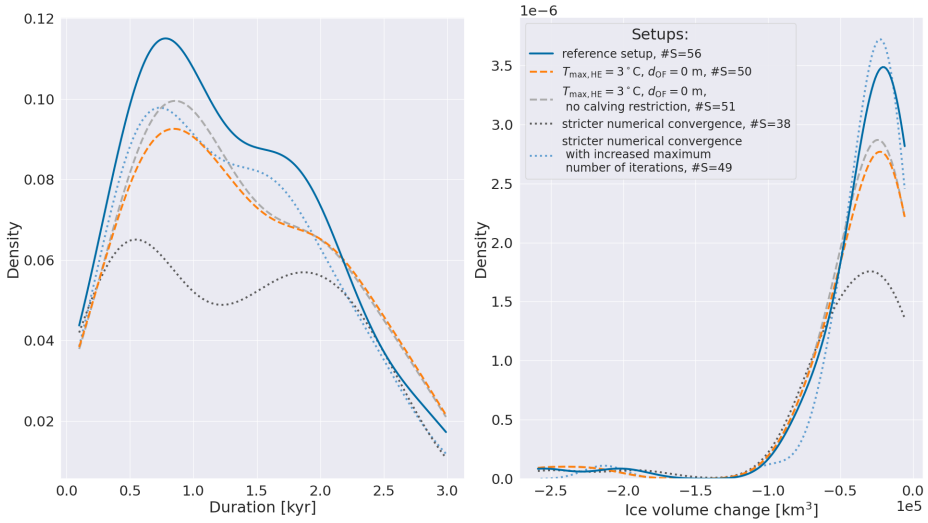

Figure B.29: Kernel density plot for the full ensemble. The $T_{\mathrm{max,HE}} = 3°\mathrm{C}$, $d_{\mathrm{OF}} = 0$ m setup inhibits calving when the 2 m summer surface temperature is below $-2.0°\mathrm{C}$ (see Sec. 3.2.5 for details). #S indicates the total number of surges across all runs of the sub-ensemble.

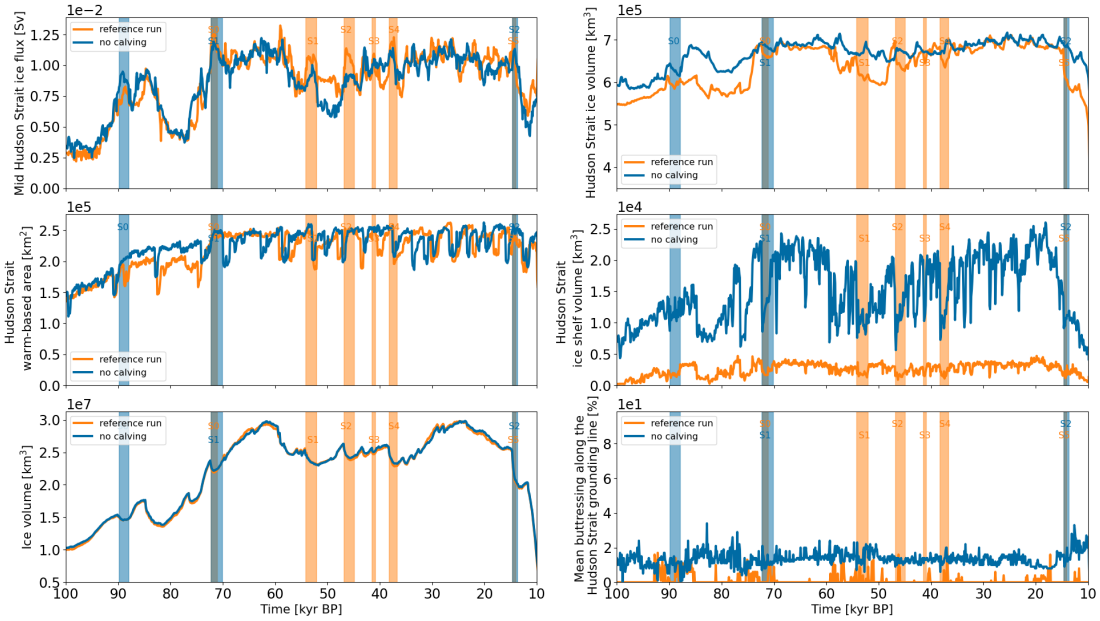

Figure B.30: Time series of parameter vector 3 for the reference setup and a run without calving in the *ocean forcing area* after 100 kyr BP (BE_4 in Sec. 3.2.5.3). Otherwise as Fig. 3.4.

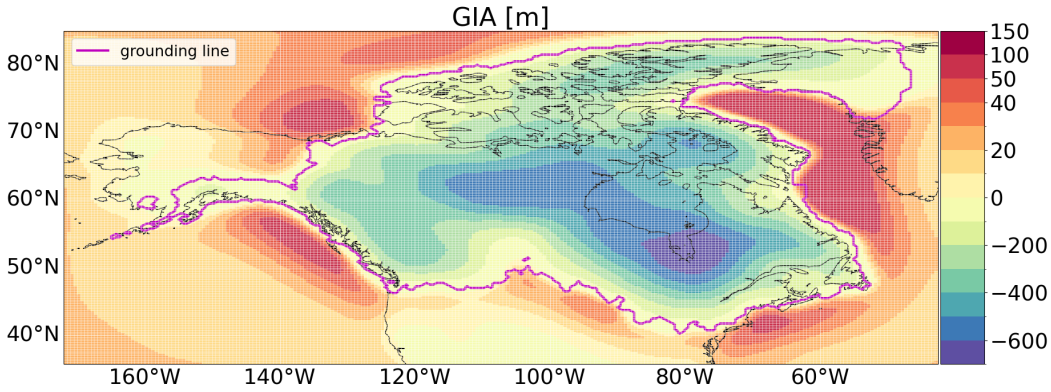

Figure B.31: GIA for parameter vector 5 at 20 kyr BP compared to the bed topography at 120 kyr BP. The black contour is the present-day coastline provided by *cartopy* (Met Office, 2010 - 2015).

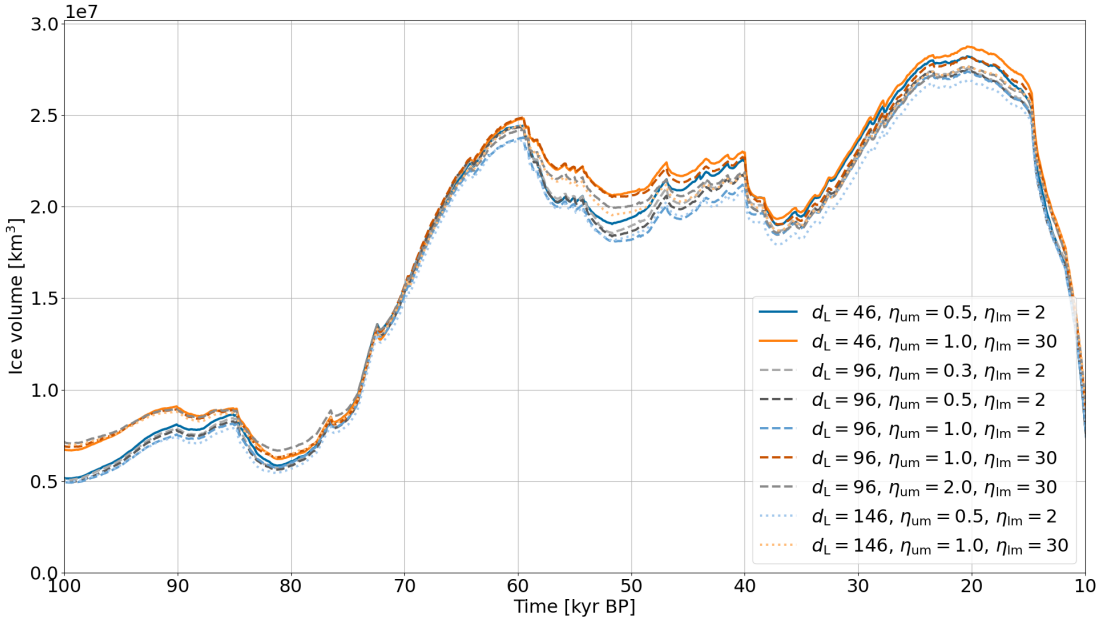

Figure B.32: Mean North American ice volume across all 20 parameter vectors for 9 different earth rheology models of the global GIA model. d_L, η_{um}, and η_{lm} are the thickness of the Lithosphere, the viscosity of the upper mantle and the viscosity of the lower mantle, respectively.

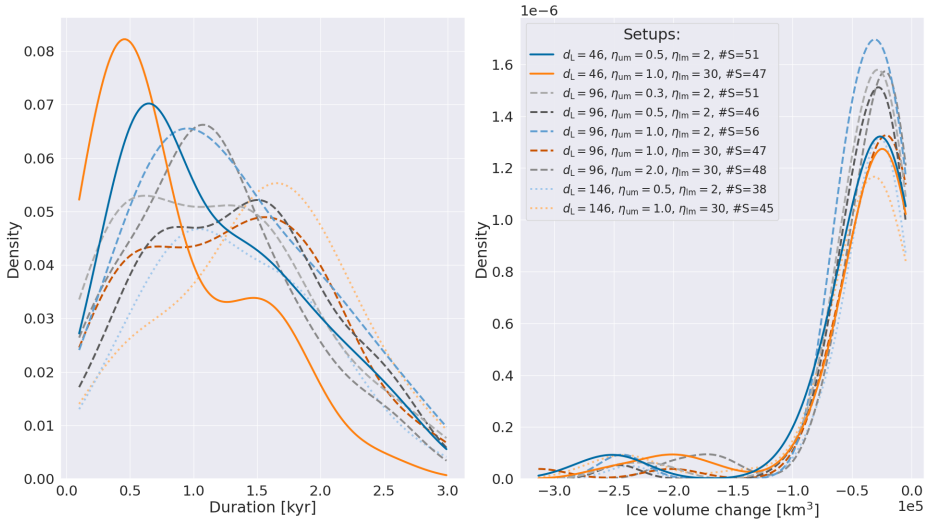

Figure B.33: Kernel density plot for different earth rheologies when using the global GIA model. Each line is based on the surges within all runs with the same earth rheology model. d_L, η_{um}, and η_{lm} are the thickness of the Lithosphere (km), the viscosity of the upper mantle and the viscosity of the lower mantle (10^{21} Pa s), respectively. #S indicates the total number of surges across all runs of the sub-ensemble.

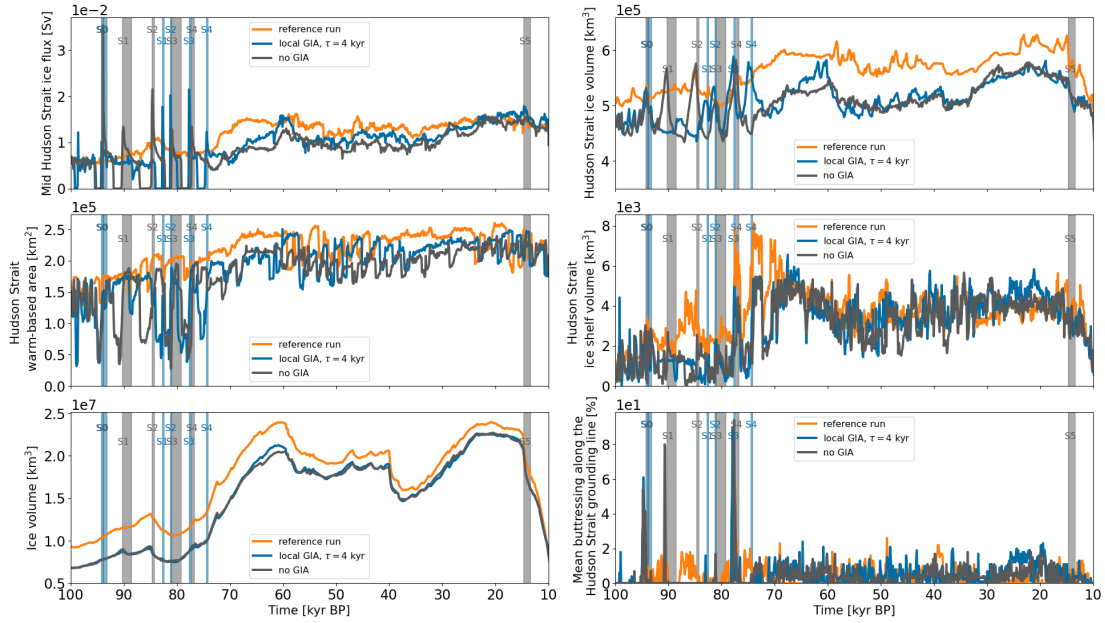

Figure B.34: Time series of parameter vector 16 when using different GIA models. Otherwise as Fig. B.7.

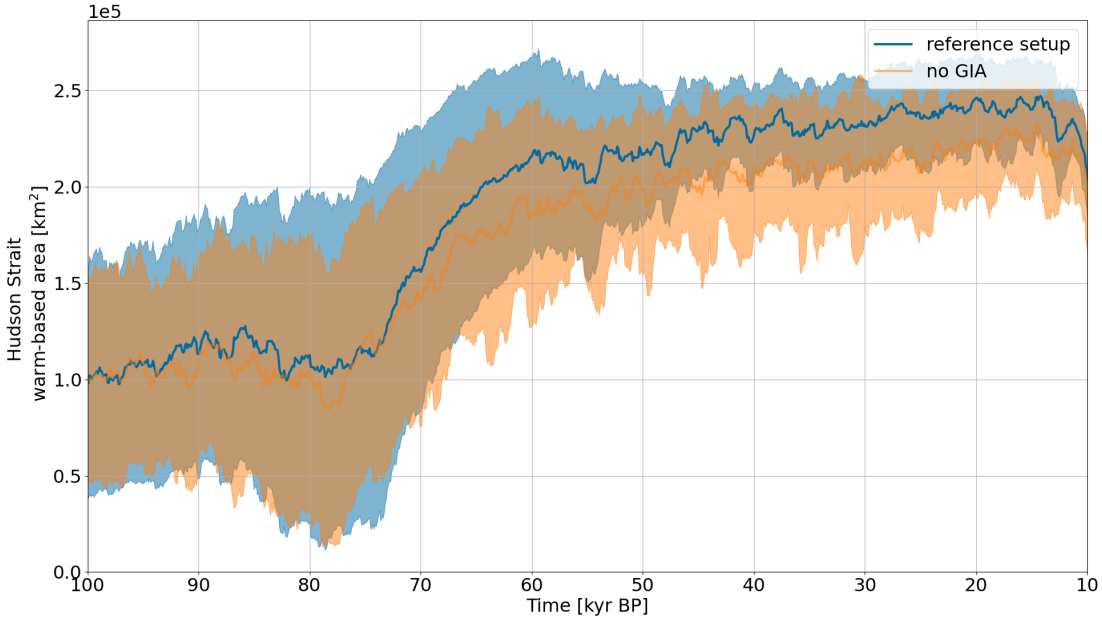

Figure B.35: Hudson Strait warm-based area for the reference setup (global GIA model) and runs without GIA. The thick line represents the mean of the 20 run ensemble. The shaded area marks the minimum and maximum of the ensemble.

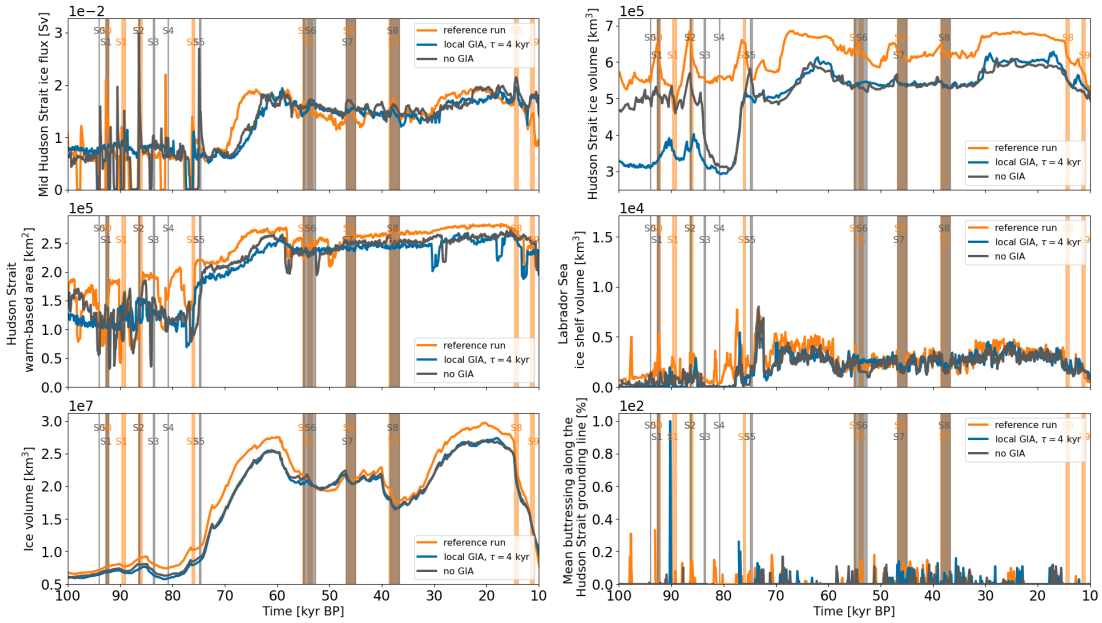

Figure B.36: Time series of parameter vector 11 when using different GIA models. Otherwise as Fig. B.7.

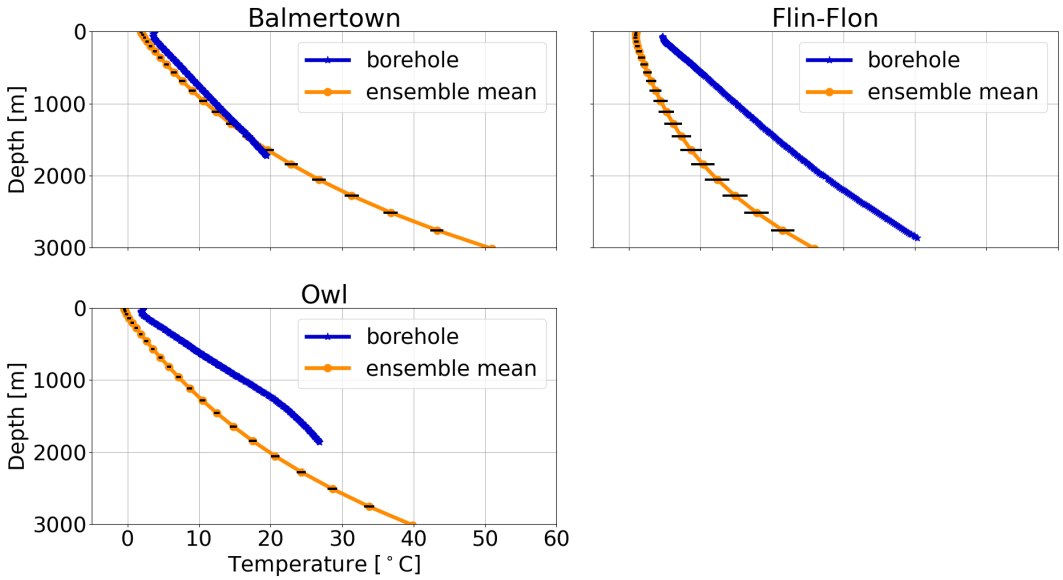

Figure B.37: Bed temperature profiles for the Balmertown (93.7167°W, 51.0333°N, Rolandone et al., 2003), Flin-Flon (102.0°W, 54.717°N, J. C. Mareschal, personal communication, 2006), and Owl (97.86°W, 55.67°N, Rolandone et al., 2002) boreholes and the corresponding GSM grid cells. The location of the boreholes is shown in Fig. B.38. The orange lines and black horizontal bars represent the present-day ensemble mean and standard deviation of the GSM reference setup (default GHF, Davies, 2013), respectively.

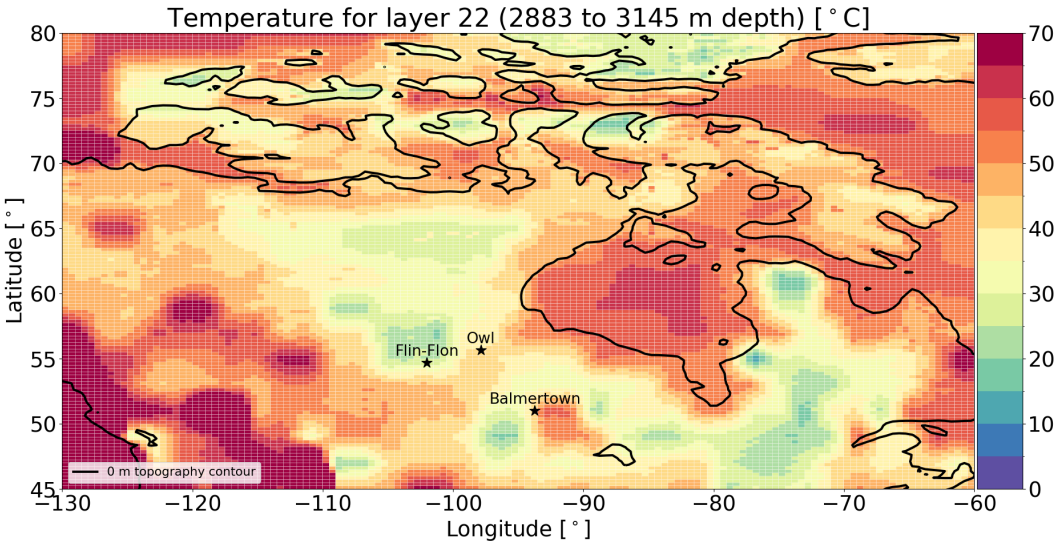

Figure B.38: Bed temperature field between 2883 and 3145 m depth in the GSM. The default GHF was used (Davies, 2013). The black asterisks mark the locations of the boreholes shown in Fig. B.37. The black contour line shows the present-day sea level used in the GSM

Appendix C

Supplement for P3

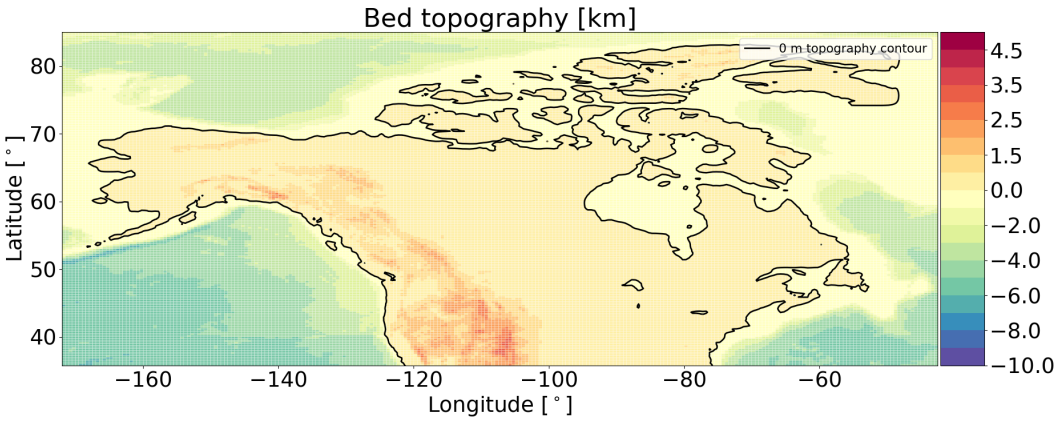

Figure C.1: GSM input present-day bed topography for the full model domain. The black contour line shows the present-day sea level (coastline) used in the GSM. Note the change in the color bar step at 0 km.

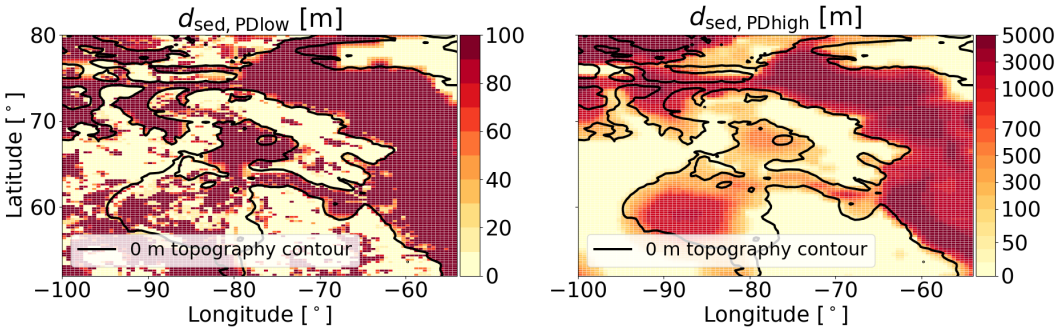

Figure C.2: Present-day sediment thickness distributions based on Geological Survey of Canada (2014) (left panel) and Laske and Masters (1997) (right panel). The black contour line shows the present-day sea level used in the GSM. To prevent ice sheet growth over Greenland, the landmask in the corresponding area has been set to below sea level aside from a North-West Greenland stub to enable ice growth across Nares Strait.

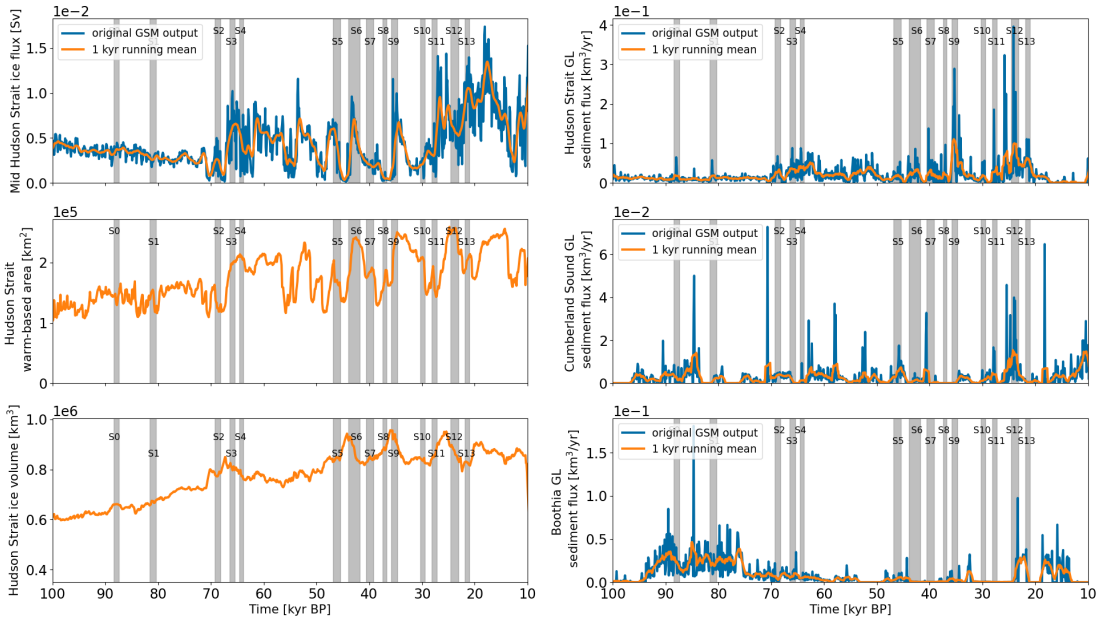

Figure C.3: Time series of parameter vector 8 for the GSM reference setup. The orange lines represent the time series used throughout this study. The blue lines show the original GSM output for metrics for which a 1 kyr running mean is applied to the time series. The Hudson Strait sediment peaks are not highlighted for clarity. Otherwise as Fig. 4.7.

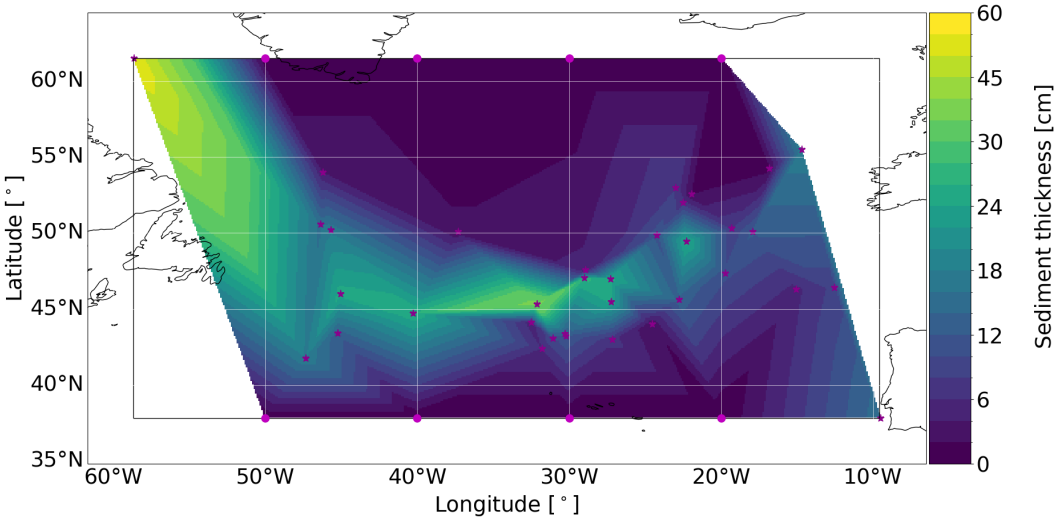

Figure C.4: Sediment thickness distribution based on the piecewise-linear interpolation. Otherwise as Fig. 4.2.

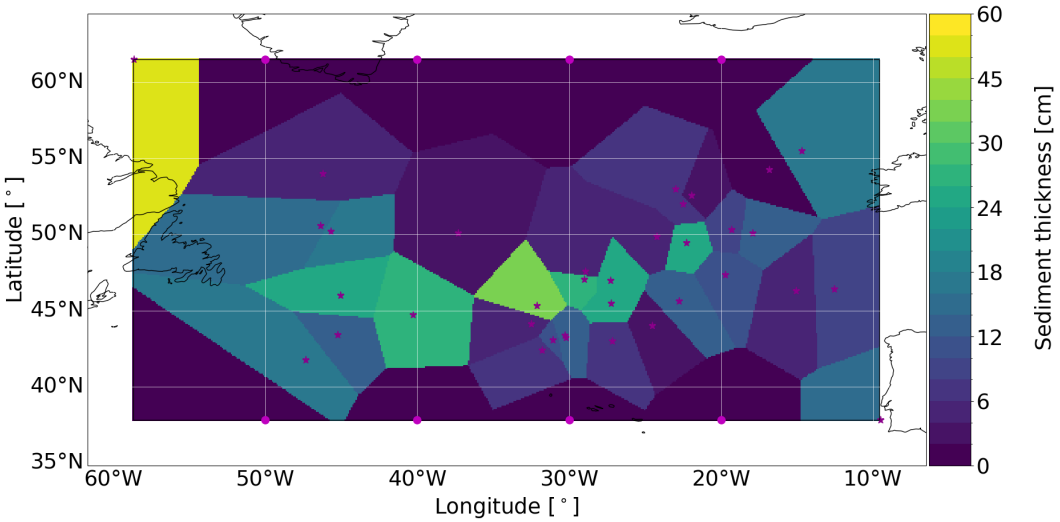

Figure C.5: Sediment thickness distribution based on the nearest-neighbor interpolation. Otherwise as Fig. 4.2.

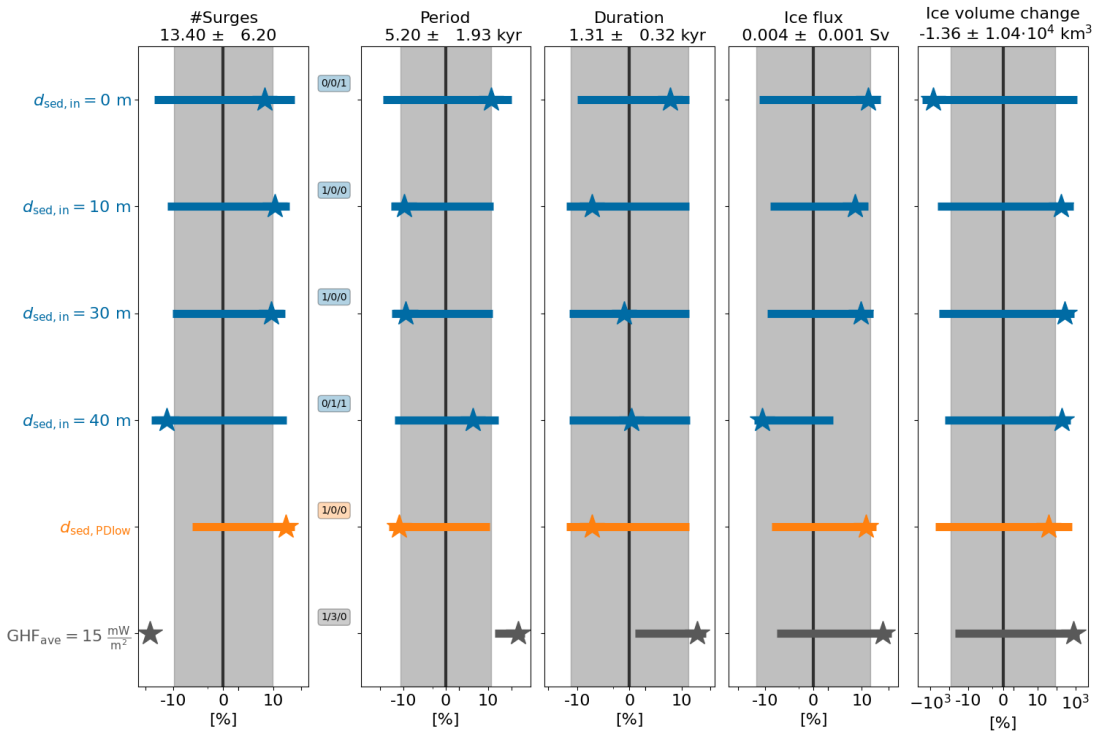

Figure C.6: Percentage differences in mid-Hudson Strait surge characteristics compared to the GSM reference setup ($d_{\text{sed,in}} = 20$ m). The shaded regions represent the MNEEs. The different colors provide visual alignment of the individual model setups. The stars and horizontal bars are the ensemble mean percentage differences and standard deviations, respectively. The three numbers between the first and second column show the number of crashed runs, the number of runs without a surge, and the number of runs with only one surge in the comparison setup. The x-axes are logarithmic. The model setups, from top to bottom, are: $d_{\text{sed,in}} = [0, 10, 30, 40]$ m and average geothermal heat flux in the Hudson Bay and Hudson Strait $\text{GHF}_{\text{ave}} = 15\ \frac{\text{mW}}{\text{m}^2}$ ($d_{\text{sed,in}} = 20$ m, Hank and Tarasov, 2023, in preparation). Note that $d_{\text{sed,in}}$ experiments with $\text{GHF}_{\text{ave}} = 15\ \frac{\text{mW}}{\text{m}^2}$ lead to similar results (Fig. C.14).

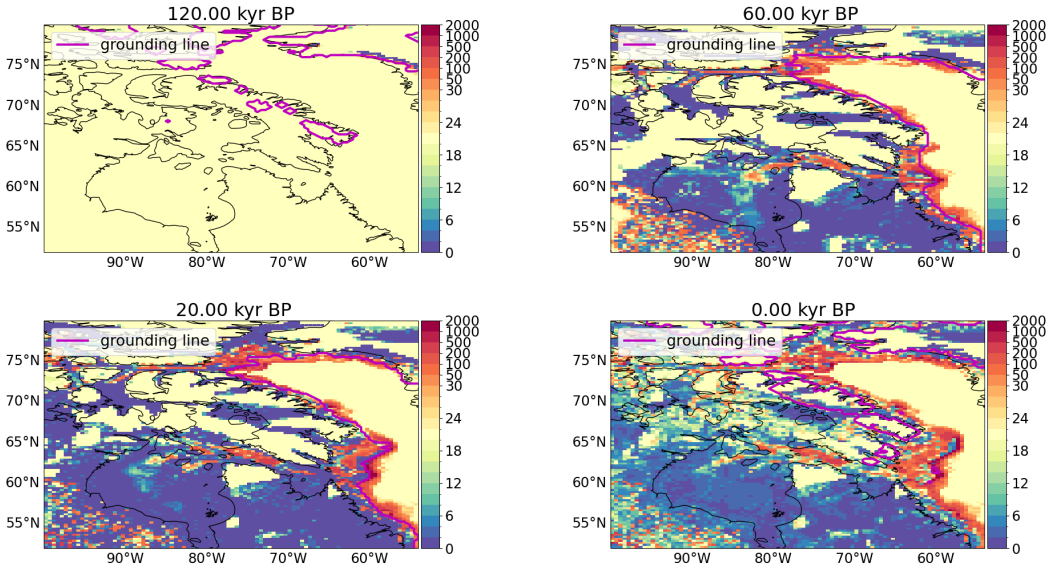

Figure C.7: Sediment thickness distribution across the eastern North American continent for parameter vector 6 in meters. The initial sediment thickness is 20 m. The black contour is the present-day coastline provided by *cartopy* (Met Office, 2010 - 2015).

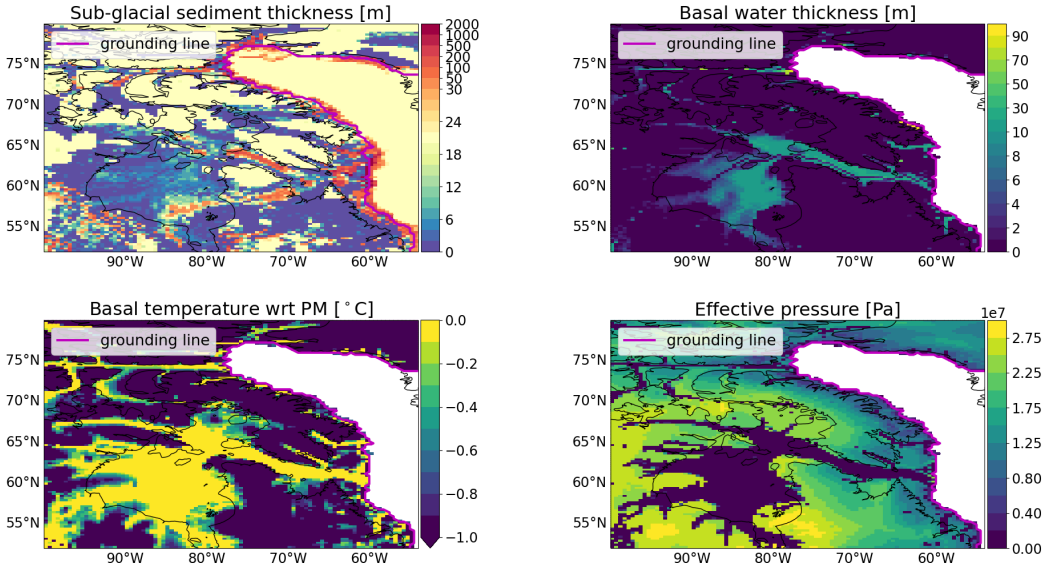

Figure C.8: Sub-glacial sediment thickness, basal water thickness, basal temperature with respect to the pressure melting point, and effective pressure for parameter vector 8 at 20 kyr BP. The initial sediment thickness is 20 m. The black contour is the present-day coastline provided by *cartopy* (Met Office, 2010 - 2015).

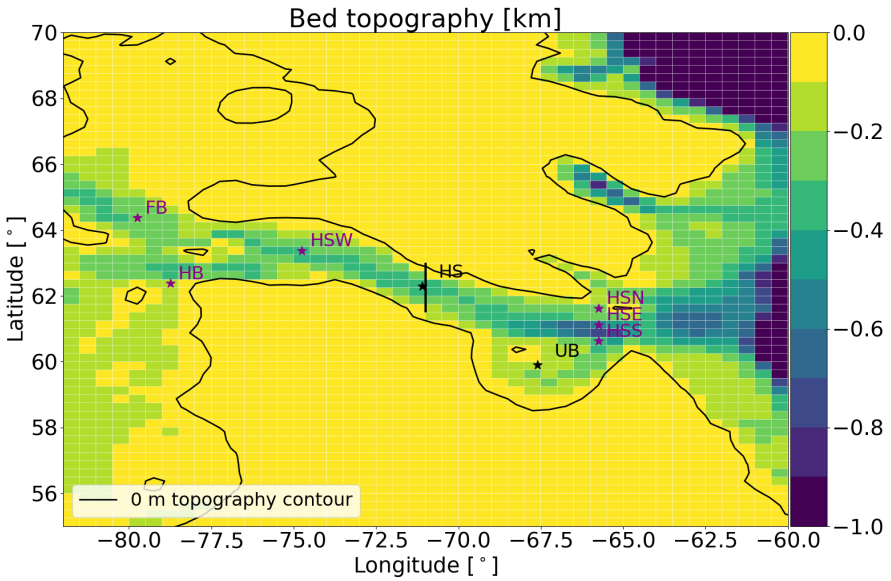

Figure C.9: GSM input present-day bed topography. The magenta asterisks mark the additional sediment stations for which the englacial sediment concentration is examined: Hudson Bay (HB), Foxe Basin (FB), Hudson Strait West (HSW), Hudson Strait East (HSE), Hudson Strait South (HSS), Hudson Strait North (HSN). Otherwise as Fig. 4.1.

Metric	sediment flux characteristics (mean ± SD)	surge characteristics (mean ± SD)	HE estimates
number of peaks	11.7 ± 3.4	13.4 ± 6.2	6 to 10 (Table 6.3 in Bradley, 2014)
period	5.1 ± 0.8 kyr	5.2 ± 2.0 kyr	4 to 15 kyr, mean= 8.0 ± 2.7 kyr (Table 6.3 in Bradley, 2014)
duration	1.2 ± 0.2 kyr	1.3 ± 0.3 kyr	0.2 to 2.3 kyr (Hemming, 2004)

Table C.1: Comparison of the sediment flux and surge characteristics of the reference setup.

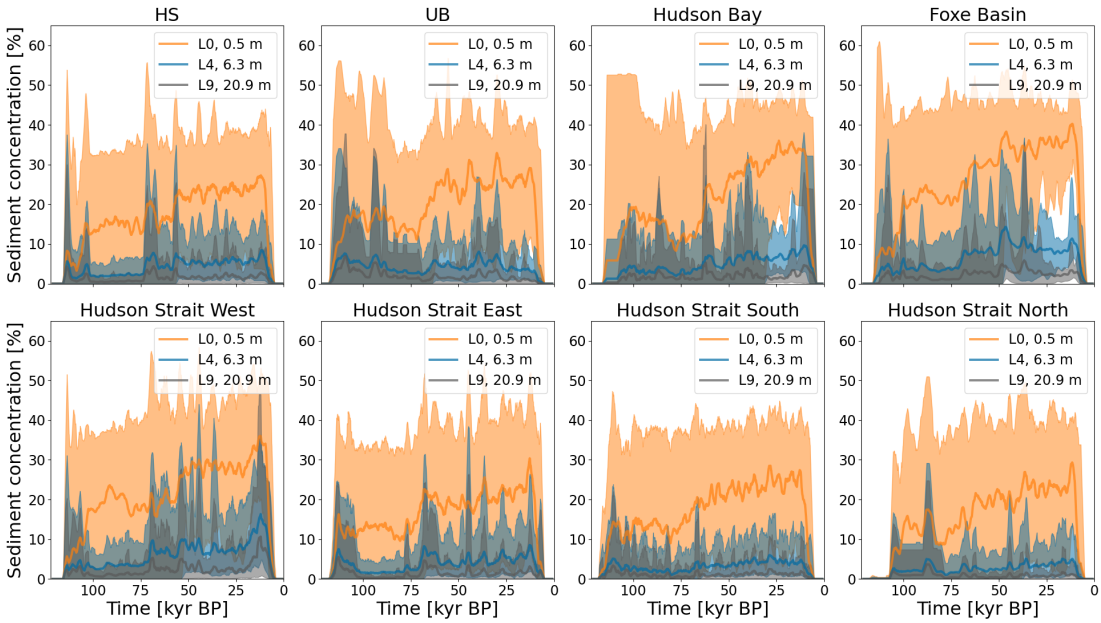

Figure C.10: Englacial sediment concentrations within 3 different layers of the sediment model. The thick lines represent the mean of the different layers. The shaded areas mark the minimum and maximum of the corresponding layer. The time series were smoothed with a 2 kyr running mean. L0 and L9 represent the bottom and top layers, respectively. The second numbers denote the height of the center of each layer. The locations of the sediment stations are shown in Fig. C.9.

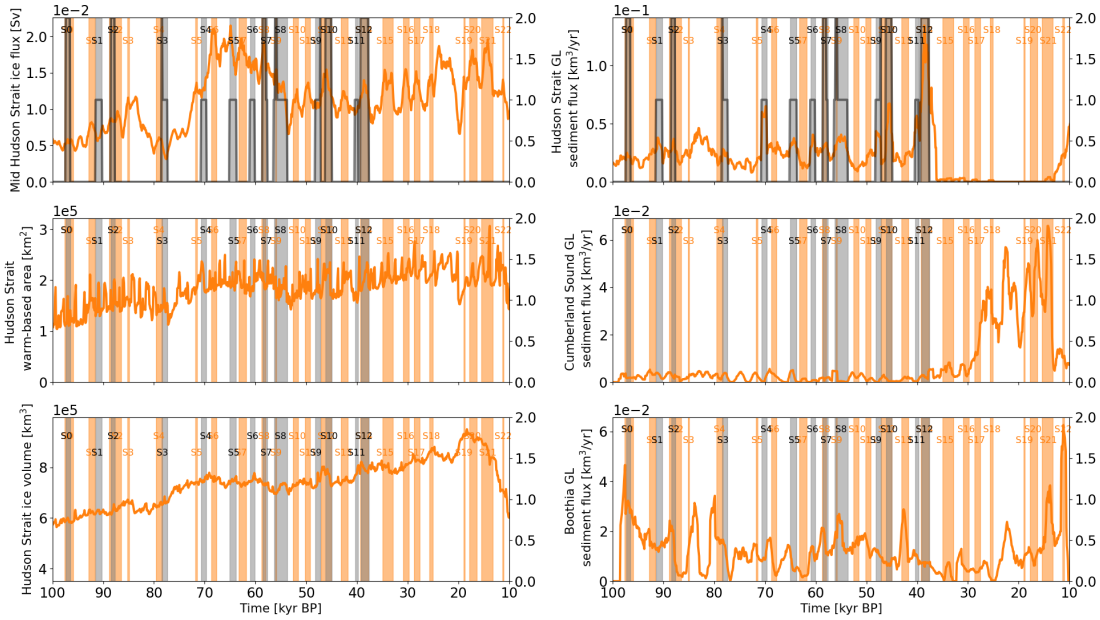

Figure C.11: Time series of parameter vector 6. The shaded orange areas and numbers mark the Hudson Strait ice stream surges as determined by the automated detection algorithm (Sec. 4.2.5). The black line indicates the overlap between the Hudson Strait sediment peaks and ice stream surges (right axis, 0 =no sediment peak, 1 =sediment peak, 2 =sediment peak and surge). Otherwise as Fig. 4.7.

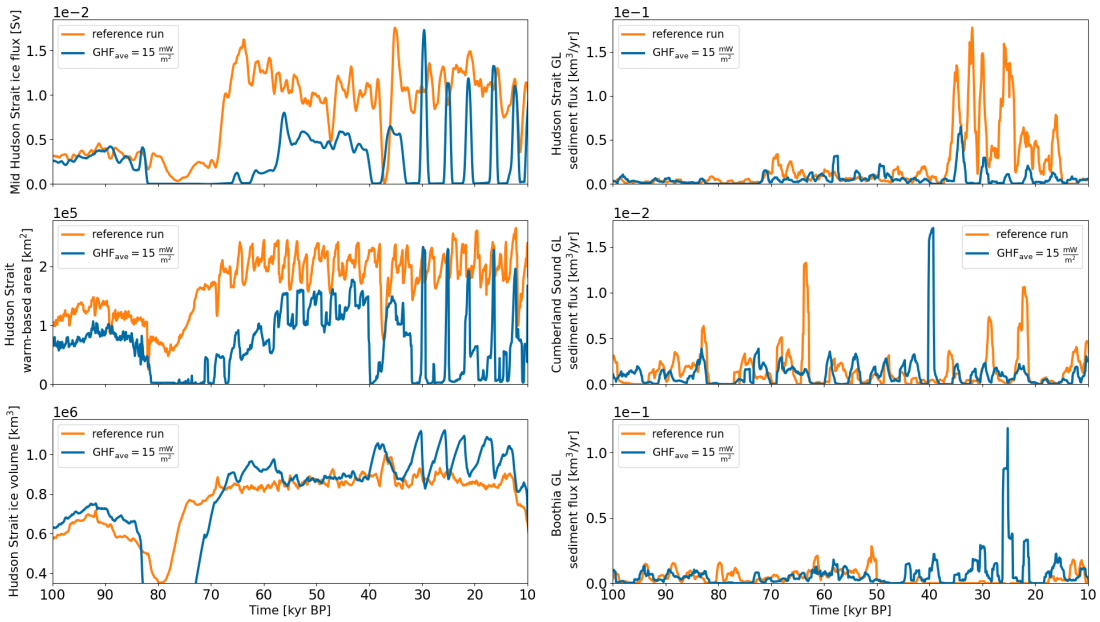

Figure C.12: Time series of parameter vector 1 for the GSM reference setup and a setup with lower GHF in the Hudson Strait and Hudson Bay. The Hudson Strait sediment peaks are not highlighted for clarity. Otherwise as Fig. 4.7.

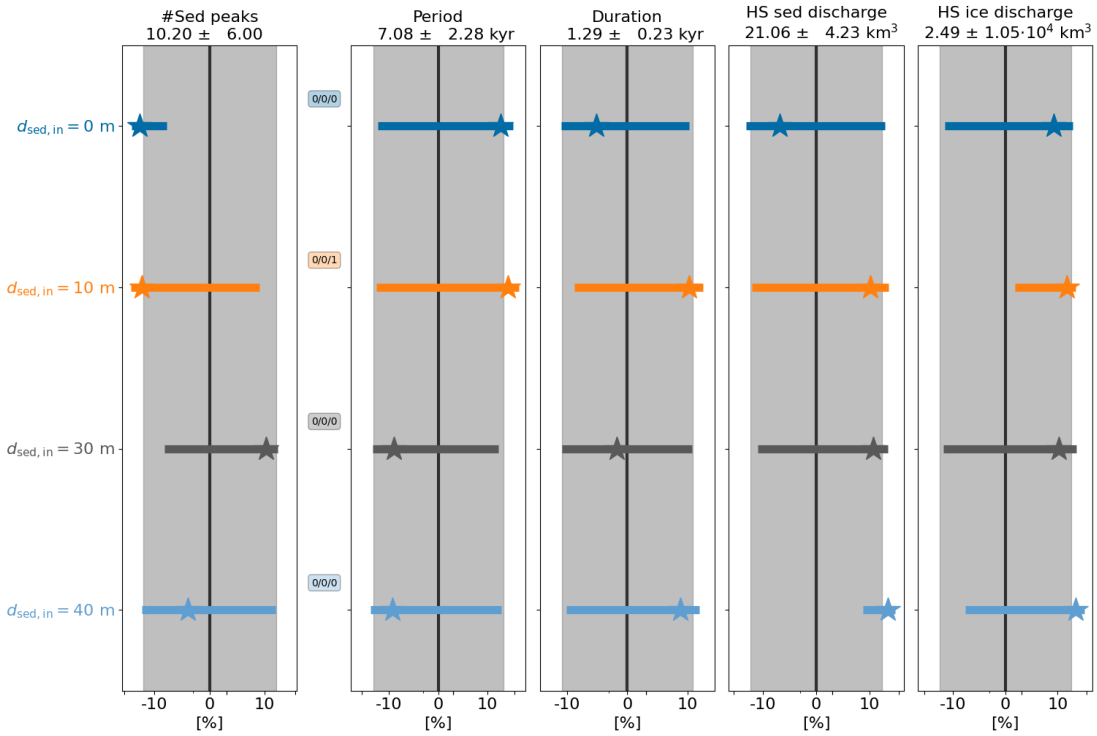

Figure C.13: Percentage differences in sediment flux characteristics compared to the $\mathrm{GHF_{ave}} = 15\ \frac{\mathrm{mW}}{\mathrm{m^2}}$ setup (uniform initial sediment thickness $d_{\mathrm{sed,in}} = 20$ m). All experiments, including the shown MNEEs, also use $\mathrm{GHF_{ave}} = 15\ \frac{\mathrm{mW}}{\mathrm{m^2}}$ (Hank and Tarasov, 2023, in preparation). The model setups, from top to bottom, are: $d_{\mathrm{sed,in}} = [0, 10, 30, 40]$ m. Otherwise as Fig. 4.4.

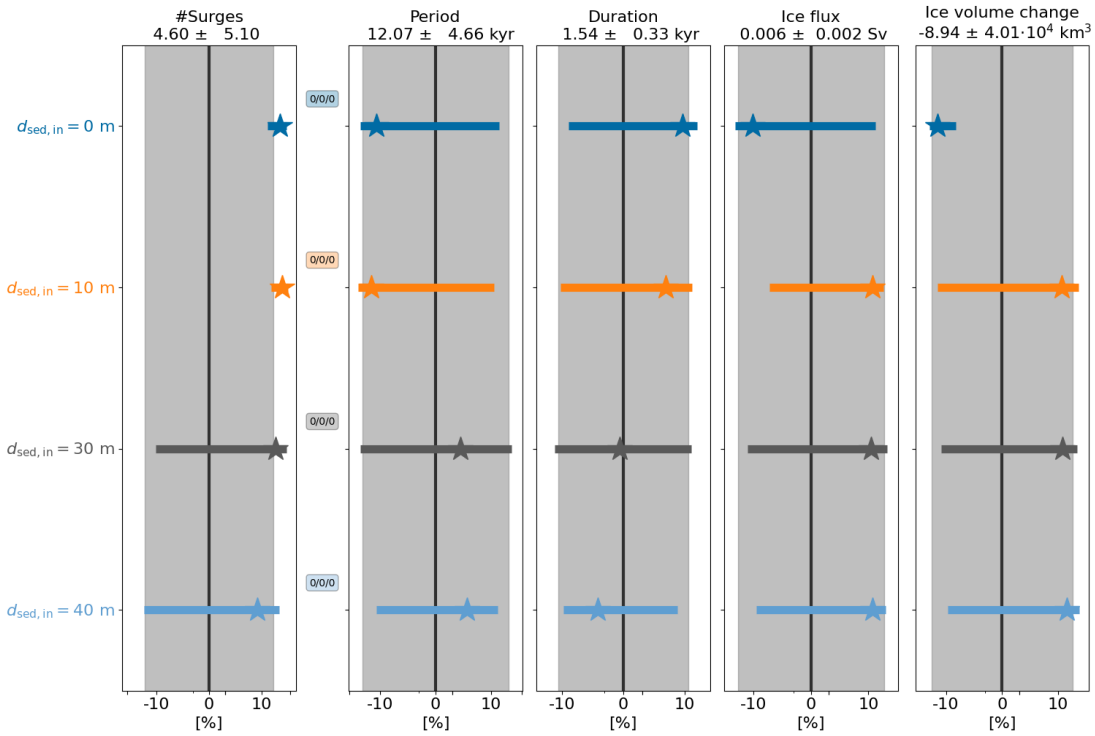

Figure C.14: Percentage differences in mid-Hudson Strait surge characteristics compared to the $\mathrm{GHF_{ave}} = 15\ \frac{\mathrm{mW}}{\mathrm{m^2}}$ setup (uniform initial sediment thickness $d_{\mathrm{sed,in}} = 20$ m). All experiments, including the shown MNEEs, also use $\mathrm{GHF_{ave}} = 15\ \frac{\mathrm{mW}}{\mathrm{m^2}}$ (Hank and Tarasov, 2023, in preparation). The model setups, from top to bottom, are: $d_{\mathrm{sed,in}} = [0, 10, 30, 40]$ m. Otherwise as Fig. C.6.

Metric	reference setup (mean ± SD)	$GHF_{ave} = 15\ \frac{mW}{m^2}$	HE estimate
number of sediment peaks	11.7 ± 3.4	10.2 ± 6.0	6 to 10 (Table 6.3 in Bradley, 2014)
period	5.1 ± 0.8 kyr	7.1 ± 2.3 kyr	4 to 15 kyr, mean= 8.0 ± 2.7 kyr (Table 6.3 in Bradley, 2014)
duration	1.2 ± 0.2 kyr	1.3 ± 0.2 kyr	0.2 to 2.3 kyr (Hemming, 2004)
Hudson Strait sediment discharge	46.9 ± 19.2 km^3	21.1 ± 4.2 km^3	-
Cumberland Sound sediment discharge	1.7 ± 1.1 km^3	1.4 ± 0.8 km^3	-
Boothia sediment discharge	7.3 ± 6.1 km^3	9.5 ± 4.2 km^3	-
total sediment discharge	~ 55.9 km^3	~ 32.0 km^3	100 to 400 km^3 (Hemming, 2004), 11 to 472 km^3 (Sec. 4.3.1)
Hudson Strait ice discharge	$4.3 \pm 2.4 \cdot 10^4$ km^3	$2.5 \pm 1.1 \cdot 10^4$ km^3	-
Cumberland Sound ice discharge	$0.3 \pm 0.2 \cdot 10^4$ km^3	$0.2 \pm 0.1 \cdot 10^4$ km^3	-
Boothia ice discharge	$0.8 \pm 0.5 \cdot 10^4$ km^3	$0.7 \pm 0.4 \cdot 10^4$ km^3	-
total ice discharge	$\sim 5.4 \cdot 10^4$ km^3	$\sim 3.4 \cdot 10^4$ km^3	3 to $946 \cdot 10^4$ km^3 (Roberts et al., 2014, and references therein)

Table C.2: Sediment flux characteristics of the GSM reference setup compared to a setup with a lower geothermal heat flux in the Hudson Bay/Hudson Strait (Hank and Tarasov, 2023, in preparation) and literature estimates. The HE estimates are based on the time between 100 kyr BP and 10 kyr BP.

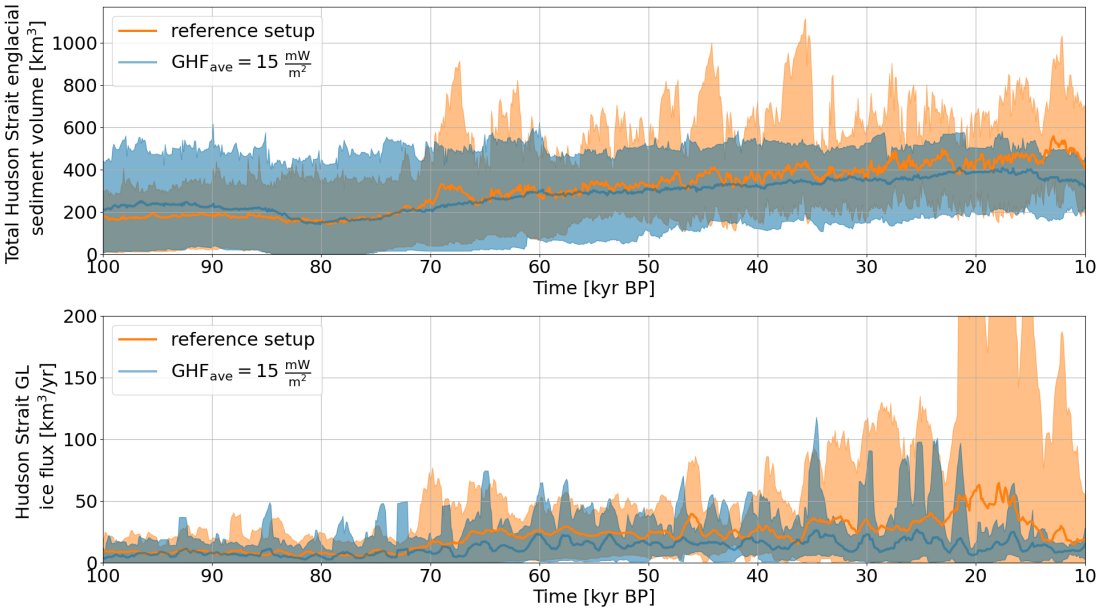

Figure C.15: Total Hudson Strait englacial sediment volume and mean ice flux across the Hudson Strait grounding line for the reference setup and a setup with lower GHF. The thick lines represent the mean of the different model setups. The shaded areas mark the minimum and maximum of the corresponding setup. The Hudson Strait area considered for the englacial sediment volume is outlined in Fig. 4.1.

Appendix D

Supplement for basic ice dynamics

D.1 Ice Flow Approximations

The following subsections are mainly based on Larour et al. (2020).

D.1.1 Full Stokes

$$\begin{pmatrix} \frac{\partial}{\partial x}\left(2\mu\frac{\partial u}{\partial x}\right) & + & \frac{\partial}{\partial y}\left(\mu\frac{\partial u}{\partial y}+\mu\frac{\partial v}{\partial x}\right) & + & \frac{\partial}{\partial z}\left(\mu\frac{\partial u}{\partial z}+\mu\frac{\partial w}{\partial x}\right) & - & \frac{\partial p}{\partial x} & = 0 \\ \frac{\partial}{\partial x}\left(\mu\frac{\partial u}{\partial y}+\mu\frac{\partial v}{\partial x}\right) & + & \frac{\partial}{\partial y}\left(2\mu\frac{\partial v}{\partial y}\right) & + & \frac{\partial}{\partial z}\left(\mu\frac{\partial v}{\partial z}+\mu\frac{\partial w}{\partial x}\right) & - & \frac{\partial p}{\partial y} & = 0 \\ \frac{\partial}{\partial x}\left(\mu\frac{\partial u}{\partial z}+\mu\frac{\partial w}{\partial x}\right) & + & \frac{\partial}{\partial y}\left(\mu\frac{\partial v}{\partial z}+\mu\frac{\partial w}{\partial y}\right) & + & \frac{\partial}{\partial z}\left(2\mu\frac{\partial w}{\partial z}\right) & - & \frac{\partial p}{\partial z}-\rho g & = 0 \end{pmatrix} \tag{D.1}$$

$$\frac{\partial u}{\partial x}+\frac{\partial v}{\partial y}+\frac{\partial w}{\partial z}=0 \tag{D.2}$$

where:

- u, v, and w are the ice velocity components in a 3D Cartesian space (x, y, z)

- μ is the ice effective viscosity
- p is the ice pressure
- ρ is density of ice
- g is the gravitational constant

D.1.2 Shallow Shelf Approximation

$$\begin{pmatrix} \frac{\partial}{\partial x}\left(4H\bar{\mu}\frac{\partial u}{\partial x} + 2H\bar{\mu}\frac{\partial v}{\partial y}\right) & + & \frac{\partial}{\partial y}\left(H\bar{\mu}\frac{\partial u}{\partial y} + H\bar{\mu}\frac{\partial v}{\partial x}\right) & = \rho g H \frac{\partial s}{\partial x} \\ \frac{\partial}{\partial x}\left(H\bar{\mu}\frac{\partial u}{\partial y} + H\bar{\mu}\frac{\partial v}{\partial x}\right) & + & \frac{\partial}{\partial y}\left(4H\bar{\mu}\frac{\partial v}{\partial y} + 2H\bar{\mu}\frac{\partial u}{\partial x}\right) & = \rho g H \frac{\partial s}{\partial y} \end{pmatrix} \tag{D.3}$$

where:

- $\bar{\mu}$ is the depth-averaged viscosity
- H is the ice thickness
- s is the upper surface elevation

D.1.3 Shallow Ice Approximation

$$\begin{pmatrix} \frac{\partial}{\partial z}\left(\mu\frac{\partial u}{\partial z}\right) & = \rho g \frac{\partial s}{\partial x} \\ \frac{\partial}{\partial z}\left(\mu\frac{\partial v}{\partial z}\right) & = \rho g \frac{\partial s}{\partial y} \end{pmatrix} \tag{D.4}$$